FABRICATION AND PROCESS OPTIMIZATION OF GEL CASTED SiO_2–Si_3N_4–BN CERAMIC COMPOSITES FOR RADOMES

Submitted in partial fulfilment of the requirements

for the award of the degree of

Doctor of Philosophy

by

KANDI KISHORE KUMAR

Roll No: 701240

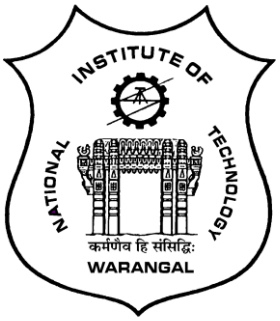

Department of Mechanical Engineering
NATIONAL INSTITUTE OF TECHNOLOGY
WARANGAL – 506004
Telangana State, INDIA.

October – 2016

FABRICATION AND PROCESS OPTIMIZATION OF GEL CASTED SiO_2–Si_3N_4–BN CERAMIC COMPOSITES FOR RADOMES

Submitted in partial fulfilment of the requirements

for the award of the degree of

Doctor of Philosophy

by

KANDI KISHORE KUMAR

Roll No: 701240

Supervisor:

Dr. C.S.P. Rao

Professor

Department of Mechanical Engineering
NATIONAL INSTITUTE OF TECHNOLOGY
WARANGAL – 506004
Telangana State, INDIA.
October – 2016

THESIS APPROVAL FOR Ph.D.

This thesis entitled **"Fabrication and Process Optimization of Gel casted SiO_2–Si_3N_4–BN Ceramic Composites for Radomes"** by **Mr. Kandi Kishore Kumar** is approved for the degree of Doctor of Philosophy.

Examiners

_____

_____

_____

Supervisor

Dr. C. S. P. Rao

Professor, Mechanical Engineering Department, NIT Warangal

Chairman

Prof. S. Srinivasa Rao

Head, Mechanical Engineering Department, NIT Warangal

NATIONAL INSTITUTE OF TECHNOLOGY

WARANGAL – 506 004, Telangana State, INDIA

CERTIFICATE

This is to certify the thesis entitled **"Fabrication and Process Optimization of Gel casted SiO_2–Si_3N_4–BN Ceramic Composites for Radomes"** submitted by **Mr. Kandi Kishore Kumar** for, Roll No. 701240, to **National Institute of Technology, Warangal** in partial fulfilment of the requirements for the award of the degree of **Doctor of Philosophy in Mechanical Engineering** is a record of bonafide research work carried out by him under my supervision and guidance. This work has not been submitted elsewhere for the award of any degree.

Place: Warangal.
Date:

Dr. C.S.P. Rao
(Supervisor)
Professor,
Department of Mechanical Engineering,
National Institute of Technology,
Warangal, Telangana State.

NATIONAL INSTITUTE OF TECHNOLOGY

WARANGAL – 506 004, Telangana State, INDIA

DECLARATION

This is to certify that the work presented in the thesis entitled "**Fabrication and Process Optimization of Gel casted SiO_2–Si_3N_4–BN Ceramic Composites for Radomes**", is a bonafide work done by me under the supervision of **Dr. C.S.P. Rao**, Professor, Department of Mechanical Engineering, NIT Warangal, India and has not been submitted for the award of any degree to any other University or Institute.

I declare that this written submission represents my ideas in my own words and where ever others ideas or words are included have been adequately cited and referenced with the original sources. I also declare that I have adhered to all principles of academic honesty and integrity and have not misrepresented or fabricated or falsified any idea/data/fact/source in my submission. I understand that any violation of the above will cause for disciplinary action by the institute and can also evoke penal action from the sources which have thus not been properly cited or from whom proper permission has not been taken when needed.

Place: Warangal.
Date:

Kandi Kishore Kumar
Roll No. 701240

Dedicated to my Gurus,

my parents, my wife Madhavi,

and my lovely children

Rushikesh & Shashikesh

“Research is what I’m doing when I don’t know what I’m doing.”

-Wernher von Braun

ACKNOWLEDGEMENTS

Firstly, I would like to express my sincere gratitude to my beloved supervisor **Dr. C.S.P. Rao**, Professor, Department of Mechanical Engineering for the continuous support during my research work, for his patience, motivation, and immense knowledge. His guidance helped me in all the time of research and writing of this thesis. I could not have imagined having a better advisor and tremendous mentor for my Ph.D. study. His advice on both research as well as on my career have been priceless. Without his guidance and persistent help this dissertation would not have been possible.

My heartfelt tribute and thanks to Late **Dr. B. Siva Prasad Reddy**, Associate Professor, Department of Mechanical Engineering. I would not have been in this position without his initial support and encouragement. I missed him a lot.

I would like to extend my sincere thanks to my Doctoral Scrutiny Committee members, **Prof. S. Srinivasa Rao**, Head, Department of Mechanical Engineering, **Prof. L. Krishnanand**, former Head, **Dr. N. Selvaraj**, Professor, **Dr. R. Narasimha Rao**, Associate Professor and **Dr. P. Subhash Chandra Bose**, Assistant Professor, Department of Mechanical Engineering, and **Dr. N. Narasaiah**, Associate Professor, Department of Metallurgical and Materials Engineering for serving as my committee members even at hardship. I would also like to thank them for their insightful comments and encouragement, but also for the hard question which incented me to widen my research from various perspectives.

I express my sincere thanks to the Director, National Institute of Technology, Warangal for providing necessary facilities for my research and for the encouragement by providing necessary financial assistance for attending the conferences.

I am also grateful to **Dr. Sumit Kumar Pal**, Assistant Professor, Department of Ceramic Engineering, National Institute of Technology, Rourkela for enlightening me the first glance of research. I am extremely thankful and indebted to him for sharing expertise, and sincere and valuable guidance and encouragement extended to me. Without his precious support it would not be possible to conduct this research. My sincere thanks also go to **Dr. S.K. Prathihar**, Associate Professor, Head, Department of Ceramic Engineering, National Institute of Technology, Rourkela who provided me an access to their laboratory and research facilities.

I take this opportunity to express gratitude to the entire Faculty Members of Mechanical Engineering department for their help and support.

I would like to thank administrative and technical staff members of the institute who have been kind enough to advise and help in their respective roles.

I thank my friends **M. Sreenivasa Rao**, **M. Sandeep Kumar**, **N. Shiva Kumar**, **A. Manmadha Chary** and **P. Naresh** for all the fun we have had in the last four years. Also I thank my co-researchers **Mrs. T. Nagaveni**, **V. Jeevan**, **N. Vishnumurthy**, **P. Gurabvaiah, T. Gopal Rao, P. Madhukar** and **C. Naresh**. I cherish to remember my association with **Shantan**, **Yusuf Salim**, **Anand** and **Nikhil** who contributed either directly or indirectly in successful completion of this research work. I also wish to thank **Mr. Rangilal**, Technical Assistant, **Mr. Ilaiah** and **Mr. Raju** Lab Technicians in Production Engineering Section for their help.

A special thanks to my parents **Mrs. Sujatha** and **Mr. Yadagiri** for the unceasing encouragement, support, attention and for all of the sacrifices they have made on my behalf and incented me to strive towards my goal.. Words cannot express how grateful I am to my mother-in law **Mrs. Padma** and father-in-law **Mr. Sambaiah** for helping us financially when the pockets are empty.

At the end I would like express appreciation to my beloved wife **Mrs. Madhavi** for her patience and sacrifice throughout my course. Without her, this dissertation would never have been completed.

I have to thank my lovely sons **Rushikesh** and **Shashikesh**, for their love, patience, understanding, and allowing me to spend most of the time on my research by sparing their playtime and enjoyment.

Last but not least, I thank God, the almighty for giving me the strength, will and wisdom to carry out my work successfully.

Kandi Kishore Kumar

PUBLICATIONS

1. Effect of Monomers Content and their Ratio on Gelcasting of Fused Silica Ceramics, *Transactions of the Indian Ceramic Society*, 75(3), 1-4 (2016).

2. Development of Silicon Nitride-Based Ceramic Radomes–A Review, *International Journal of Applied Ceramic Technology*, 12(5) 909–920 (2015).

3. Effect of Dispersant on the Rheological Properties of Gelcast Fused Silica Ceramics, *Journal of Material Science and Engineering*, 149 (2016) 012063 (IOP Science, UK).

4. Preparation and Characterization of Si_3N_4-BN Ceramic Composites by Gelcasting, *Material Science Research India*, 13(1), 28-33 (2016).

5. Modeling of Process Parameters of Gelcast Fused Silica Ceramics using Response Surface Methodology, *Materials Today: Proceedings* (Elsevier). (Accepted)

6. Modeling and Optimization of Process Parameters of SiO_2-Si_3N_4 Gelcast Ceramic Composites Using RSM, *Materials Today: Proceedings* (Elsevier). (Accepted).

7. Preparation and Modeling of Gelcast Si_3N_4 Ceramics Using Multi Gene Genetic Programming, *Materials Today: Proceedings* (Elsevier). (Accepted)

8. Modeling of Gelcast Ceramics using GP and Multi Objective Optimization using NSGA-II, *Materials Today: Proceedings* (Elsevier). (Accepted)

9. An Evolutionary Approach for Modeling and Optimization of Gelcasting of Ceramics, *Materials Today: Proceedings* (Elsevier). (Accepted)

10. Aqueous Gelcasting of SiO_2-Si_3N_4-BN Ceramic Composites and Optimization using RSM. *International Journal of Applied Ceramic Technology*. (Communicated)

ABSTRACT

Ceramics are highly regarded for their mechanical properties such as strength, durability, and hardness. These are widely used in electronic applications such as semiconductors, conductors, insulators, and magnets due to their electrical and magnetic properties. Advanced ceramics have been progressively used in aerospace, automotive engine, defense, construction, biomedical, nuclear industries, chemical, petrochemical, oil/gas, and industrial wear because of their high strength at elevated temperature, high thermal and chemical stability, low density and high wear resistance. Some applications include space shuttle engine components, tank armor, superconductors and piezoelectric devices.

Radar plays a major role in governing sea and air transportation, predicting the weather, surveying, remote sensing, monitoring certain areas, and defense. A radome is essential to guard the radar against environmental aspects. The radome is an aerodynamic structural part attached to the fore-end of a missile. It transmits electromagnetic signals with minimum attenuation and also protects radar communication system, and thus, the radomes are made of ceramics as they have desirable properties required by the radomes. The flexural strength, dielectric constant, and loss tangent values of various ceramic materials used in the development of radomes are important in the selection of radome materials. Different nose cone shapes of missile radomes are also important. Ceramic materials show variation in properties with sintering time, temperature, and other additives. The existing different near-net shape fabrication techniques for manufacturing of ceramic radomes are discussed and compared. Gelcasting is one of the manufacturing techniques to produce radomes with homogeneous and high green strength.

Literature gaps are identified and a problem is defined for the present state of work. A problem related to gelcasting of SiO_2, SiO_2–Si_3N_4, SiO_2–BN and SiO_2–Si_3N_4–BN ceramic composites is formulated. Experiments were conducted on SiO_2 based composites using gelcasting method by varying precursor amounts, solid loadings, monomers and its contents to identify the best suitable material for wave transparent materials. Silicon nitride (Si_3N_4) and Boron nitride (BN) powders were added to SiO_2 to improve the flexural strength keeping porosity and dielectric constant in range, which are required for wave transparent materials. Effect of various process parameters of gelcasting on rheological, mechanical and dielectric properties are studied on these SiO_2 based ceramic composites. A new composite of SiO_2,

Si_3N_4 and BN is proposed for wave transparent materials (radomes) which have got excellent properties. Colloidal stability and various colloidal processing techniques are discussed in this work.

The detailed experimental plans involving a number of experiments for gelcasting of SiO_2, SiO_2–Si_3N_4, SiO_2–BN and SiO_2–Si_3N_4–BN ceramic composites were designed using Design Expert 9.0 software. A face-centered central composite design of RSM with 6 center points has been used in the experimental plan. The levels of input parameters solid loading (i.e. SiO_2, Si_3N_4 and BN content), monomer content, and ratio of monomers were fixed based on the results of trial experiments. SiO_2, SiO_2–Si_3N_4, SiO_2–BN and SiO_2–Si_3N_4–BN ceramic composites were prepared by gel casting technique by varying solid loading, Si_3N_4 content, BN content monomer content, and ratio of monomers. Trial experiments were conducted and the sintering temperature has been fixed as 1250°C for sintering all the ceramic composites. Characteristics like flexural strength, porosity, and dielectric constants are planned to measure as per the design of experiments. Research objectives are projected and a work plan is derived to achieve the objectives.

The rheological behavior of the SiO_2 suspensions including SiO_2–Si_3N_4, SiO_2–BN and SiO_2–Si_3N_4–BN by varying dispersant content, pH value and solid loading has been thoroughly studied and useful ranges of solid loading (SL), monomer content (MC), ratio of monomers (RM), Si_3N_4 and BN contents were decided based on trial experiments and they are solid loading: 68 to 72 vol% for SiO_2 ceramics and 42 to 50 vol% for SiO_2–Si_3N_4, SiO_2–BN and SiO_2–Si_3N_4–BN ceramic composites, monomer content: 10 to 15 wt%, ratio of monomers: 3 to 7, Si_3N_4 content: 5 to 15 wt%, BN content: 5 to 15 wt%. Darvan 821A is recommended as a dispersant and a dosage of 0.5 wt% showed better results over other dispersants in the suspension of ceramic particles as 0.5 wt% Darvan 821A gives the maximum zeta potential value for all SiO_2 suspensions.

The author had developed porous SiO_2, SiO_2–Si_3N_4, SiO_2–BN and SiO_2–Si_3N_4–BN ceramic composites by gelcasting method at varying solid loading (SL), monomer content (MC) and ratio of monomers (RM) as per RSM and DOE basis and evaluated flexural strength, porosity, and dielectric constant using sophisticated instrumentation. Flexural strength, porosity, and dielectric constant are very important properties of radomes. The regression models for the analysis of responses such as flexural strength, porosity, and

dielectric constant are developed and the effects of the process parameters on these responses are studied. The optimum process parameters for maximum flexural strength, maximum porosity and minimum dielectric constant were evaluated using RSM coupled with desirability function to optimize multiple responses.

The optimum process parameters for maximum flexural strength, maximum porosity and minimum dielectric constant were evaluated using RSM coupled with desirability function to optimize multiple responses. The values of responses i.e. flexural strength, porosity and dielectric constant obtained by experimental runs are compared with predicted regression models for flexural strength, porosity, and dielectric constant for SiO_2, SiO_2–Si_3N_4, SiO_2–BN and SiO_2–Si_3N_4–BN ceramic composites. Flexural strength of the ceramic composite has been increased by the addition of Si_3N_4 and BN ceramics. Porosity and dielectric constant are in range with SiO_2 ceramics. It has been found that SiO_2 ceramics is having a lower flexural strength and good porosity and dielectric constant, hence such material may be considered for lower range missile radomes.

CONTENTS

ACKNOWLEDGEMENTS **i-ii**

PUBLICATIONS **iii**

ABSTRACT **iv-vi**

CONTENTS **vii-xii**

LIST OF FIGURES **xiii-xvii**

LIST OF TABLES **xviii-xxi**

ABBREVIATIONS **xxii**

NOMENCLATURE **xxiii**

CHAPTER 1 INTRODUCTION **1-33**

1.1 Introduction to ceramics 1

1.2 Ceramic composites 2

1.2.1. Advantages 3

1.2.2. Applications 3

1.3 Radome 3

1.3.1. Different shapes of missile radomes 5

1.4 Colloidal processing techniques 9

1.4.1. Physical gelation methods 12

1.4.1.1. Direct Coagulation Casting 12

1.4.1.2. Temperature induced forming 13

1.4.1.3. Temperature induced gelation 13

1.4.1.4. Colloidal isopressing 14

1.4.2. Chemical gelation methods 14

1.4.2.1. Freeze casting 14

1.4.2.2. Aqueous injection molding 15

1.4.2.3. Hydrolysis assisted solidification 15

1.4.2.4. Gelcasting 16

1.5 Applications of gelcasting 19

1.6 Rheology 21

1.6.1. Viscosity 21

1.6.2. Zeta potential and pH value 23

1.6.3. Dispersion 24

1.6.4. Solid loading 24

1.7 Properties required for a radome 25
1.7.1. Flexural strength 25
1.7.2. Bulk density and apparent porosity 25
1.7.3. Dielectric constant and loss tangent 26
1.8 Design of experiments 27
1.8.1. Response surface methodology 28
1.8.2. Central composite design 29
1.8.2.1. Factorial points 29
1.8.2.2. Star or axial points 30
1.8.2.3. Center points 30
1.8.3. Desirability function for optimization 31
1.9 Organization of thesis 32
1.10 Summary 33
CHAPTER 2 LITERATURE REVIEW 34-51
2.1 Introduction 34
2.2 Radome materials 34
2.3 Sintering aids for nitrides 35
2.4 Review on SiO_2 ceramics 37
2.5 Review on SiO_2–Si_3N_4 ceramic composites 38
2.6 Review on SiO_2–BN ceramic composites 39
2.7 Review on BN–Si_3N_4 ceramic composites 41
2.8 Review on Si_3N_4–BN–SiO_2 ceramic composites 43
2.9 Gap analysis 48
2.10 Problem formulation 48
2.11 Research objectives 48
2.12 Work plan 49
2.13 Summary 51
CHAPTER 3 MATERIALS AND EXPERIMENTAL SETUP 52-75
3.1 Introduction 52
3.2 Ceramic materials 52
3.2.1. Fused Silica 52
3.2.2. Silicon nitride 54
3.2.3. Boron nitride 55
3.3 Dispersant 57

3.4 Monomers 57
3.4.1. Methacrylamide 58
3.4.2. *N*,*N'*-Methylenebisacrylamide 59
3.5 Initiator and Catalyst 60
3.6 Surfactant 61
3.7 Equipment used in this work 61
3.7.1. Magnetic stirrer 61
3.7.2. Rotational Rheometer 62
3.7.3. Zeta Potential Analyzer 63
3.7.4. Desiccators 64
3.7.5. Humidity Controlled Oven 65
3.7.6. Moulds 66
3.7.7. High-Temperature Programmable Tube Furnace 67
3.7.8. X-ray Diffractometer 69
3.7.9. Scanning Electron Microscope 69
3.7.10. Diamond Cut-Off Saw 70
3.7.11. Universal Testing Machine 71
3.7.12. Electronic Analytical Precision Balance 72
3.7.13. Impedance Analyzer 73
3.8 Summary 74
CHAPTER 4 PREPARATION OF CERAMIC COMPOSITES BY GELCASTING 75-111
4.1 Introduction 75
4.2 Pilot experimentation for gelcasting of SiO_2 ceramics 75
4.2.1. Materials 75
4.2.2. Slurry preparation 76
4.2.3. Results and analysis of pilot experiments 78
4.2.3.1. Zeta potential and pH value 78
4.2.3.2. Dispersant 79
4.2.3.3. Solid loading 80
4.2.3.4. Mechanical properties 81
4.2.3.5. Summary of pilot experimentation 84
4.3 Pilot experimentation for gelcasting of SiO_2–Si_3N_4, SiO_2–BN and SiO_2–Si_3N_4–BN ceramic composites 84
4.3.1. Materials 84

4.3.2. Slurry preparation 85
4.3.3. Results and analysis of pilot experiments of SiO_2–Si_3N_4 ceramic composites 89
4.3.3.1. Zeta potential and pH value 89
4.3.3.2. Solid loading 90
4.3.3.3. X-Ray diffraction analysis and Microstructure 91
4.3.4. Results and analysis of pilot experiments of SiO_2–BN ceramic composites 93
4.3.4.1. Zeta potential and pH value 93
4.3.4.2. Solid loading 94
4.3.4.3. X-Ray diffraction analysis and Microstructure 94
4.3.5. Results and analysis of pilot experiments of SiO_2–Si_3N_4–BN ceramic composites 96
4.3.5.1. Zeta potential and pH value 96
4.3.5.2. Solid loading 97
4.3.5.3. X-Ray diffraction analysis and Microstructure 98
4.3.6. Pilot experimentation for gelcasting of SiO_2–Si_3N_4, SiO_2–BN and SiO_2–Si_3N_4–BN ceramic composites 99
4.4 Design of experiments 99
4.4.1. Experimental plan for SiO_2 ceramics 100
4.4.2. Experimental plan for SiO_2–Si_3N_4 ceramic composites 102
4.4.3. Experimental plan for SiO_2–BN ceramic composites 104
4.4.4. Experimental plan for SiO_2–Si_3N_4–BN ceramic composites 107
4.5 Summary 111
CHAPTER 5 RESULTS AND DISCUSSION 112-187
5.1 Introduction 112
5.2 Results and analysis for SiO_2 ceramics 112
5.2.1. Regression model for flexural strength 112
5.2.1.1. Optimization of flexural strength using desirability function 115
5.2.2. Regression model for porosity 116
5.2.2.1. Optimization of porosity using desirability function 119
5.2.3. Regression model for dielectric constant 120
5.2.3.1. Optimization of dielectric constant using desirability function 122
5.2.4. Multi-response optimization using desirability function 124

5.2.5. Confirmation test 127
5.3 Results and analysis for SiO_2–Si_3N_4 ceramic composites 129
5.3.1. Regression model for flexural strength 129
5.3.1.1. Optimization of flexural strength using desirability function 131
5.3.2. Regression model for porosity 132
5.3.2.1. Optimization of porosity using desirability function 135
5.3.3. Regression model for dielectric constant 137
5.3.3.1. Optimization of dielectric constant using desirability function 140
5.3.4. Multi-response optimization using desirability function 142
5.3.5. Confirmation test 144
5.4 Results and analysis for SiO_2–BN ceramic composites 147
5.4.1. Regression model for flexural strength 147
5.4.1.1. Optimization of flexural strength using desirability function 149
5.4.2. Regression model for porosity 150
5.4.2.1. Optimization of porosity using desirability function 154
5.4.3. Regression model for dielectric constant 155
5.4.3.1. Optimization of dielectric constant using desirability function 158
5.4.4. Multi-response optimization using desirability function 160
5.4.5. Confirmation test 162
5.5 Results and analysis for SiO_2–Si_3N_4–BN ceramic composites 165
5.5.1. Regression model for flexural strength 165
5.5.1.1. Optimization of flexural strength using desirability function 167
5.5.2. Regression model for porosity 169
5.5.2.1. Optimization of porosity using desirability function 173
5.5.3. Regression model for dielectric constant 175
5.5.3.1. Optimization of dielectric constant using desirability function 177
5.5.4. Multi-response optimization using desirability function 179
5.5.5. Confirmation test 181
5.6 Comparison of all responses of SiO_2, SiO_2–Si_3N_4, SiO_2–BN and SiO_2–Si_3N_4–BN ceramic composites 185

5.7 Summary 187

CHAPTER 6 CONCLUSIONS AND SCOPE FOR FUTURE WORK 188-190

6.1 CONCLUSIONS 188

6.2 SCOPE FOR FUTURE WORK 190

APPENDIX 191-195

REFERENCES 196-210

LIST OF FIGURES

Number	Title	Page No.
1.1	Few ceramic components in practice	2
1.2	The typical structure of a radome	4
1.3	Different types of radome nose cone	5
1.4	Performance of drag on various nose shapes	6
1.5	Tangent ogive formed from the segment of a circle	7
1.6	Schematic diagram of radome wall structure	8
1.7	Overview of ceramic processing techniques	11
1.8	Schematic of the gel formation	16
1.9	Ceramic products produced with gelcasting	20
1.10	Illustration of the connection between suspension microstructure, inter-particle forces, and rheological behaviour	22
1.11	Possible rheological responses of colloidal systems	23
1.12	Schematic of three point bending	25
1.13	Schematic of Archimedes setup	26
1.14	Central composite design	30
2.1	The complete work plan	50
3.1	The microstructure of SiO_2 powder	53
3.2	The microstructure of Si_3N_4 powder	54
3.3	The microstructure of BN powder	56
3.4	Formation of polymer–solvent gel	58
3.5	Structure of Methacrylamide	58
3.6	The structure of *N*,*N*′-Methylenebisacrylamide	59
3.7(a)	The structure of Ammonium persulfate	60
3.7(b)	The structure of *N*,*N*,*N*′,*N*′-Tetramethylethylenediamine	60

3.8	The structure of Polyethylene glycol-400	61
3.9	Magnetic stirrer setup	62
3.10	Setup showing computer controlled Rheometer	63
3.11	Setup showing Zeta Potential Analyzer	64
3.12	Desiccators with vacuum pump	64
3.13	Humidity Controlled Oven	65
3.14	Molds for gelcasting	66
3.15	High-Temperature Tube Furnace	67
3.16	X-ray Diffractometer	69
3.17	Scanning Electron Microscope with sputtering setup	70
3.18	High-speed diamond cut-off saw	70
3.19	A Universal Testing Machine with three point bending setup	71
3.20	Electronic Analytical Precision Balance with Archimedes setup	72
3.21	Setup showing Impedance Analyzer	73
4.1	A detailed flowchart of gelcasting process of SiO_2 ceramics	76
4.2	Schematic showing the samples of SiO_2 ceramics	77
4.3	Zeta potential of SiO_2 slurries with various dispersants and wt.%	79
4.4	Variation of viscosities of slurries at various solid loadings	80
4.5	SEM micrograph of sintered fused silica ceramics	81
4.6	Bulk density and apparent porosity of sintered bodies	82
4.7	Effect of sintering temperature on flexural strength	82
4.8	XRD patterns of sintered fused silica ceramics	83
4.9	Effect of sintering temperature on dielectric constant and loss tangent	84
4.10	A detailed flowchart of gelcasting process of concern ceramic composite	86
4.11	Sintered samples of SiO_2–Si_3N_4, SiO_2–BN and SiO_2–Si_3N_4–BN ceramic composites	87

4.12	Zeta potential of SiO_2–Si_3N_4 slurries with dispersant Darvan 821A	90
4.13	Variation of viscosity of slurries at various solid loadings	91
4.14	XRD patterns of SiO_2–Si_3N_4 ceramic composite	92
4.15	SEM micrograph of sintered SiO_2–Si_3N_4 ceramic composite	92
4.16	Zeta potential of SiO_2–BN slurries with dispersant Darvan 821A	93
4.17	Variation of viscosity of slurry at various solid loadings	94
4.18	XRD patterns of SiO_2–BN ceramic composite	95
4.19	SEM micrograph of sintered SiO_2–BN ceramic composite	95
4.20	Zeta potential of SiO_2–Si_3N_4–BN slurries with dispersant Darvan 821A	96
4.21	Variation of viscosities of slurries at various solid loadings	97
4.22	XRD patterns of SiO_2–Si_3N_4–BN ceramic composite	98
4.23	SEM micrograph of sintered SiO_2–Si_3N_4–BN ceramic composite	99
5.1	Effect of process parameters on flexural strength	114
5.2	Ramp graphs of desirability function of flexural strength of SiO_2 ceramics	116
5.3	Bar graphs of desirability function	117
5.4	Effect of process parameters on porosity	118
5.5	Ramp graphs of desirability function for porosity	120
5.6	Bar graphs of desirability function for porosity	120
5.7	Effect of process parameters on dielectric constant	122
5.8	Ramp graphs of desirability function for dielectric constant	124
5.9	Bar graphs of desirability function for dielectric constant	124
5.10	Ramp graphs of desirability function for SiO_2 ceramics	126
5.11	Bar graphs of desirability function for SiO_2 ceramics	126
5.12	Effect of process parameters on flexural strength	130

5.13	Ramp graphs of desirability function for flexural strength of SiO_2–Si_3N_4 ceramic composite	132
5.14	Bar graph of desirability function	132
5.15	Effect of process parameters on porosity	134-135
5.16	Ramp graphs of desirability function for porosity of SiO_2–Si_3N_4 ceramic composite	137
5.17	Ramp graphs of desirability function for porosity of SiO_2–Si_3N_4 ceramic composite	137
5.18	Effect of process parameters on dielectric constant	139-140
5.19	Ramp graph of desirability function for dielectric constant of SiO_2–Si_3N_4 ceramic composite	142
5.20	Bar graph of desirability function for dielectric constant	142
5.21	Ramp graphs of desirability function for SiO_2–Si_3N_4 ceramic composite	144
5.22	Bar graphs of desirability function for SiO_2–Si_3N_4 ceramic composite	144
5.23	Effect of process parameters on flexural strength	148
5.24	Ramp graph of desirability function for flexural strength of SiO_2–BN ceramic composite	150
5.25	Bar graph of desirability function	150
5.26	Effect of process parameters on porosity	152-153
5.27	Ramp graph of desirability function for porosity of SiO_2–BN ceramic composite	155
5.28	Bar graph of desirability function for porosity	155
5.29	Effect of process parameters on dielectric constant	157-158
5.30	Ramp graph of desirability function for dielectric constant of SiO2 – BN ceramic composite	160
5.31	Bar graph of desirability function for dielectric constant	160
5.32	Ramp graphs of desirability function for SiO_2–BN ceramic composite	162
5.33	Bar graphs of desirability function for SiO_2–BN ceramic composite	162
5.34	Effect of process parameters on flexural strength	167

5.35	Ramp graphs of desirability function for flexural strength of SiO_2–Si_3N_4–BN ceramic composite	169
5.36	Bar graph of desirability function	169
5.37	Effect of process parameters on porosity	172-173
5.38	Ramp graphs of desirability function for porosity of SiO_2–Si_3N_4–BN ceramic composite	174
5.39	Bar graph of desirability function for porosity	175
5.40	Effect of process parameters on dielectric constant	177
5.41	Ramp graph of desirability function for dielectric constant of SiO_2–Si_3N_4–BN ceramic composite	179
5.42	Bar graph of desirability function for dielectric constant	179
5.43	Ramp graphs of desirability function for SiO_2–Si_3N_4–BN ceramic composite	181
5.44	Bar graphs of desirability function for SiO_2–Si_3N_4–BN ceramic composite	181
5.45	Comparison of flexural strength obtained for various ceramic composites	185
5.46	Comparison of porosity obtained for various ceramic composites	186
5.47	Comparison of dielectric constant obtained for various ceramic composites	186

LIST OF TABLES

Number	Title	Page No.
1.1	Summary of various direct casting techniques	18
1.2	Comparison of near-net shape fabrication techniques	19
2.1	Characteristics of commonly used Radome materials	36
2.2	Summary of manufacturing of SiO_2 and Si_3N_4–SiO_2 ceramic composites	45
2.3	Summary of manufacturing of BN-SiO_2 and Si_3N_4–BN ceramic composites	46
2.4	Summary of manufacturing of Si_3N_4–BN–SiO_2 ceramic composites	47
3.1	Typical properties of fused silica	53
3.2	Typical properties of Si_3N_4	55
3.3	Typical properties of BN	56
3.4	Dispersants used for slurry stabilization	57
3.5	Specifications of the Magnetic stirrer	62
3.6	Specifications of Rheometer	63
3.7	Specifications of Humidity Controlled Oven	65
3.8	Specifications of High-Temperature Tube Furnace	68
3.9	Specifications of Diamond Cut-Off Saw	71
3.10	Specifications of the Universal Testing Machine	72
3.11	Specifications of Electronic Analytical Precision Balance	73
4.1	Recipe for 75 ml of ceramic suspension with 70 vol% solid loading	78
4.2(a)	Recipe for 75 ml slurry with 50 vol% solid loading of SiO_2–Si_3N_4	88
4.2(b)	Recipe for 75 ml slurry with 50 vol% solid loading of SiO_2–BN	88
4.2(c)	Recipe for 75 ml slurry with 50 vol% solid loading of SiO_2–Si_3N_4–BN	89

4.3	Process parameters: Ranges and levels	100
4.4	Experimental plan for fabrication of SiO_2 ceramics	100
4.5	Experimental results for SiO_2 ceramics	101
4.6	Process parameters: Ranges and levels	102
4.7	Experimental plan for fabrication of SiO_2–Si_3N_4 ceramic composites	102
4.8	Experimental results for SiO_2–Si_3N_4 ceramic composites	103
4.9	Process parameters: Ranges and levels	104
4.10	Experimental plan for fabrication of SiO_2–BN ceramic composites	105
4.11	Experimental results for SiO_2–BN ceramic composites	106
4.12	Process parameters: Ranges and levels	107
4.13	Experimental plan for fabrication of SiO_2–Si_3N_4–BN ceramic composites	107
4.14	Experimental results for SiO_2 – Si_3N_4 – BN ceramic composites	109
5.1	ANOVA results for flexural strength	112
5.2	The range of input parameters and flexural strength for desirability	115
5.3	Optimal solutions for flexural strength	115
5.4	ANOVA results for porosity	117
5.5	The range of input parameters and porosity for desirability	119
5.6	Optimal solutions for porosity	119
5.7	ANOVA results for dielectric constant	121
5.8	The range of input parameters and dielectric constant for desirability	123
5.9	Optimal solutions for dielectric constant	123
5.10	Range of input parameters and responses for desirability	125
5.11	Set of optimal solutions for SiO_2 ceramics	125
5.12	Error between experimental and predicted values	127

5.13	ANOVA results for flexural strength	129
5.14	The range of input parameters and flexural strength for desirability	131
5.15	Optimal solutions for flexural strength	131
5.16	ANOVA results for porosity	133
5.17	The range of input parameters and porosity for desirability	136
5.18	Optimal solutions for porosity	136
5.19	ANOVA results for dielectric constant	138
5.20	The range of input parameters and dielectric constant for desirability	141
5.21	Optimal solutions for dielectric constant	141
5.22	The range of input parameters and responses for desirability	143
5.23	Set of optimal solutions for SiO_2–Si_3N_4 ceramic composite	143
5.24	Error between experimental and predicted values	145
5.25	ANOVA results for flexural strength	147
5.26	The range of input parameters and flexural strength for desirability	149
5.27	Optimal solutions for flexural strength	149
5.28	ANOVA results for porosity	151
5.29	The range of input parameters and porosity for desirability	154
5.30	Optimal solutions for porosity	154
5.31	ANOVA results for dielectric constant	156
5.32	The range of input parameters and dielectric constant for desirability	159
5.33	Optimal solutions for dielectric constant	159
5.34	The range of input parameters and responses for desirability	161
5.35	Set of optimal solutions for SiO_2–BN ceramic composite	161
5.36	Error between experimental and predicted values	163
5.37	ANOVA results for flexural strength	165

5.38	The range of input parameters and flexural strength for desirability	168
5.39	Optimal solutions for flexural strength	168
5.40	ANOVA results for porosity	170
5.41	The range of input parameters and porosity for desirability	173
5.42	Optimal solutions for porosity	174
5.43	ANOVA results for dielectric constant	175
5.44	The range of input parameters and dielectric constant for desirability	178
5.45	Optimal solutions for dielectric constant	178
5.46	The range of input parameters and responses for desirability	180
5.47	Set of optimal solutions for SiO_2–Si_3N_4–BN ceramic composite	180
5.48	Error between experimental and predicted values	182
5.49	Comparison of S1, S2, S3 and S4 ceramic composites	187

ABBREVIATIONS

AIM	Aqueous Injection Molding
ANOVA	Analysis of variance
APS	Ammonium persulfate
CCD	Central composite design
DCC	Direct Coagulation Casting,
DE	Dielectric constant
DOE	Design of Experiments
FS	Flexural strength
HAS	Hydrolysis Assisted Solidification
MAM	Methacrylamide
MBAM	*N*,*N'*-Methylenebisacrylamide
MC	Monomers content
Por.	Porosity
PEG	Polyethylene glycol
SL	Solid loading
RM	Ratio of monomers
RSM	Response surface methodology
SEM	Scanning electron microscopy
TEMED	*N*,*N*,*N'*,*N'*- Tetramethylethylenediamine
TIF	Temperature Induced Forming
TIG	Temperature Induced Gelation
XRD	X-Ray Diffractometer

NOMENCLATURE

η	Viscosity
τ	Shear stress
γ	Shear rate
P	Fracture load
L	Length of support span
b	Width of the sample
h	Height
BD	Bulk Density
AP	Apparent porosity
DW	Dry Weight
SW_1	Soaked Weight
SW_2	Suspended weight
ρ	Density
K	Dielectric constant
c	Capacitance
d	Thickness of the specimen
A	Area of the cross-sectional surface
ε	Permittivity of the medium
ε_0	Permittivity of free space or vacuum
ε_r'	Relative permittivity
ε_r''	The ratio of energy loss
Y	Response

CHAPTER 1

INTRODUCTION

1.1. Introduction to ceramics

The term “ceramic” is originated from the Greek term “keramikos”, which is referred to pottery. The growing need for higher strength materials is driving modern industries toward the development of advanced ceramic materials. Generally, ceramics are termed as “inorganic, heat-formed and non-metallic materials that are normally manufactured using clay and other minerals obtained from earth or other chemically processed powders”. Ceramics can further be defined as “solid materials, which demonstrate exceptionally strong ionic bonding and in few cases covalent bonding” (Ahmed, 2015). They include glasses, or non-crystalline varieties, as well as traditional clays. Bricks of a brick building, dishes, and coffee mugs are some recognizable ceramics. However, today, ceramics have found use in advanced applications.

Ceramics are highly regarded for their mechanical properties such as strength, durability, and hardness. These are widely used in electronic applications such as semiconductors, conductors, insulators, and magnets due to their electrical and magnetic properties. Advanced ceramics have been progressively used in aerospace, automotive engine, defense, construction, biomedical, nuclear industries, chemical, petrochemical, oil/gas, and industrial wear because of their high strength at elevated temperature, high thermal and chemical stability, low density and high wear resistance. Some applications include space shuttle engine components, tank armor, superconductors and piezoelectric devices. Some of the ceramic components used in practice are shown in Figure 1.1.

Ceramic materials have high resistance to heat, corrosion, wear and abrasion. Thus makes them advantageous over other engineering materials including metals. These properties give complications in processing ceramic materials to the desired shapes and dimensions (Li et al., 2012). Its competence to near net shape fabrication by pressing and sintering process makes the economic production of ceramics possible; however, machining processes are yet to ensure dimensional and geometrical accuracy (Chelule et al., 2003). Unfortunately, ceramic

materials are difficult to machine and often fractured during the machining process (Zeng and Liu, 2015).

Figure 1.1. Few ceramic components in practice

Ceramics possess high-temperature resistance, corrosion resistance, stiffness, high hardness, and compressive strength. Despite of these advantages, the use of ceramic components in many engineering applications have been limited due to the inability to reproducibly and economically fabricate complex shaped components with a uniform homogeneous microstructure. Advanced ceramics possess a distinctive combination of light weight, hardness, and chemical inertness, hence often used in wear resistant applications (Hsu and Shen, 2004). Catastrophic failure occurs in ceramics when these are subjected to mechanical loading because they don't undergo plastic deformation like as metals deform owing to their intense mobility of dislocation. Even a minor crack can propagate so quickly that result in a sudden failure. Ceramic material properties strongly depend on the ceramic powder morphology, impurity, sintering aids and their composition, and forming and sintering parameters (Faoite et al., 2012).

1.2. Ceramic composites

A composite is a structural material that consists of two or more ingredients that are integrated are not soluble in each other. The most important advantage of a composite material over other material is the combination of different properties that are not often found in the conventional materials. Properties include improved fatigue and corrosion resistance, high strength to weight ratio, high thermal expansion resistance, exceptional magnetic and optical properties, combined fracture toughness and wear resistance etc (Narendra Kumar and Siva RamaKrishna, 2015). Nowadays there are several situations in industries that demand the

extraordinary combination of mechanical/electrical/electronic properties of materials and hence ceramic composites. Some of the disadvantages of ceramic composites are processing routes involve high temperatures hence only high-temperature reinforcements can be employed. These are intended to improve the strength of monolithic ceramics, the principal drawbacks include brittleness. Expensive in processing and difficult to fabricate complex shapes. Thermal stresses are developed in the composites on cooling from the processing temperatures due to the divergence in the thermal expansion coefficients amidst the medium and the reinforcement.

1.2.1. Advantages

- Excellent wear and corrosion resistance
- High strength to weight proportion
- High strength retention at superior temperatures
- High chemical inertness
- Non-catastrophic failure
- High stiffness
- Lightweight

1.2.2. Applications

Components made of ceramic composites are widely used in defense. Some are heat shield systems, rocket engines, gas turbines components like combustion chambers, stator vanes, and turbine blades, hot gas ducts, components for burners, flame holders, bearing components that require high wear and corrosion resistance, brake disks and brake system components for airplanes or cars that undergo excessive thermal shock. Ceramic radomes are widely used in rockets.

1.3. Radome

Radar plays a major role in governing sea and air transportation, predicting the weather, surveying, remote sensing, monitoring certain areas, and defense. A radome is essential to guard the radar against environmental aspects.

The radome is an aerodynamic structural part attached to the fore-end of a missile. A radome (the word is a contraction of radar and dome) is a lightweight structural, weatherproof enclosure that protects a microwave or radar antenna. The radome is made of some material that minimally attenuates to the electromagnetic signal transmitted or received by the antenna. In other words, the radome is transparent to radar or radio waves. The radome is often used to prevent ice and freezing rain from accumulating directly onto the metal surface of the antennas. Radomes can be manufactured into the desired shape and are widely used in marines, naval shipboard, aircraft, missiles, stationary antennas, and radar dishes to protect radar antenna from the wind, blowing sand, snow, ice, rain, ultraviolet sunlight, temperature, fungus, and corrosion.

Radome must have sufficient structural strength and fracture resistance to withstand the aerodynamic forces and foreign object impingement and also it should offer minimal aerodynamic resistance. The radome should have minimal attenuation and distortion of the outgoing and incoming radar energy (Kirby et al., 2000). A typical structure of a radome is shown in Figure 1.2.

Figure 1.2. The typical structure of a radome.

Materials used for the construction of radomes for high-speed missile applications should possess high flexural strength, low dielectric constant, low loss tangent, high thermal shock resistance, high rain erosion resistance, etc (Wang et al., 2010). The toughness of a radome is one of its significant properties. Nevertheless, a well-built radome should not increase drastically the entire Radar's weight. The expenditure of a radome is a further

concern. The expense of a radome must be much less than the expense of the Radar. Radomes are widely made of ceramics as they were light in weight and have good mechanical and electronic properties. Ceramic radomes are typically used for missiles intended to operate at speeds of Mach 4 or higher, also called hypersonic regime (Robert Traut, 1982). Numerous investigations are going on for the development of radomes with ceramic materials for high-speed missiles.

1.3.1. Different Shapes of Missile Radomes

The most common nose shapes for radomes are conical, tangent or secant ogive, elliptical or hemispherical, power series, parabolic series, haack series, or Von Karman. Some of the radome nose shapes are shown in Figure 1.3.

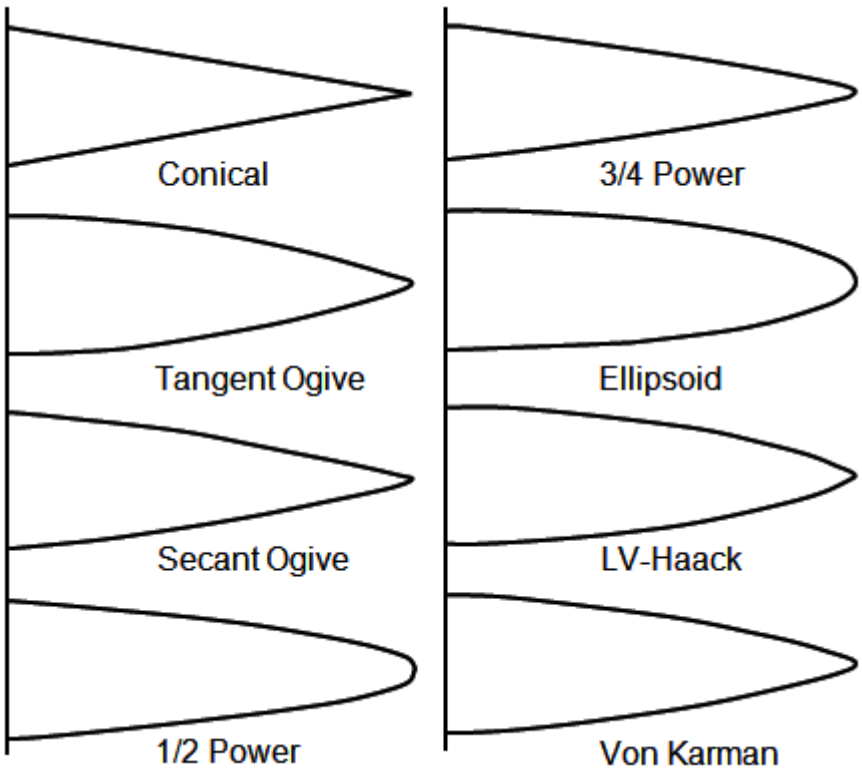

Figure 1.3. Different types of radome nose cone.

Below Mach 0.8, the nose pressure drag is essentially zero for all shapes and the pressure drag increases dramatically in the transonic region and beyond, where, the effect of nose shape on drag becomes highly significant. The factors influencing the pressure drag are the general shape of the nose cone, its fineness ratio, and its bluffness ratio. The ratio of the

length of a nose cone compared with its base diameter is known as the fineness ratio. At supersonic speeds, the fineness ratio has a very significant effect on nose cone wave drag. Fineness ratio of 5 is critical as the fineness ratio increases, and the wetted area and the skin friction component of drag increases (Crowell, 1996).

Sharp tips are ideally formed in most of the nose cone shapes and are often blunt to some degree for ease of manufacturing, resistance to handling, flight damage, and safety. This blunt is most often specified as a hemispherical "tip diameter" of the nose cone. The term bluffness ratio is often used to describe a blunt tip and is equal to the tip diameter divided by the base diameter. Fortunately, there is little or no drag increase for slight blunt of a sharp nose shape. In fact, there is a decrease in drag for bluffness ratios up to 0.2, with an optimum of 0.15 for constant overall lengths. Most commercially made tangent ogive nose cones are blunt to a bluffness ratio of about 0.1. Comparison of drag for different nose shapes of the radomes is shown in Figure 1.4.

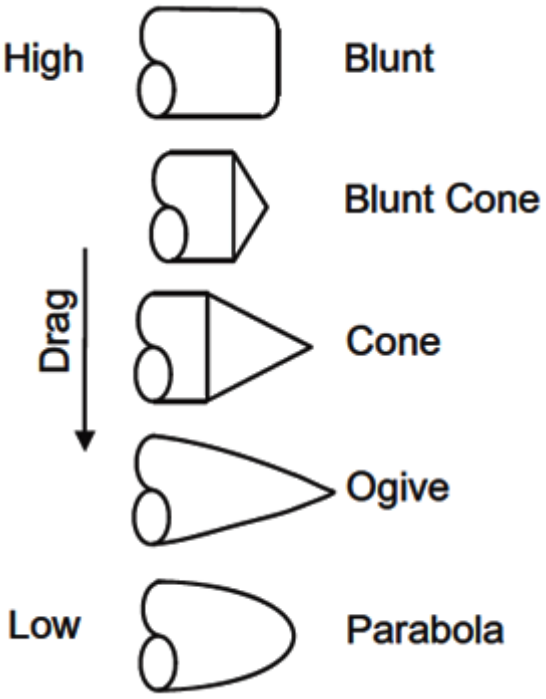

Figure 1.4. Performance of drag on various nose shapes.

For airborne radomes, the shape is chosen to be a tangent ogive to withstand the aerodynamic drag (Renuka and Borkar, 2005). The ogive shape has several advantages such as slightly greater volume for a given base and length, a blunter nose, providing structural superiority and lower drag (Chin, 1961). The profile of tangent ogive is formed by a segment

of a circle such that the rocket body is tangent to the curve of the nosecone at its base, and the base is on the radius of the circle as shown in Figure 1.5.

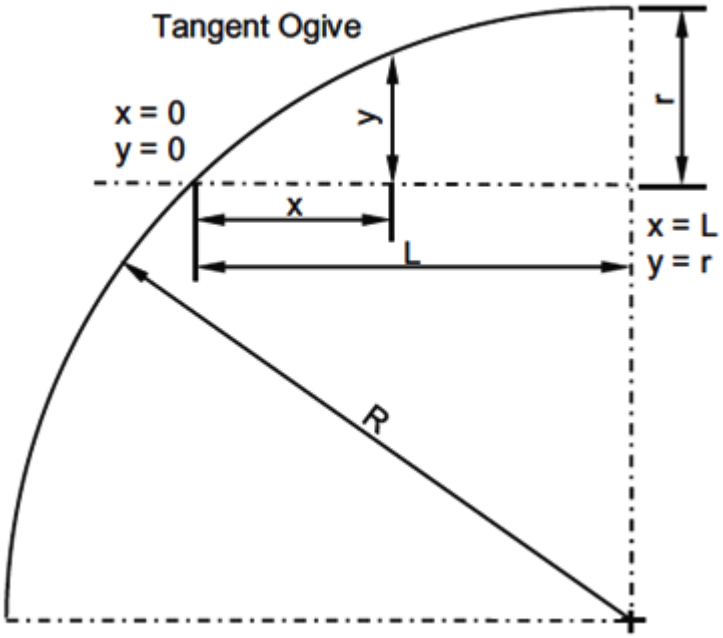

Figure 1.5. Tangent ogive formed from the segment of a circle.

The radius of the circle that forms the ogive is called the ogive radius 'R', and it is related to the length and base radius of the nose cone 'r':

$$R = \frac{r^2 + L^2}{2r} \tag{1.1}$$

The radius ***y*** at any point ***x***, as ***x*** varies from 0 to L is:

$$y = \sqrt{R^2 - (x - L)^2} + (r - R) \tag{1.2}$$

The nosecone length 'L' should be equal to, or less than the ogive radius. If they are equal, then the shape is a hemisphere (Crowell, 1996). The fore-end of missile shell radius is equal to the base radius 'r' of the radome.

As shown in Figure 1.6, the radome wall structure greatly determines the use of the defined frequencies or broadband (1‑18 GHz) wave transmissions (Nie et al., 2005) and for the defined frequency application, the half-wave wall structure is used (Gu et al., 2009).

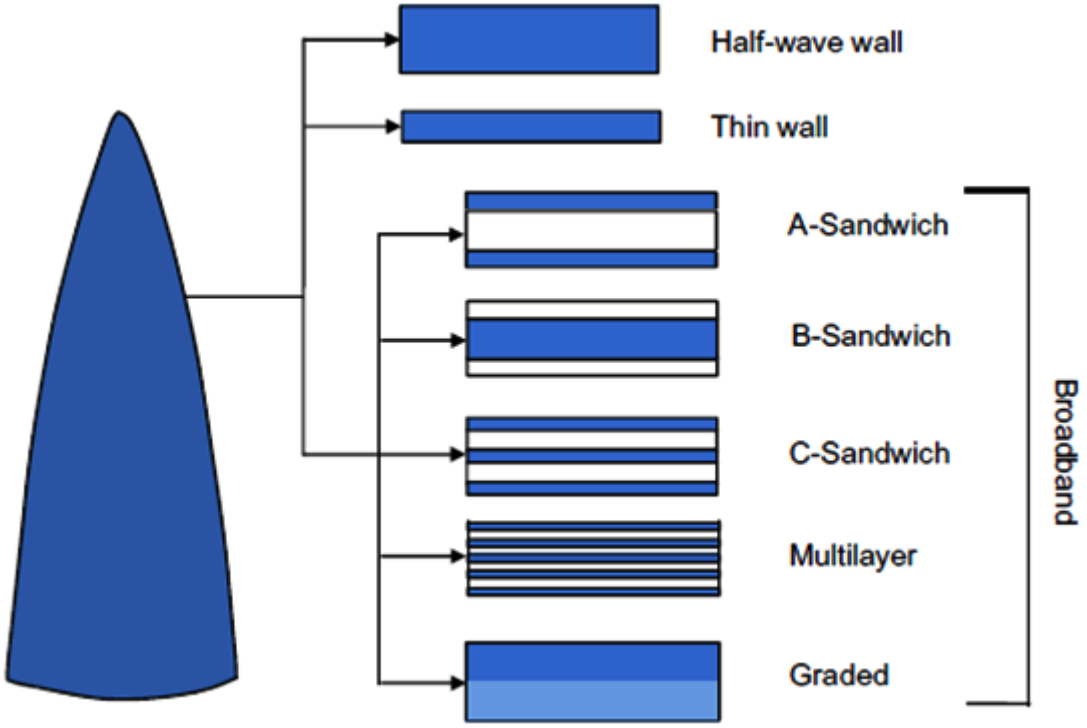

Figure 1.6. Schematic diagram of radome wall structure.

The most frequently used and reported radomes include A-sandwich, C-sandwich, and multilayer wall structures. On the other hand, these are unsuitable for the high-temperature conditions owing to large discrepancy in the thermal properties of each layer, that might restrict their application in the high-speed missile radome (Chen et al., 2010). The structure is designed to be composed of an odd multiple of five or more layers with no central matching layers at the design frequency. Investigations indicate that the multilayer structure exhibits multiband transmission property. The central layer thickness can be chosen in the range of 0.1-6 wavelengths, so as to provide sufficient mechanical strength and structural rigidity for the whole radome structure. The multilayer structure at a design frequency of 65 GHz turns to be a broadband radome wall structure in the 16‑100 GHz frequency range for both centimeter and millimeter waves applications (Zhou et al., 2012). To relieve the thermal stress between the layers, specially designed functionally graded materials have been developed and are used for ultrahigh temperature application (Mortensen and Suresh, 1995).

1.4. Colloidal Processing Techniques

Colloidal processing techniques are used as forming and processing techniques for ceramics and they are critical since the final finished properties of the components often depend on the various stages of colloidal processing (A detailed note on colloidal processing is given in Appendix). Defects introduced during the forming process may remain even after sintering process. Figure 1.7 shows a general overview of different ceramic processing techniques. These techniques can be divided into three categories: dry shaping, wet forming, and plastic shaping. Dry shaping is a very common method of producing ceramics in industry. Here predominately axial pressing techniques are used due to economic efficiencies and cost advantages. However, axial pressing has several disadvantages. Typical green strengths are relatively weak, which do not allow green machining. In addition during dry powder compaction, agglomerates can be formed in the green body. This can result in flaws in the final sintered part and therefore lower the mechanical properties. Dry pressing techniques such as hot pressing and hot isostatic pressing apply pressure during sintering (Kong et al., 2015). Components with higher densities and better mechanical behavior than axial pressing are produced using these techniques. Unfortunately hot pressing and hot isostatic pressing are expensive and cannot be used to produce complex shapes and hence are not efficient. This confines their usage in industry. All dry pressing techniques have limitations in producing complex shapes and geometries. This is due to the compaction tooling constraints due to the powder fill and part ejection mechanisms that occur during dry shaping. Forming complex shaped components (near net shaping) is one of the driving forces for the developments of direct casting techniques, which will be explained in detail later (Richerson, 1992).

Plastic forming techniques include extrusion and powder injection molding. Plastic forming involves the combination of powder and large concentrations of binder which results in a mixture that is deformable under pressure. The concentration of binder that is required to achieve adequate plasticity for forming is about 25-50 volume percent. The major problem of plastic forming is due to this large concentration of organics, which causes problems during the binder burnout step. Burnout of the binder can take up to several days with risks of warpage, distortion, cracks and slumping. Agglomerates will form in the green body with dry shaping, which will degrade the sintered strengths and fracture toughness. Also during the

removal of the organic phase, there is a concern for environmental pollution problems as well as health and safety issues (Reed, 1995).

Due to the inherent deficiencies of the dry shaping and, plastic shaping techniques, research efforts have concentrated on direct casting, which is a wet forming process. Wet forming has several advantages over dry shaping and plastic forming. Wet forming essentially uses the ceramic powder in a slurry form, which will allow for the stable dispersion of the colloidal ceramic particles. The slurry will undergo various mixing steps such as ball milling which allows for the break-up of agglomerates (potential sources of flaws). The ability to produce ceramics with finest packing and homogenous microstructure is one of the advantages of wet processing techniques in colloidal ceramic processing (Sigmund et al., 2000). Maximum flaw size reduction and an increase in reliability have been exhibited in Si3N4 ceramics through colloidal processing (Pujari et al., 1995). In addition, near net shape complex components can be formed with wet forming techniques.

Wet forming methods may be classified into two groups. They are drain casting and direct casting. In ceramic industries drain casting is extensively used. Slip casting, pressure casting, and centrifugal casting are the methods in drain casting. A porous mold is used in these methods, which by capillary forces causes a liquid-solid partition to fabricate a solid green body (Sigmund et al., 2005). Stress gradients are generated by the capillary forces which give rise to unreliable densities in green bodies that limit the production of thin walled complex shaped components. Research has been concentrated to build up other alternative techniques such as direct casting for colloidal ceramic processing in which the ceramic bodies are obtained directly from the slurry without removing the liquid. This makes direct casting advantageous over drain casting technique.

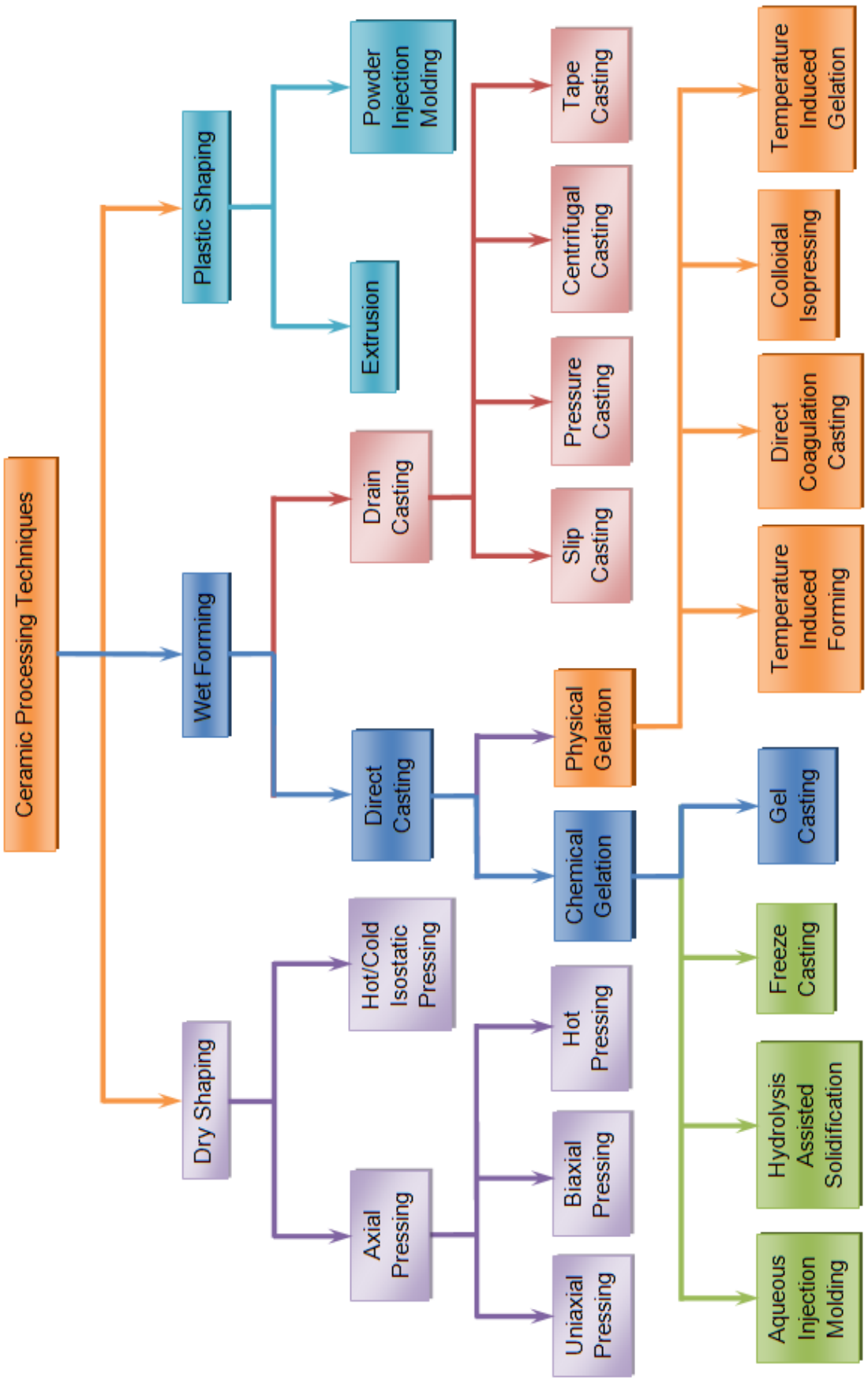

Figure 1.7. Overview of ceramic powder processing techniques

Direct casting involves using colloidal suspensions to mold the liquid slurry into a stiff demoldable gel. Research efforts have resulted in a number of approaches to develop a reliable cost effective direct casting forming technology. Based on the fundamental principles of physics and chemistry of the mechanism in dispersion and gelation reaction, direct casting is able to be categorized into physical gelation and chemical gelation. A percolating particle network is formed due to the transformation in the colloidal properties that causes the entire slurry to gel and this gelation is referred as physical gelation. Gelation caused by liquid immobilization or consuming the liquid chemically as soon as the dispersing medium transforms its properties as a result of a chemical reaction is referred as chemical gelation. A brief treatment of colloidal processing is required to enhance the manufacturing of ceramic composites. This is given below.

Direct Coagulation Casting (DCC), Temperature Induced Forming (TIF), Temperature Induced Gelation (TIG) and Colloidal Isopressing are physical gelation techniques. Chemical gelation techniques include Freeze Casting, Aqueous Injection Molding (AIM), Hydrolysis Assisted Solidification (HAS) and Gelcasting (Tari, 2003 and Sigmund et al., 2005). Each of the direct casting techniques has advantages and disadvantages. These forming methods will be briefly described below.

1.4.1. Physical Gelation methods

Physical gelation methods include Direct coagulation casting, Temperature-induced forming, Temperature-induced gelation and Colloidal isopressing. These processes were in detail presented below.

1.4.1.1. Direct coagulation casting

In Direct Coagulation Casting (DCC), gelation of the ceramic suspensions in a mold is accomplished by coagulation, by changing the force among the particles in the suspension from repulsive to attractive system (Baader et al., 1996, Balzer et al., 1999, Gauckler et al., 1999 and Prabhakaran et al., 2009). The force among the particles can be changed from repulsive to attractive system either by changing the pH value of the suspension to its isoelectric point by time-delayed reaction involving generation of an acid/base or by compression of electrical double layer by a time-delayed reaction involving generation of

excess electrolytes (Graule et al., 1995, Graule et al., 1996, Si et al., 1999 and Prabhakaran et al., 2002).

Advantages of DCC include ease in the fabrication of ceramic components with the complex shape at a low cost. Recyclable and economical molds made of metals or plastic can be used for casting the components at room temperature. This is independent of component size, shape, and thickness. Since the low volume of organic compounds such as dispersants and enzymes are used, a separate burnout step is not required (Gauckler et al., 1999). Disadvantages include low green strengths, limited time stability and a narrow pH window.

1.4.1.2. Temperature-induced forming

Temperature-induced forming (TIF) involves electric double layer stabilized slurry (Appendix), which is flocculated by temperature control (Bell et al., 1999, Yang et al., 2002 and Yang et al., 2001). To gel the slurry TIF employs the temperature dependency of the solubility. At room temperature, the electric double layer stabilized slurries perhaps be prepared, which will flocculate at about 80°C with an increase in the ionic strength. By polymer bridging, this process can be improved. At room temperature, the high surface charge is induced in TIF for stabilization of slurry by adsorbing a low molecular weight dispersant (Kissa, 1999).

In comparison with the conventional slip casting process, TIF has numerous advantages. When compared to drain casting technique green ceramic bodies with low stress are produced. The rheology of the slurry can be controlled by using temperature only. By changing the process parameters for example temperature and time, the extent of gelation perhaps altered since it is a physical gelation method. This flexibility enables fabrication of ceramic parts layer by layer without delamination problems (Bell et al., 1999).

1.4.1.3. Temperature-induced gelation

Temperature-induced gelation (TIG) involves flocculation of sterically stabilized slurries by the change of temperature (Bergstrom and Sjostrom, 1999). As the solvency is reduced to a significant stage the polymer network will catastrophe. This will lead to flocculation as soon as the Van der Waals forces surmount the outstanding steric repulsive forces. The addition of non-solvent or change in the temperature will reduce the solvency.

Transformation of this slurry into a flocculated state from a dispersed state will take place at room temperature.

Disadvantages of TIF include long times for consolidation of the green ceramic body. The strength of the green ceramic part produced by TIF is also relatively weak. A major disadvantage of TIG is the non-aqueous solvents used which pose as environmental hazards.

1.4.1.4. Colloidal Isopressing

Colloidal isopressing of ceramic powders has been introduced as a new method to form ceramic components from colloidal suspensions (Yu and Lange, (2001). The process is initiated with the removal of the strength degrading inclusions in the slurry by filtering. Shape forming necessitates a small amount of pressure for isopressing within the mold, after creating a semi-fluid consolidated body by a low-pressure consolidation. Following shaping, the green body can be quickly dried with no shrinkage, heated directly to the densification temperature. Advantages of CIP are strength degrading inclusions can be separated by filtering the slurry in the initial stage, forming period is short, complex shapes can be formed with high relative density and drying with no shrinkage (Joray et al.,2002). Disadvantages include low green strengths.

1.4.2. Chemical Gelation methods

Chemical gelation methods include Freeze casting, Aqueous injection molding, Hydrolysis assisted solidification and Gelcasting. These processes were in detail presented below.

1.4.2.1. Freeze casting

In freeze casting process, the water-based ceramic slurry was frozen in a mold simultaneously controlling the growth direction of ice, and sublimation of the ice was caused by drying it at a condensing pressure (Fukasawa et al., 2001). The frozen solvent will work as a strong binder holding the green ceramic body together (Sigmund et al., 2005). As a result, minimal organic binders are needed that lead to ceramic part with higher purity and these organic binders can be eliminated in the binder burnout stage. The solvent can be removed by a sublimation process to avoid the capillary forces normally present during drying that

eradicates cracking and warping during drying and shrinkage. This process does have several disadvantages in that heat transfers during solidification can be a problem as well as poor green strength parts are produced (Jones, 2000, Koch et al., 2003, Laurie et al., 1992, Sofie and Dogan, 2001 and Statham et al., 1998).

1.4.2.2. Aqueous injection molding

Aqueous injection molding was invented by Rivers in 1978 (Rivers, 1978). This process involves the use of methylcellulose polymers which are mixed with a concentrated suspension of particles. The methylcellulose polymer is soluble at room temperature. As the temperature is increased, the hydrated methylcellulose polymers release water molecules. This results in a viscosity decrease until about 50°C. At this temperature, the polymer is dehydrated enough to cause strong polymer chain-polymer chain interaction and therefore gel forms. Advantages of aqueous injection molding are that this process is a safe, water based and a low-cost technique. This process has many disadvantages in that the addition of methylcellulose to a colloidal suspension results in the high viscous slurry. The remedy for this is to lower the solids loading of the suspension (Lu, 2012). This lowers the green strength and results with components with poor green and sintered densities.

1.4.2.3. Hydrolysis assisted solidification

Hydrolysis assisted solidification (HAS) method is similar to freeze casting, to some extent, in which it undergoes an inorganic reaction consuming the dispersing medium (Krnel and Kosmac, 2003, Kosmac et al., 2001, Kosmac, 1999 and Novak and Kosmac, 1998). The method utilizes the thermally excited and/or accelerated hydrolysis of aluminium-nitride powder added to ceramic suspensions with high solid loading (Novak et al., 2002). Ammonia is formed by consuming water during hydrolysis of aluminium nitride that consecutively increases the pH value of the ceramic suspension. These mechanisms can be used to increase the viscosity of the slurry and cast a ceramic green body (Kosmac et al., 1997).

In HAS process precipitation of aluminium hydroxide takes place. Hence, the green strength in ceramic parts increases that allows manufacture of thin walled complex shapes with low shrinkage during drying. The major drawback of this process is the yielding of

Al_2O_3 in the sintered component during hydrolysis reaction thus restraining its use to few applications.

1.4.2.4. Gelcasting

Gelcasting was first developed at Oak Ridge National Laboratory (ORNL) in the 1960s for hard metals and further developed for ceramic materials by combining traditional slip processing with polymer chemistry (Omatete et al., 1991 and Omatete et al., 1997). The general principle in this process is the ceramic particles suspended are surrounded by a three-dimensional network of the cross-linked polymers. For obtaining maximum solid loading typically a dispersant is used which causes the particles in the ceramic slurry to disperse by means of an electric double layer or steric stabilization (Appendix). Shrinkage can be minimized during sintering process and dense ceramics can be obtained by high solid loading. The free-radical reaction leads to the formation of micro-gels of monomer and cross-linker inside the suspension, which eventually combine to form a macro-gel network. The gel network formed inside the suspension holds the particles together collectively (Figure 1.8) to mold a dense green body that is demoldable and takes the form of the mold cavity. Molds can be made up of metal or plastic materials that are nonporous (Omatete et al., 1991 and Omatete et al., 1997).

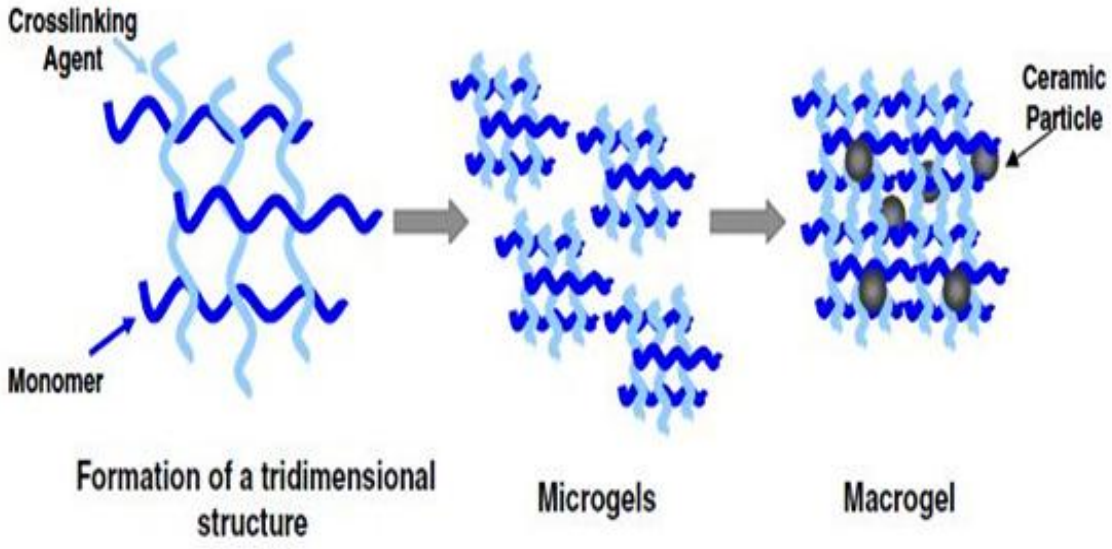

Figure 1.8. Schematic of the gel formation.

In this process, the concentrated ceramic slurry is obtained by mixing ceramic powder and monomer solution. After this ceramic suspension is poured into a mold to get the desired shape and during heating in-situ polymerization takes place to form a gel network to hold the ceramic particles collectively into a hard green body (Ranjith Kumar et al., 2007). The first gel monomer developed was acrylamide (AM) (Young et al., 1991). However, industry has been reluctant to use this technique because AM is a neurotoxin (Wan et al., 2014). AM was then replaced by a low toxic monomer methacrylamide (MAM). An initiator and catalyst are added to the milled mixture to initiate and accelerate the polymerization. The slurry was then cast into a non-porous mold. The liquid surrounding the ceramic particles will be permanently gelled by polymerization and holds the shape of the mold. The parts formed are then demolded and dried under controlled humidity conditions to reduce cracking and warping. In gelcasting process, drying time for green parts is usually long otherwise cracking and warping may take place. The green body can then undergo standard binder burnout and sintering processes (Omatete et al., 1997 and Janney et al., 1998).

The use of acrylamide or methacrylamide polymer materials in the gelcasting process has limited the use of this process in the industry due to the toxicity concerns. Therefore, different alternatives methods of gelcasting have been investigated. Research efforts have been focused on building up gelcasting processes which are environmentally safe and non-hazardous by examining various binders systems which gel or polymerize through either a chemical reaction process (Morissette et al., 2000, Huha and Lewis, 2000, Ma et al., 2003, Cai et al., 2003 and Zhou et al., 2000) or a thermal process (heating or cooling) (Li et al., 2014).

Materials that are naturally obtained, nontoxic and inexpensive have been successfully demonstrated as binders in gelcasting by many researchers in recent years. They include agarose (Millan et al., 2002 and Ewais and Ahmed, 2002), agar (Olhero et al., 2000 and Millan et al., 2002), chitosan (Bengisu and Yilmaz, 2002), carrageenan (Santacruz et al., 2002 and Santacruz et al., 2004), starch (Chandradass et al., 2009), gelatin (Chen et al., 1999 and Vandeperre et al., 2003), cellulose ethers (Li et al., 2008), etc. but low strength of green bodies seems inevitable in these systems (Wan et al., 2014). The disadvantage of these binders is they are not easily applicable to industrial processing. The gelcasting system developed at Oak Ridge which uses acrylamide or methacrylamide polymers did produce components which high green strengths. The major disadvantage with the alternative gelling

agents for gelcasting mentioned above is that they generally produce poor green strength components with little reliability and consistency.

Gelcasting technique was selected in this research study since it is a process which has been shown to produce high green strength components. Table 1.1 summarizes the different direct casting techniques.

Table 1.1. Summary of various direct casting techniques.

Direct Casting Technique	**Advantages**	**Disadvantages**
Gelcasting (polymer)	High green strength, Established process	Toxicity issues, expensive reagents
Gelcasting (natural additives)	Safe environmentally friendly, water-based process	Poor green strength
Hydrolysis-assisted solidification	High green density	Sensitive sample preparation, limited temperature stability
Aqueous Injection Molding	Safe environmentally friendly, water-based process	Poor green strength
Freeze Casting	Water based system, unique sublimation process	Poor green strength
Temperature Induced Gelation	Simple processing concept	Non-aqueous solvent system
Temperature-Induced Forming	Simple processing concept	Long forming times
Direct Coagulation Casting	Low organic content	Poor green strength, toxic additives

Over the conventional forming methods gelcasting has distinct advantages such as near-net shape fabrication, low contents of organic monomers, high sintered density, and ease of machinability owing to the intensity of homogeneity and high strength (Nojoomi et al., 2014). Use of non-porous metal or plastic molds that are reusable makes this process economical (Omatete et al., 1991 and Omatete et al., 1997). Gelcasting has more advantages such as the products produced are consistently defect free, uniformly dense and very strong,

and able to form very large parts compared with other forming processes shown in Table 1.2. Gelcasting is attractive for fabricating complex shapes such as radomes, turbine rotors, gears etc.

Table 1.2. Comparison of near-net shape fabrication techniques. (After Janney et al., 1998)

Property	**Gelcasting**	**Slip casting**	**Injection moulding**	**Pressure Casting**
Molding time	5-60 min	1-10 hrs	10-60 sec	10 min - 5 hr
Strength (As formed)	Moderate to high depending on gel system	Low	High	Low
Strength (Dried)	Very High	Low	N/A	Low
Mold Materials	Metal, glass, polymer, wax	Plaster	Metal	Porous plastic
Binder Burnout	2-3 hours	2-3 hours	Up to 7 days	2-3 hours
Molding defects	Minimal	Minimal	Significant	Minimal
Maximum part dimension	> 1 meter	> 1 meter	~30 cm, one dimension must be ≤ 1 cm	~0.5 meter
Warpage during drying/binder removal	Minimal	Minimal	Can be severe	Minimal
Thick/thin sections	No problem	Thick section increases time of cast	Problems with binder removal in thick sections	Thick section increases time of cast
Particle size	Viscosity goes up as size goes down	Casting time goes up as size goes down	Viscosity goes up as size goes down	Casting time goes up as size goes down

1.5. Applications of gelcasting

Gelcasting is a ceramic forming process which is close to traditional slurry processing. As a result, there is no significant change in equipment which is required conventionally for gelcasting. Therefore, it can be said that it is possible many ceramic components from other

forming processes can be produced with gelcasting. Meanwhile, a large difference between gelcasting and other processes is that solid loading is higher in gelcasting. Generally, the solid loading needs up to at least 50vol% while in slip casting and spray drying, the solid loading is about from 25 to 55vol% (Janney et al., 1998a).

Gelcasting provides an efficient method to manufacture complex-shaped component such as turbine rotors which need highly uniform properties. Also, gelcasting can be used in manufacturing large components with a simple shape such as a ceramic ring. In addition, gelcasting can be used in metal powder forming as well such as tool steel, a nickel-based superalloy and so on (Janney et al., 1998a).

About decade ago, it was researched if gelcasting could be used in industrial production. Silicon nitride was used as the materials for the blade and vane of turbine rotor as shown in Figure 1.9(a). The density of blade with gelcasting was uniform while the density of blade slip casting was varied. Figure 1.9(b) and 1.9(c) show silicon nitride tensile test bars and alumina gears. Figure 1.9(d) show a silicon nitride turbine wheel which was manufactured for commercial aircraft and use in on-board engines in the military. This kind turbine was usually manufactured by injection molding and slip casting. Compared to these two forming process, gelcasting can provide a higher percentage of defect-free products.

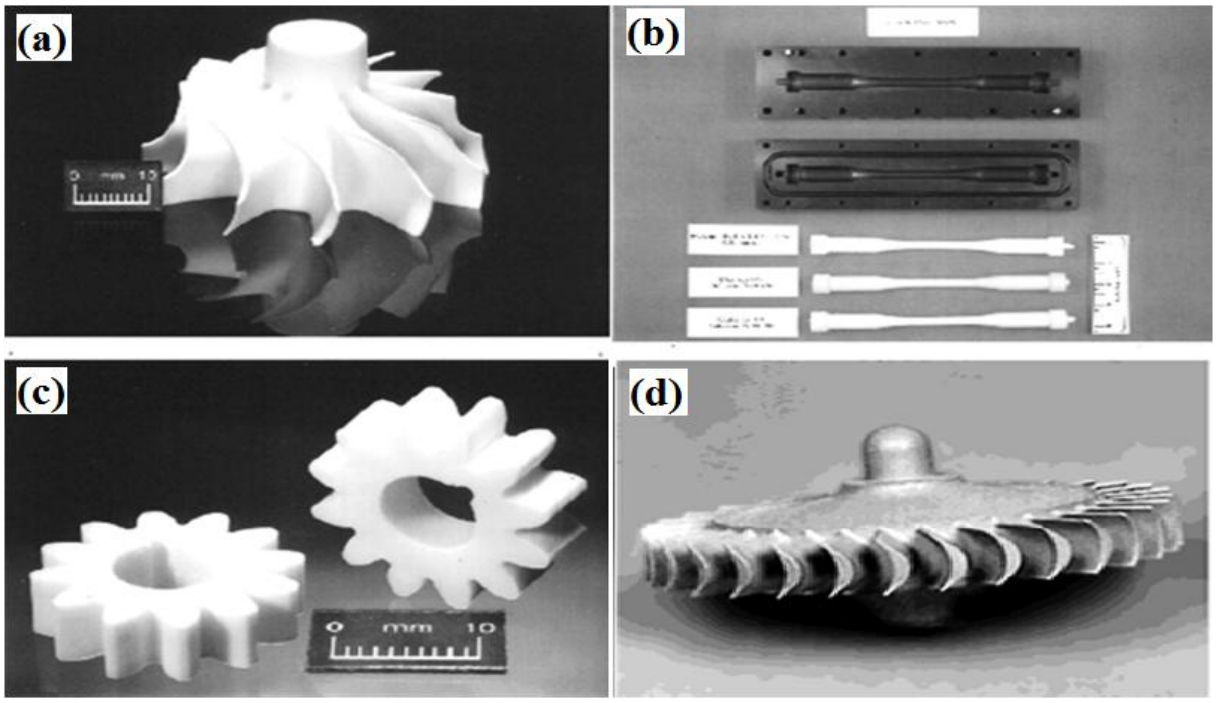

Figure 1.9. Ceramic products produced with gelcasting.

1.6. Rheology

Rheology is the study of flow and deformation of materials (Dobraszczyk and Morgenstern, 2003). The rheology of the ceramic suspension is important in ceramic processing as it often determines the properties of the finishing product. The state of dispersion is linked to the quality of the ceramic in its final consolidated form and rheology is a tool that can be used to measure this behavior. Successful colloidal ceramic processing requires slurries of high solids loading and low viscosity. A high solids loading is essential to achieve a high packing density, during the forming process (Lu, 2012). The packing density is related to the green and sintered densities, which therefore dictates many of the final properties of the ceramic. A low viscosity is also very important as the ceramic slurry needs to be deaired and easily poured (Yang and Sigmund, 2001).

It is important to understand the role of particle interactions in determining the slurry rheology shown in Figure 1.10 to control the parameters such as zeta potential, pH, dispersant amount, monomer content, and solid loading which have a strong effect on mechanical properties of the ceramic body and also have an influence on process viability for manufacturing. Therefore, it is necessary to understand how an optimum suspension of ceramic particles can be created (Sigmund et al., 2000).

1.6.1. Viscosity

A very important rheological property of a colloidal suspension is its viscosity. The viscosity discloses how easy a suspension will flow when it is sheared. Viscosity measurements are used to determine the maximum solids loading intended for a colloidal system. By controlling the viscosity, it is possible to create suspensions with high packing densities that will have optimal green properties after forming (Yang et al., 2003). Viscosity may be defined as the internal resistance of the liquid against flow and given as:

$$\eta = \frac{\tau}{\dot{\gamma}} \qquad (1.3)$$

where η is the viscosity, τ is the shear stress, and $\dot{\gamma}$ is the shear rate.

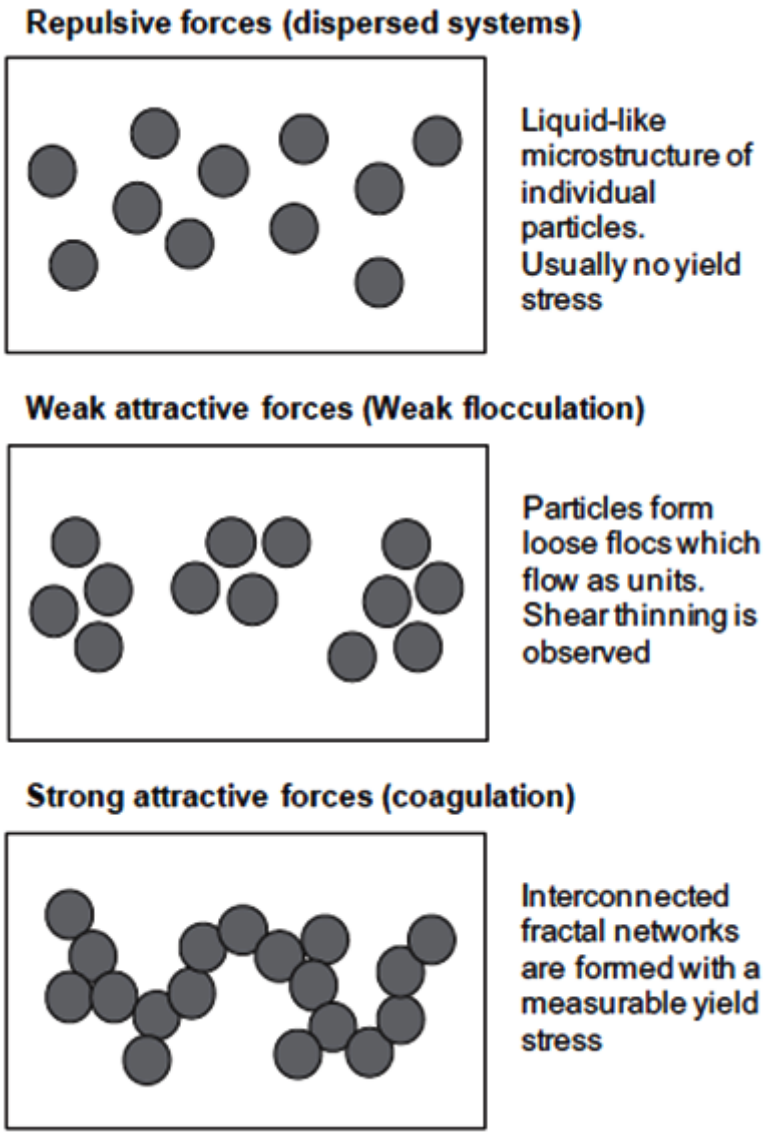

Figure 1.10. Illustration of the connection between suspension microstructure, inter-particle forces, and rheological behavior. (After Sigmund et al., 2000).

There are several possible material responses to a continuously applied shear stress as shown in Figure 1.11. The simplest case is Newtonian behavior as shown in curve a. The viscosity of Newtonian fluids is constant and therefore independent of the shear rate of the suspension. For colloidal suspensions, the response is typically more complicated with the viscosity changing with the shear rate. Therefore, colloidal systems typically show non-Newtonian behavior as given by curve b-e in Figure 1.11. In many cases, the viscosity decreases with increase in the shear rate. This is termed as shear thinning and shown in curves b and e. The shear thinning behavior could be explained by particle arrangement of the solid phase. On the increase in the shear rate, the order of the particles decreases, that reduces the resistance to

flow and ultimately leads to a lower viscosity. This depends on the particle shape, size, and solids loading.

Curve e shows a thinning with a yield stress. Yield stresses are important considerations as this is the amount of stress that must be exceeded before flow will occur. In ceramic colloidal processing yield stress can cause problems since the removal of air bubbles may be hindered. The trapped air bubbles may cause pores in the final ceramic part. Shear thickening behavior (curve b) occurs when viscosity increases with increasing shear rates. This can occur in slurries with very high solids loading where dilatant behavior will occur with increasing shear. A possible reason for this response is that during flow, the colloidal particles will collide. As shear rate increases, the collisions also increase which will result in an increase in the viscosity (Reed, 1995).

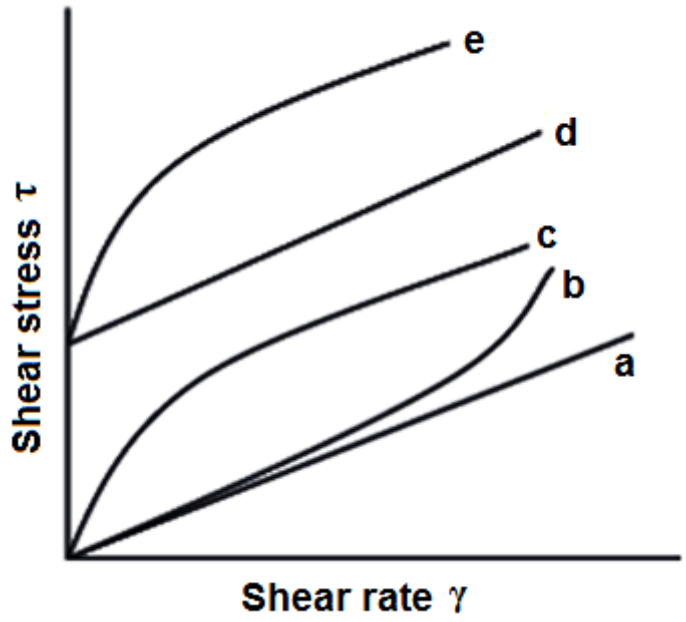

Figure 1.11. Possible rheological responses of colloidal systems:
(a) Newtonian, (b) Shear thickening, (c) Shear thinning,
(d) Bingham, (e) Shear thinning with yield stress.

1.6.2. Zeta potential and pH value

The zeta potential of the particle is defined as the electrical potential between the shear plane surrounding the particle and the bulk solution in a suspension (Huang and Yang, 2010). Zeta potential is the most significant parameter of an electric double layer (Appendix) and an

excellent measure of the magnitude of the attraction or repulsion among particles. Zeta potential analysis gives a thorough insight into the cause of dispersion, aggregation, coagulation or flocculation. This can be applied to develop the formation of dispersions, suspensions, and emulsions.

The factors influencing the stability and fluidity of the slurries are its pH value and dispersant. Dispersants are added to enhance the ceramic particles dispersion in a solvent. The relation between stability and zeta potential is that the ceramic particles with a higher absolute value of zeta potential exhibit higher stability (Mohajeri et al., 2011) due to the higher electrostatic repulsion between particles in slurries.

The pH value of slurry also plays an important role on the rheological properties of slurries (Yang et al., 2003). A high absolute zeta potential value is obtained by increasing the pH value which increases the dispersibility of the slurry.

1.6.3. Dispersion

Dispersants are added to enhance the ceramic particles dispersion in a solvent and to attain higher solids loading. As soon as dispersants are dissolved into the slurry the dispersant molecules are absorbed on top of the surface of the ceramic particle that transforms the charge distribution on the particle surface. In general, ceramic particles possessing high zeta potential usually exhibit high stability in the slurry (Moreno, 1992 and Moreno, 1992a). At higher pH value the absolute value of zeta potential can be increased by the addition of dispersant in the slurry, thus improving the dispersion of ceramic particles in the slurry. The effect of dispersant on the interaction of particles in the slurry can be observed in Figure 1.10.

1.6.4. Solid loading

The viscosity as a function of shear rate is strongly related to the volume fraction of solids. Increasing the solids loading may result in network formation, which gives rise to the viscosity of the suspension. For concentrated suspensions, the effect of solids loading on viscosity is more complicated. As more particles are added to a suspension, the resulting solids loading increases until there is continuous particle contact throughout the system. When this happens, the no flow will take place since the particles are so close together.

Higher solid loading of ceramic slurries is required to improve the mechanical properties of gelcast bodies. But viscosity increases as the solid loading increases which make the slurry difficult to cast in the mold. This is due to flocculation and coagulation caused by the reduction of solvent (water) present in between the ceramic particles (Li and Guo, 2008 and Kong et al., 2007).

1.7. Properties required for a Radome

The properties required for a radome are flexural strength, porosity and dielectric constant and loss tangent. These properties are measured using various equipment and are presented in Chapter-3.

1.7.1. Flexural strength

Flexural strength (Modulus of Rupture) is defined as "the ability of the material to withstand bending forces applied perpendicular to its longitudinal axis". The flexural strength was measured by the three-point flexural method as shown in Figure 1.12 with a span length of 40 mm and at a crosshead speed of 0.5 mm/min using a universal testing machine as per ASTM-C1161-02C (2006) and is determined as given in Eqn. 1.4.

$$\sigma_f = \frac{3PL}{2bh^2} \qquad (1.4)$$

where P = fracture load, L = length of support span, b = width of the sample and h = height of the sample.

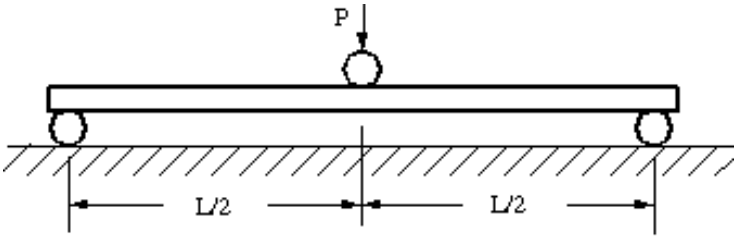

Figure 1.12. Schematic of three-point bending.

1.7.2. Bulk density and apparent porosity

Bulk density is defined as "the ratio of mass to volume that includes the cavities in a porous material".

$$BD = \frac{DW}{SW_1 - SW_2} \times \rho \qquad (1.5)$$

Apparent porosity is defined as "the ratio of open pore volume to total volume"

$$AP = \frac{SW_1 - DW}{SW_1 - SW_2} \times 100 \qquad (1.6)$$

where BD = Bulk Density, AP =Apparent porosity, DW =Dry Weight, SW_1 = Soaked Weight, SW_2 = Suspended weight, ρ = Density of kerosene oil = 0.78 gm/cc

Bulk density and apparent porosity of ceramic bodies were measured by Archimedes principle as per ASTM C373-88(2006) using kerosene as solvent as shown in Figure 1.13. The specimens were cut into 20 × 20 × 8 mm in size.

Archimedes principle states that "when an object is partially or fully immersed in a fluid it experiences an upward force that is equal to the weight of the fluid displaced by it".

Figure 1.13. Schematic of Archimedes setup.

1.7.3. Dielectric constant and loss tangent

Dielectric constant is defined as "a quantity measuring the ability of a substance to store electrical energy in an electric field".

The dielectric constant can be calculated by Eqn. 1.7 by measuring the capacitance:

$$K = \varepsilon_r' = \frac{c.d}{A} = \frac{\varepsilon}{\varepsilon_0} \tag{1.7}$$

Where K is the dielectric constant; ε_r' is relative permittivity, c is the capacitance; d is the thickness of the specimen; A is the area of the cross-sectional surface, ε is permittivity of the medium, ε_0 is permittivity of free space or vacuum.

Loss tangent is defined as "the ratio of energy loss (ε_r'') to relative permittivity (ε_r')".

$$\tan\delta = \frac{\varepsilon_r''}{\varepsilon_r'} \tag{1.8}$$

Loss tangent quantifies a dielectric material's inherent dissipation of electromagnetic energy.

1.8. Design of experiments

The design of experiments was invented by Ronald A. Fisher in the 1920s and 1930s at Rothamsted Experimental Station, London (Telford, 2007). Experiments are to be designed and conducted systematically for analyzing of any system or process effectively, efficiently and economically. The aim of any experimental design is to provide an insight into the relationship between process parameters with their responses, the influence of various process parameters and also their percentage contributions. One-Variable-At-a-Time (OVAT) approach is used in manufacturing industries, where one variable is varied at a time keeping the remaining variables in the experiment fixed. This type of experimentation requires large resources to be obtained and also involves many constraints such as it depends on guesswork, luck, experience and instinct for its success. Therefore, these are generally considered as unreliable, inefficient, time consuming and may yield false optimum conditions for the process.

In an experiment, one or more process variables (or factors) are changed in order to observe the effect on one or more response variables. The design of experiments (DOE) is an efficient procedure for planning experiments so that the data obtained can be analyzed to yield

valid and objective conclusions (Green and Launsby, 1995). DOE provides a powerful means to achieve breakthrough improvements in product quality and process efficiency (Kim, 2008). It begins with determining the goals of an experiment and selecting the process factors for the study. An experimental design gives a detailed experimental plan in advance for conducting the experiments. Well-chosen experimental designs maximize the amount of information that can be obtained for a given amount of experimental effort (Telford, 2007).

Various types of DOE methods are

- Completely randomized design
- Randomized block design
- Full factorial design
- Fractional factorial design
- Response surface design

Factorial design of experiments is mostly used to simultaneously determine the significance of multiple independent variables and their interactions. In a full factorial design of experiments two or more factors with discrete values or levels are considered with all the possible combinations. However, it is costly to perform full factorial experiments. Instead, a fractional factorial design, which is a subset of full factorial design, is generally used which requires fewer runs. A factorial design is less preferable when more than two levels are considered. This is needed, as the number of experiments required for such designs will be considerably greater than their two level counterparts. Generally, factors in real engineering problems are continuous, but the two-level factorial design assumes that the effect is linear. In order to consider a quadratic effect, a more complicated experiment is to be selected such as central composite design. Response surface methodology (RSM) is mostly used while optimizing factors that could have quadratic effects (Rao, 2011).

1.8.1. Response Surface Methodology

Response surface methodology (RSM) is defined as “a collection of mathematical and statistical techniques useful for the modeling and analysis of problems in which a response (output variable) of interest is influenced by several variables (input variables) and the goal is to optimize the responses that are influenced by the input process parameters” (Montgomery, 2012).

Originally, RSM is developed to model experimental responses and then migrated into the modeling of numerical experiments (Box and Draper, 1987). They can be applied for modeling and optimization of any engineering problems. Sufficient data is gathered through the experimental design layout and mathematical models for the desired responses as a function of selected variables were developed by applying the multiple regression analysis on the experimental data. The general second order regression equation is given by Eq. 1.9.

$$Y = \beta_0 + \sum_{i=1}^{n} \beta_i x_i + \sum_{i=1}^{n} \beta_{ii} x_i^2 + \sum_{i<j}^{n} \beta_{ij} x_i x_j + \varepsilon \qquad (1.9)$$

where Y is the response (dependent variables); β_0 is the constant coefficient; β_i, β_{ii} and β_{ij} are regression coefficients for linear, quadratic, and interaction effects respectively; n is the number of process parameters; x_i and x_j are factors (independent variables), and ε is the standard error. This regression modeling is done to generate the fitness equations for the output responses.

The quality of developed models is determined by the coefficients of determination (R-square) while the ANOVA (analysis of variance) is used to evaluate the statistical significance of the model.

1.8.2. Central Composite Design (CCD)

The most popular response surface method (RSM) design is the central composite design (CCD). Central composite designs are used extensively in building second-order response surface models. A CCD shown in Figure 1.14 has three groups of design points:

(a) Two-level factorial or fractional factorial design points

(b) Axial points (at times called "star" points)

(c) Center points.

1.8.2.1. Factorial Points

The two-level factorial part of the design consists of all possible combinations of the +1 and -1 levels of the factors. For the two factor case there are four design points:

(-1, -1) (+1, -1) (-1, +1) (+1, +1)

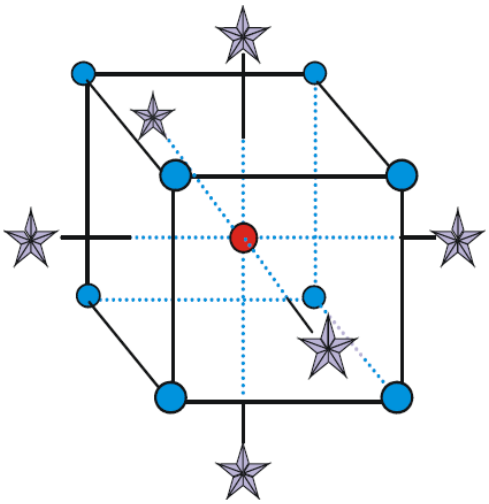

Figure 1.14. Central composite design

1.8.2.2. Star or Axial Points

The star points have all of the factors set to 0, the midpoint, except one factor, which has the value +/- α. For a two-factor problem, the star points are:

(-α, 0) (+α, 0) (0, -α) (0, +α)

The value for Alpha is calculated in each design for both rotatability and orthogonality of blocks. The experimenter can choose between these values or enter a different one. The default value is set to the rotatable value. Another position for the star points is at the face of the cube segment on the design. This is usually referred to as a face-centered central composite design.

1.8.2.3. Center Points

Center points, as implied by the name, are points with all levels set to coded level 0 - the midpoint of each factor range (0, 0). Center points are usually repeated 4-6 times to get a good estimate of experimental error (pure error). For example, with two factors the design will be created with five center points by default.

Optimization study in RSM is carried out in three stages. The first stage is to determine the independent input parameters and their levels for experimentation. In the second stage, selection of experimental design, prediction, and verification of the model equation is performed. Lastly, the response surface plots and contour plots of these response

functions are used to determine the optimum points. RSM has several advantages as compared to classical experimental methods as listed below.

- RSM delivers more information from less number of experiments. Whereas, classical methods are more time consuming with a large number of experiments to explain the behavior of a system.
- It is possible to determine the interaction effect of the parameters on the responses. RSM model can easily clarify these interaction effects for a binary combination of the independent parameters (Rao, 2011).
- The empirical model is also developed which helps to obtain the nature or trend of the response with respect to the input parameters in the given process.

On the contrary, the major drawback of RSM is to fit the data to a second order polynomial. It cannot be said that all systems containing curvature are well accommodated by the second order polynomial (Rao, 2011). Therefore, preliminary experiments are required to be carried out to determine the range of independent input parameter.

1.8.3. Desirability Function for Optimization

The desirability function approach to multi-objective optimization was originally proposed by Harrington in 1965. Essentially, the approach is to translate the functions to a common scale [0, 1], combine them using the geometric mean and optimize the overall metric (Balamurugana et al., 2014).

Firstly each response y_i is converted into an individual desirability function d_i that varies over the range

$$0 \le d_i \le 1$$

where if the response y_i is at its goal or target, then $d_i = 1$ and if the response is outside an acceptable region, $d_i = 0$. Then the design variables are chosen to maximize the overall desirability

$$D = (d_1 \times d_2 \times ..... \times d_m)^{\frac{1}{m}} \qquad (1.10)$$

where there are m responses. The overall desirability will be zero if any of the individual responses is undesirable.

- If the objective or target T for the response y is a maximum value,

$$d = \begin{cases} 0 & y < L \\ \left(\dfrac{y-L}{T-L}\right)^{r} & L \le y \le T \\ 1 & y > T \end{cases}$$

- If the target for the response is a minimum value,

$$d = \begin{cases} 0 & y < T \\ \left(\dfrac{U-y}{U-T}\right)^{r} & T \le y \le U \\ 1 & y > U \end{cases}$$

- If the target is located between the lower (L) and upper (U)limits,

$$d = \begin{cases} 0 & y < T \\ \left(\dfrac{y-L}{T-L}\right)^{r_1} & L \le y \le T \\ \left(\dfrac{U-y}{U-T}\right)^{r_2} & T \le y \le U \\ 0 & y > U \end{cases}$$

1.9. Organization of thesis

The thesis is organized into six chapters.

Chapter: 1 contains a brief insight into ceramic composites and their applications. Radome and their various nose shapes are also presented. Various colloidal processing techniques are described. At the end of the chapter design of experiments is also explained briefly.

Chapter: 2 contain detailed literature review on the research work reported in the past by various researchers in the field of the topics related to fabrication of SiO_2 based ceramics.

Based on literature survey, research gaps are identified and objectives are formulated at the end of this chapter.

Chapter: 3 outlines the description of materials and equipment used in the present study to measure the responses.

Chapter: 4 gives the detailed experimental plans involving a number of experiments for gelcasting of SiO_2, SiO_2–Si_3N_4, SiO_2–BN and SiO_2–Si_3N_4–BN ceramic composites are given. A brief description of preparation of ceramic composites using the gelcasting technique by varying parameters is given in this chapter.

Chapter: 5 outlines the influence of input parameters on responses Multi-response optimization of process parameters using desirability approach is then presented. Thereafter, results of confirmatory experiments are presented.

Chapter: 6 is all about the conclusions drawn from the results obtained by conducting experimental investigations, modeling, and optimization. This chapter also highlights the limitation of the study and scope for future work in this area. This chapter is followed by references.

Summary

Introduction to ceramic composites, their advantages, drawbacks, and applications are presented in this chapter. Introduction to radome, their shapes, and wall structures are explored. Colloidal stability and various colloidal processing techniques are discussed in this chapter. The design of experiments, response surface methodology and desirability function for optimization are discussed and presented.

CHAPTER 2

LITERATURE REVIEW

2.1. Introduction

Nowadays ceramic composites being used for engineering applications are being manufactured mostly by gelcasting method. The reason for the extensive use of gelcasting is due to its ability to produce complex and irregular shapes and thus the research on gelcasting is gaining importance day by day. A thorough literature review is presented in this chapter dealing with materials for radomes, sintering aids, property evaluation, applications of gelcasting and reviews on SiO_2 based ceramic composites.

2.2. Radome materials

In olden times, for constructing radomes, a range of materials such as balsa and plywood have been used in early structures. Modern ground-based and ship-based radomes are manufactured using composite materials such as fiberglass, quartz, and aramid fibers held together with polyester, epoxy, and other resins (Kozakoff, 1997). Materials for developing ceramic radomes include fused silica (SiO_2) (Neil et. al., 1990 and Lyons and Starr, 1994), silicon nitride-barium aluminum silicate composites (Si_3N_4/BAS) (Hunn et al., 1995 and Koetje et al., 1987), aluminum phosphate-mullite composites ($AlPO_4/3Al_2O_3.2SiO_2$) (Wang and Liu, 2009), silica‑aluminum nitride composites (SiO_2-AlN) (Wu et al., 2000), silica fiber reinforced silica‑boron nitride composites (SiO_{2f}/SiO_2-BN) (Li et al., 2012), aluminum borate whisker/aluminum phosphates composites ($9Al_2O_3.2B_2O_3/AlPO_4$) (Lu et al., 2008), liquid-phase silicon nitride (Hsieh et al., 1984), Si_2N_2O composites (Shin et al., 1995), reaction-bonded silicon nitride (Heieh, 1987), β-$Si_4Al_2O_2N_4$ (Ganesh et al., 2008a), β-$Si_4Al_2O_2N_4$-SiO_2 (Ganesh et al., 2008), β-SiAlON (Ganesh and Sundararajan, 2010 and Ganesh, 2011). Few of these materials with efficient properties with considerable importance are shown in Table 2.1.

Fused silica can be used only for low-speed radomes because of its low strength (40-50 Mpa) but has an excellent dielectric constant of 4.01 and has loss tangent <0.01 at 1000°C (Neil et. al., 1990). Preparing Si_2N_2O composites repeatedly with consistent properties is not possible because of its final chemical composition as it depends on the extent of oxidation of

α-Si_3N_4 materials that occur upon calcinations in atmospheric air and does not depend on the initial precursor material compositions although the dielectric properties of these materials are good (Gilde et al., 1997). Preparing radome structure was quite difficult using Si_3N_4/BAS, although it poses high flexural strength (420 MPa) (Hunn et al., 1995). β-SiAlON material can be shaped into radome structures and can be sintered to full density without disturbing the structure, but fixing the best chemical composition based on the required properties and processing of these materials is quite difficult (Ganesh and Sundararajan, 2010 and Ganesh, 2011). Si_3N_4 ceramic can be shaped into radome structures using near-net shape forming techniques, and the major drawback of dense sintered silicon nitride materials is its poor sintering ability although it possesses exceptionally high flexural strength (600-1000 MPa) (Faoite et al., 2012) and it can withstand high temperatures and has well-acceptable dielectric properties. Low-density porous silicon nitride ceramic has been used as radome materials owing to its rather low dielectric constant and loss tangent, high chemical stability, high melting point and extremely low coefficient of thermal expansion. The existence of the pores in the silicon nitride ceramic will lower the dielectric constant and the dielectric loss tangent according to Bruggeman theory (Xu et al., 2008).

2.3. Sintering aids for nitrides

The addition of certain oxides in the sintering of ceramic nitrides is a well-known technique for producing dense ceramics for engineering applications (Tsuge et al., 1974). Many of the oxide materials such as magnesium oxide (MgO) (Terwilliger, 1974), yttria (Y_2O_3) and alumina (Al_2O_3) (Tsuge et al., 1975, Albano and Garrido, 2003, and Yang et al.,1998), beryllia (BeO) (Mizutani, 1986), zirconia (ZrO_2) (Rice and Donough, 1975), calcium oxide (CaO) (Geith et al., 1993), ceria (CeO_2) (Ekstrom and Soderlund, 1990), hafnia (HfO_2) (Goto and Komatsu, 1999), yttria and hafnia (HfO_2) (Park et al., 1998), lutetium oxide (Lu_2O_3) and silica (SiO_2) (Zeng et al., 2005), ytterbium oxide (Yb_2O_3) and silica (SiO_2) (Zheng et al., 2001), yttria and neodymium oxide (Nd_2O_3) (Hirosaki and Okada, 1989), lanthanum oxide (La_2O_3) (Mandal and Hoffmann, 1999) are used as sintering aids.

Table 2.1. Characteristics of commonly used Radome materials.

S. No	Authors	Year	Method	Materials	Flexural Strength (MPa)	Dielectric Constant (ε)	Loss tangent (tanδ)
1	Zou, C. et al.	2013	Gelcasting and Gas Pressure Sintering	Porous Si_3N_4	235	3.68	3.5 x10^{-3}
2	Li, D. et al.	2012	Sol-gel	SiO_{2f}/SiO_2-BN	58.9	3.22	3.9 x10^{-3}
3	Wang, H.et al.	2010	Isostatic Pressing	Porous Si_3N_4	176	3.39	3.5 x 10^{-3}
4	Ganesh, I.	2011	Gelcasting	β-SiAlON	266	7.34	4 x 10^{-3}
5	Wang, Y. and Liu, J.	2009	Sol-gel	$AlPO_4$- SiO_2	168	3.42	4.75 x 10^{-3}
6	Ganesh, I. et al.	2008	Gelcasting	β-$Si_4Al_2O_2N_6$	226	7.72	--
7	Ganesh, I. et al.	2008a	Gelcasting	β-$Si_4Al_2O_2N_6$ –SiO_2	199	6.32	2 x 10^{-3}
8	Lu, Z. et al.	2008	Pressure Sintering	$9Al_2O_3.2B_2O_3$/$AlPO_4$	215.3	4.23	2.4 x 10^{-3}
9	Tong, Q. F. et al.	2008	Hot Pressing	Si_2N_2O/ β-Cristobalite	391	5.4	2 x 10^{-3}
10	Shin, H. et al.	1995	Hot Pressing	Si_2N_2O	190	4.8	2.5 x 10^{-3}
11	Hunn, D. L. et al.	1995	Isostatic Pressing	Si_3N_4-BAS	420	8.16	-
12	Lyons, J. S. and Starr, T. L.	1994	Slip Casting	Fused SiO_2	50	3.9	0.3 x 10^{-3}
13	Hampshire, S.	1991	Reaction Bonded Sintering	Si_3N_4	700	9	2 x 10^{-3}
14	Neil, J. T. et al.	1990	Slip Casting	Fused Silica	50	4.01	1x 10^{-2}

Diffusional mass transport by solid-state diffusion is very slow as there is a high degree of covalent bonding crystal structure in silicon nitride and hence by liquid phase sintering the silicon nitride powders are converted into a dense body. Generally, 1‑5 wt% silica (SiO_2) is contained by the Si_3N_4 as a surface oxidation layer as an oxide additive at certain high temperatures reacts with the SiO_2 to form silicate liquid that aids densification (Rahaman, 2003). During sintering of silicon nitride ceramics, silica naturally acts as a sintering aid, which reacts with other sintering aids and plays an important role in determining the final mechanical properties of silicon nitride ceramics (Zhou et al., 2002).

2.4. Review on SiO_2 ceramics

Wan et. al., (2014) fabricated silica ceramics with high strength, low porosity, low dielectric constant and low dielectric loss by gelcasting using a low-toxicity *N′*,*N*-dimethyl acrylamide (DMAA) gel system. Investigations were done on the properties of green and sintered ceramics, effect solid loading on the rheology of the slurry. The maximum flexural strength obtained for green bodies and sintered ceramics at a solids loading of 64 vol% and 66 vol% were 15.4 Mpa and 67.4 Mpa. The dielectric constant and low dielectric loss obtained at a solid loading of 64 vol% were 3.27 and 7.82×10^{-4} (at 1 MHz).

Wan et. al., (2014a) fabricated fused silica ceramics with excellent properties by gelcasting using *N′*,*N*-dimethylacrylamide, a low toxic gel system. The results were compared with 2-hydroxyethyl methacrylate and toxic acrylamide systems. Investigations were done on the properties such as thermal shock resistance, mechanical and dielectric properties and effects of sintering temperature on the microstructure. The maximum flexural strength was as high as 81.32 Mpa at 1275 °C and after thermal shock at 600°C, the residual flexural strength was reduced. Excellent properties were obtained at 1250°C with the similar flexural strength of 67.43 Mpa and 65.45 Mpa (after thermal shock), the dielectric constant of 3.34, and the low dielectric loss of 1.20×10^{-3} (at 1 MHz).

Wan et. al. (2014b) made an attempt using a natural and non-toxic gel, glutinous rice flour as a binder in the gelcasting of fused silica glass. It was found that glutinous rice flour performed exceptionally in the gelcasting process. Fused silica green bodies with 3 wt% glutinous rice flour have a flexural strength of 11.87 Mpa and those sintered at 1275 °C has a flexural strength of 40.02 Mpa with a bulk density of 1.75 g/cm^3.

Manivannan et. al. (2013) used colloidal silica as a binder to develop an aqueous gelcasting for fused silica ceramics. It was found that the slurry with a maximum solid loading of 73 vol% with a viscosity of 0.70Pa.s is suitable for gelcasting. The maximum flexural strength of green and sintered samples was found to be 9 Mpa and 65 Mpa with a theoretical density of 88% and 95%. The nano-silica particles of the binder are stuffing the interstitial spots filling the interstitial spots strengthening the mechanical properties in the developed fused silica green body.

Mao et. al. (2006) prepared porous silica ceramics by a starch consolidation casting method. Slurries with various fractions of starch were prepared by ball-milling. The bending strength of the sintered samples varied in the range of 10 Mpa-20 Mpa and the low dielectric constant in the range of 2-2.4 with the porosity of 42%-56%.

2.5. Review on SiO_2–Si_3N_4 ceramic composites

Lin et. al. (2016) fabricated silicon oxynitride (Si_2N_2O) based wave transparent material with multilayer structures by a two-step sintering route. The effects of atmosphere and temperature on the properties and microstructure of the materials were studied. It was observed that disintegration of Si_2N_2O caused the formation of the multilayer structure. By regulating the disintegration temperature the thickness of β-Si_3N_4 outer layers and the Si_2N_2O inner layer may perhaps be tailored. The flexural strength of the samples sintered at 1800 °C varied in the range of 210 Mpa-236 Mpa, the dielectric constant < 4.8 and loss tangent < 0.0044. This process allows these ceramic composites to be broadly used as radomes in military applications.

Jia et. al. (2003) investigated the mechanical properties of two types of hot-pressed fused silica matrix composites, SiO_2+5 vol.% Si_3N_4 and SiO_2+5 vol.% Si_3N_4+ 10 vol.% C_f. The fracture toughness and ambient strength were significantly improved with the addition of Si_3N_4. The fracture toughness increased sharply from 1.22 to 2.4 $Mpa.m^{1/2}$ by incorporating chopped carbon fibers. The maximum flexural strength of two composites at 1000 °C was found to be 168.9 and 130.6 Mpa which were 77.0 and 77.4% higher than their ambient strength, respectively.

Zou et. al. (2012) prepared porous Si_3N_4 ceramics by gelcasting and pressureless sintering and used these as frames for Si_3N_4–SiO_2 composites. By repeating the sol–gel

infiltration and sintering process amorphous SiO_2 of different contents were introduced into porous Si_3N_4 frames. Si_3N_4–SiO_2 composites with enhanced thermal shock resistance and mechanical properties were obtained. The flexural strength, fracture toughness, density and dielectric constant of Si_3N_4–SiO_2 composites were increased from 92.6 Mpa, 1.05 $Mpam^{1/2}$, 1.62 g/cm^3 and 2.65 to 148.1 Mpa, 1.70 $Mpam^{1/2}$, 2.18g/cm^3 and 3.61 while the porosity decreased from 49.3% to 22% and the dielectric loss is in the range of $3.23x10^{-3}$ to $3.84x10^{-3}$ with the increase of SiO_2 content from 0 to 25.9 vol%.

Li et. al. (2009) developed a novel process to fabricate a porous Si_3N_4–SiO_2 ceramic composite by combining oxidation-bonding with sol–gel infiltration-sintering. The mechanical and dielectric properties of porous Si_3N_4–SiO_2 ceramic composite were enhanced by Sol–gel infiltration and sintering at 1250°C. The flexural strength, porosity, fracture toughness, Vickers hardness, dielectric constant and a dielectric loss were found to be 120 Mpa, 23.9%, 1.4 $Mpam^{1/2}$, 4.1 Gpa, 3.80 and 3.11×10^{-3} (at 14 GHz).

Ganesh and Sundararajan (2010) prepared dense β-SiAlON–SiO_2 ceramic composites from β-$Si_4Al_2O_2N_6$ and fused silica varying SiO_2=20, 40, 50, 60, and 80 wt% by sintering at 1500–1750°C for 3–4 h. Thin-wall radomes fabricated by hydrolysis induced aqueous gelcasting (GCHAS) have demonstrated green strengths greater than 20 Mpa. A flexural strength of ~140 Mpa, fracture toughness of 4.2$Mpa.m^{1/2}$, coefficient of thermal expansion of $3.5x10^{-6}$/°C, Young's modulus of 214 Gpa, hardness of 1390 kg/mm^2, dielectric constant of 5.896 and tan δ of 0.002 at 17 GHz was exhibited by silicon oxynitride formed from a powder mixture of 60 wt% β-$Si_4Al_2O_2N_6$ and 40 wt% SiO_2 sintered at 1750°C for 3 h.

2.6. Review on SiO_2–BN ceramic composites

Wen, G. et. al. (2000) processed BN-SiO_2 composites by hot pressing of BN+SiO_2 powder blends ranging from 15 to 90 vol% BN, with a composition interval of 15 vol%. Plate-like grains of BN was conversely aligned by hot pressing and uniformly distributed in the SiO_2 matrix. The properties of SiO_2 such as bending strength and fracture toughness were significantly improved by 1.4 and 2.2 times with the addition of 15 vol% BN. The bending strength and fracture toughness at 60 vol% BN were found to be 246 Mpa and 2.87 $Mpa.m^{1/2}$.

Jia et. al. (2011) prepared pressureless sintered 15 vol% BNp/SiO_2 composites by cold isostatic pressing (CIP) and gel-casting routes, respectively. Two types of SiO_2 powders with a particle size of 5.82 and 3.24 μm in d50, respectively, were used. The gel-casting pre-forming route has an awesome advantage above CIP route on the thermal stability of fused silica matrix. The maximum bending strength, fracture toughness, and Young's modulus were 101.5±4.3 Mpa, 1.57±0.04 Mpa.$m^{1/2}$, and 61.3±2.4 Gpa, respectively.

Duan et al. (2012) prepared silica fiber reinforced silica and boron nitride-based composites (SiO_{2f}/SiO_2-BN) via the sol-gel method and then the urea route. Investigations were done on the microstructure, mechanical and dielectric properties, and the effects of oxidation treatment on the component. The flexural strength, elastic modulus, density, dielectric constant and loss tangent of SiO_{2f}/SiO_2-BN ceramic composites were 113.9 Mpa, 36.5 Gpa, 1.81 g/cm^3, 3.22 and 0.0039, respectively. The flexural strength, elastic modulus, and density after oxidation treatment were decreased to 58.9 Mpa, 9.4 Gpa and 1.80 g/cm^3. But there is no significant effect of oxidation treatment on the dielectric properties of the composite.

Du et. al. (2011) employed two types of h-BN (boron nitride nanotubes (BNNTs) and boron nitride nanoparticles (BNNPs) to emphasize SiO_2 matrix consecutively to overcome intrinsic brittleness and poor mechanical properties of SiO_2. Investigations were done on the mechanical and dielectric properties. The formation of cristobalite is controlled and the fracture type and surface features were altered with the addition of BNNTs and BNNPs. Exceptional mechanical properties and low dielectric constant were demonstrated by 5 wt% BNNTs/SiO_2 and 5 wt% BNNPs/SiO_2 composites in contrast to monolithic SiO_2. The flexural strength and fracture toughness were increased from 52.2 Mpa and 0.58 Mpa.$m^{1/2}$ to 120.2 Mpa and 1.22 Mpa.$m^{1/2}$ by adding 7 wt% BNNPs.

Zhai et. al. (2007) prepared BN-SiO_2 composite ceramics by hot pressing sintering, using h-boron nitride powder and silica sol as raw materials by varying silica from 10 wt% to 40 wt%. The maximum flexural strength obtained at 70 wt% h-BN was 180.30 Mpa and a maximum fracture toughness of 3.20 Mpa.$m^{1/2}$ was obtained at 80 wt% h-BN. The dielectric constant is in the range of 2.5-2.8 and the loss tangent with a magnitude of 10^{-3} (1MHz to 2GHz) was achieved.

2.7. Review on BN–Si_3N_4 ceramic composites

Wang et. al., (2013) fabricated porous BN/Si_3N_4 ceramic composite using gelcasting with various contents of BN. Investigations were done on the rheology of suspensions, mechanical and dielectric properties, and microstructure of BN/Si_3N_4 ceramic composite. The thermal shock resistance and dielectric properties were improved with the increase of BN content while there is a partial decrease in the mechanical properties. The flexural strength, porosity and dielectric constant of porous Si_3N_4 ceramic with no BN content were 128Mpa, 48.1% and 4.1 and for 10 vol% BN/Si_3N_4 porous ceramic composite, they were 106.6Mpa, 49.4% and 3.8 respectively which indicates that these ceramic composites are an ideal candidate material for high-temperature wave-transparent applications.

Feng et. al., (2016) prepared porous BNp/Si_3N_4 ceramics using the gas pressure sintering technique. The analysis was done on the microstructures, phase compositions, mechanical and dielectric properties with the addition of 0 wt% to 15 wt% BN particles. As the BN content is increased, the apparent porosity of the BNp/Si_3N_4 ceramics increased significantly from 2.3% to 21.2%. The dielectric properties of porous BN/Si_3N_4 were enhanced while there is a partial decrease in the mechanical properties. The bending strength, fracture toughness, porosity and dielectric loss of porous BNp/Si_3N_4 ceramic with 10 wt% BN particles were 190.1 Mpa, 4.16Mpa.$m^{1/2}$, 20.5% and 0.0085 that are required for wave transparent materials.

Liu et. al., (2013) prepared Si_3N_4-BN composites via die pressing and precursor infiltration and pyrolysis (PIP) route using borazine as the precursor. The Si_3N_4-BN composites were pyrolyzed at temperatures from 1200 to 1750 °C and are composed of α-Si_3N_4, β-Si_3N_4 and h-BN with only 0.17-3.9 wt.% phase transition of Si_3N_4. The Si_3N_4-BN composites pyrolyzed at 1750 °C possess the flexural strength of 219.1 Mpa, the elastic modulus of 75.5 Gpa, and fracture toughness of 2.62 Mpa $m^{1/2}$, respectively.

Dong et. al. (2012) prepared porous Si_3N_4/BN composite ceramics by tertbutyl alcohol (TBA)-based gelcasting process and SiO_2, Y_2O_3, and Al_2O_3 as sintering additives. The effects of Y_2O_3 and Al_2O_3 contents on flexural strength, phase composition porosity, microstructure, dielectric constant and pore size distribution were analyzed. The results demonstrated that by regulating the contents of sintering additives, ceramics with porosity differing from 55% to

68% can be prepared. As the contents of Y_2O_3 and Al_2O_3 are increased flexural strength and dielectric constant also increased and they were found to be within the range of 29.9 Mpa to 60.9 Mpa and 2.30 to 2.85, respectively.

Zhao, Y. et al. (2015) prepared porous BN/Si_3N_4 composites with different Y_2O_3–MgO nanopowders by a pressureless sintering method. The microstructures, phase compositions, mechanical and dielectric properties of BN/Si_3N_4 composites were explored. The mechanical properties of ceramics initially improved with Y_2O_3–MgO additions of up to 20 wt% and then declined whereas the dielectric properties reduced as the contents of Y_2O_3–MgO increased. The flexural strength, porosity and dielectric constant attained by porous BN/Si_3N_4 ceramics with 20 wt% Y_2O_3–MgO powders are 243.6 Mpa, 21.9% and 5.5, respectively. These results signify that these ceramic composites may perhaps be a candidate material for wave-transparent applications.

Liu et. al., (2015) prepared Si_3N_4-BN composites by die pressing and precursor infiltration and pyrolysis (PIP) route using borazine as the precursor. The microstructures, phase compositions, mechanical and dielectric properties of the composites with varied porosities were analyzed. The porosity of the ceramics was efficiently increased using a pore-forming substance, starch. From the liquid precursor borazine, Si_3N_4 preforms were drawn and during curing the pressure was decreased. As the porosity of the Si_3N_4-BN composites increased, the dielectric properties were enhanced while the mechanical properties were declined. The flexural strength, porosity, density, and Young's modulus of the composites were 48.05Mpa, 29.78%, 1.70 $g.cm^{-3}$, and 32.45Gpa, respectively at 20 wt.% starch. The dielectric constant and loss tangent were within the range of 4.20-4.44 and 0.48-3.42$\times 10^{-3}$ (7~18GHz).

Liu et. al., (2014) prepared Si_3N_4-BN composites by gelcasting and precursor infiltration and pyrolysis (PIP) route using borazine as the precursor. The microstructures, phase compositions, mechanical and dielectric properties of the composites were evaluated. The flexural strength, porosity, density, fracture toughness, and Young's modulus of the composites are 185.59 Mpa, 17.8%, 2.21g/cm^3, 2.47 $Mpa.m^{1/2}$, and 69.13 Gpa, respectively. The dielectric constant and loss tangent were within the range of 4.507-4.635 and $1.06x10^{-3}$-$1.97x10^{-3}$ (7-18 GHz).

2.8. Review on Si_3N_4–BN–SiO_2 ceramic composites

Dong et. al. (2012) fabricated porous Si_3N_4/SiO_2/BN ceramic composites with high strength and low dielectric constant by the dry-pressing process and pressureless sintering at 1750°C for 1.5 h in flow nitrogen. The effects of BN contents on flexural strength, phase composition porosity, microstructure and dielectric properties were investigated. The results demonstrated that by adjusting the BN content, the porous Si_3N_4/SiO_2/BN ceramic composites with porosity differing from 29% to 48% can be fabricated. The flexural strength and dielectric constant were within the range of 78-215 Mpa and 3.9-5 (1 MHz).

Long et. al. (2012) fabricated porous Si_3N_4 ceramics incorporated with h-BN and SiO_2 nanoparticles by pressureless sintering at moderately low temperature. Stearic acid, a pore forming agent was used for fabrication of porous BN–SiO_2–Si_3N_4 composites. Microstructure, flexural strength, fracture toughness, porosity, thermal shock resistance, and Young's modulus, were explored. Incorporation of h-BN and SiO_2 nanoparticles enhanced the mechanical properties of ceramics. A maximum flexural strength of 130 Mpa was obtained at room temperature and 60 Mpa at 1000 °C.

Han et. al. (2010) fabricated porous Si_3N_4–BN–SiO_2 ceramics in air at 1100 °C by partial sintering using starch as consolidator and pore former. The effect of porosity on the bending strength of the ceramic composite was studied. A maximum bending strength of 60 ± 4.11 Mpa was attained at an ultimate apparent porosity of 0.140. The dielectric constant and loss tangent were 2.67 at an ultimate apparent porosity of 0.732 and $3.9x10^{-3}$ (18-40 GHz).

Weiru et. al. (2008) prepared Si_3N_4-BN-SiO_2 microwave-transparent materials by gas pressure sintering. Investigations were done on the influence of nano-SiO_2 and BN contents on the properties, microstructure, and reinforcement of ceramic composites. The results revealed that by regulating the contents of nano-SiO_2 and BN, a series of Si_3N_4-BN-SiO_2 wave-transparent materials can be prepared. The flexural strength, dielectric constant and loss tangent were within the range of 74.7-174.83Mpa, 3.5-4.2 and 0.5×10^{-3}- 4.5×10^{-3}.

Jiang et. al. (2007a) prepared SiO_{2f}/Si_3N_4–BN composites through repeated infiltration of hybrid preceramic precursor and pyrolysis at high temperature in an ammonia atmosphere. SiO_{2f}/Si_3N_4–BN composites moisture behavior and effects of moisture on the microstructure

and mechanical properties of composites were investigated. By controlling the humidity of the as-received composites, a flexural strength of 161.7 Mpa can be attained.

Jiang et al. (2007b) used the hybrid preceramic precursor to fabricate 2.5D SiO_{2f}/Si_3N_4-BN matrix by repeated infiltration and pyrolysis process at a high temperature in an ammonia atmosphere. Dense composites can be produced by this route due to excellent wettability and low viscosity of the hybrid preceramic polymers. The flexural strength, dielectric constant and loss tangent were found to be 101.8 Mpa, 3.4, and 0.006.

Tables 2.2 give the gist of authors who produced SiO_2 and Si_3N_4–SiO_2 ceramic composites, their fabrication method, and their strengths. Tables 2.3 give the gist of authors who produced BN–SiO_2 and Si_3N_4–BN ceramic composites, their fabrication method and their strengths. Tables 2.4 give the gist of authors who produced Si_3N_4–BN–SiO_2 ceramic composites, their fabrication method, and their strengths respectively.

Table 2.2. Summary of manufacturing of SiO_2 and Si_3N_4–SiO_2 ceramic composites

S. No	Authors	Year	Method	Materials	Flexural Strength (MPa)	Dielectric Constant (ε)	Loss tangent (tanδ)
SiO_2							
1	Wan, W.et. al.	2014a	Gelcasting	Fused Silica	81.32	3.34	1.20×10^{-3}
2	Wan, W. et. al.	2014	Gelcasting	Silica	67.4	3.27	7.82×10^{-4}
3	Wan, W.et. al.	2014b	Gelcasting	Fused Silica	47.02	--	--
4	Manivannan et. al.	2013	Gelcasting	Fused Silica	60	--	--
5	Mao, X.J. et. al.	2006	Starch Consolidation Casting	Silica	20	2.4	--
Si_3N_4 – SiO_2							
1	Lin, S. et. al.	2016	Isostatic Pressing	Si_3N_4–SiO_2	236	4.8	4.4×10^{-3}
2	Zou, C. et. al.	2012	Gelcasting	Si_3N_4–SiO_2	92.6	3.61	3.84×10^{-3}
3	Ganesh and Sundararajan	2010	Gelcasting	β-SiAlON–SiO_2	140	5.896	2×10^{-3}
4	Li, X. et. al.	2009	Sol–gel infiltration	Si_3N_4–SiO_2	120	3.8	3.11×10^{-3}
5	Jia, D.C. et. al.	2003	Hot-Pressing	SiO_2+5 vol.% Si_3N_4	168.9	--	--

Table 2.3. Summary of manufacturing of BN-SiO_2 and Si_3N_4–BN ceramic composites

S. No	Authors	Year	Method	Materials	Flexural Strength (MPa)	Dielectric Constant (ε)	Loss tangent (tanδ)
BN – SiO_2							
1	Duan, L. et al.	2012	Sol-gel	SiO_{2f}/SiO_2-BN	58.9	3.22	3.9×10^{-3}
2	Du, M. et. al.	2011	Hot-Pressing	BNNPs/SiO_2	120.2	--	--
3	Jia, D. et. al.	2011	Gelcasting	BNp/SiO2	101.5	--	--
4	Zhai, H. et. al.	2007	Hot-Pressing	BN-SiO_2	180.3	2.8	1×10^{-3}
5	Wen, G. et. al.	2000	Hot-Pressing	BN-SiO_2	246	--	--
Si_3N_4 – BN							
1	Feng, Y.et. al.	2016	Gas Pressure Sintering	BN/Si_3N_4	190.1	5.14	8.5×10^{-3}
2	Liu, K. et. al.	2015	Die Pressing and PIP	Si_3N_4-BN	48.05	4.44	3.42×10^{-3}
3	Zhao, Y. et al.	2015	Pressureless Sintering	BN/Si_3N_4	243.6	5.5	--
4	Liu, K. et. al.	2014	Gelcasting and PIP	Si_3N_4-BN	185.59	4.635	1.97×10^{-3}
5	Wang, S. et. al.	2013	Gelcasting	BN/Si_3N_4	106.6	3.8	--
6	Liu, K. et. al.	2013	Die Pressing and PIP	Si_3N_4-BN	219.1	--	--
7	Dong, W. et. al.	2012	TBA-based Gelcasting	Si_3N_4-BN	60.9	2.85	--

Table 2.4. Summary of manufacturing of Si_3N_4–BN–SiO_2 ceramic composites

S. No	Authors	Year	Method	Materials	Flexural Strength (MPa)	Dielectric Constant (ε)	Loss tangent (tanδ)
Si_3N_4 – BN – SiO_2							
1	Dong, W. et. al.	2012	Dry-pressing	Si_3N_4/SiO_2/BN	215	5	--
2	Long, N.N. et. al.	2012	Pressureless Sintering	BN–SiO_2–Si_3N_4	130	--	--
3	Han, J. C. et. al.	2010	Starch Consolidation Casting	Si_3N_4–BN–SiO_2	60 ± 4.11	2.67	3.9×10^{-3}
4	Weiru, Z. et. al.	2008	Gas Pressure Sintering	Si_3N_4–BN–SiO_2	174.83	4.2	4.5×10^{-3}
5	Jiang, Y.G. et. al.	2007	Precursor Infiltration and Pyrolysis	SiO_{2f}/Si_3N_4–BN	161.7	--	--
6	Jiang, Y. G. et al.	2007	Precursor Infiltration and Pyrolysis	2.5D SiO_{2f}/Si_3N_4-BN	101.8	3.4	6×10^{-3}

2.9. Gap analysis

Very few literature is available on the processing of wave transparent ceramic materials with desired properties required for radomes. After a thorough literature review, few gaps are identified. So far much work has been done on the fabrication of Si_3N_4 based ceramic composites to achieve the properties required for a radome. But there is not much work done on the fabrication of SiO_2 based ceramic composites to enhance the properties. No research work has been reported on the modeling and optimization of fused silica ceramics. SiO_2 based radomes are popular for lower range missiles and very a few works are published. Several works are under patenting. Hence SiO_2 based ceramic composites fabrication is taken in this study.

2.10. Problem formulation

After identifying the gap, the problem is formulated on ceramic processing and characterization of SiO_2–Si_3N_4–BN ceramic composites using gelcasting method by varying precursor amounts, solid loadings, monomers and their ratio. Effects of various process parameters on mechanical and dielectric properties of porous SiO_2, SiO_2–Si_3N_4, SiO_2–BN and SiO_2–Si_3N_4–BN will be studied. The properties of SiO_2 may greatly enhance by the addition Si_3N_4-BN particles. Such enhanced properties are highly desirable for ceramic radomes used in lower range missiles. The present work will reflect the impact of solid loading, Si_3N_4 content, BN content, monomer content and ratio of monomers with the help of RSM using a central composite face-centered design on fused silica ceramic composites.

2.11. Research Objectives

Following objectives are formulated for the present work.

- To develop porous SiO_2 based ceramic composites. Hence pure SiO_2 is taken as base and Si_3N_4, BN powders are mixed independently and combinedly to develop SiO_2–Si_3N_4, SiO_2–BN and SiO_2–Si_3N_4–BN ceramic composites for evaluation of best composite for radomes.

- To develop porous SiO_2, SiO_2–Si_3N_4, SiO_2–BN and SiO_2–Si_3N_4–BN ceramic composites by gelcasting method and to evaluate mechanical and dielectric properties, and microstructure analysis.

- To study the rheological behavior of the SiO_2 suspensions including SiO_2–Si_3N_4, SiO_2–BN and SiO_2–Si_3N_4–BN by varying dispersant content, pH value and solid loading by conducting initial trial experiments. Thus the range of solid loading (SL), monomer content (MC) and ratio of monomers (RM) are decided for further experimentation.

- To fabricate SiO_2 based ceramic composites using gelcasting method at varying solid loading (SL), monomer content (MC) and ratio of monomers (RM) as per RSM and DOE basis and evaluate flexural strength, porosity and dielectric constant using sophisticated instrumentation. Flexural strength, porosity, and dielectric constant are very important properties of radomes.

- To develop regression models for the analysis of responses such as flexural strength, porosity and dielectric constant and to study the effects of the process parameters on these responses.

- To evaluate optimum process parameters for maximum flexural strength, maximum porosity and minimum dielectric constant using RSM coupled with desirability function to optimize multiple responses.

2.12. Work Plan

The complete work plan of this research is planned, executed and presented as shown Figure 2.1.

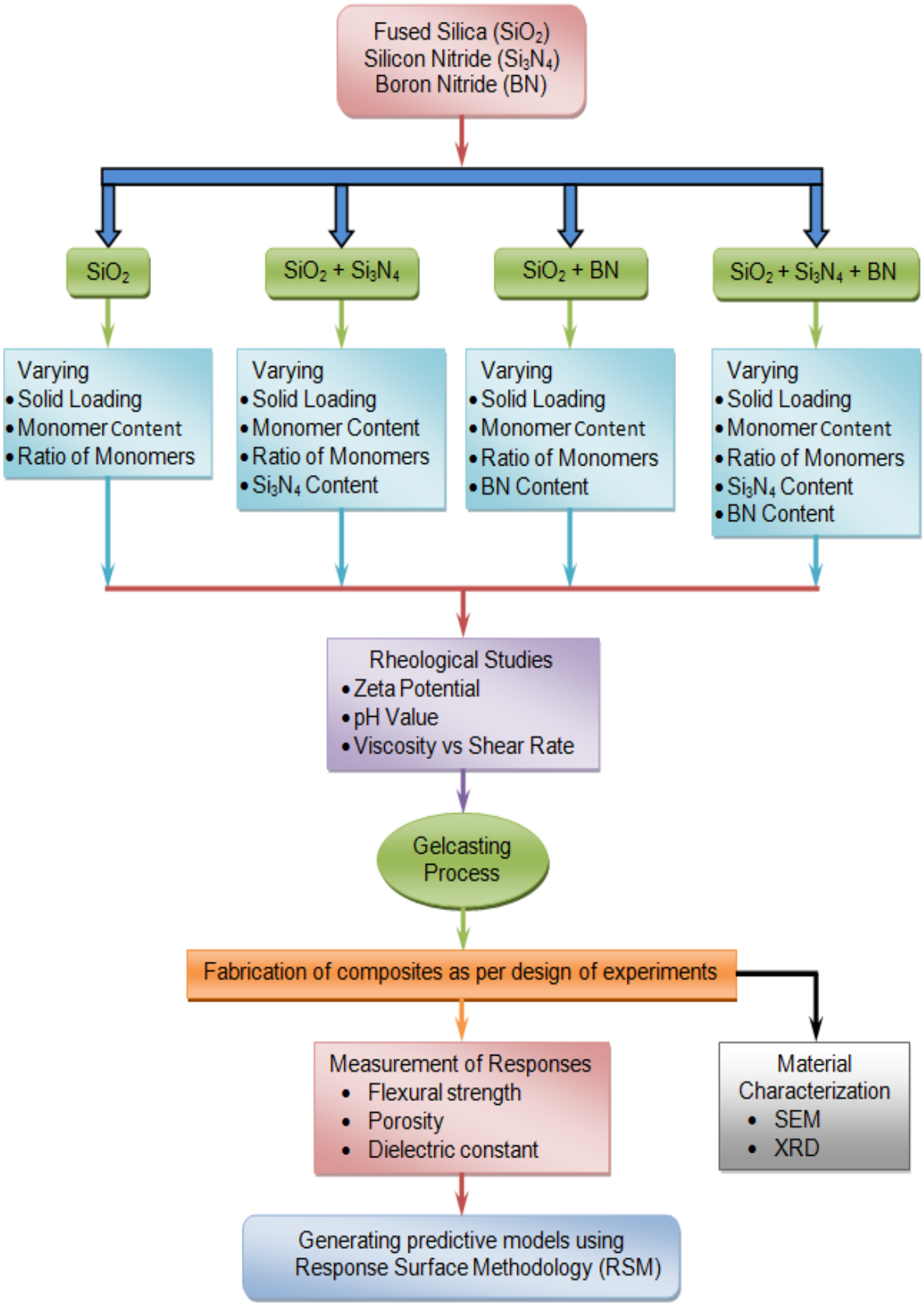

Figure 2.1. The complete work plan.

Summary

A thorough literature review is presented in this chapter dealing with materials for radomes, sintering aids, property evaluation and reviews on SiO_2 based ceramic composites. About 100 journals published in the contemporary literature referring the works up to 2015 is presented. Literature gaps are identified. Thus a problem is defined for the present state of work. A problem related to gelcasting of SiO_2, SiO_2–Si_3N_4, SiO_2–BN and SiO_2–Si_3N_4–BN ceramic composites is formulated to develop porous SiO_2 based ceramic composites. Hence pure SiO_2 is taken as base and Si_3N_4, BN powders are mixed independently and combinedly to develop SiO_2–Si_3N_4, SiO_2–BN and SiO_2–Si_3N_4–BN ceramic composites for evaluation of best composite for radomes. To fabricate SiO_2 based ceramic composites using gelcasting method at varying solid loading (SL), monomer content (MC) and ratio of monomers (RM) as per RSM and DOE basis and evaluate flexural strength, porosity and dielectric constant using sophisticated instrumentation. Flexural strength, porosity, and dielectric constant are very important properties of radomes. Characteristics like flexural strength, porosity, and dielectric constants are planned to measure as per the design of experiments. Research objectives are projected and a work plan is derived to achieve the objectives.

CHAPTER 3

MATERIALS AND EXPERIMENTAL SETUP

3.1. Introduction

Analysis of any response of a system greatly depends on how well the experiments are designed, conducted and measured. The measurement process may also include calculations. For example, porosity cannot be measured directly. It can be estimated by measuring the weights of work material. Therefore conducting experiments and measuring the responses is a crucial part of any investigation. Ranges of variables were identified and fixed after trial experimentation. In the present study, RSM has been used for the experimental plan and also for developing predictive models for various responses such as flexural strength, porosity and dielectric constant. However, to develop robust predictive models, accurate measurement or estimation of response is essential. This chapter describes the details of the materials and various equipment used during fabrication of composites and measurement of responses such as flexural strength, porosity and dielectric constant.

3.2. Ceramic Materials

3.2.1. Fused silica (SiO_2)

Fused silica is a non-crystalline form of silicon dioxide (quartz, sand) commonly made by fusion of pure silica sand (Wan et al. 2014a). Nowadays fused silica is one of the essential materials for many engineering and aerospace applications such as radomes, heat shields, antenna window, and crucibles, because of its interesting and prominent properties such as resistant to thermal shock and corrosion, a low thermal expansion coefficient, high softening temperature, a low and stable dielectric constant, and excellent chemical inertness (Haris and Welsh, 1973). These properties suggest that the SiO_2 ceramics are an ideal candidate material for high-temperature wave-transparent applications and radomes. However, the relatively low mechanical strength of sintered SiO_2 ceramics is inadequate to meet the requirements of advanced re-entry vehicles, especially hypersonic spacecraft. In order to overcome these shortcomings, additives including h-BN, Si_3N_4, fibers, and graphene have been utilized as

reinforcements to improve the mechanical strength of ceramics. Microstructure and typical properties of fused silica powder are shown in Figure 3.1 and Table 3.1 respectively.

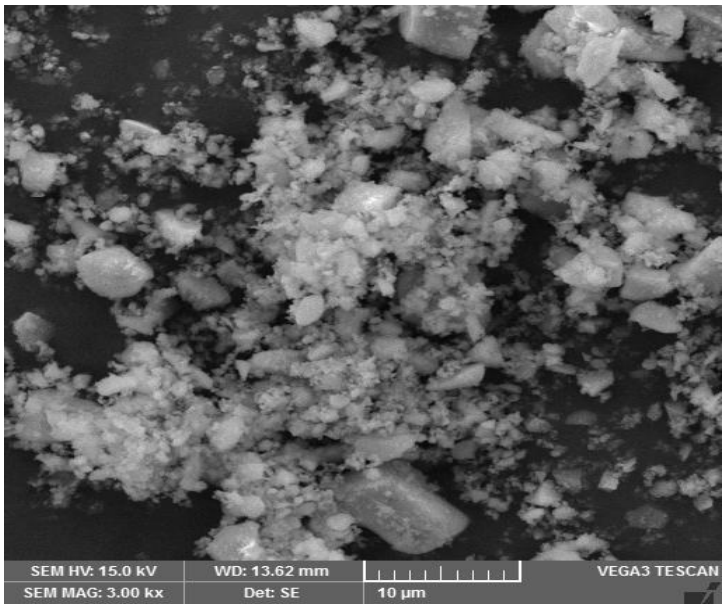

Figure 3.1. The microstructure of SiO_2 powder.

Table 3.1. Typical properties of fused silica.

Density	2.203 g/cm3
Color	White
Hardness	5.3–6.5 (Mohs scale), 8.8 GPa
Tensile strength	48.3 MPa
Compressive strength	>1.1 GPa
Bulk modulus	~37 GPa
Rigidity modulus	31 GPa
Young's modulus	71.7 GPa
Poisson's ratio	0.17
Coefficient of thermal expansion	5.5×10^{-7}/°C (average from 20 °C to 320 °C)
Thermal conductivity	1.3 W/(m·K)
Specific heat capacity	45.3 J/(mol·K)
Softening point	1665 °C
Annealing point	1140 °C
Strain point	1070 °C
Electrical resistivity	$>10^{18}$ Ω·m
Dielectric constant	3.75 at 1 MHz
Dielectric loss factor	less than 0.0004 at 1 MHz

3.2.2. Silicon nitride (Si_3N_4)

Silicon nitride based ceramics are extensively applied in various industrial fields owing to numerous properties, such as high hardness, superior corrosion resistance, excellent mechanical and chemical stability, excellent wear resistance, high decomposition temperature, high strength, and toughness, etc. Si_3N_4 is produced by reacting SiCl with NH_3 (Jong, B.W. et al.,1992). To attain a high extent of quality, components are spark plasma sintered, hot pressed or reaction sintered as dense parts cannot be produced through direct sintering. At lower temperatures, the bonding of Si_3N_4 particles is attained by addition of sintering aids which normally encourage liquid-phase sintering. Even at elevated temperatures, Si_3N_4 ceramics upholds their strength.

Nowadays, various processing techniques have been developed to prepare both the porous and dense Si_3N_4 ceramics for structural and functional applications (Chen et al., 2010). These materials can be densified under pressureless sintering conditions by adding a certain amount of sintering aids at high temperatures (1750‑2000°C). Si_3N_4 may be well stabilized electrostatically against agglomeration in aqueous slips either at pH of <5 or >9, having either a positive charge or negative charge, respectively (Greil, 1989). Microstructure and typical properties of Si_3N_4 powder are shown in Figure 3.2 and Table 3.2 respectively.

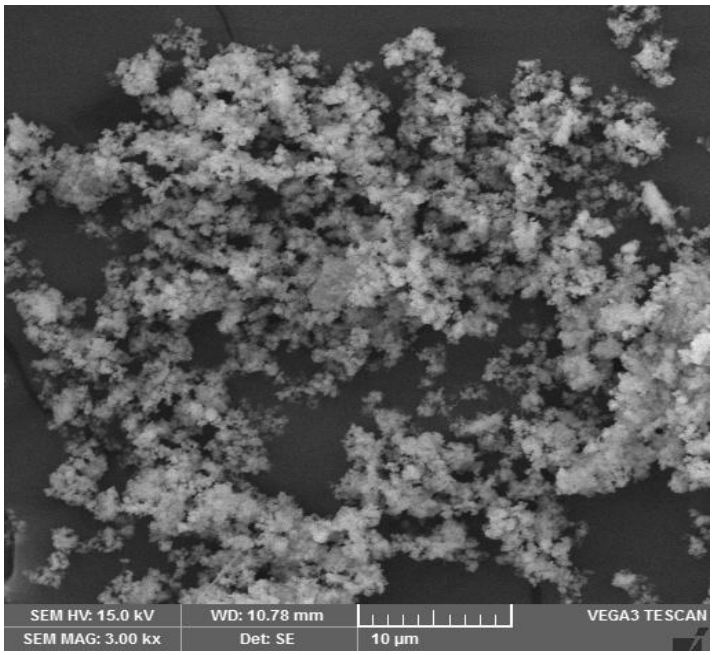

Figure 3.2. The microstructure of Si_3N_4 powder.

Table 3.2. Typical properties of Si_3N_4.

Density	3.31 g/cm3
Color	Dark gray
Hardness	9 (Mohs scale), 21.5 GPa
Tensile Strength	360-434 MPa
Compressive Strength	689-2760 MPa
Young's Modulus	317 GPa
Poisson's Ratio	0.23
Flexural Strength	679-896 MPa
Coefficient of thermal expansion	2.8×10^{-6}/°C (average from 40 °C to 400 °C)
Fracture Toughness	5.0-8.0 MPa x $m^{1/2}$
Thermal Shock Resistance	750 ºC
Thermal Conductivity	27 W/(m-K)
Specific Heat	0.17 cal/g-ºC
Electrical Resistivity	10^{13} Ωcm
Dielectric Constant	7.0 @ 1 MHz

3.2.3. Boron nitride (BN)

Boron nitride is a flexible material to facilitate in a number of applications owing to its distinctive combination of properties. Properties include good thermal shock resistance, chemical inertness, low thermal expansion, low dielectric constant and loss tangent, and high electrical resistance. This flexible material is currently used in a number of applications such as metal industry, automotive industry, high-temperature furnaces, etc (Eichler and Lesniak, 2008). On the other hand, the sinterability of BN ceramics is extremely poor and BN ceramics are normally manufactured by hot isostatic pressing or hot pressing at temperatures above 1800 °C, which is comparatively costly for their extensive use (Yuan et al., 2009). Compared to Si_3N_4, BN possesses better thermal shock resistance and dielectric properties (Dong et al., 2012). Microstructure and typical properties of BN powder are shown in Figure 3.3 and Table 3.3 respectively.

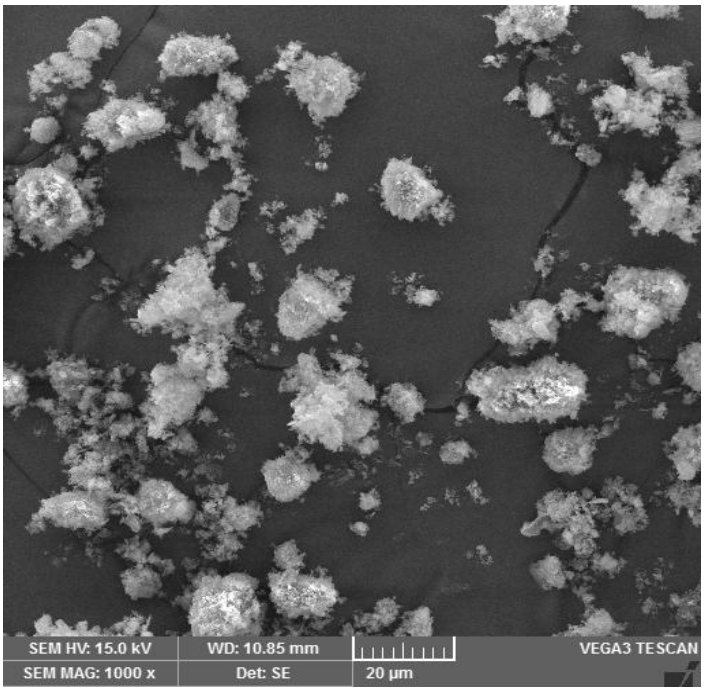

Figure 3.3. The microstructure of BN powder.

Table 3.3. Typical properties of BN.

Density	2.28 g/cm3
Color	White
Hardness	2 (Mohs scale), 1.96 GPa
Tensile Strength	2.41 MPa
Compressive Strength	23.5 MPa
Young's Modulus	675 GPa
Poisson's Ratio	0.05
Flexural Strength	51.8 MPa
Coefficient of thermal expansion	2×10^{-6}/°C (average from 40 °C to 400 °C)
Fracture Toughness	2.6 MPa x $m^{1/2}$
Thermal Shock Resistance	750 ºC
Thermal Conductivity	20 W/(m-K)
Specific Heat	0.19 cal/g-ºC
Electrical Resistivity	10^{13} Ωcm
Dielectric Constant	4.08 @ 1 MHz

3.3. Dispersant

Dispersants are added to enhance the ceramic particles dispersion in a solvent and to attain higher solids loading. As soon as dispersants are dissolved into the slurry the dispersant molecules are absorbed on top of the surface of the ceramic particle that transforms the charge distribution on the particle surface. In gelcasting, the uniform particle dispersion allows obtaining uniform sintering and high relative density when the castings are produced with high solids loading (Shanti et al., 2009). It is, therefore, necessary to understand how an optimum suspension of ceramic particles can be created (Sigmund et al., 2000). The influence of dispersant addition on the interaction among particles in ceramic aqueous suspension can be observed via zeta potential measurements, and some of the dispersants used for slurry stabilization are listed in Table 3.4.

Table 3.4. Dispersants used for slurry stabilization.

Dispersant	**Manufacturer**	**Chemical basis**
Darvan 821A	R.T Vanderbilt, Norwalk, CT	Poly(acrylic acid) – ammonium salt
Darvan C-N	R.T Vanderbilt, Norwalk, CT	Ammonium polymethacrylate
Dolapix A88	Zschimmer & Schwarz, Lahnstein, Germany	Amino alcohol
Dolapix CE64	Zschimmer & Schwarz, Lahnstein, Germany	Carboxylic acid preparation

3.4. Monomers

The heart of gel casting technology is the use of an organic monomer solution that can be polymerized to form a strong and cross-linked polymer-solvent gel, and the macromolecular gel network resulting from the in situ polymerization holds the ceramic particles in the given mold shape. The monomer solution consists of the solvent (typically water), a chain forming monomer, a chain branching (cross-linking) monomer, and a free radical initiator. The process of gel formation is shown in Figure 3.4. Here, the chain building monomer is depicted as “M”, and the chain branching or cross-linking monomer is depicted as “X”. Upon the addition of free radicals to the solution, the “M” monomers react to form long chains that are occasionally caused to branch by the incorporation of the “X” monomers. The result is a very high molecular weight polymer that fills space and traps the solvent molecules among its branches and the macroscopic result is a polymer-solvent gel (Janney et al., 1998a).

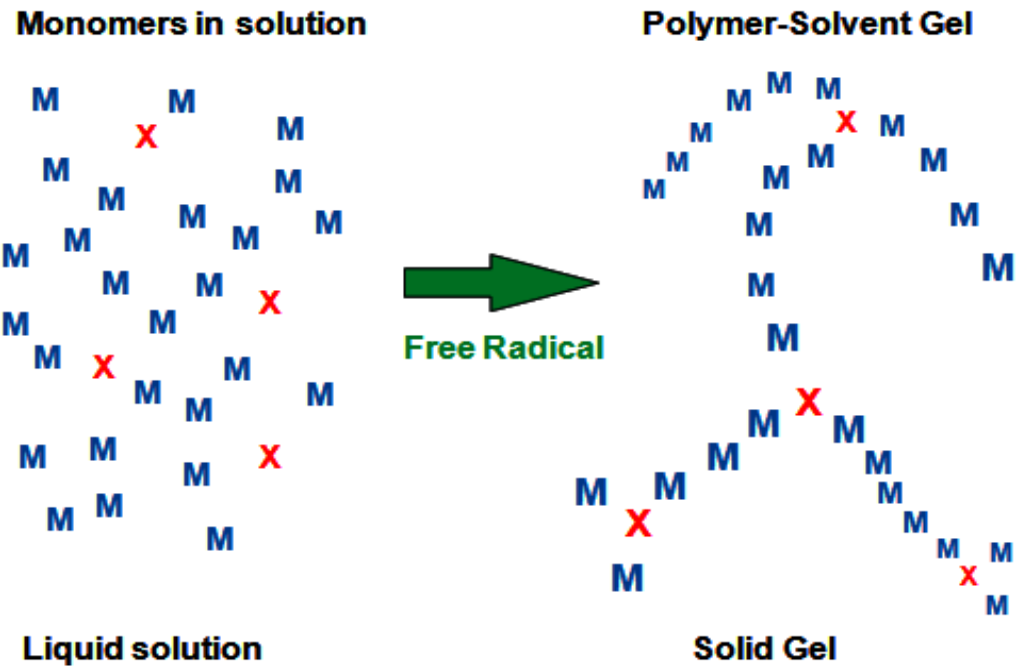

Figure 3.4. Formation of polymer–solvent gel.

3.4.1. Methacrylamide (MAM)

Methacrylamide (C_4H_7NO) is a chemical used in industries for producing polymers and copolymers. The structure of MAM is shown in Figure 3.5. It combines the ceramic particles by capturing the space between them. Two particles are held together by MAM so that at the time of sintering, monomers get vaporized leaving ceramic particles closer and particles get directly attached. MAM is obtained by the methylation of acrylamide.

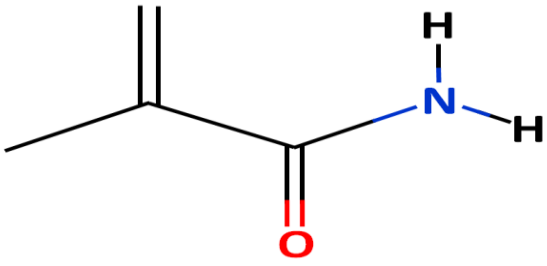

Figure 3.5. Structure of Methacrylamide

Acrylamide is found to be neurotoxic in nature (Kokabi et al, 2006 and Wan et al., 2013) and has significant effects on humans when exposed. Acrylamide is as well a skin irritant and perhaps initiates a tumor in the skin, probably causing skin cancer. So to overcome the toxic

nature of acrylamide, methacrylamide is used in place of acrylamide. Methacrylamide is non-toxic or extremely low toxic as compared to acrylamide.

3.4.2. *N,N'*-Methylenebisacrylamide (MBAM)

N,N'-Methylenebisacrylamide ($C_7H_{10}N_2O_2$) is used as a cross-linker while forming the polymers for instance polyacrylamide. One of the compounds of the polyacrylamide gel is the bisacrylamide that is used in biochemistry. Bisacrylamide undergoes polymerization with AM or MAM and is able to create cross-links between polyacrylamide chains, therefore generating a network of polyacrylamide. The monomer solution consists of monomers which are responsible for developing a chain and cross-linked structure respectively. For forming a linear polymer chain one double bond and for a cross-linking polymer at least two double bonds in monomers are required. The structure of MBAM is shown in Figure 3.6.

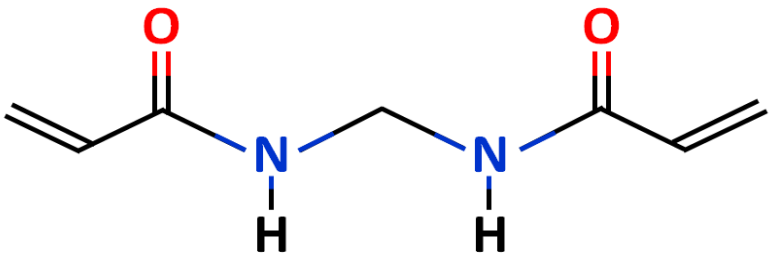

Figure 3.6. The structure of *N,N'*-Methylenebisacrylamide.

In addition, from the newest research, less toxic monomers were found. The system of methacrylamide– *N,N'*-methylenebisacrylamide (MAM–MBAM) monomers was suitable for aqueous gel casting because of their relatively low toxicity (Yang et al., 2011). In this new system, MAM is the preferred chain former and MBAM is the preferred branching former. In MAM-MBAM system, the monomer content is typically about 10-20 wt.% in solution and ratio of MAM and MBAM is between 3:1 to 10:1. Besides, other common monomers such as Hydroxymethylacrylamide (HMAM), N-Vinylpyrrolidone (NVP) and Methoxy poly(ethyleneglycol) mono methacrylate (MPEGMA) are used as chain forming monomers and poly(ethylene glycol) dimethacrylate (PEGDMA) is used as crosslinker (Janney et al., 1998a). Thus, the two common monomer systems which are used in the practical experiment are MAM-MBAM and MAM-PEGDMA. In fact, besides consideration of monomers' toxicity, the selection of monomer system depends on strength, the toughness of gel, wet and

dry material strength, stiffness, green machinability, reactivity, and price. In general, if the monomer concentration or ratio between cross-linker and chain monomer is higher, the gel strength will be higher and final ceramic parts will be stronger and stiffer with gelcasting process.

3.5. Initiator and Catalyst

In gel-casting, the free radical initiator system also plays an important role. The initiator can make monomers react each other to form polymer molecules. Under free radical initiator activation, chain forming monomers form a longer polymer chain with reaction and cross-linker reacts with chain monomer to form branch polymer molecules. The formation of high molecular weight polymer fill space between particles in the ceramic slurry and thus cause the ceramic powder to form near network structure together with the polymer. Gelation usually takes place at an elevated ambient temperature in between 40-80ºC.

The commonly used initiators are Ammonium persulfate ($(NH_4)_2S_2O_8$)/ *N*,*N*,*N'*,*N'*-Tetramethylethylenediamine ($C_6H_{16}N_2$) (APS-TEMED), Azobis (2-amidinopropane) HCl (AZAP) and Azobis [2-(2-imidazolin-2-yl) propane] HCl (AZIP), etc., (Janney et al., 1998). However, toxicity data indicate that APS and TEMED cause skin irritation in humans. The structure of APS and TEMED are shown in Figure 3.7 (a) and (b).

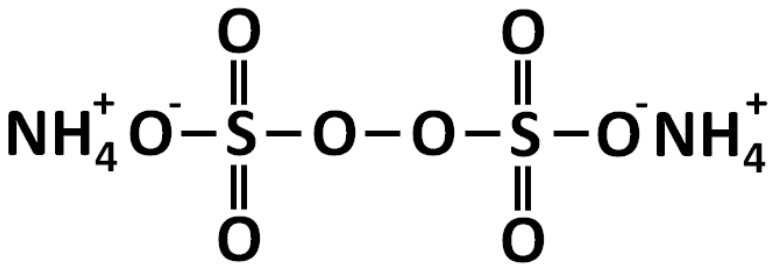

Figure 3.7(a). The structure of Ammonium persulfate.

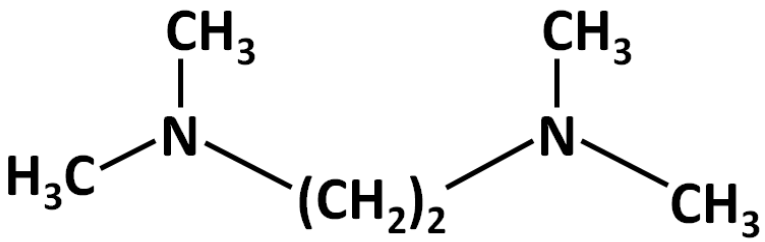

Figure 3.7(b). The structure of *N*,*N*,*N'*,*N'*-Tetramethylethylenediamine.

3.6. Surfactant

Atmospheric oxygen inhibits the free radical reaction method known as polymerization, ensuing surface-exfoliation phenomenon in green bodies (Ha, 2000). Therefore, the polymerization process is generally carried out in a nitrogen atmosphere that increases the cost of fabrication. Various polymers that are based on the adhesive aid of polymer molecules were added to the slurry to avoid the surface-exfoliation phenomenon by preventing the inhibition effect of oxygen in gel-casting (Li et al., 2004, Ma et al., 2002a and Ma et al., 2002b). The difference between surface and inside still exists, which will lead to defects and cracks during drying and sintering (Mao et al., 2009). Polyethylene glycol-400 is a non-ionized water-soluble polymer with a simple structure as shown in Figure 3.8. It is a viscous, colorless, and transparent fluid. PEG-400 is extensively used in pharmaceutical industries. PEG-400 possesses good stability, wettability, low toxicity and burnt out completely during sintering and resulting in the application of gel-casting process.

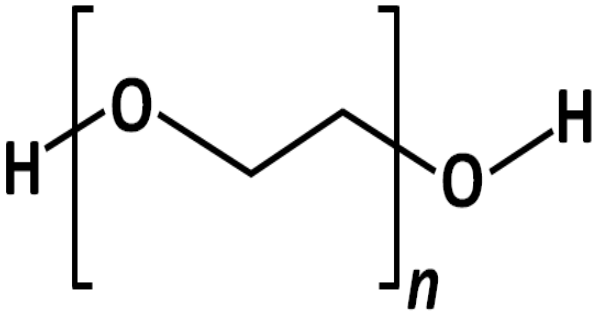

Figure 3.8. The structure of Polyethylene glycol-400.

3.7. Equipment used in this work

3.7.1. Magnetic stirrer

A magnetic stirrer (REMI 5 MLH) shown in Figure 3.9 is used for stirring the slurry. At lower speeds also permanent magnet DC (PMDC) motor in the magnetic stirrer provides high torque and retains speed constancy in spite of variation in volume or viscosity. The specifications of magnetic stirrer are given in Table 3.5.

Figure 3.9. Magnetic stirrer setup

Table 3.5. Specifications of the Magnetic stirrer.

Power [W]	500
Max. stirring quantity (Water)(Litres)	5
Motor rating input [W]	18
Motor rating output [W]	10
Speed range [rpm]	100-1500
Speed display	LCD
Speed display resolution [rpm]	1
Dimensions (WxDxH) (mm)	200 x 225 x 185
Heating power [W]	500
Temperature Range	Up to 340°C
External Temperature sensor	PT-1000
Weight (kg)	2.8

3.7.2. Rotational Rheometer

The rheological behavior of the slurry was measured by a Rotational Rheometer (RheolabQC, Anton Paar Corp., Germany) with sandblasted concentric cylinder measuring system (CC27) as shown in Figure 3.10. This is a computer controlled Rheometer with

Rheoplus software. This instrument was used to measure the rheological properties of liquid or gel- like materials. The flow measurements were conducted between 0.1 and 100s^{-1} shear stress at constant temperature 27 °C. The specifications of Rheometer are given in Table 3.6.

Figure 3.10. Setup showing computer controlled Rheometer

Table 3.6. Specifications of Rheometer

Speed	0.01 to 1200 1/min
Torque	0.20 to 75 mNm
Shear stress	0.5 to 3 x 10^4 Pa
Shear rate	10^{-2} to 4000 1/s
Viscosity range (depending on the measuring system)	1 to 10^9 mPas
Temperature range	-20 °C to 180 °C
Angular resolution	2 µrad
Dimensions (W x H x D)	300 x 720 x 350 mm
Weight	14 kg

3.7.3. Zeta Potential Analyzer

The stability of the particles in the slurry is measured by Zeta Potential Analyzer. Zeta potential measurements of ceramic powders (SiO_2, Si_3N_4, and BN) in the presence of dispersant will be conducted as a function of pH value (in the range of 1–11) via Zeta Potential Analyzer (Zetasizer Nano ZS, Malvern, UK) as shown in Figure 3.11.

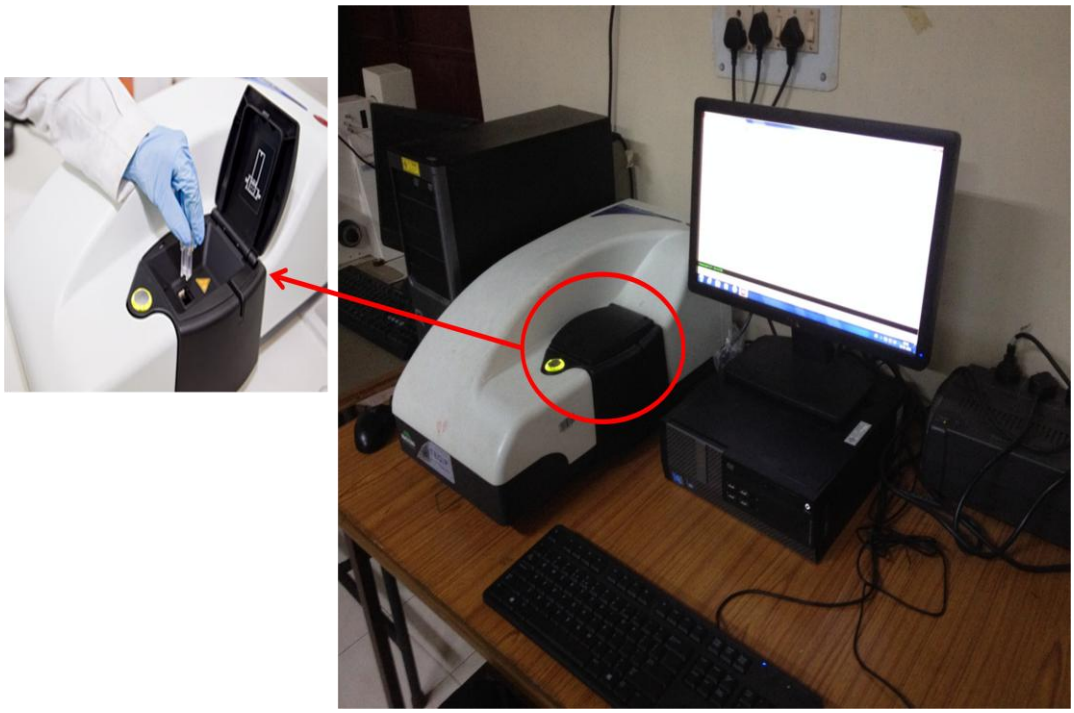

Figure 3.11. Setup showing Zeta Potential Analyzer

3.7.4. Desiccators

De-airing of the slurry was done in a desiccator (Tarsons Products Pvt. Ltd., India) using a vacuum pump (IVP 250LPM, INDVAC Pumps, India) to remove the air bubbles in the slurry. It is a double stage air-cooled, direct-drive rotary high vacuum pump. De-airing was also done for samples during porosity and density measurement in kerosene medium. A typical de-airing arrangement using desiccators is shown in Figure 3.12.

Figure 3.12. Desiccators with a vacuum pump.

3.7.5. Humidity Controlled Oven

After gelation, the green parts are demolded and dried under controlled temperature and humidity conditions using the Humidity Controlled Oven (Thermo Spectrum Instruments Pvt. Ltd., India) shown in Figure 3.13. This may avoid cracking and deformations caused by rapid drying. The specifications of the humidity controlled oven are given in Table 3.7.

Figure 3.13. Humidity Controlled Oven.

Table 3.7. Specifications of Humidity Controlled Oven.

Temperature range	10.0°C to 60.0°C. Accuracy / Uniformity: ±0.1°C/±1°C
Humidity range	25% to 95% RH. Accuracy/Uniformity ±2% RH/±3% RH
Temperature / Humidity display	Digital LED 3½ digit
Control	Microprocessor based PID control. With Autotune
Resolution	0.1 °C/1% RH
Temperature sensor	PT – 100
RH sensor	Direct capacitance type
Heating	'U' shaped Nichrome wire heater in SS sheathing
Steam injection	Boiler with reservoir made of thick stainless steel, with heater, water inlet control, low water level safeguard
Air circulation	Flange motor with impeller / blower
Construction	Double wall, with insulation, outer door key lockable

3.7.6. Moulds

Various mold materials such as aluminum, glass, and polyvinylchloride (PVC) were used in this study. Hard anodized aluminum is the most excellent alternative as a mold material for stable molds. It is inexpensive and can be easily machined with suitable tolerances. The gelled parts can be removed easily from the anodized aluminum mold than a normal aluminum mold. For preliminary castings in the lab, glassware such as Petri dishes, beakers etc. are broadly used. The gelled parts can be easily removed from glass molds by using a small volume of mold release agents such as Vaseline, petroleum jelly etc. For producing tubes, rods, and rings PVC material is used broadly in gelcasting. On the surface of the green body a thin, ungelled layer is formed that acts as a lubricant for easy removal of the gelcast part irrespective of the mold release agent used. In this study, petroleum gel is used as a mold release agent for extracting the gelled parts from the mold. Few molds used in this study are presented in Figure 3.14.

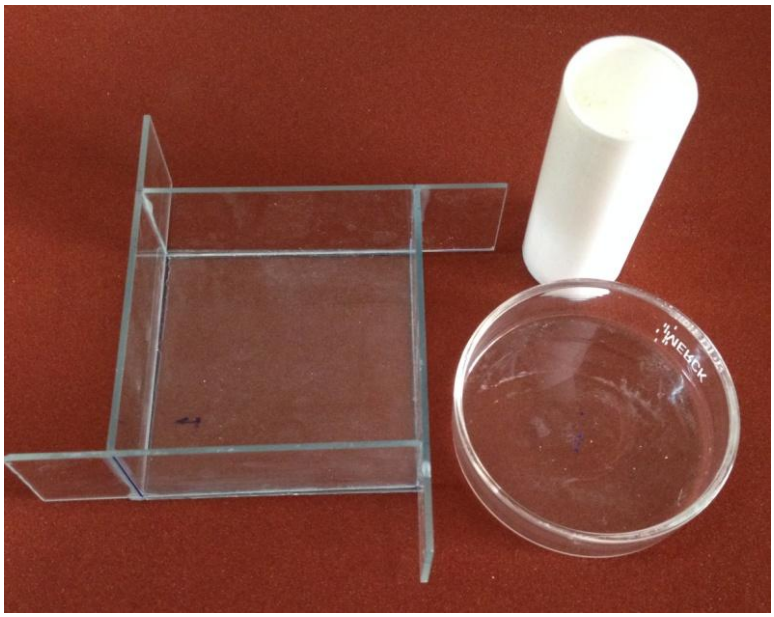

Figure 3.14. Molds for gelcasting.

3.7.7. High Temperature Tube Furnace

The samples are sintered in a High-Temperature Tube Furnace, MT-17P (Figure 3.15) connected with an N_2 cylinder for gas purging. This tube furnace is designed for heating purpose in typical lab applications and small production workloads to a working temperature

of 1600 °C. The complete furnace assembly consists of the tube furnace with a ceramic tube and control panel featuring a digital display controller, a power module, and a single circuit breaker for the furnace heating system. The tube furnace specifications are given in Table 3.8. High-temperature oxidation of BN and Si_3N_4 is inevitable, which will deteriorate the mechanical and dielectric properties in addition to the ablation resistance of the SiO_2 matrix, especially for BN-reinforced fused silica ceramics. Hence, sintering is done in N_2 atmosphere.

Figure 3.15. High-Temperature Tube Furnace.

Table 3.8. Specifications of High-Temperature Tube Furnace.

Maximum Temp.	1700 °C
Working Temp.	1600 °C
Heating Elements	Molybdenum disilicide ($MoSi_2$) heating elements, easily replaceable
Inner Chamber	Ceramic Brick/ Board , with heating elements placed on the side walls
Insulation	Ultra high purity alumina low thermal mass insulation.
Construction	Triple walled with air insulation on the outer side for minimal skin temperature.
Body	Made of mild steel duly powder coated.
Tube Material	High purity Alumina
Tube Size	Tube dia. = 100 mm Hot zone length = 300 mm Overall length = 600 mm
Gas Purging	Ends of the tube have Aluminium couplers with a cooling attachment for purging of gasses.
Power Control	SCR unit (phase angle thyristor) with current limit and soft start facility and step down air cooled transformer
Temperature Control	Microprocessor based PID programmable temperature controller. Dual display of Set & Actual temperature with soft touch keys. With thermocouple break protection & cold junction compensation.
Sensor	Pt / Pt - Rh 'B' type
Safety	High-speed semiconductor safety fuse for overload protection. Thermocouple broke indication with automatic tripping. Soft start and stop facility, suitable for heating elements. Over current and short circuit protection. High-temperature alarm.
Power supply	415 Volts, 3 phase AC supply.

3.7.8. X-ray Diffractometer

X-ray Diffractometer (PANalytical X'Pert Powder, Almelo, Netherlands) shown in Figure 3.16 is used to observe the phase formation behavior of ceramic bodies. Phase identification may be done using X'Pert HighScore software containing ICDD (International Centre for Diffraction Data) files.

Figure 3.16. X-ray Diffractometer.

3.7.9. Scanning Electron Microscope

The morphology and microstructure of as-received powder and gel casted bodies were observed by Scanning Electron Microscope (VEGA 3 LMU, TESCAN, Czech Republic) shown in Figure 3.17. The surface of each specimen was sputtered with gold metal to ensure high conductivity during the electron microscopy.

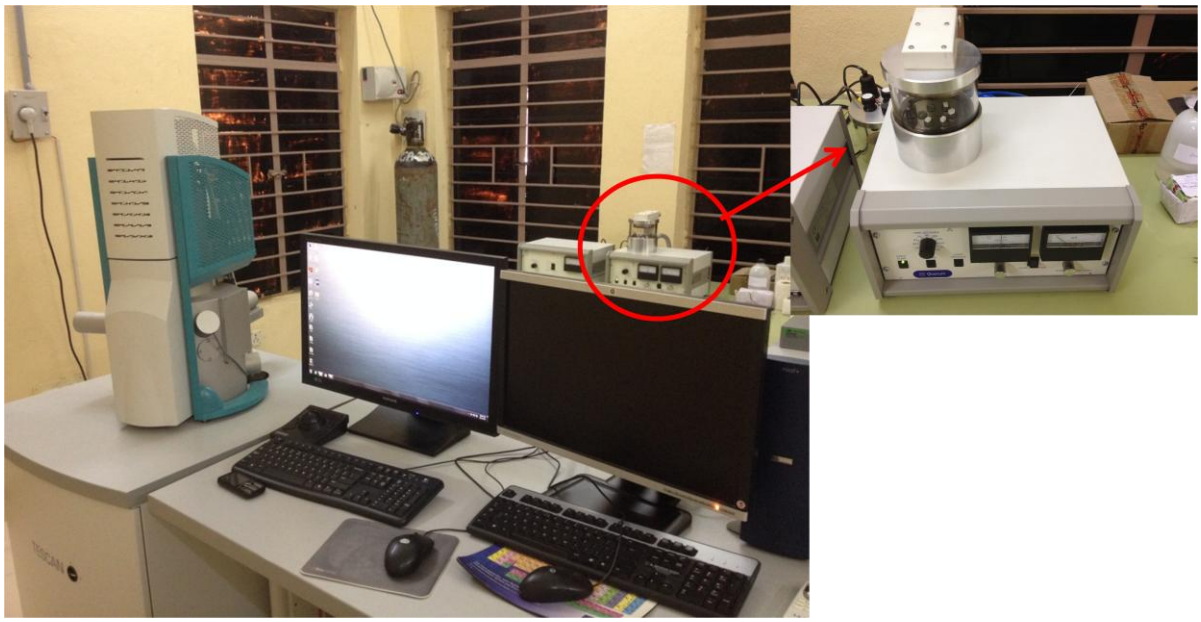

Figure 3.17. Scanning Electron Microscope with the sputtering setup.

3.7.10. Diamond Cut-Off Saw

The ceramic samples were cut into rectangular bars of dimensions 3mm x 4mm x 40mm using a high-speed Diamond Cut-Off Saw (MTI Corporation, USA). Figure 3.18 is a typical Diamond Cut-Off Saw and the specifications are given in Table 3.9.

Figure 3.18. High-speed diamond cut-off saw.

Table 3.9. Specifications of Diamond Cut-Off Saw.

Power	Voltage: 110V AC 50/60hz
Motor & Spindle	Speed Range from 400 to 3250 RPM.
Cutting Blade	Impregnated diamond blade of 4" Dia x 0.014" (0.35 mm) thickness x 1/2" arbor
Transformer	300W AC to AC Transformer (Dual Change 220/240V = 110/120V)

3.7.11. Universal Testing Machine

The flexural strength was measured by the three-point flexural method with a span length of 40 mm and at a crosshead speed of 0.5 mm/min using a Universal Testing Machine (H10K-S, Tinius Olsen Testing Machine Company, USA) shown in Figure 3.19. The specifications of the Universal Testing Machine are given in Table 3.10.

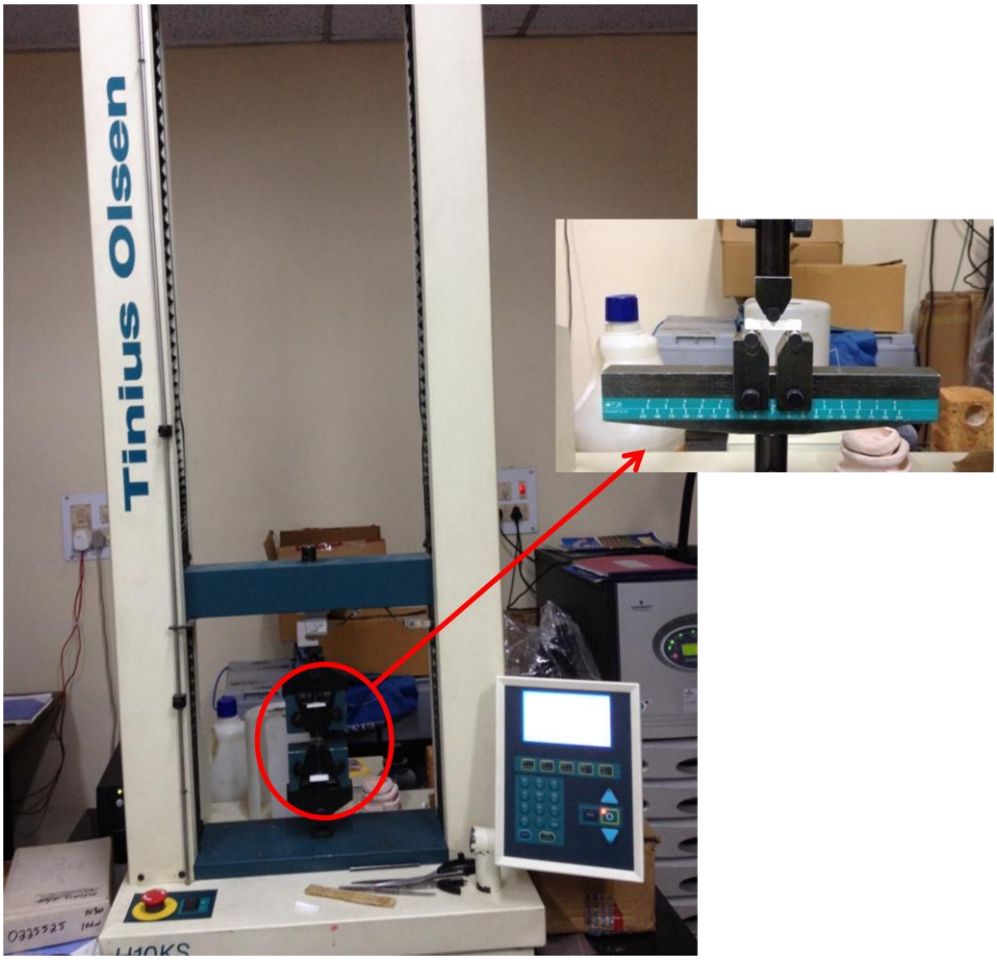

Figure 3.19. A Universal Testing Machine with three-point bending setup.

Table 3.10. Specifications of the Universal Testing Machine.

Capacity	10 kN
Clearance between columns	405 mm
Load cells	Rapid change, low profile Z type load cells with digital encoding for automatic recognition and scaling available – 10kN, 5kN, 2.5kN, 1kN, 500N, 250N, 100N, 50N, 10N, 5N
Maximum crosshead Travel	Measurement direct from ball screw – fully auto scaling of single measurement range 1100 mm
Testing speed Range	0.001 to 1000 mm/min
Capacity at Maximum speed	5 kN
Maximum speed at capacity	500 mm/min
Jog speed	0.001 to 1000 mm/min
Return speed	0.001 to 750 mm/min
Dimensions (H x W x D)	1600 x 650 x 450 mm
Weight	115 kg

3.7.12. Electronic Analytical Precision Balance

An Electronic Analytical Precision Balance (Afcoset, ER-120A, India) shown in Figure 3.20, is used to measure the weights of specimens for measuring the bulk density and apparent porosity. The specifications of Electronic Analytical Precision Balance are given in Table 3.11.

Figure 3.20. Electronic Analytical Precision Balance with Archimedes setup.

Table 3.11. Specifications of Electronic Analytical Precision Balance.

Max. Capacity	120 g
Readability	0.1 mg
Repeatability	0.1 mg (Std Dev) max capacity
Non-linearity	±0.1 mg (10g change)
	±0.2 mg (0-max. capacity)
Sensitivity Drift	±2 ppm/°C
Stabilisation Time	5 Sec (Approx)
Operating Temp.	5°C - 40°C
Pan Diameter	85mm/3.3″
Weighing Chamber (WxDxH)	178mm x 154mm x 186mm
Ext. Dimensions (WxDxH)	195mm x 411mm x 266mm
Weight	11 kg
AC input	220, 240 V AC (50 Hz) 11 VA

3.7.13. Impedance Analyzer

Dielectric properties are measured at room temperature using Impedance Analyzer (MTZ-35, Bio-Logic Science Instruments Pvt. Ltd, France) shown in Figure 3.21. Disc-shaped specimens (ϕ10 x 0.8 mm) are used for measuring the dielectric constant.

Figure 3.21. Setup showing Impedance Analyzer.

Summary

In this chapter, the details of the materials used for fabrication of SiO_2, SiO_2–Si_3N_4, SiO_2–BN and SiO_2–Si_3N_4–BN ceramic composites are presented. The equipment namely magnetic stirrer, Rotational Rheometer, Zeta Potential Analyzer, Desiccators, Humidity Controlled Oven, Moulds, Programmable Tube Furnace, X-ray Diffractometer, Scanning Electron Microscope, Diamond-Cut-Off Saw, Universal Testing Machine, Electronic analytical precision balance and Impedance Analyzer used during fabrication of composites and measurement of the responses are presented along with the specifications.

CHAPTER 4

PREPARATION OF CERAMIC COMPOSITES BY GELCASTING

4.1. Introduction

Various methods of fabrication of ceramics were reported and discussed in detail in Chapter-1. From the review, it can be understood that gelcasting process is one of the latest and most accepted methods for casting ceramics to a near net shape with ease (Omatete et al., 1991 and Omatete et al., 1997). The process has shown a sudden development from the laboratory to industries. It was also noticed in the literature that the gelcasting process involves reactive chemical constituents and the prediction of final product characteristics from these constituent proportions is a major challenge in gelcasting process. This chapter deals with the fabrication of ceramic composites to achieve better mechanical and dielectric properties by gelcasting, a near-net shape fabrication technique. Experimentation was carried out to determine the suitable dispersant and effects of dispersant percentage, pH value, zeta potential, and solid loading on the rheological properties of the SiO_2 suspensions. Pilot experiments were conducted to fix the ranges and levels of solid loading, monomer content and monomer ratio.

4.2. Pilot experimentation for gelcasting of SiO_2 ceramics

4.2.1. Materials

Commercial fused silica powder of 99.9% purity (M/s. Ants Ceramics Pvt. Ltd., Thane, India) with an average particle size of 1-5 μm having a density of 2.2 g/cm^3 is used in this study. Deionized water was used as a solvent. In the process of gelcasting Methacrylamide and *N*,*N'*-Methylenebisacrylamide (both Alfa Aesar) were used as the organic monomer and cross-linker respectively. Ammonium persulfate (Alfa Aesar) was used as an initiator. Dispersants such as Darvan 821A, Darvan C-N, Dolapix A88 and Dolapix CE64 were used for dispersing fused silica in the slurry at high solid loading and low viscosity. Surface exfoliation phenomenon in green bodies was eliminated by adding

Polyethylene glycol 400 (Alfa Aesar). Diluted Nitric acid and Ammonium hydroxide (both S.D. fine chemicals, India) were used for pH adjustment.

4.2.2. Slurry preparation

The detailed scheme of gelcasting process is shown in Figure 4.1. Firstly, premix solution was prepared by completely dissolving known amounts of dispersant (0-0.75 wt%, based on fused silica concentration), PEG (3 wt%, based on fused silica concentration), MAM and MBAM (10-15 wt%, based on fused silica concentration in the ratio of 3:1 to 7:1) in deionized water using magnetic stirrer.

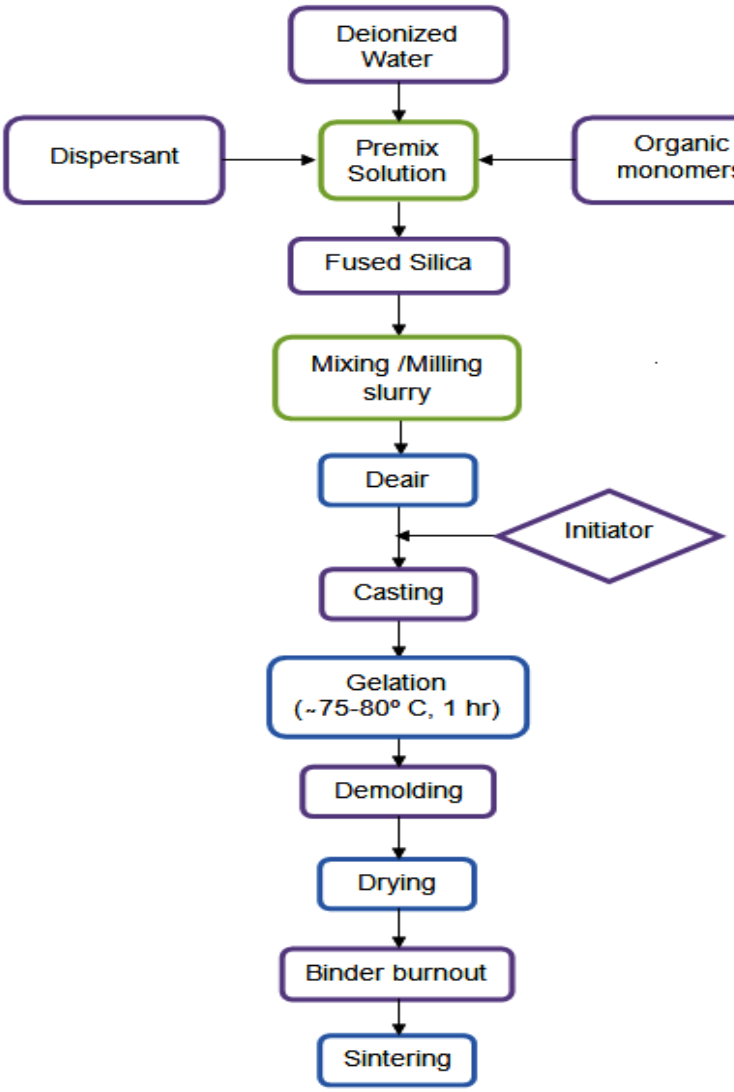

Figure 4.1. A detailed flowchart of gelcasting process of SiO_2 ceramics.

Secondly, fused silica powder was added in regular intervals for homogenous dispersion of ceramic particles into the premix solution by magnetic stirring for about 6 h in a glass beaker. Then the slurry was degassed for 20-25 min in a vacuum deaeration container after addition of APS (1 wt% of monomers). Gelation of the slurry can be accelerated using a catalyst or heat-driven process. The addition of the Catalyst, *N*,*N*,*N'*,*N'*-Tetramethylethylenediamine (TEMED) caused immediate consolidation of the slurry, and acceleration of the reaction was too fast to be under control. Hence, the heat-driven process is applied for gelation of the slurry. The slurry was cast into a nonporous glass mold and soaked at 75-80 ºC for 1 h for polymerization to take place. After gelation, the green part was demolded, and dried under controlled temperature and humidity conditions to avoid cracking and deformations caused by rapid drying. The green bodies were sintered in a high-temperature tube furnace with molybdenum disilicide ($MoSi_2$) as heating elements, under air atmospheric conditions at 1º/min up to 600ºC and soaked for 1 h to pyrolyze organic compounds. These samples were then heated at 2º/min to the sintering temperature of 1150 ºC to 1300ºC and were soaked for 3 h. Sintered samples of SiO_2 ceramics were shown in Figure 4.2.

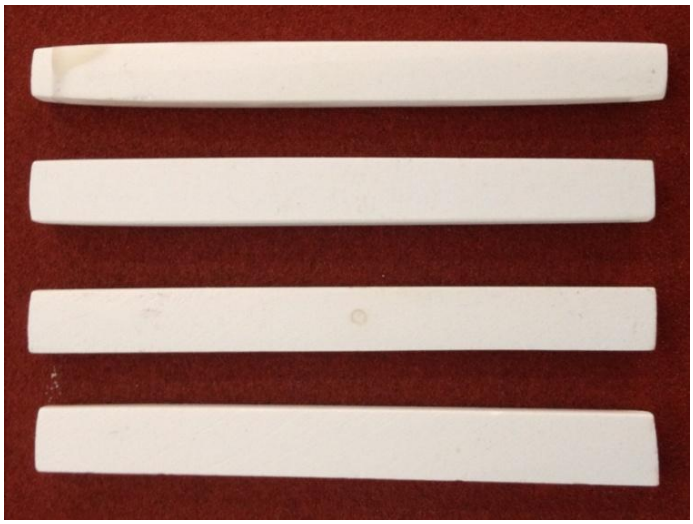

Figure 4.2. Schematic showing the samples of SiO_2 ceramics.

Table 4.1. shows a sample calculation for preparing a SiO_2 slurry with 70 vol% solid loading as per the rule of mixtures. The density of fused silica powder was 2.2 gms/cc.

Table 4.1. Recipe for 75 ml of ceramic suspension with 70 vol% solid loading.

Recipe for suspension	**Weight percent (%)**	**Weight (gms)**
Water	----	22.5
SiO_2	100 wt% of solid loading	115.5
Dispersant	0.5 wt % of solid loading	0.5775
PEG-400	3 wt % of solid loading	3.4650
MAM	15 wt % of solid loading in	14.4375
MBAM	the ratio of 5:1	2.8875
APS	1 wt % of monomer content	0.1733

4.2.3. Results and analysis of pilot experiments

4.2.3.1. Zeta potential and pH value

The potential difference between the dispersion medium (solvent) and the stationary layer of fluid attached to the dispersed ceramic particle is the zeta potential. The factors influencing the fluidity and stability of the slurry are its pH value and dispersant. To improve the dispersion of ceramic particles in a solvent, dispersants are added. The relation between stability and zeta potential is that higher the zeta potential of particles leads to higher stability of the suspension. The higher absolute value of zeta potential exhibit higher stability due to higher electrostatic repulsion between the particles in the slurry. The zeta potential of SiO_2 particles in the slurry is studied by varying different dispersants in the range of 0-0.75 wt% as a function of pH value. The trend is depicted in Figure 4.3.

The zeta potential of SiO_2 particles without dispersant are found to be vary from 6.61 mV at pH 1 to -45.9 mV at pH 9. It can be seen that the isoelectric point (IEP) is at pH 2.4 and the absolute value of zeta potential increases as pH value increases, but in some cases, zeta potential is decreased. It is also observed that of all the dispersants addition of 0.5 wt% Darvan 821A gives the maximum value of zeta potentials which is about -68.6 mV at pH 11, which is most suitable for obtaining well dispersed fused silica slurries. The other dispersants having good zeta potential other than 0.5 wt% Darvan 821A are 0.75 wt% Dolapix A88, 0.25 wt% Darvan 821A, 0.25 wt% Darvan CN, 0.75 wt% Dolapix CE64 and 0.5 wt% Dolapix A88. The corresponding zeta potential values are -52.9 mV, -51.9 mV, -51.8 mV, -48 mV and

-47.5 mV at pH 11 respectively. The zeta potentials of the remaining slurries are found to be lower than that of slurry without a dispersant and hence not considered.

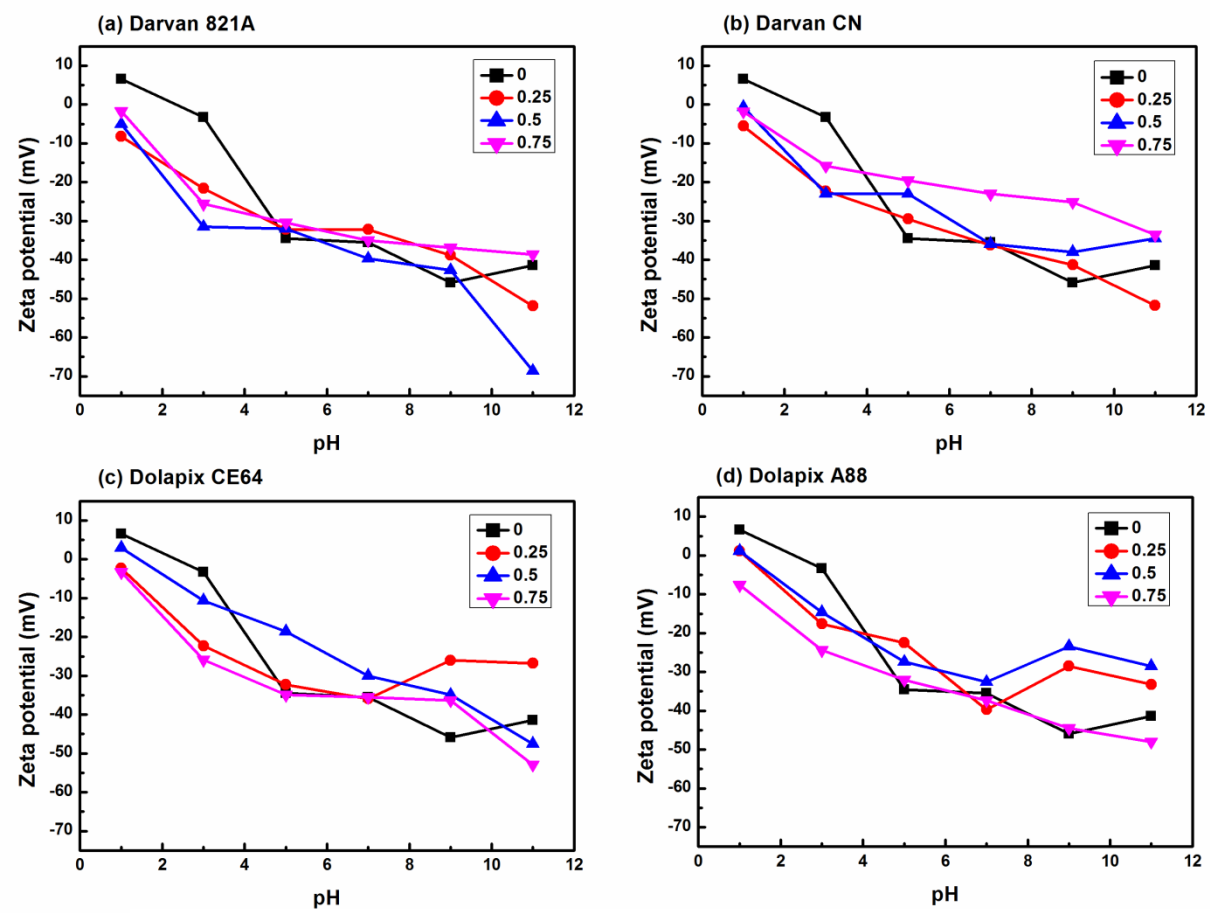

Figure 4.3. Zeta potential of SiO_2 slurries with various dispersants and wt.%.

The pH of the slurry also plays an important role on the rheological properties. It is observed that high absolute zeta potential value is obtained by increasing the pH value of the slurry which increases the dispersibility of the slurry. But at higher pH values, the slurry becomes viscous due to the formation of hydroxide layer on the surface of SiO_2 particles and this process is known as hydrolyzation (Trompette and Meireles, 2003). Diluted HNO_3 and NaOH were used for adjusting the pH value of the slurries.

4.2.3.2. Dispersant

Dispersants are added for uniform dispersion of ceramic particles in the slurry. This enables the slurry to form unified properties after gelcasting. High relative density is easily reached when gels are produced with high solids loading. In gelcasting process, the

homogeneous dispersion of particle allows obtaining uniform sintering and high relative density when the castings are produced with high solids loading. It is, therefore, necessary to understand how an optimum suspension of ceramic particles can be achieved. The zeta potential of fused silica slurry is higher at 0.5 wt% of Darvan 821A as shown in Figure 4.3. Each type of dispersant gives a different zeta potential value at particular amounts. Fused silica ceramics without the addition of dispersant shows a maximum zeta potential value of -4.5 mV at pH 5 respectively, which shows that the slurry at pH 4 to 4.5 can be gelcast without the addition of a dispersant.

4.2.3.3. Solid loading

Higher solid loading of fused silica is required to improve the mechanical properties of gelcast parts. But viscosity of slurry increases as the solid loading increases due to agglomeration at higher solid loading, which make the slurry difficult to pour into the mold. This is due to flocculation and coagulation caused by the reduction of solvent (water) present in between the ceramic particles. Slurries with viscosity lower than 1 Pa.s at the shear rate of $20s^{-1}$ are suitable for casting into the mold with better fluidity. Hence, slurry with 73 vol.% solid loading and 0.5 wt% Darvan 821A is found most suitable for casting into the mold. The variation of viscosity as a function of the shear rate ranging from 0.1–100 s^{-1} for different solid loadings is shown in Figure 4.4.

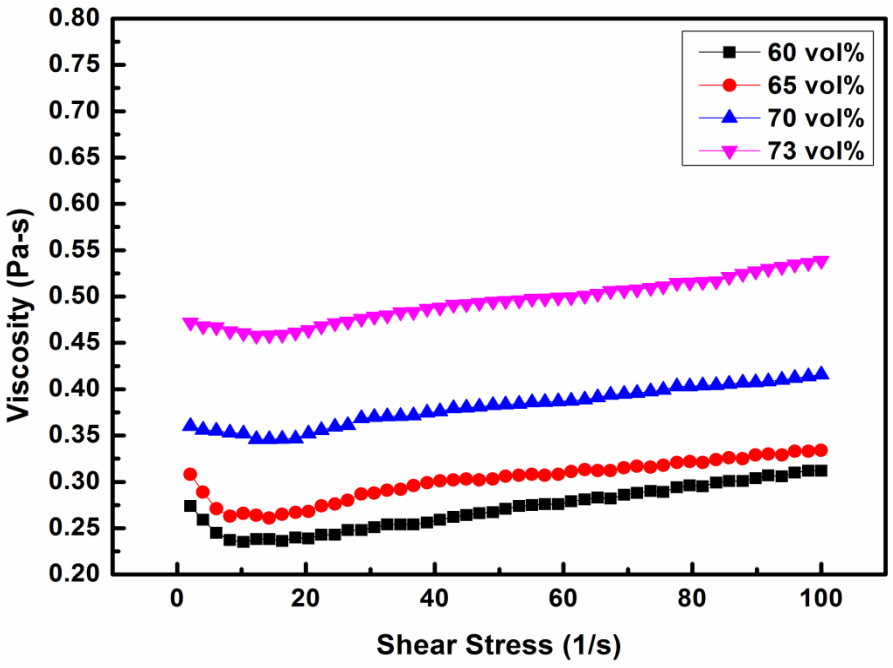

Figure 4.4. Variation of viscosities of slurries at various solid loadings.

The amount of dispersant, Darvan 821A was 0.5 wt% based on the weight of fused silica powders. From the curve it can be seen that there is an increase in viscosity from 0.224 to 0.352 Pa.s for increase in solid loadings from 60 to 70 vol.% and for solid loading 73 vol.% viscosity is 0.465 Pa.s with shear thinning behavior at the shear rate of 1–20 s^{-1} and over this shear rate exhibits shear-thickening behavior.

4.2.3.4. Mechanical Properties

The microstructure of sintered fused silica ceramics is shown in Figure 4.5. The variation of bulk density and apparent porosity of fused silica ceramics with 0.5 wt% Darvan 821A as a function of solid loading for sintered ceramics are shown in Figure 4.6. As the solid loading increases from 60 vol.% to 73 vol.%, the bulk density increases from 1.52 to 1.88 g/cm^3 and the apparent porosity decreases from 41.94 to 32.71% respectively. This variation is due to flocculation and coagulation.

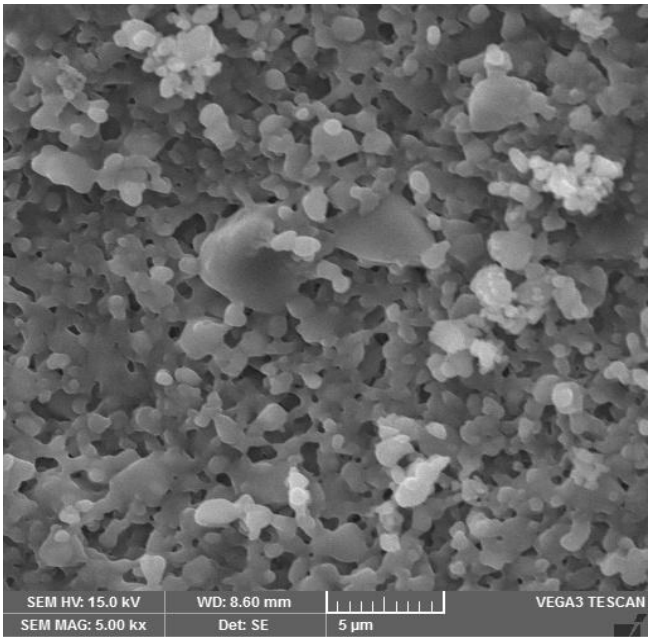

Figure 4.5. SEM micrograph of sintered fused silica ceramics.

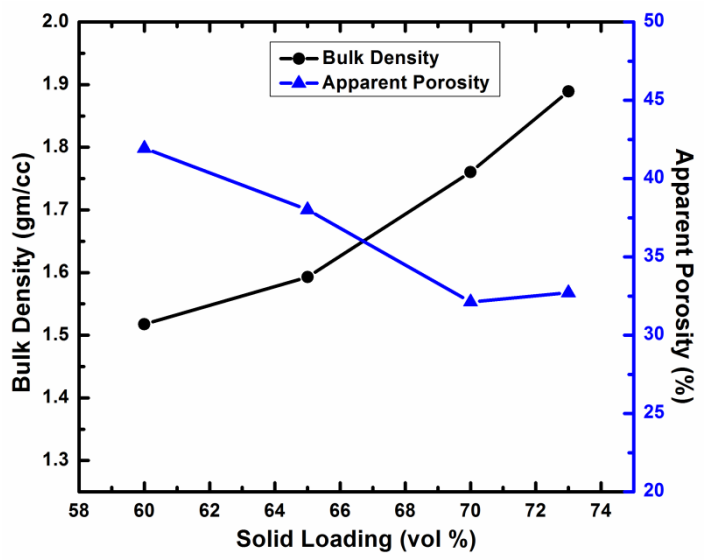

Figure 4.6. Bulk density and apparent porosity of sintered bodies.

The variation of flexural strength with sintering temperature is shown in Figure 4.7. It can be seen that the flexural strength gradually increases with the increase in sintering temperature up to 1250 ºC and on a further increase of temperature, flexural strength is decreased. This is because of the formation of cristobalite structure due to excessive crystallization of the silica. Cristobalite has a coefficient of thermal expansion (0.27×10^{-4}/°C) which is much higher than that of amorphous silica (0.54×10^{-6}/°C) and its strength is less than that of amorphous silica (Wan et al., 2013).

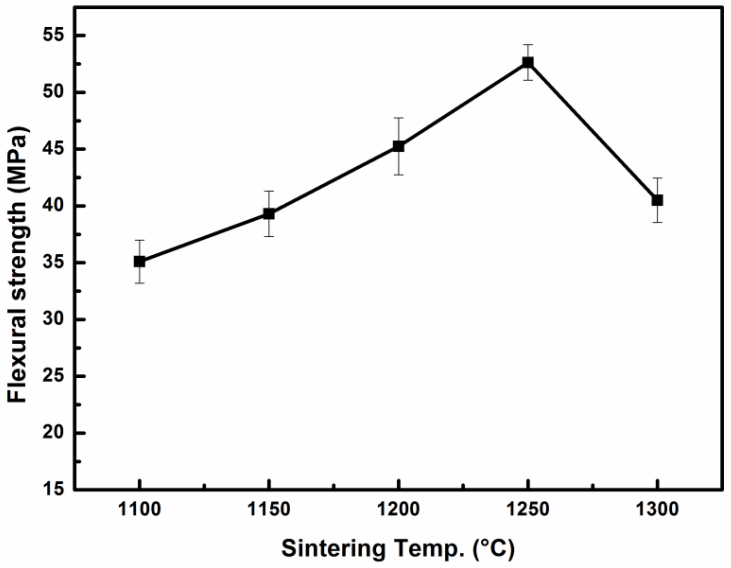

Figure 4.7. Effect of sintering temperature on flexural strength.

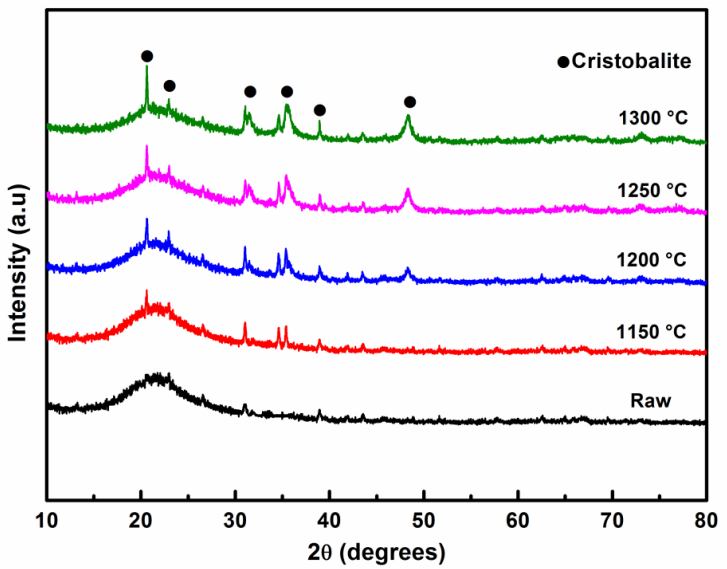

Figure 4.8. XRD patterns of sintered fused silica ceramics.

Also upon cooling, cristobalite will undergo a phase transformation from α to β which may lead to volume variation and thus micro-cracks are formed. This is observed in silica ceramics sintered at 1300 ºC and reduction in the strength of sintered fused silica ceramics. XRD patterns of fused silica sintered at various temperatures can be seen in Figure 4.8. The maximum flexural strength obtained for sintered fused silica ceramics is 52.3 MPa at 1250 ºC.

The dielectric constant and loss tangent (1 MHz) of fused silica ceramics obtained at 1250 ºC with 70 vol.% were 3.25 and 1.52×10^{-3} as shown in Figure 4.9. Dielectric constant normally relies on the porosity of materials. The dielectric constant increases gradually with increase in sintering temperature. However, the loss tangent decreases and increases with sintering temperature. These are due to excessive crystallization and formation of cristobalite structure.

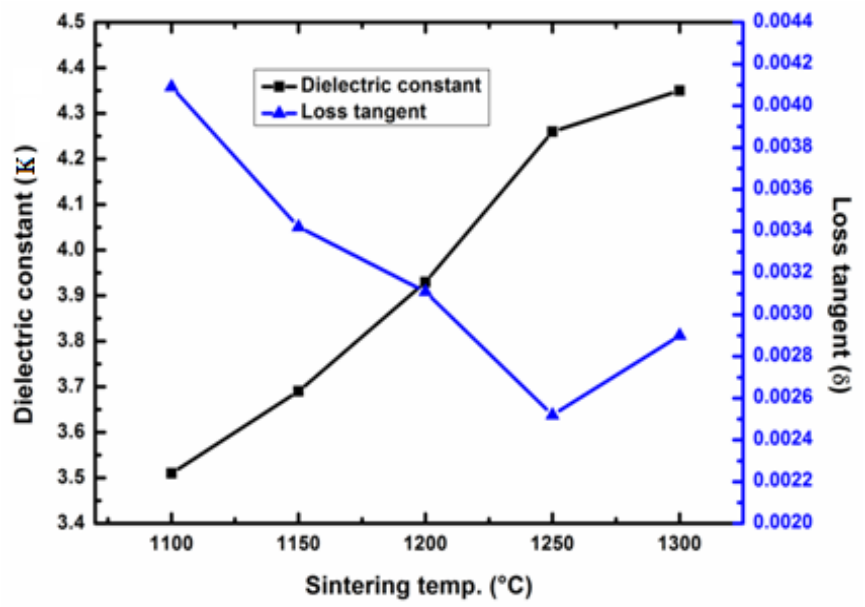

Figure 4.9. Effect of sintering temperature on dielectric constant and loss tangent.

4.2.3.5. Summary of pilot experimentation

The following conclusions are drawn after the pilot experimentation. Darvan 821A is used as a dispersant and a dosage of 0.5 wt% showed better results over other dispersants in the suspension of fused silica particles. Viscosity and fluidity of SiO_2 slurries are found good at a solid loading of 73 vol.%. The maximum flexural strength obtained is as high as 52.3 MPa for a solid loading of 70 vol.% respectively. The dielectric constant and loss tangent (1 MHz) of fused silica ceramics were as low as 3.25 and 1.52×10^{-3} respectively. These values are taken as the basis for further experimentation.

4.3. Pilot experimentation for gelcasting of SiO_2–Si_3N_4, SiO_2–BN and SiO_2–Si_3N_4–BN ceramic composites

4.3.1. Materials

Commercially available SiO_2 and BN (both M/s. Ants Ceramics Pvt. Ltd., Thane, India) with an average particle size of 1-5 μm, and Si_3N_4 (M/s. Denka Company Ltd., Japan) with an average particle size of <10 μm are used in this study. Deionized water is used as a solvent. Commercially available dispersants such as Darvan 821A and Darvan C-N (both R.T

Vanderbilt, Norwalk, CT), Dolapix A88 and Dolapix CE64 (both Zschimmer & Schwarz, Lahnstein, Germany) are used for dispersing ceramic particles in slurries for high solid loading and low viscosity. In the process of gelcasting Methacrylamide and N,N'-methylenebisacrylamide (both Alfa Aesar) are used as the organic monomer and cross-linker respectively. Ammonium persulfate (APS) and N,N,*N'*,*N'*-Tetramethylethylenediamine (TEMED) (both Alfa Aesar, United Kingdom) are used as the initiator and catalyst. Surface exfoliation phenomenon green bodies cast in the air was eliminated by adding Polyethylene glycol 400 (Alfa Aesar, United Kingdom). Diluted Nitric acid and Ammonium hydroxide (both S.D. fine chemicals, India) were used for pH adjustment.

4.3.2. Slurry preparation

Gelcasting of SiO_2 ceramics is presented in Section 4.2.2. Gelcasting of SiO_2, Si_3N_4, and BN ceramic composite was carried out at various solid loadings using different monomer content and monomers ratio. A premix solution was prepared by mixing dispersant (1 wt % of monomer content), surfactant (3 wt % of monomer content), monomers MAM and MBAM (10-15 wt% of solid loading) in distilled water by magnetic stirring. SiO_2 was added to the premix solution and then Si_3N_4 was added in regular intervals for fabrication of SiO_2–Si_3N_4 ceramic composite by gelcasting. BN was added in regular intervals for gelcasting of SiO_2–BN ceramic composite, and Si_3N_4 and BN were added in regular intervals for gelcasting of SiO_2–Si_3N_4– BN ceramic composite and varied from 5 to 15 wt. % of solid loading and stirred for about 6 hrs and pH of the slurry was adjusted to 11 using diluted Nitric acid and Ammonium Hydroxide. The slurry was deaired for 15-20 min and then the initiator APS and catalyst TEMED (1 wt % of monomer content) is added for initiation and polymerization. Finally, the slurry was cast into a glass mold and after the monomers had polymerized, the green bodies were demolded. The samples were then dried in a controlled humidity oven for 24 h. Then binder burnout was carried out in a high-temperature furnace at 600 °C for 1 h with a heating rate of 2 °C/min. Then the samples were sintered at 1250 °C with a heating rate of 4 °C/min for 3h in Nitrogen atmosphere. The detailed flowchart of gelcasting process for the preparation of any of the ceramic composite concern i.e. SiO_2–Si_3N_4, SiO_2–BN and SiO_2–Si_3N_4–BN respectively is shown in Figure 4.10. Sintered samples of SiO_2–Si_3N_4, SiO_2–BN and SiO_2–Si_3N_4–BN ceramic composites were shown in Figure 4.11.

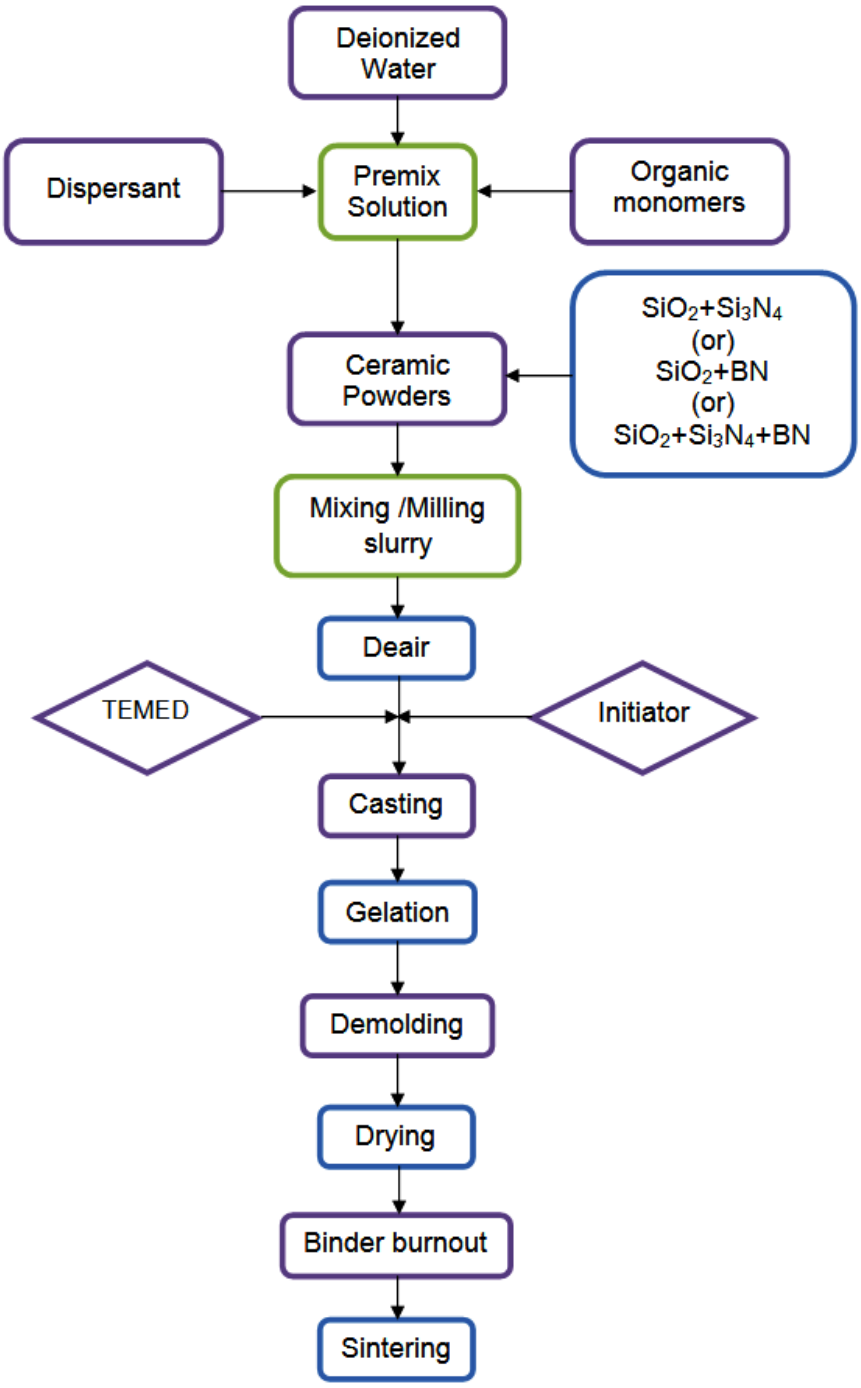

Figure 4.10. A detailed flowchart of gelcasting process of concern ceramic composite.

(a) SiO_2–Si_3N_4

(b) SiO_2–BN

(c) SiO_2–Si_3N_4–BN

Figure 4.11. Sintered samples of SiO_2–Si_3N_4, SiO_2–BN and SiO_2–Si_3N_4–BN ceramic composites.

Table 4.2(a), (b) and (c) show a sample calculation for the preparation of SiO_2–Si_3N_4, SiO_2–BN and SiO_2–Si_3N_4–BN respectively for a slurry with 50 vol% solid loading as per the rule of mixtures. The density of SiO_2 powder was 2.2 gms/cc, Si_3N_4 was 3.44 gms/cc and BN was 2.29 gms/cc SiO_2–Si_3N_4, SiO_2–BN and SiO_2–Si_3N_4–BN respectively.

Table 4.2(a). Recipe for 75 ml slurry with 50 vol% solid loading of SiO_2–Si_3N_4.

Recipe for suspension	**Weight (gms)**	**Weight percent (%)**
Water	37.5	----
SiO_2	70.125	85 wt% of solid loading
Si_3N_4	19.35	15 wt% of solid loading
Dispersant	0.4474	0.5 wt % of solid loading
PEG-400	2.6843	3 wt % of solid loading
MAM	11.1844	15 wt % of solid loading in
MBAM	2.2369	the ratio of 5:1
APS	0.1342	1 wt % of monomer content
TEMED	0.1342	1 wt % of monomer content

Table 4.2(b). Recipe for 75 ml slurry with 50 vol% solid loading of SiO_2–BN.

Recipe for suspension	**Weight (gms)**	**Weight percent (%)**
Water	37.5	----
SiO_2	70.125	75 wt% of solid loading
BN	12.8813	10 wt% of solid loading
Dispersant	0.4150	0.5 wt % of solid loading
PEG-400	2.4902	3 wt % of solid loading
MAM	10.3758	15 wt % of solid loading in
MBAM	2.0752	the ratio of 5:1
APS	0.1245	1 wt % of monomer content
TEMED	0.1245	1 wt % of monomer content

Table 4.2(c). Recipe for 75 ml slurry with 50 vol% solid loading of SiO_2–Si_3N_4–BN.

Recipe for suspension	**Weight (gms)**	**Weight percent (%)**
Water	37.5	----
SiO_2	61.875	75 wt% of solid loading
Si_3N_4	19.35	15 wt% of solid loading
BN	8.5875	10 wt% of solid loading
Dispersant	0.4491	0.5 wt % of solid loading
PEG-400	2.6944	3 wt % of solid loading
MAM	11.2266	15 wt % of solid loading in
MBAM	2.2453	the ratio of 5:1
APS	0.1347	1 wt % of monomer content
TEMED	0.1347	1 wt % of monomer content

4.3.3. Results and analysis of pilot experiments of SiO_2–Si_3N_4 ceramic composites

4.3.3.1. Zeta potential and pH value

The zeta potential of SiO_2–Si_3N_4 particles in the slurry is studied by varying the dispersant (Darvan 821A) in the range of 0-0.75 wt% as a function of pH value and is depicted in Figure 4.12.

The zeta potential of SiO_2–Si_3N_4 slurries without dispersant is found to be vary from 5.3 mV at pH 1 to -29.5 mV at pH 11. It can be seen that the isoelectric point (IEP) is at pH 3.8 and the absolute value of zeta potential increases as pH value increases. It is also observed that addition of 0.5 wt% Darvan 821A gives the maximum value of zeta potentials which is about -53.5 mV at pH 11, which is most suitable for obtaining well dispersed SiO_2–Si_3N_4 slurries. The other dispersant levels having good zeta potential other than 0.5 wt% Darvan 821A are 0.75 wt% Darvan 821A and 0.25 wt% Darvan 821A. The corresponding zeta potential values are -43.2 mV and -42.3 mV at pH 11 respectively. The zeta potentials of the remaining slurries are found to be lower and hence not considered.

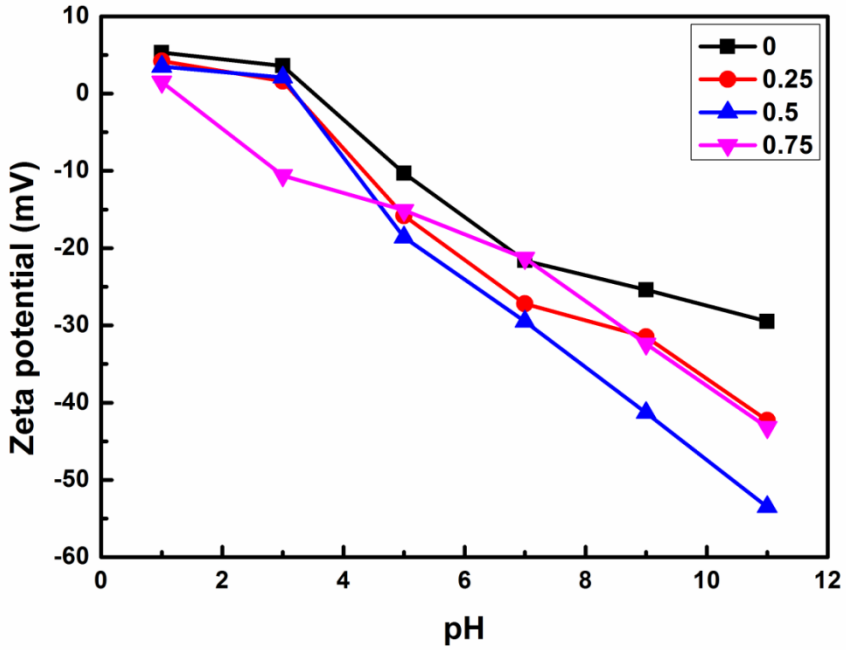

Figure 4.12. Zeta potential of SiO_2–Si_3N_4 slurries with dispersant Darvan 821A.

The pH value of slurry also play an important role on the rheological properties It is observed that high absolute zeta potential value is obtained by increasing the pH value of the slurry which increases the dispersibility of the slurry. The formation of hydroxide layer on the surface of SiO_2 particles is eliminated by the addition of Si_3N_4 particles.

4.3.3.2. Solid loading

Higher solid loading of SiO_2–Si_3N_4 slurry is required to improve the mechanical properties of gelcast parts. The solid loading of the slurries are varied from 42 to 50 vol% in which Si_3N_4 content varies from 5 to 15 wt% and remaining is SiO_2. But viscosity increases as the solid loading increases due to agglomeration at higher solid loading which make the slurry difficult to pour into a mold for casting. This is due to flocculation and coagulation caused by the reduction of solvent (water) present in between the ceramic particles. Hence, slurry with 50 vol% solid loading and 15 wt% Si_3N_4 content is suitable for casting into the mold. The variation of viscosity as a function of the shear rate ranging from 0.1–100 s^{-1} for slurries of 50 vol% solids loading and with Si_3N_4 content varying from 5 – 15 wt% is shown in Figure 4.13.

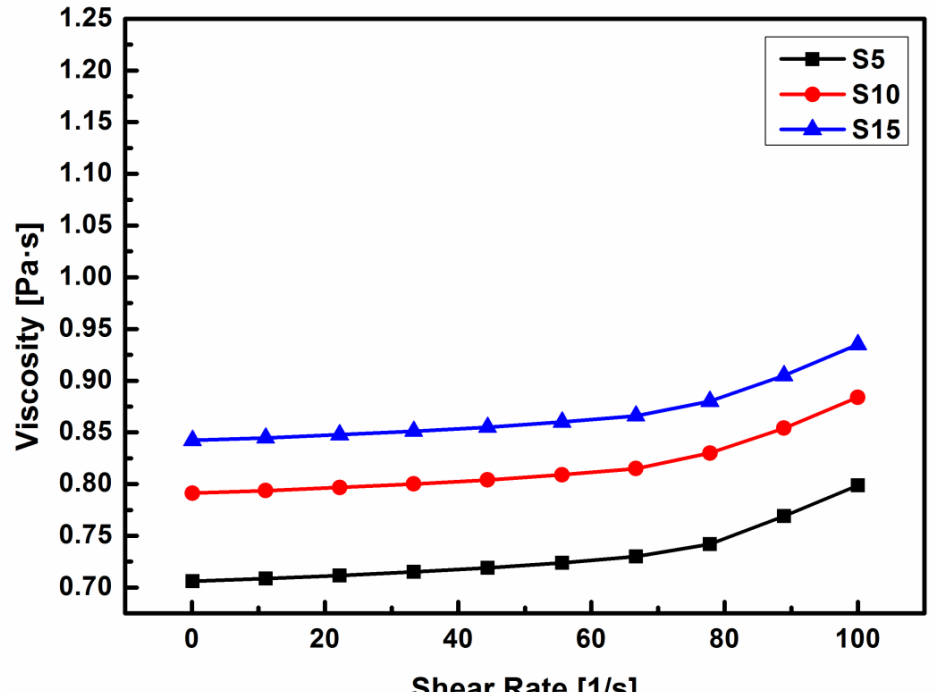

Figure 4.13. Variation of the viscosity of slurries at various solid loadings.

From Figure 4.13 it can be seen that there is an increase in viscosity from 0.706 to 0.842 Pa.s with an increase in Si_3N_4 content from 5 to 15 wt% and the gel exhibits shear-thickening behavior. The increase in viscosity is due to the agglomeration at high solid loadings.

4.3.3.3. X-Ray diffraction analysis and Microstructure

X-ray diffraction patterns of SiO_2–Si_3N_4 ceramic composite sintered at various temperatures are shown in Figure 4.14. X-ray diffraction analysis is done both on raw ceramics and ceramic composite sintered at 1250 ºC. It can be seen that at 1250 ºC, SiO_2 is transformed into cristobalite phase. The microstructure of sintered SiO_2–Si_3N_4 ceramic composite is shown in Figure 4.15.

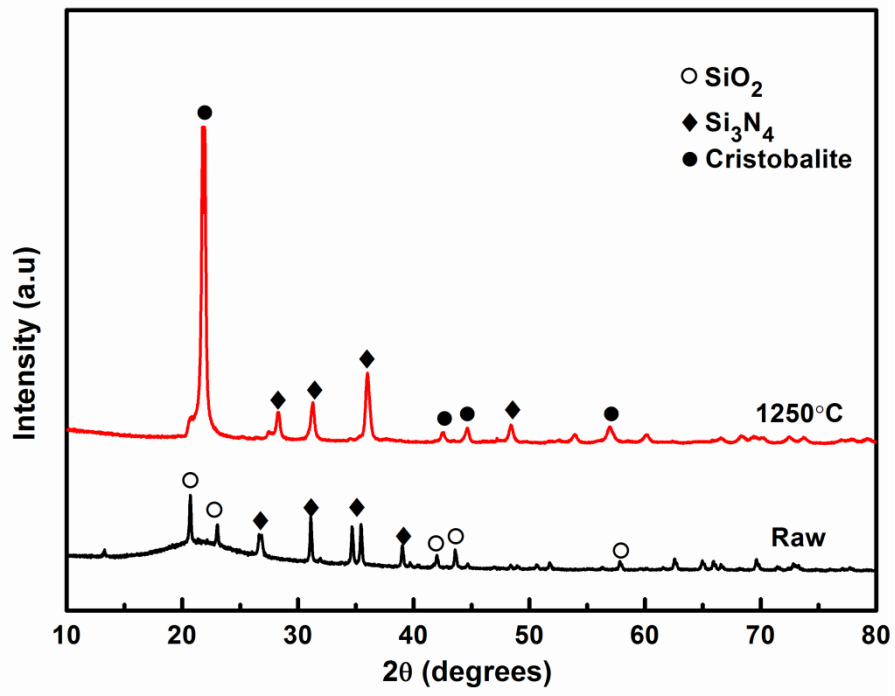

Figure 4.14. XRD patterns of SiO_2–Si_3N_4 ceramic composite.

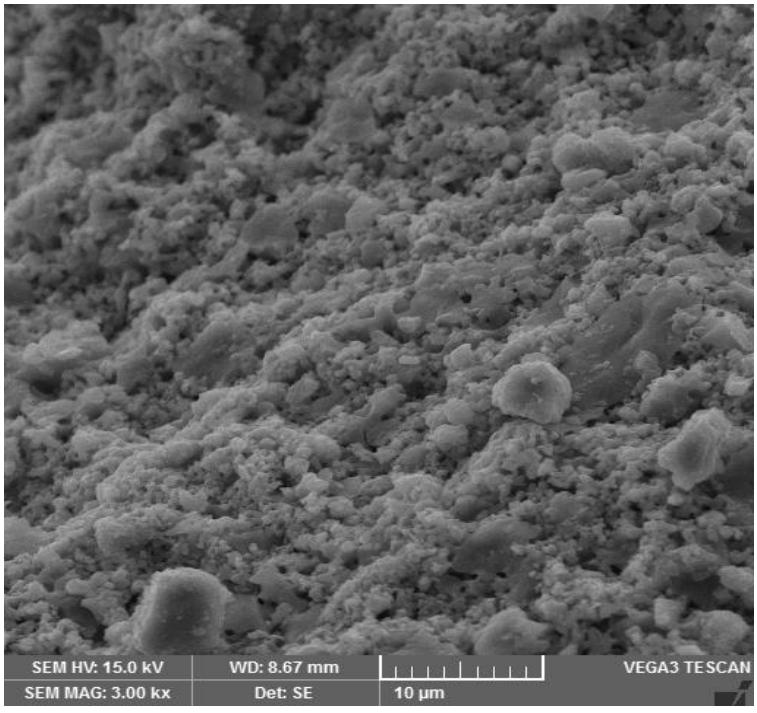

Figure 4.15. SEM micrograph of sintered SiO_2–Si_3N_4 ceramic composite.

4.3.4. Results and analysis of pilot experiments of SiO_2–BN ceramic composites

4.3.4.1. Zeta potential and pH value

The zeta potential of SiO_2–BN slurries is studied by varying the dispersant (Darvan 821A) in the range of 0-0.75 wt% as a function of pH value and is depicted in Figure 4.16. The zeta potential of SiO_2–BN slurry without dispersant is found to be vary from 4.2 mV at pH 1 to -35.8 mV at pH 11. It can be seen that the isoelectric point (IEP) is at pH 3.1 and the absolute value of zeta potential increases as pH value increases. It is also observed that addition of 0.5 wt% Darvan 821A gives the maximum value of zeta potentials which is about -56.3 mV at pH 11, which is most suitable for obtaining well dispersed SiO_2 – BN slurries. The other dispersant levels having good zeta potential other than 0.5 wt% Darvan 821A are 0.25 wt% Darvan 821A and 0.75 wt% Darvan 821A. The corresponding zeta potential values are -44.5 mV and -42.6 mV at pH 11 respectively. The zeta potentials of the remaining slurries are found to be lower and hence not considered.

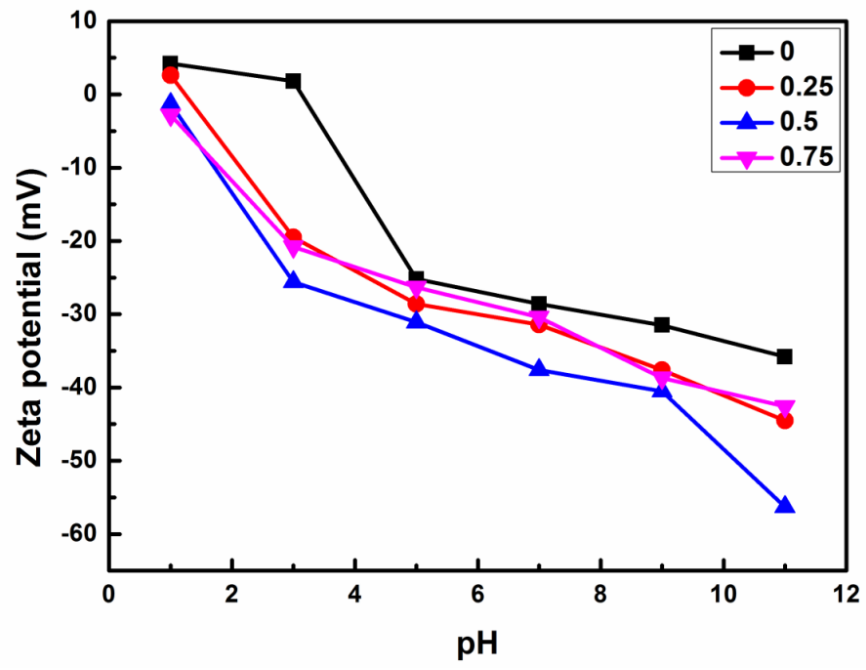

Figure 4.16. Zeta potential of SiO_2–BN slurries with dispersant Darvan 821A.

The pH value of slurry also play an important role on the rheological properties It is observed that high absolute zeta potential value is obtained by increasing the pH value of the slurry

which increases the dispersibility of the slurry. The formation of hydroxide layer on the surface of SiO_2 particles is eliminated by the addition of BN particles.

4.3.4.2. Solid loading

Higher solid loading of SiO_2–BN slurry are required to improve the mechanical properties of gelcast parts. The solid loading of the slurries are varied from 42 to 50 vol%, in which BN content varies from 5 to 15 wt% and remaining is SiO_2. As the solid loading increases the viscosity also increases making the slurry difficult to pour into mold for casting. This may be due to agglomeration at higher solid loading. The variation of viscosity as a function of the shear rate ranging from 0.1–100 s^{-1} for slurries of 50 vol% solids loading and with BN content varying from 5 – 15 wt% is shown in Figure 4.17. It can be seen that there is an increase in viscosity from 0.398 to 0.53 Pa.s with an increase in BN content from 5 to 15 wt% and the gel exhibits shear-thinning behavior. Hence, slurry with 50 vol% solid loading and 15 wt% BN content is suitable for casting into the mold.

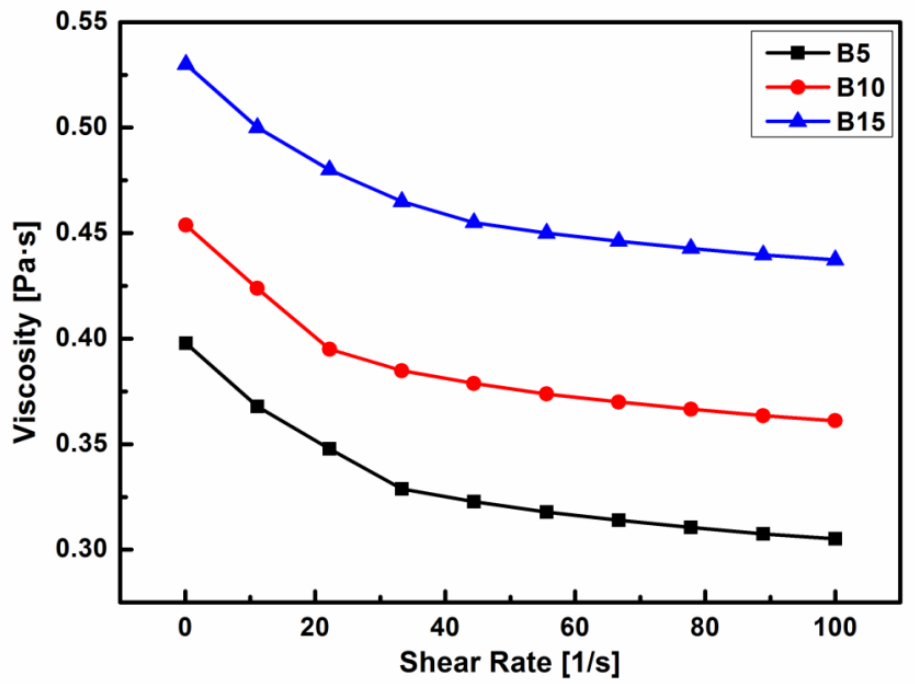

Figure 4.17. Variation of the viscosity of slurry at various solid loadings.

4.3.4.3. X-Ray diffraction analysis and Microstructure

X-ray diffraction patterns of SiO_2–BN ceramic composite sintered at various temperatures are shown in Figure 4.18. X-ray diffraction analysis is done both on raw SiO_2–

BN ceramics and ceramic composite sintered at 1250 ºC. It can be seen that at 1250 ºC, SiO_2 is transformed into cristobalite phase. The microstructure of sintered SiO_2–BN ceramic composite is shown in Figure 4.19. It can be seen that the pores are reduced in the SiO_2–BN ceramic composite.

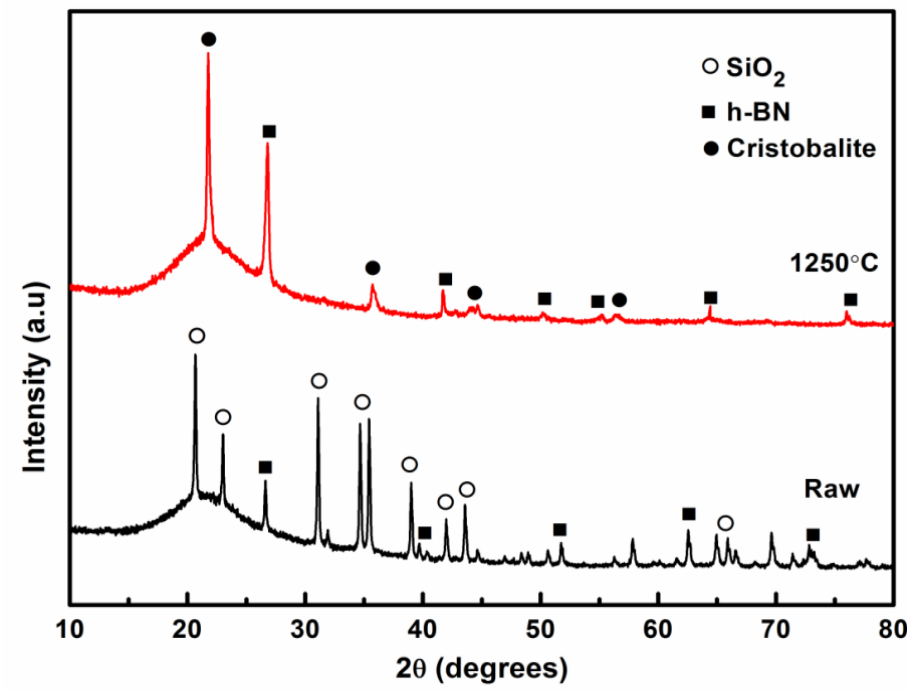

Figure 4.18. XRD patterns of SiO_2–BN ceramic composite.

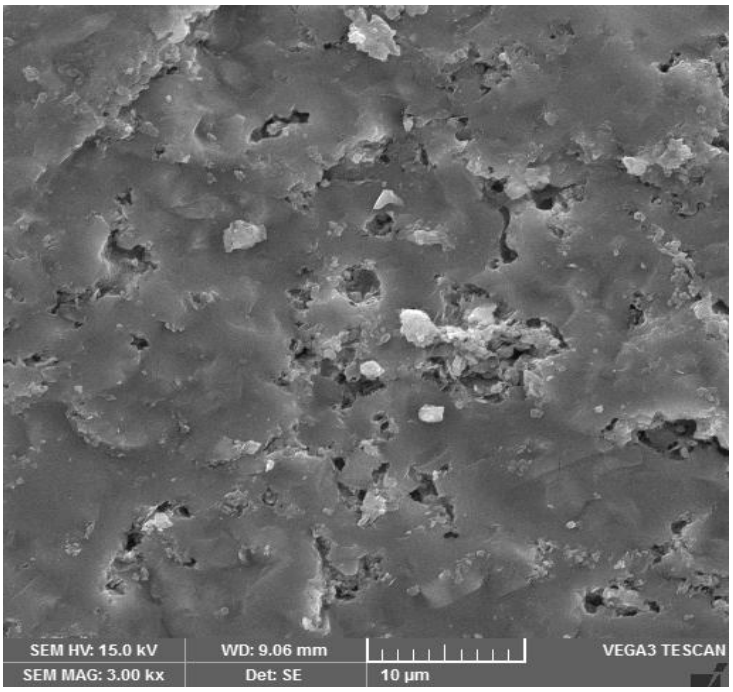

Figure 4.19. SEM micrograph of sintered SiO_2–BN ceramic composite.

4.3.5. Results and analysis of pilot experiments of SiO_2–Si_3N_4–BN ceramic composites

4.3.5.1. Zeta potential and pH value

The zeta potential of SiO_2–Si_3N_4–BN slurries is studied by varying the dispersant (Darvan 821A) in the range of 0-0.75 wt% as a function of pH value and is depicted in Figure 4.20.

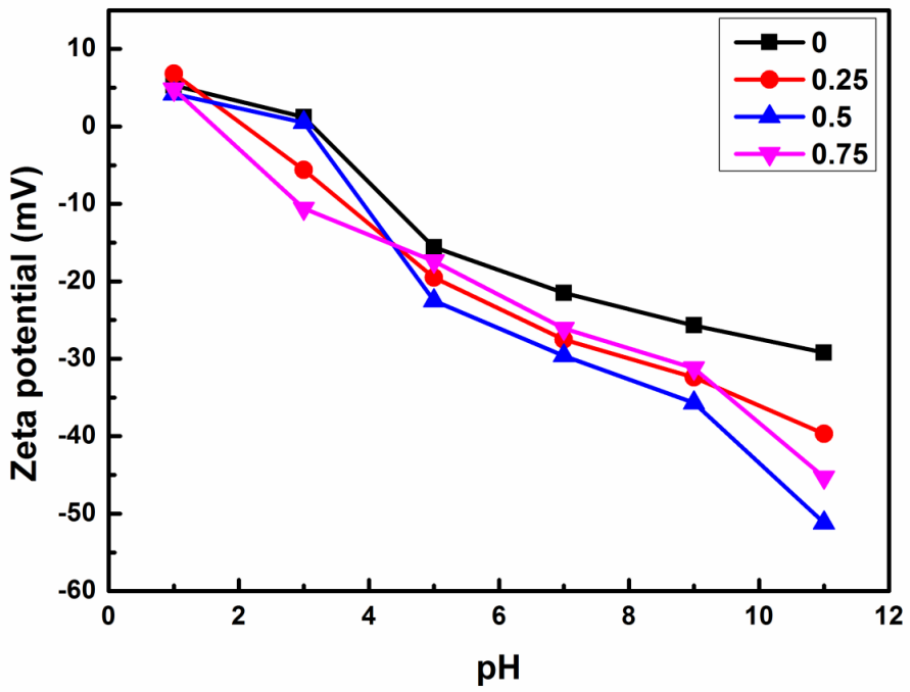

Figure 4.20. Zeta potential of SiO_2–Si_3N_4–BN slurries with dispersant Darvan 821A.

The zeta potential of SiO_2–Si_3N_4–BN slurries without dispersant is found to be vary from 5.3 mV at pH 1 to -29.2 mV at pH 11. It can be seen that the isoelectric point (IEP) is at pH 3.1 and the absolute value of zeta potential increases as pH value increases. It is also observed that addition of 0.5 wt% Darvan 821A gives the maximum value of zeta potentials which is about -51.2 mV at pH 11, which is most suitable for obtaining well dispersed SiO_2–Si_3N_4–BN slurries. The other dispersant levels having good zeta potential other than 0.5 wt% Darvan 821A are 0.75 wt% Darvan 821A and 0.25 wt% Darvan 821A. The corresponding zeta potential values are -45.3 mV and -39.7 mV at pH 11 respectively. The zeta potentials of the remaining slurries are found to be lower and hence not considered.

The pH value of slurry also plays an important role on the rheological properties of slurries. It is observed that high absolute zeta potential value is obtained by increasing the pH value of the slurry which increases the dispersibility of the slurry. The formation of hydroxide layer on the surface of SiO_2 particles is eliminated by the addition of Si_3N_4 and BN ceramic particles.

4.3.5.2. Solid loading

Higher solid loading of SiO_2–Si_3N_4–BN slurry is required to improve the mechanical properties of gelcast parts. The solid loading of the slurries is varied from 42 to 50 vol% with Si_3N_4 and BN content varying from 5 to 15 wt%. But viscosity increases as the solid loading increases due to agglomeration at higher solid loading which make the slurry difficult to cast in the mold. This is due to flocculation and coagulation caused by the reduction of solvent present in between the ceramic particles. Hence, a slurry of 50 vol% solid loading with 15 wt% Si_3N_4 content and 15 wt% BN content is suitable for casting into the mold. The variation of viscosity as a function of the shear rate ranging from 0.1–100 s^{-1} for slurries of 50 vol% solids loading with Si_3N_4 content and BN content varying from 5 – 15 wt% is shown in Figure 4.21.

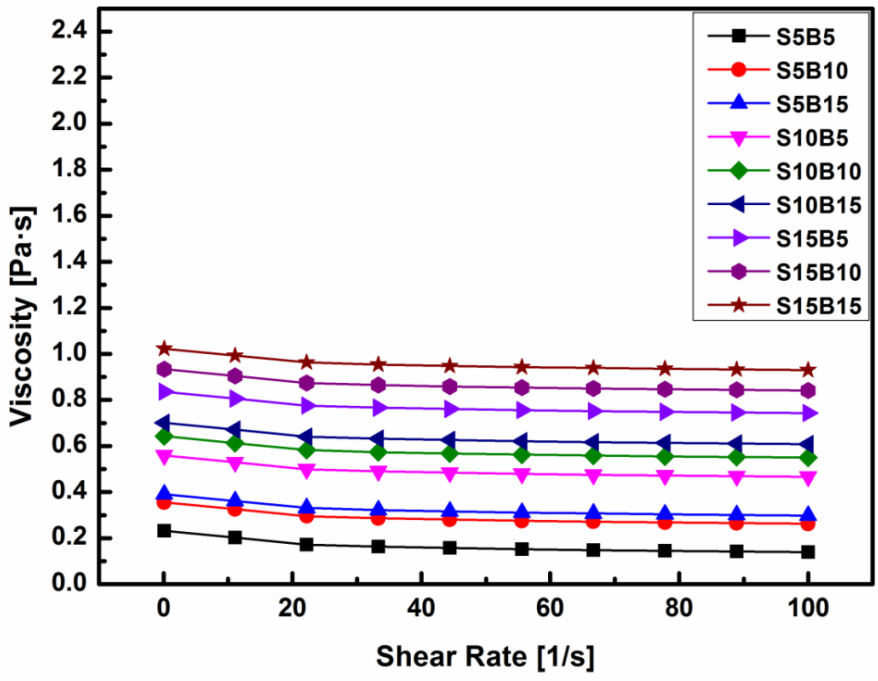

Figure 4.21. Variation of viscosities of slurries at various solid loadings.

From Figure 4.21 it can be seen that there is an increase in viscosity from 0.232 to 1.023 Pa.s with an increase in Si_3N_4 content and BN content from 5 to 15 wt%. The increase in viscosity is due to the increase in Si_3N_4 content from 5 to 15 wt%. Shear-thinning behavior is exhibited by the slurries as BN added to the slurries acts as a lubricating agent.

4.3.5.3. X-Ray diffraction analysis and Microstructure

X-ray diffraction patterns of SiO_2–Si_3N_4–BN ceramic composite sintered at 1250 ºC temperature can be seen in Figure 4.22. X-ray diffraction analysis is done on raw ceramics and ceramic composite sintered at 1250 ºC. It can be seen that at 1250 ºC, SiO_2 is transformed into cristobalite phase. The addition of Si_3N_4 and BN ceramics to SiO_2 ceramics could be able to reduce the excessive formation of excess cristobalite. The microstructure of sintered SiO_2–Si_3N_4–BN ceramic composite is shown in Figure 4.23. It can be seen that the ceramic particles are homogeneously distributed and pores are formed uniformly which is required for a radome.

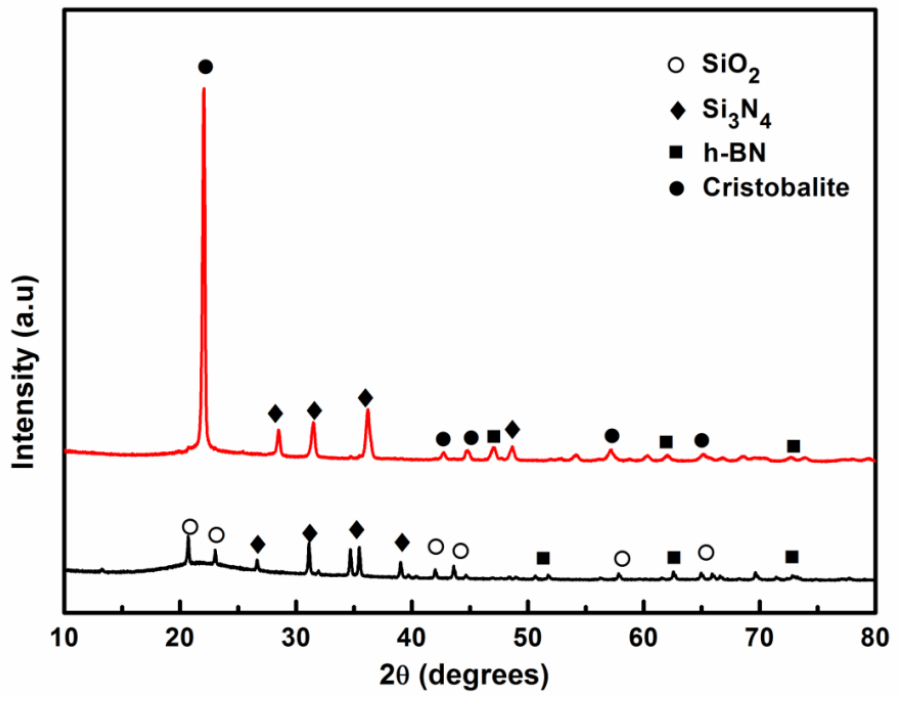

Figure 4.22. XRD patterns of SiO_2–Si_3N_4–BN ceramic composite.

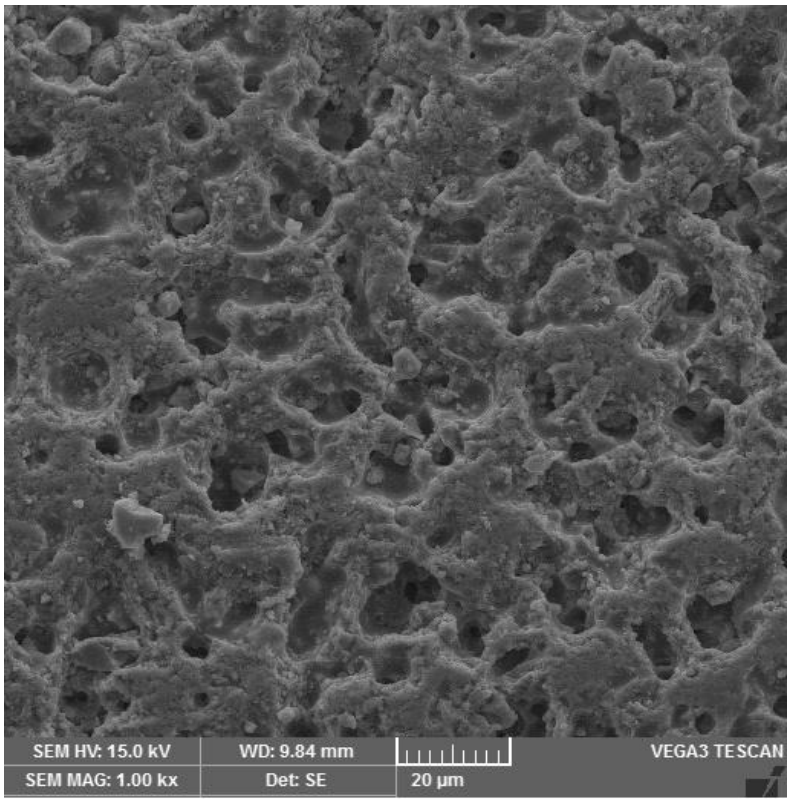

Figure 4.23. SEM micrograph of sintered SiO_2–Si_3N_4–BN ceramic composite.

4.3.6. Summary of pilot experimentation of SiO_2–Si_3N_4, SiO_2–BN and SiO_2–Si_3N_4–BN ceramic composites

The following conclusions are drawn after the pilot experimentation. Darvan 821A is used as a dispersant and a dosage of 0.5 wt% showed better results in the suspension of ceramic particles. Solid loading as high as 50 vol.% with low viscosity and good fluidity are obtained. Si_3N_4 and BN can be varied in the range of 5-15 wt% of solid loading, together 25 wt% in total. These conclusions are taken as the basis for further experimentation.

4.4. Design of experiments

Response surface methodology consists of mathematical and statistical techniques utilized in the development of ample functional relationships among responses and process parameters. Analysis of any response of a system greatly depends on how well the experiments are designed, conducted and measured. Therefore conducting experiments and measuring the responses is a crucial part of any investigation. In the present study, a face-

centered central composite design of RSM with 6 center points have been used in the experimental plan. The detailed experimental plan involving a number of experiments have been given in this chapter. Design Expert 9.0 software is used in the present work for RSM analysis. The measured and calculated responses flexural strength, porosity and dielectric constant are tabulated after conducting the experiments.

4.4.1. Experimental plan for SiO_2 ceramics

After thorough trial experiments the levels of solid loading, monomer content, and ratio of monomers have been fixed and the levels were presented in Table 4.3.

Table 4.3. Process parameters: Ranges and levels

Variables	Units	Level 1 (-1)	Level 2 (0)	Level 3 (1)
Solid Loading	Vol %	68	70	72
Monomer Content	Wt %	10	12.5	15
Ratio of Monomers	--	3	5	7

A total of 20 experiments is conducted for fabrication of SiO_2 ceramics including 6 center points as presented in Table 4.4 and the results are presented in Table 4.5.

Table 4.4. Experimental plan for fabrication of SiO_2 ceramics

Run order	SL (vol %)	MC (wt %)	RM
1	0	0	0
2	-1	0	0
3	0	0	0
4	0	-1	0
5	0	0	-1
6	-1	1	1
7	1	-1	-1
8	1	0	0
9	-1	-1	1
10	0	0	0
11	0	0	0
12	0	0	0
13	-1	1	-1

14	-1	-1	-1
15	1	-1	1
16	0	1	0
17	1	1	-1
18	0	0	1
19	0	0	0
20	1	1	1

Table 4.5. Experimental results for SiO_2 ceramics

Run order	SL (vol %)	MC (wt %)	RM	FS (MPa)	Por. (%)	DE
1	70	12.5	5	49.2	33.42	4.11
2	68	12.5	5	43.9	37.19	3.94
3	70	12.5	5	49.6	33.67	4.09
4	70	10	5	52.3	32.55	4.15
5	70	12.5	3	48.6	34.36	4.06
6	68	15	7	44.5	38.14	3.92
7	72	10	3	47.5	32.35	4.15
8	72	12.5	5	49.2	34.16	4.07
9	68	10	7	45.9	35.97	4.01
10	70	12.5	5	49.8	33.91	4.1
11	70	12.5	5	50.1	34.25	4.07
12	70	12.5	5	51.2	32.92	4.13
13	68	15	3	42.3	38.51	3.9
14	68	10	3	43.6	34.55	4.05
15	72	10	7	49.5	32.68	4.15
16	70	15	5	49.3	35.37	4.02
17	72	15	3	47.3	37.63	3.91
18	70	12.5	7	50.9	33.39	4.11
19	70	12.5	5	50.6	34.54	4.05
20	72	15	7	48.2	36.91	3.95

4.4.2. Experimental plan for SiO_2–Si_3N_4 ceramic composites

The levels of solid loading, Si_3N_4 content, monomer content, and ratio of monomers have been fixed and the levels were presented in Table 4.6.

Table 4.6. Process parameters: Ranges and levels

Variables	Units	Level 1 (-1)	Level 2 (0)	Level 3 (1)
Solid Loading	Vol %	42	46	50
Si_3N_4 content	Wt %	5	10	15
Monomer Content	Wt %	10	12.5	15
Ratio of Monomers	--	3	5	7

A total of 30 experiments is conducted for fabrication of SiO_2–Si_3N_4 ceramic composites including 6 center points as presented in Table 4.7 and the results are presented in Table 4.8.

Table 4.7. Experimental plan for fabrication of SiO_2–Si_3N_4 ceramic composites

Run order	SL (vol %)	Si_3N_4 (wt %)	MC (wt %)	RM
1	-1	-1	-1	-1
2	0	0	0	1
3	1	1	-1	-1
4	-1	1	-1	-1
5	0	-1	0	0
6	-1	-1	1	-1
7	-1	1	1	1
8	0	0	0	0
9	0	0	0	-1
10	-1	1	1	-1
11	0	1	0	0
12	1	-1	1	1
13	1	1	1	1
14	0	0	0	0

15	1	1	-1	1
16	0	0	0	0
17	0	0	0	0
18	1	-1	-1	-1
19	-1	1	-1	1
20	0	0	1	0
21	0	0	-1	0
22	1	-1	-1	1
23	1	-1	1	-1
24	1	0	0	0
25	0	0	0	0
26	0	0	0	0
27	1	1	1	-1
28	-1	0	0	0
29	-1	-1	-1	1
30	-1	-1	1	1

Table 4.8. Experimental results for SiO_2–Si_3N_4 ceramic composites

Run order	SL (vol %)	Si3N4 (wt %)	MC (wt %)	RM	FS (MPa)	Por. (%)	DE
1	42	5	10	3	56.19	37.53	7.22
2	46	10	12.5	7	83.16	37.18	7.32
3	50	15	10	3	92.66	32.61	7.81
4	42	15	10	3	67.89	38.41	6.95
5	46	5	12.5	5	75.02	34.16	7.71
6	42	5	15	3	58.13	40.36	6.82
7	42	15	15	7	70.69	38.94	6.89
8	46	10	12.5	5	82.67	37.67	7.29
9	46	10	12.5	3	76.15	39.82	6.85
10	42	15	15	3	69.15	41.28	6.8
11	46	15	12.5	5	85.16	35.87	7.72

12	50	5	15	7	89.36	35.13	7.76
13	50	15	15	7	93.88	33.15	7.81
14	46	10	12.5	5	80.98	36.59	7.35
15	50	15	10	7	95.12	31.95	8.14
16	46	10	12.5	5	82.59	36.48	7.41
17	46	10	12.5	5	78.26	37.92	7.34
18	50	5	10	3	84.22	32.55	8.03
19	42	15	10	7	68.12	37.23	7.33
20	46	10	15	5	84.38	37.95	7.15
21	46	10	10	5	78.13	36.34	7.51
22	50	5	10	7	87.29	33.11	7.91
23	50	5	15	3	88.59	36.71	7.63
24	50	10	12.5	5	87.26	33.58	8.01
25	46	10	12.5	5	78.19	37.16	7.43
26	46	10	12.5	5	81.09	37.55	7.21
27	50	15	15	3	92.19	35.18	7.64
28	42	10	12.5	5	65.23	38.47	7.41
29	42	5	10	7	57.88	38.19	6.99
30	42	5	15	7	63.27	37.16	6.92

4.4.3. Experimental plan for SiO_2–BN ceramic composites

After thorough trial experiments the levels of solid loading, BN content, monomer content, and ratio of monomers have been fixed and the levels were presented in Table 4.9.

Table 4.9. Process parameters: Ranges and levels

Variables	Units	Level 1 (-1)	Level 2 (0)	Level 3 (1)
Solid Loading	Vol %	42	46	50
BN content	Wt %	5	10	15
Monomer Content	Wt %	10	12.5	15
Ratio of Monomers	--	3	5	7

A total of 30 experiments is conducted for fabrication of SiO_2–BN ceramic composites including 6 center points as presented in Table 4.10 and the results are presented in Table 4.11.

Table 4.10. Experimental plan for fabrication of SiO_2–BN ceramic composites

S.No.	SL (vol %)	BN (wt %)	MC (wt %)	RM
1	0	0	1	0
2	0	0	0	-1
3	1	1	-1	-1
4	0	0	-1	0
5	0	0	0	0
6	0	0	0	1
7	1	-1	-1	-1
8	0	-1	0	0
9	1	-1	-1	1
10	-1	1	-1	1
11	1	0	0	0
12	-1	1	1	1
13	1	-1	1	-1
14	1	1	1	1
15	0	0	0	0
16	-1	1	-1	-1
17	0	0	0	0
18	-1	0	0	0
19	-1	-1	-1	1
20	0	0	0	0
21	0	0	0	0
22	1	1	-1	1
23	-1	-1	1	1
24	1	-1	1	1
25	-1	1	1	-1
26	0	1	0	0

27	-1	-1	1	-1
28	0	0	0	0
29	1	1	1	-1
30	-1	-1	-1	-1

Table 4.11. Experimental results for SiO_2–BN ceramic composites

Run order	SL (vol %)	BN (wt %)	MC (wt %)	RM	FS (MPa)	Por. (%)	DE
1	46	10	15	5	66.28	22.13	4.34
2	46	10	12.5	3	57.43	23.86	4.35
3	50	15	10	3	71.65	19.08	4.98
4	46	10	10	5	61.13	21.35	4.61
5	46	10	12.5	5	62.77	21.31	4.58
6	46	10	12.5	7	64.98	21.75	4.51
7	50	5	10	3	66.29	17.46	5.12
8	46	5	12.5	5	59.84	19.85	4.9
9	50	5	10	7	69.18	17.83	5.1
10	42	15	10	7	51.19	23.89	4.12
11	50	10	12.5	5	75.18	17.12	5.23
12	42	15	15	7	52.51	23.71	4.21
13	50	5	15	3	70.58	21.22	4.82
14	50	15	15	7	76.45	17.8	5
15	46	10	12.5	5	64.37	20.83	4.62
16	42	15	10	3	49.89	23.12	4.14
17	46	10	12.5	5	61.08	20.51	4.55
18	42	10	12.5	5	47.22	21.91	4.6
19	42	5	10	7	39.88	23.58	4.25
20	46	10	12.5	5	65.42	21.69	4.49
21	46	10	12.5	5	60.24	20.94	4.6
22	50	15	10	7	78.19	17.23	5.16
23	42	5	15	7	45.22	23.15	4.32
24	50	5	15	7	71.22	20.53	4.95
25	42	15	15	3	50.34	22.23	4.52

26	46	15	12.5	5	67.13	20.24	4.91
27	42	5	15	3	40.35	23.99	4.35
28	46	10	12.5	5	63.67	20.76	4.48
29	50	15	15	3	73.21	19.13	4.83
30	42	5	10	3	38.11	21.35	4.41

4.4.4. Experimental plan for SiO_2–Si_3N_4–BN ceramic composites

After thorough trial experiments the levels of solid loading, Si_3N_4 content, BN content, monomer content, and ratio of monomers have been fixed and the levels were presented in Table 4.12.

Table 4.12. Process parameters: Ranges and levels

Variables	Units	Level 1 (-1)	Level 2 (0)	Level 3 (1)
Solid Loading	Vol %	42	46	50
Si_3N_4 content	Wt %	5	10	15
BN content	Wt %	5	10	15
Monomer Content	Wt %	10	12.5	15
Ratio of Monomers	--	3	5	7

A total of 50 experiments is conducted for fabrication of SiO_2–Si_3N_4–BN ceramic composites including 6 center points as presented in Table 4.13 and the results are presented in Table 4.14.

Table 4.13. Experimental plan for fabrication of SiO_2–Si_3N_4–BN ceramic composites

Run order	SL (vol %)	Si_3N_4 (wt %)	BN (wt %)	MC (wt %)	RM
1	0	1	0	0	0
2	0	0	0	0	0
3	1	1	-1	-1	1
4	0	0	0	0	0
5	1	1	-1	1	-1
6	-1	-1	1	-1	1
7	-1	-1	1	-1	-1

8	0	0	0	0	0
9	1	1	-1	1	1
10	-1	1	-1	-1	-1
11	-1	-1	-1	1	1
12	1	1	1	-1	1
13	0	0	0	0	0
14	0	0	0	0	0
15	1	-1	-1	1	1
16	-1	-1	-1	1	-1
17	0	0	1	0	0
18	-1	-1	-1	-1	-1
19	1	-1	-1	-1	-1
20	1	1	1	1	1
21	1	-1	1	-1	-1
22	0	0	0	0	-1
23	0	0	-1	0	0
24	-1	1	1	1	-1
25	-1	0	0	0	0
26	1	0	0	0	0
27	1	1	1	1	-1
28	1	-1	-1	1	-1
29	-1	-1	1	1	-1
30	-1	1	-1	1	-1
31	-1	1	-1	1	1
32	-1	1	1	-1	-1
33	-1	-1	1	1	1
34	1	1	1	-1	-1
35	0	0	0	0	0
36	0	0	0	0	0
37	-1	1	-1	-1	1
38	0	0	0	0	0
39	1	-1	1	-1	1
40	0	0	0	1	0
41	1	1	-1	-1	-1
42	-1	-1	-1	-1	1
43	-1	1	1	1	1
44	1	-1	1	1	-1

45	0	0	0	0	1
46	0	0	0	-1	0
47	1	-1	-1	-1	1
48	-1	1	1	-1	1
49	0	-1	0	0	0
50	1	-1	1	1	1

Table 4.14. Experimental results for SiO_2 – Si_3N_4 – BN ceramic composites

Run order	SL (vol %)	Si3N4 (wt %)	BN (wt %)	MC (wt %)	RM	FS (MPa)	Por. (%)	DE
1	46	15	10	12.5	5	108.72	32.45	6.43
2	46	10	10	12.5	5	103.97	33.14	5.45
3	50	15	5	10	7	96.59	33.41	6.47
4	46	10	10	12.5	5	102.52	31.58	5.83
5	50	15	5	15	3	93.11	35.86	5.65
6	42	5	15	10	7	73.15	38.91	4.29
7	42	5	15	10	3	71.94	39.26	4.45
8	46	10	10	12.5	5	104.53	31.82	6.08
9	50	15	5	15	7	95.23	32.24	5.98
10	42	15	5	10	3	65.48	37.63	5.97
11	42	5	5	15	7	64.29	38.94	4.26
12	50	15	15	10	7	131.26	26.15	6.45
13	46	10	10	12.5	5	103.76	31.25	5.78
14	46	10	10	12.5	5	106.87	34.56	5.82
15	50	5	5	15	7	91.23	37.21	5.03
16	42	5	5	15	3	56.54	38.48	4.45
17	46	10	15	12.5	5	103.26	33.25	5.85
18	42	5	5	10	3	56.53	36.36	4.45
19	50	5	5	10	3	83.59	33.68	5.39
20	50	15	15	15	7	129.64	27.64	6.39
21	50	5	15	10	3	107.23	32.54	4.81
22	46	10	10	12.5	3	101.24	32.75	5.95
23	46	10	5	12.5	5	84.75	37.52	6.09

24	42	15	15	15	3	99.25	36.37	6.18
25	42	10	10	12.5	5	86.28	36.31	4.68
26	50	10	10	12.5	5	118.28	29.48	6.02
27	50	15	15	15	3	127.47	28.37	6.15
28	50	5	5	15	3	87.19	37.54	4.86
29	42	5	15	15	3	75.42	38.12	4.68
30	42	15	5	15	3	69.54	39.38	6.22
31	42	15	5	15	7	68.29	38.57	5.93
32	42	15	15	10	3	98.71	37.13	6.12
33	42	5	15	15	7	78.37	37.82	4.34
34	50	15	15	10	3	126.78	27.39	6.39
35	46	10	10	12.5	5	99.68	32.11	6.06
36	46	10	10	12.5	5	103.52	33.14	5.68
37	42	15	5	10	7	71.51	38.75	5.64
38	46	10	10	12.5	5	105.42	33.85	5.84
39	50	5	15	10	7	105.15	32.86	4.41
40	46	10	10	15	5	98.37	32.12	6.05
41	50	15	5	10	3	91.36	33.47	6.29
42	42	5	5	10	7	58.94	38.64	4.38
43	42	15	15	15	7	102.35	32.38	6.16
44	50	5	15	15	3	109.48	32.19	4.35
45	46	10	10	12.5	7	105.48	32.39	5.98
46	46	10	10	10	5	100.28	33.25	5.45
47	50	5	5	10	7	85.37	33.87	5.25
48	42	15	15	10	7	99.58	36.29	5.32
49	46	5	10	12.5	5	98.76	35.84	4.97
50	50	5	15	15	7	112.35	31.08	4.49

Summary

In this chapter, the detailed experimental plans involving a number of experiments for gelcasting of SiO_2, SiO_2–Si_3N_4, SiO_2–BN and SiO_2–Si_3N_4–BN ceramic composites were designed using Design Expert 9.0 software. A face-centered central composite design of RSM with 6 center points has been used in the experimental plan. The levels of input parameters solid loading (i.e. SiO_2, Si_3N_4 and BN content), monomer content, and ratio of monomers were fixed based on the results of trial experiments. SiO_2, SiO_2–Si_3N_4, SiO_2–BN and SiO_2–Si_3N_4–BN ceramic composites were prepared by gel casting technique by varying solid loading, Si_3N_4 content, BN content monomer content, and ratio of monomers. Trial experiments were conducted and the sintering temperature has been fixed as 1250 °C for sintering all the ceramic composites.

CHAPTER 5

RESULTS AND DISCUSSION

5.1. Introduction

Samples of SiO_2, SiO_2–Si_3N_4, SiO_2–BN and SiO_2–Si_3N_4–BN ceramic composites were prepared by gelcasting method and as per the design of experiments. The important properties of gelcast components (hereafter we call responses) such as flexural strength (FS), porosity (Por), and dielectric constant (DE) are measured. RSM analysis is carried on these responses. The parameters that influence these responses are solid loading (SL), monomer content (MC), ratio of monomers (RM), Si_3N_4 content, and BN content. ANOVA has been applied on the experimental results for each response to investigate the significance of process parameters and their contributions.

5.2. Results and analysis for SiO_2 ceramics

5.2.1. Regression model for flexural strength

A regression model for flexural strength of SiO_2 ceramics is fitted using the experimental results (Table 4.5). ANOVA has been applied on the experimental results for flexural strength and the ANOVA results are given in Table 5.1.

Table 5.1. ANOVA results for flexural strength

Source	Sum of Squares	df	Mean Square	F Value	p-value Prob > F	Percentage Contribution
Model	124.556	9	15.72379	29.87404	< 0.0001	95.946
A-SL	56.225	1	46.225	87.82407	< 0.0001	43.310
B-MC	8.184	1	5.184	9.849215	0.0105	6.304
C-RM	11.409	1	9.409	17.8764	0.0017	8.788
AB	0.180	1	0.18	0.341987	0.5716	0.139
AC	0.320	1	0.32	0.607976	0.4536	0.246
BC	0.180	1	0.18	0.341987	0.5716	0.139

A^2	46.474	1	40.47364	76.8969	< 0.0001	35.799
B^2	0.471	1	0.470511	0.893937	0.3667	0.362
C^2	1.114	1	1.113636	2.115826	0.1764	0.858
Residual	5.263	10	0.526336			4.054
Cor Total	129.819	19				100.000

R-Square: 97.88% Adjusted R-square: 94.96% Predicted R-square: 85.35%

Where A is solid loading (SL), B is monomer content (MC), C is ratio of monomers (RM)

From the above results, it has been observed that SL, MC, RM, and SL^2, are significant model terms, and the response of each A, B and C are shown in the Figures 5.1(a), (b) and (c) respectively. The regression model generated for flexural strength was given in Eqn. 5.1, in the coded form.

$$FS = 50.20 + 2.15A - 0.72B + 0.97C + 0.15AB - 0.20AC - 0.15BC - 3.84A^2 + 0.14B^2 - 0.64C^2 \quad (5.1)$$

From Figure 5.1(a), it is observed that flexural strength increases with solid loading, reaches a maximum and then decreases. Micro-cracks occur in green bodies when the solid loading is low. This may be due to the increase of drying and sintering shrinkages as the space between any two particles in the slurry is huge. In the interim, too low solid loading decreases the density of the sintered body. Therefore, the flexural strength of porous SiO_2 sintered body is low at lower solids loading and increases with the solid loading. However higher solid loading results in the increase of micro-cracks because of the formation of cristobalite structure due to excessive crystallization of the silica.

With the increase of monomer content, the flexural strength decreases, as shown in Figure 5.1(b). The crosslink density of gel is low when monomer content is low, and the stability and uniformity of green body are poor. However, when monomer content is high, the crosslink density of gel is enormous, and the stability and uniformity of slurry are sound. Hence the increase in monomer content makes the three-dimensional cross-linking network structure that enhances the flexural strength of green body. On the other hand increase in monomer content increase macromolecular gel network and during sintering the monomer

content burns out completely and leaves large pores in the ceramic structure that decrease the flexural strength.

Figure 5.1(c) shows that the flexural strength of sintered body increases with the increase of the ratio of monomer to cross-linker. As the ratio of monomer to cross-linker increases, cross-linking points of gel increases, which builds the three-dimensional network compact structures. The ceramic particle distribution in the network of the gel is also more uniform. Consequently, the probability of micro-crack incidence reduces during the drying of the green body that may increase the flexural strength of sintered body.

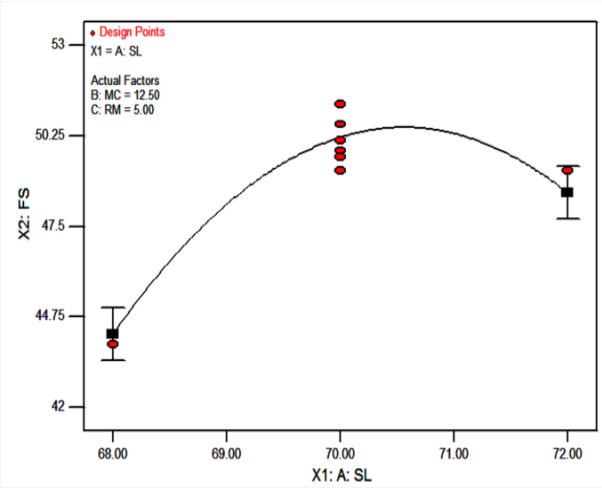

Figure 5.1.(a). Effect of SL on FS

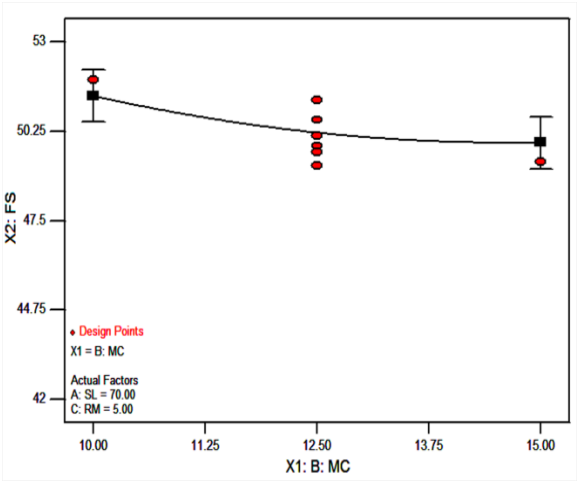

Figure 5.1.(b). Effect of MC on FS

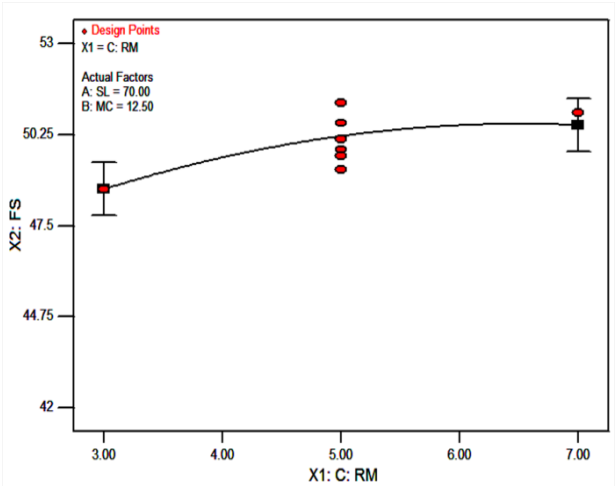

Figure 5.1.(c). Effect of RM on FS.

Figure 5.1.Effect of process parameters on flexural strength

5.2.1.1. Optimization of flexural strength using desirability function

The optimum value of flexural strength is calculated using desirability function (Refer section 1.8.3) where the user can opt for goal, lower and upper limits of various variables (here A, B, and C) as shown in Table 5.2.

Table 5.2. Range of input parameters and flexural strength for desirability

Name	Goal	Lower Limit	Upper Limit
A-SL (vol %)	maximize	68	72
B-MC (wt %)	is in range	10	15
C-RM	is in range	3	7
FS (MPa)	maximize	42.3	52.3

The aim of optimization is to evaluate the best combinational set of inputs for maximization of flexural strength. This is indicated by the desirability of RSM analysis. The maximum value of flexural strength is to be chosen for maximum desirability index for various sets of inputs. A set of 10 optimal solutions is derived and tabulated in Table 5.3 for the particular set of input range (Table 5.2). The desirability of flexural strength is shown in Figures 5.2 as ramp graph. The desirability of each parameter and flexural strength and combined parameters is shown in Figures 5.3 as a bar graph. The prediction of response to a particular response characteristic is indicated by the dot on each of the ramps. The overall desirability of the flexural strength is found to be 0.877.

Table 5.3. Optimal solutions for flexural strength

Number	SL	MC	RM	FS	Desirability
1	71.67	10	6.5	50.684	0.877
2	71.67	10	6.51	50.684	0.877
3	71.67	10	6.48	50.687	0.877
4	71.67	10	6.46	50.686	0.877
5	71.68	10	6.54	50.670	0.877
6	71.69	10	6.43	50.640	0.877
7	71.67	10	6.6	50.679	0.877
8	71.61	10	6.63	50.817	0.877
9	71.52	10	6.62	50.999	0.876
10	71.84	10	6.47	50.285	0.875

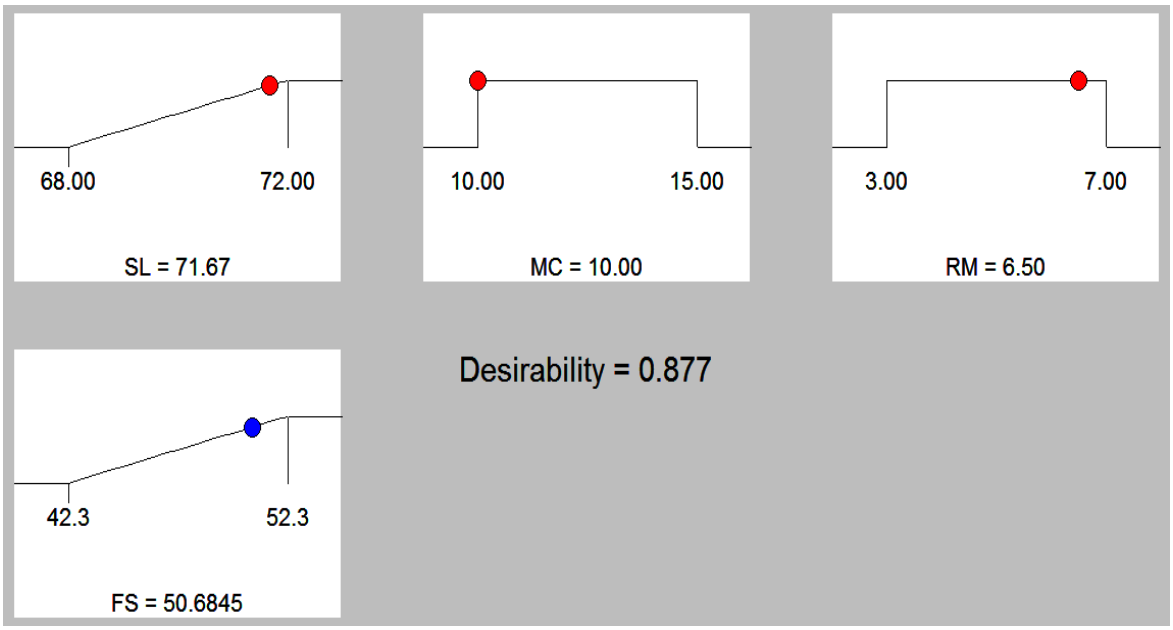

Figure 5.2. Ramp graphs of desirability function of flexural strength of SiO_2 ceramics

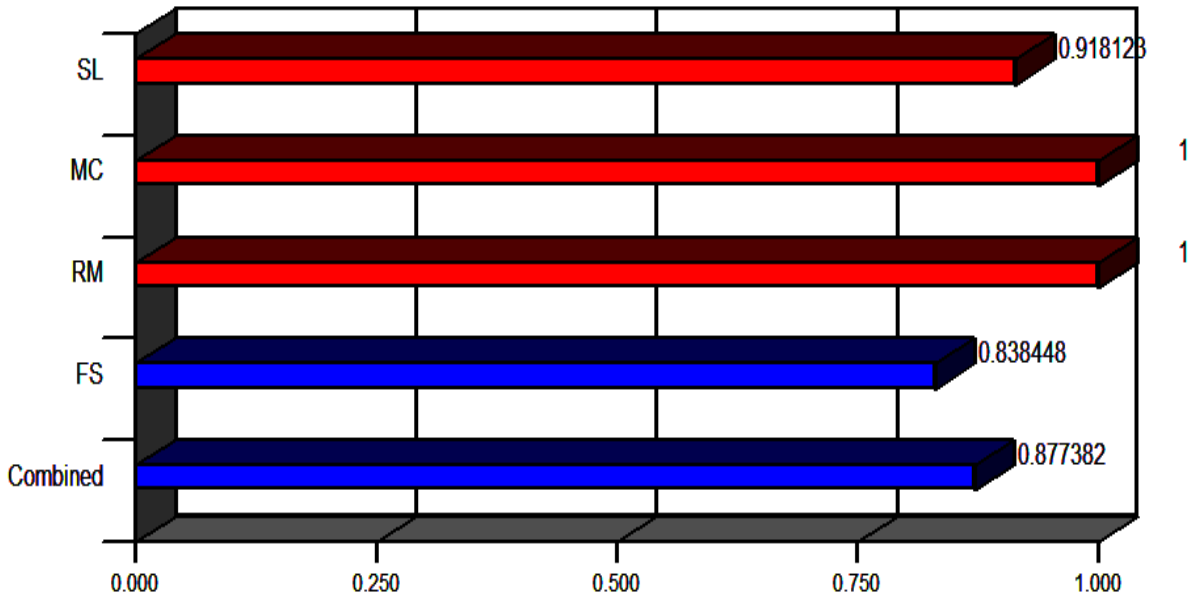

Figure 5.3. Bar graphs of desirability function

5.2.2. Regression model for porosity

A regression model for the porosity of SiO_2 ceramics is fitted using the experimental results (Table 4.5). ANOVA has been applied on the experimental results for porosity and the ANOVA results are given in Table 5.4.

Table 5.4. ANOVA results for porosity

Source	Sum of Squares	df	Mean Square	F Value	p-value Prob > F	Percentage Contribution
Model	22.7538	12	5.758126	22.78321	0.0002	92.786
A-SL	4.59045	1	4.59045	18.16306	0.0037	18.719
B-MC	3.9762	1	3.9762	15.73266	0.0054	16.214
C-RM	0.47045	1	0.47045	1.861433	0.2147	1.918
AB	1.42805	1	1.42805	5.650375	0.0491	5.823
AC	0.2592	1	0.2592	1.025578	0.3449	1.057
BC	1.0082	1	1.0082	3.989151	0.0860	4.111
A^2	9.458182	1	9.458182	37.42325	0.0005	38.569
B^2	0.053551	1	0.053551	0.211884	0.6593	0.218
C^2	0.008182	1	0.008182	0.032373	0.8623	0.033
A^2B	0.47524	1	0.47524	1.880385	0.2126	1.938
A^2C	0.51529	1	0.51529	2.038851	0.1964	2.101
AB^2	0.51076	1	0.51076	2.020927	0.1981	2.083
Residual	1.769148	7	0.252735			7.214
Cor Total	24.5229	19				100.00
R-Square: 97.50%		Adjusted R-square: 93.22%		Predicted R-square: 91.02%		

Where A is solid loading (SL), B is monomer content (MC), C is ratio of monomers (RM)

From the above results, it has been observed that SL, MC, interactions of SL and MC, and SL^2 are significant model terms, and the response of each is shown in the Figures 5.4(a), (b) and (c) respectively. The regression model generated for porosity was given in Eqn. 5.2, in the coded form.

$$Por. = 33.80 - 1.52A + 1.14B - 0.48C + 0.42AB - 0.18AC - 0.35BC + 1.85A^2 + 0.14B^2 + 0.055C^2 + 0.54A^2B + 0.57A^2C + 0.56AB^2 \quad (5.2)$$

In Figure 5.4(a), the porosity of sintered SiO_2 ceramic part decreases with the increase of solid loading and increases when solid loading exceeds a limit. As the solid loading increases the density of the sintered body increases, hence there is an initial decrease in the

porosity. If the solid loading is increased beyond a limit the porosity is found to increase due to the agglomeration of ceramic particles that causes pit holes in the final product. The porosity of sintered body increases with the increase of monomer content as seen in Figure 5.4(b). The pores of sintered body largely initiate from the left over micro-space of the organic polymers in the green body during organic binder burnout. The distribution and intensity of pores depend on the monomer content. Thus more the monomer content more porous the ceramic body. The interaction effects of solid loading and monomer content can be seen in Figure 5.4(c).

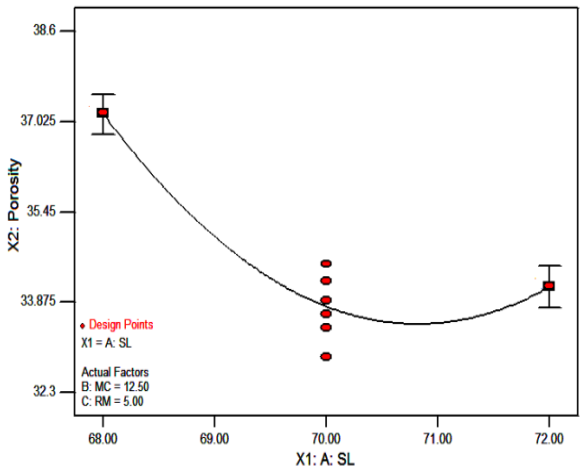

Figure 5.4(a). Effect of SL on porosity

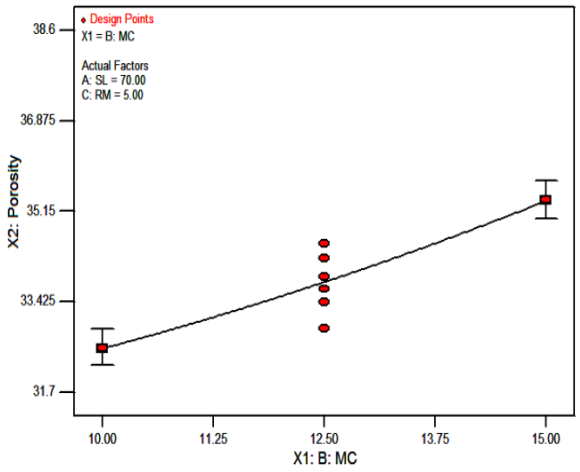

Figure 5.4 (b). Effect of MC on porosity

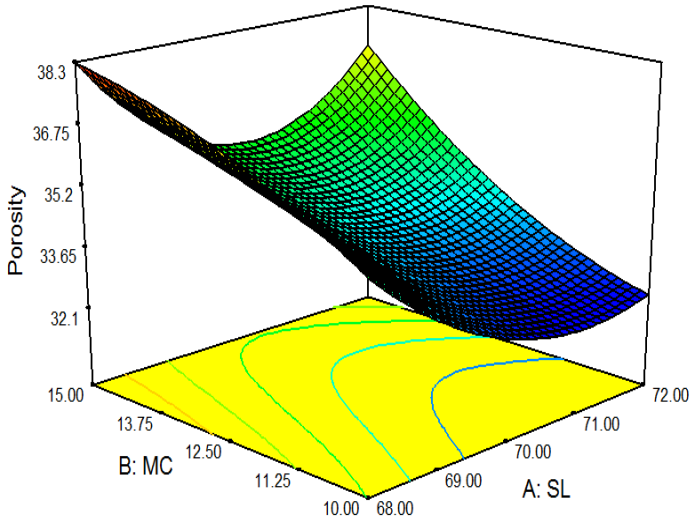

Figure 5.4 (c). Effect of SL and MC on porosity

Figure 5.4. Effect of process parameters on porosity.

5.2.2.1. Optimization of porosity using desirability function

The optimum value of porosity is calculated using desirability function of (Refer section 1.8.3) where the user can opt for goal, lower and upper limits of various variables (here A, B, and C) as shown in Table 5.5.

Table 5.5. Range of input parameters and porosity for desirability

Name	Goal	Lower Limit	Upper Limit
A-SL (vol %)	maximize	68	72
B-MC (wt %)	is in range	10	15
C-RM	is in range	3	7
Por. (%)	maximize	32.35	38.51

The aim of optimization is to evaluate the best combinational set of inputs for maximization of porosity. This is indicated by the desirability of RSM analysis. The maximum value of porosity is to be chosen for maximum desirability index for various sets of inputs. A set of 10 optimal solutions is derived and tabulated in Table 5.6 for the particular set of input range (Table 5.5). The desirability of porosity is shown in Figures 5.5 as ramp graph. The desirability of each parameter and porosity and combined parameters is shown in Figures 5.6 as a bar graph. The prediction of response to a particular response characteristic is indicated by the dot on each of the ramps. The overall desirability of the porosity is found to be 0.934.

Table 5.6. Optimal solutions for porosity.

Number	SL	MC	RM	Por.	Desirability
1	72	15	3	37.728	0.934
2	72	15	3.02	37.722	0.934
3	72	15	3.07	37.708	0.933
4	72	15	3.12	37.695	0.932
5	72	15	3.16	37.682	0.930
6	72	15	3.18	37.678	0.930
7	72	15	3.34	37.633	0.926
8	72	14.92	3	37.601	0.923
9	72	15	3.49	37.592	0.923
10	72	15	3.57	37.573	0.921

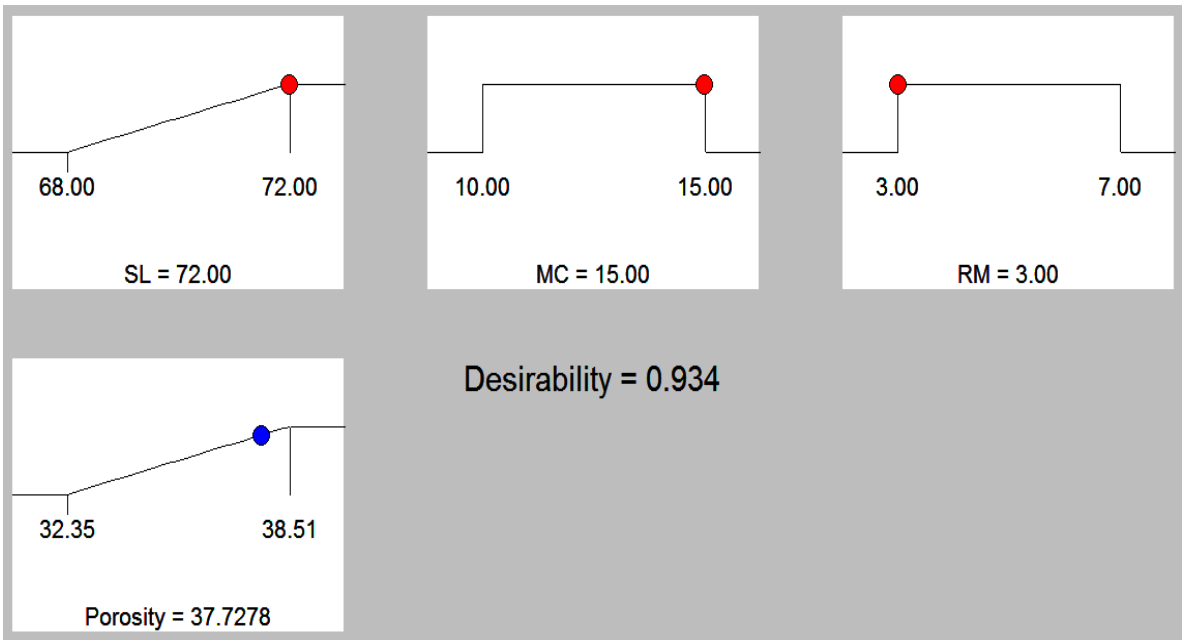

Figure 5.5. Ramp graphs of desirability function for porosity.

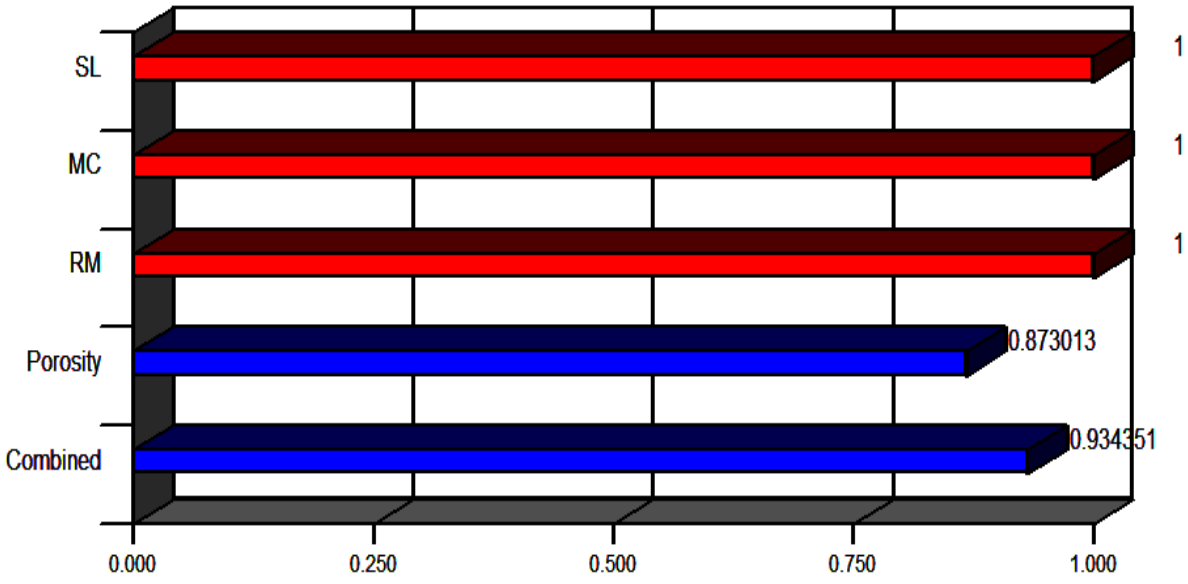

Figure 5.6. Bar graphs of desirability function for porosity.

5.2.3. Regression model for dielectric constant

A regression model for dielectric constant of SiO_2 ceramics is fitted using the experimental results (Table 4.5). ANOVA has been applied on the experimental results for dielectric constant and the ANOVA results are given in Table 5.7.

Table 5.7. ANOVA results for dielectric constant.

Source	Sum of Squares	df	Mean Square	F Value	p-value Prob > F	Percentage Contribution
Model	0.12489	7	0.017841	30.02765	< 0.0001	94.599
A-SL	0.01681	1	0.01681	28.29173	0.0002	12.733
B-MC	0.06561	1	0.06561	110.4236	< 0.0001	49.697
C-RM	0.00049	1	0.00049	0.824684	0.3817	0.371
AB	0.005	1	0.005	8.415147	0.0133	3.787
AC	0.00045	1	0.00045	0.757363	0.4012	0.341
BC	0.00125	1	0.00125	2.103787	0.1726	0.947
A^2	0.03528	1	0.03528	59.37728	< 0.0001	26.723
Residual	0.00713	12	0.000594			5.401
Cor Total	0.13202	19				100
R-Square: 94.59%		Adjusted R-square: 91.44%		Predicted R-square: 83.93%		

Where A is solid loading (SL), B is monomer content (MC), C is ratio of monomers (RM)

From the above results, it has been observed that SL, MC, interactions of SL and MC, and SL^2 are significant model terms, and the response of each is shown in the Figures 5.7(a), (b) and (c) respectively. The regression model generated for dielectric constant was given in Eqn. 5.3, in the coded form.

$$DE = 4.09 + 0.041A - 0.081B + 7\times10^{-3}C - 0.025AB + 7.5\times10^{-3}AC + 0.013BC - 0.084A^2 \quad (5.3)$$

The dielectric properties are closely related to material density. The greater the density of fused silica ceramics, the greater is the dielectric constant (Wan et al., 2014). Figure 5.7(a) show the increase in density of SiO_2 ceramics with an increase in solid loading and that will lead to the increase of dielectric constant. The density starts decreasing when the solid loading increases beyond a particular value (here it is 70.6 vol%) due to increasing in surface area of pores, and agglomeration of ceramic particles followed by formation of micro cracks. In Figure 5.7(b), as the monomer content increases the dielectric constant decreases monotonically. The increase in monomer content decreases the density of sintered ceramic

due to the formation of large pores during binder burnout. Thus an increase in the monomer content will lower the density and dielectric properties of SiO_2 ceramics. The interaction effects of solid loading and monomer content on dielectric constant can be seen in Figure 5.7(c).

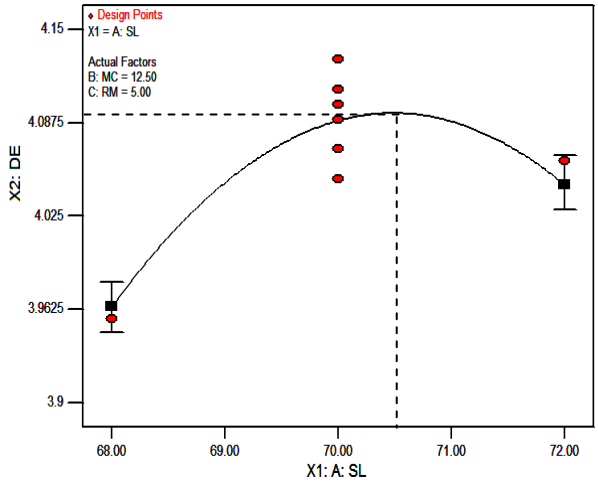

Figure 5.7(a). Effect of SL on DE.

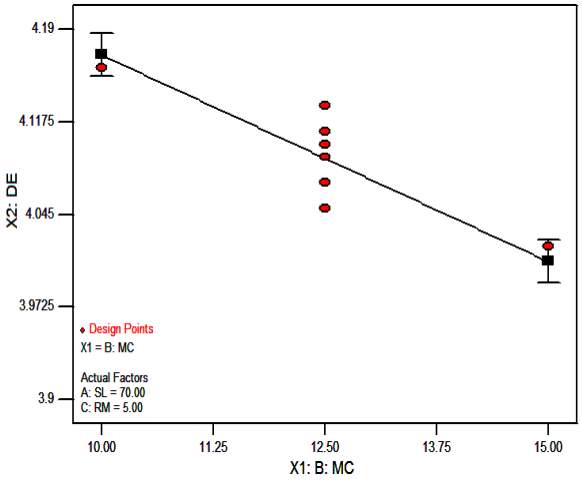

Figure 5.7(b). Effect of MC on DE.

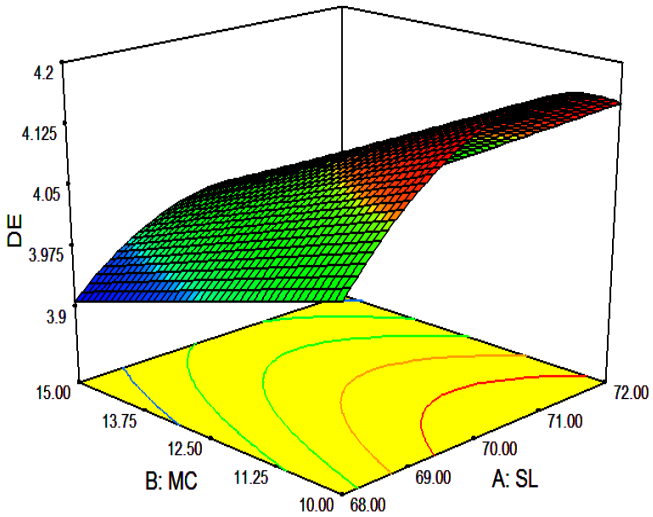

Figure 5.7(c). Effect of SL and MC on DE.

Figure 5.7. Effect of process parameters on dielectric constant.

5.2.3.1. Optimization of dielectric constant using desirability function

The optimum value of dielectric constant is calculated using desirability function of (Refer section 1.8.3) where the user can opt for goal, lower and upper limits of various variables (here A, B, and C) as shown in Table 5.8.

Table 5.8. The range of input parameters and dielectric constant for desirability.

Name	Goal	Lower Limit	Upper Limit
A-SL (vol %)	maximize	68	72
B-MC (wt %)	is in range	10	15
C-RM	is in range	3	7
DE	minimize	3.9	4.15

The aim of optimization is to evaluate the best combinational set of inputs for minimization of dielectric constant. This is indicated by the desirability of RSM analysis. The maximum value of dielectric constant is to be chosen for maximum desirability index for various sets of inputs. A set of 10 optimal solutions is derived and tabulated in Table 5.9 for the particular set of input range (Table 5.8). The desirability of dielectric constant is shown in Figures 5.8 as ramp graph. The desirability of each parameter and dielectric constant and combined parameters is shown in Figures 5.9 as a bar graph. The prediction of response to a particular response characteristic is indicated by the dot on each of the ramps. The overall desirability of the dielectric constant is found to be 0.973.

Table 5.9. Optimal solutions for dielectric constant.

Number	SL	MC	RM	DE	Desirability
1	72	15	3.01	3.913	0.973
2	72	15	3.06	3.914	0.972
3	72	15	3.08	3.914	0.972
4	72	15	3.1	3.914	0.971
5	72	14.97	3.01	3.915	0.971
6	72	15	3.15	3.915	0.969
7	71.97	14.99	3	3.916	0.965
8	72	14.9	3	3.918	0.964
9	72	15	3.5	3.920	0.960
10	72	14.85	3	3.920	0.959

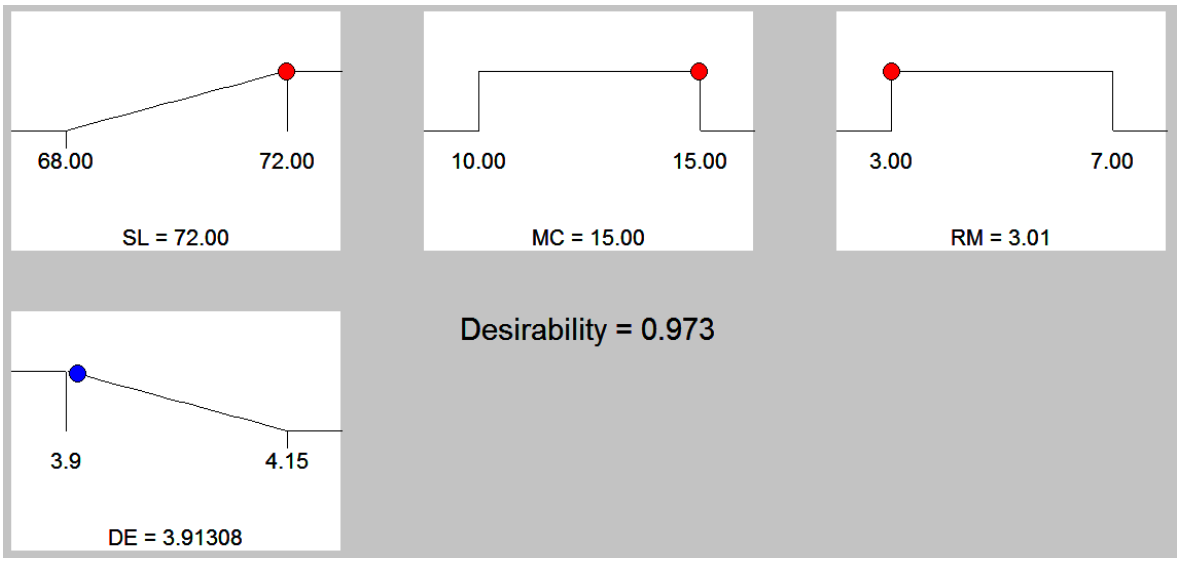

Figure 5.8. Ramp graphs of desirability function for dielectric constant.

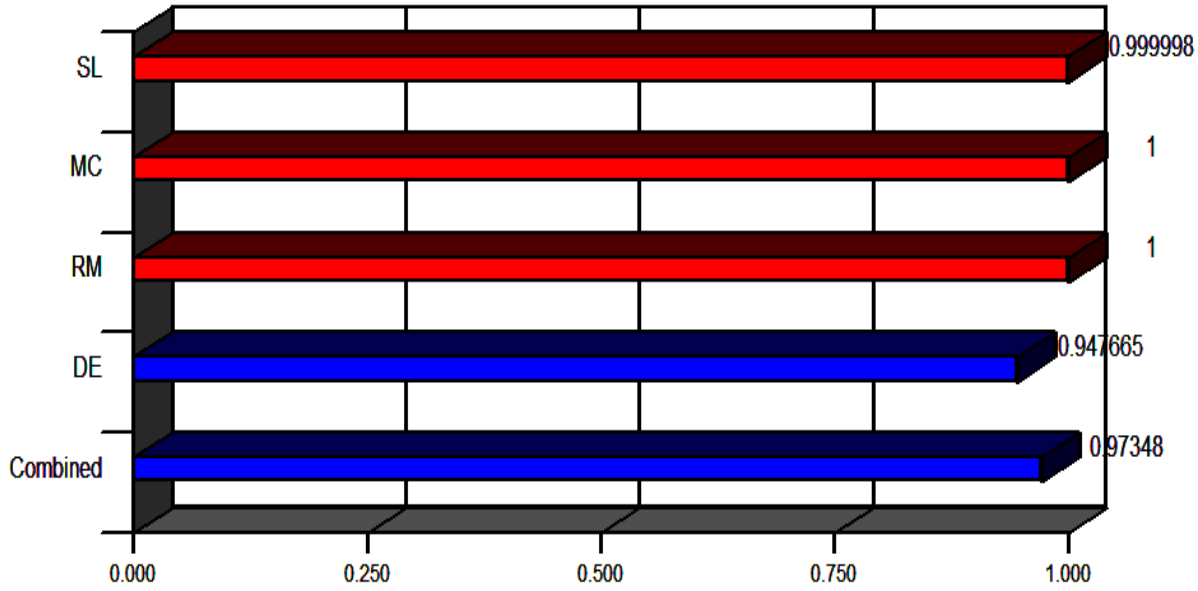

Figure 5.9. Bar graphs of desirability function for dielectric constant.

5.2.4. Multi-response optimization using desirability function

Multi-response optimization using desirability function was carried out in combination with response surface methodology to surmount the difficulty of inconsistent responses of single response optimization. The range and goals of input parameters i.e. solid loading, monomer content, and ratio of monomers and the responses i.e. flexural strength, porosity and dielectric constant are given in Table 5.10.

Table 5.10. The range of input parameters and responses for desirability.

Name	Goal	Lower Limit	Upper Limit
A-SL (vol %)	maximize	68	72
B-MC (wt %)	is in range	10	15
C-RM	is in range	3	7
FS (MPa)	maximize	42.3	52.3
Por. (%)	maximize	32.35	38.51
DE	minimize	3.9	4.15

The aim of optimization is to evaluate the best set of inputs for maximization of flexural strength and porosity, and minimization of dielectric constant. This is indicated by the desirability of RSM analysis. The optimum value of responses is to be chosen for maximum desirability index for various sets of inputs. A set of 10 optimal solutions is derived and tabulated in Table 5.11 for the particular set of input range constraints (Table 5.10). The desirability of output responses i.e. flexural strength, porosity and dielectric constant is shown in Figures 5.10 as ramp graph. The desirability of each parameter and each response and combined parameters are shown in Figures 5.11 as a bar graph. The overall desirability of the responses is found to be 0.803.

Table 5.11. Set of optimal solutions for SiO_2 ceramics

Number	SL	MC	RM	FS	Por.	DE	Desirability
1	72	15	4.03	47.914	37.452	3.927	0.803
2	72	15	4.06	47.930	37.445	3.927	0.803
3	72	15	3.97	47.876	37.467	3.926	0.803
4	72	15	3.82	47.771	37.508	3.924	0.802
5	72	15	3.74	47.719	37.527	3.923	0.802
6	72	15	4.43	48.132	37.355	3.932	0.802
7	72	15	3.64	47.650	37.552	3.922	0.801
8	72	14.99	3.87	47.806	37.474	3.925	0.801
9	72	15	3.56	47.589	37.574	3.921	0.801
10	72	15	3.49	47.533	37.593	3.920	0.800

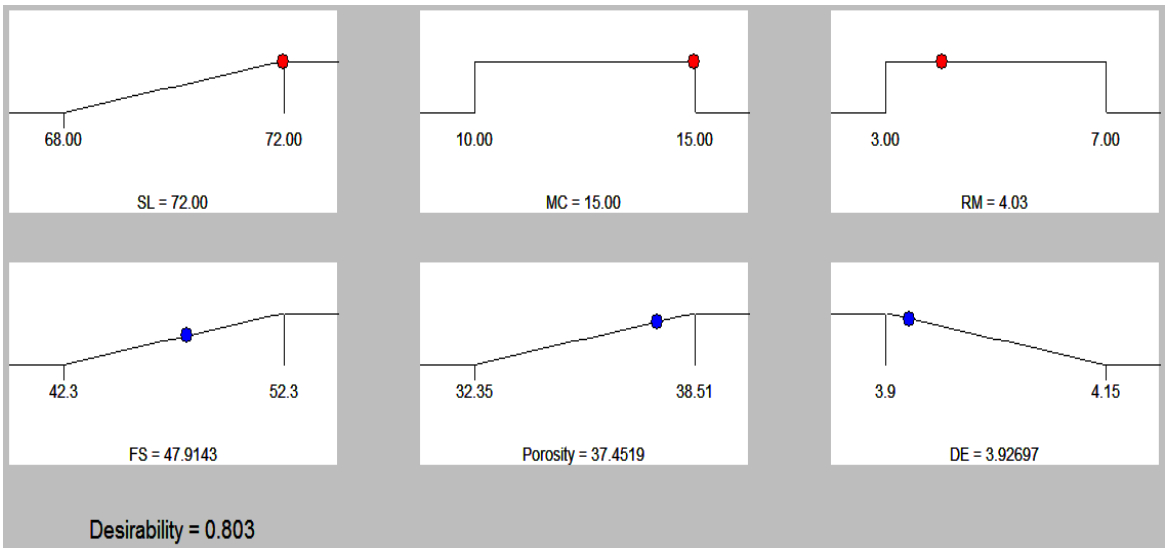

Figure 5.10. Ramp graphs of desirability function for SiO_2 ceramics.

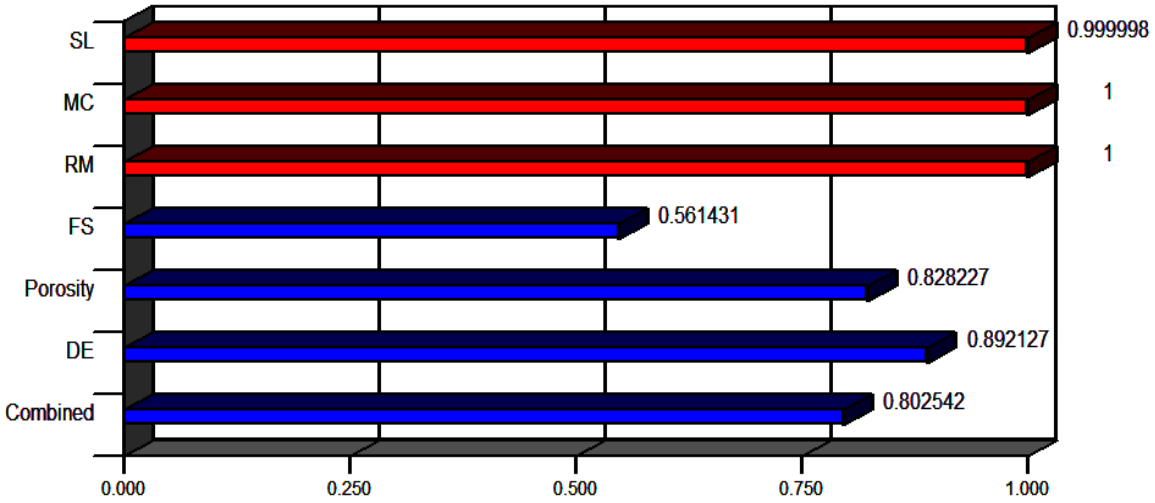

Figure 5.11. Bar graphs of desirability function for SiO_2 ceramics.

5.2.5. Confirmation tests

The values of responses i.e. flexural strength, porosity and dielectric constant obtained by experimental runs are compared with predicted regression models for flexural strength, porosity and dielectric constant for SiO_2 ceramics. The error between experimental and predicted values is predicted in Table 5.12 for all responses. It is found that a maximum error of ±2.04% in flexural strength, ±2.74% in porosity and ±0.99% in dielectric constant existing. Hence it can be declared that the predicted models are confirming with experimental values. Hence the tests are confirmed and recommended that the models are accurate.

Table 5.12. Error between experimental and predicted values

Run order	SL (vol %)	MC (wt %)	RM	Flexural Strength (MPa)			Porosity (%)			Dielectric Constant (K)		
				Expt.	Pred.	Error	Expt.	Pred.	Error	Expt.	Pred.	Error
1	70	12.5	5	49.2	50.20	-2.04	33.42	33.82	-1.20	4.11	4.09	0.51
2	68	12.5	5	43.9	44.22	-0.72	37.19	37.19	0.00	3.94	3.96	-0.61
3	70	12.5	5	49.6	50.20	-1.22	33.67	33.82	-0.45	4.09	4.09	0.02
4	70	10	5	52.3	51.34	1.84	32.55	32.55	0.00	4.15	4.17	-0.48
5	70	12.5	3	48.6	48.60	0.00	34.36	34.36	0.01	4.06	4.08	-0.54
6	68	15	7	44.5	44.15	0.80	38.14	38.26	-0.33	3.92	3.92	0.00
7	72	10	3	47.5	47.95	-0.94	32.35	32.28	0.21	4.15	4.15	0.00
8	72	12.5	5	49.2	48.52	1.39	34.16	34.16	-0.01	4.07	4.05	0.59
9	68	10	7	45.9	46.19	-0.62	35.97	35.91	0.17	4.01	4.01	0.07
10	70	12.5	5	49.8	50.20	-0.81	33.91	33.82	0.26	4.1	4.09	0.27
11	70	12.5	5	50.1	50.20	-0.21	34.25	33.82	1.25	4.07	4.09	-0.47
12	70	12.5	5	51.2	50.20	1.94	32.92	33.82	-2.74	4.13	4.09	0.99
13	68	15	3	42.3	42.11	0.46	38.51	38.44	0.18	3.9	3.90	0.10

Run order	SL (vol %)	MC (wt %)	RM	Flexural Strength (MPa)			Porosity (%)			Dielectric Constant (K)		
				Expt.	Pred.	Error	Expt.	Pred.	Error	Expt.	Pred.	Error
14	68	10	3	43.6	43.55	0.13	34.55	34.66	-0.33	4.05	4.03	0.42
15	72	10	7	49.5	49.79	-0.58	32.68	32.81	-0.39	4.15	4.15	-0.10
16	70	15	5	49.3	49.90	-1.21	35.37	35.37	0.00	4.02	4.01	0.30
17	72	15	3	47.3	47.11	0.41	37.63	37.75	-0.31	3.91	3.91	-0.08
18	70	12.5	7	50.9	50.54	0.71	33.39	33.40	-0.02	4.11	4.10	0.34
19	70	12.5	5	50.6	50.20	0.78	34.54	33.82	2.08	4.05	4.09	-0.96
20	72	15	7	48.2	48.35	-0.30	36.91	36.85	0.16	3.95	3.97	-0.43

5.3. Results and analysis of SiO_2–Si_3N_4 ceramic composites

5.3.1. Regression model for flexural strength

A regression model for flexural strength of SiO_2–Si_3N_4 ceramic composite is fitted using the experimental results (Table 4.8). ANOVA has been applied on the experimental results for flexural strength and the ANOVA results are given in Table 5.13.

Table 5.13. ANOVA results for flexural strength.

Source	Sum of Squares	df	Mean Square	F Value	p-value Prob > F	Percentage Contribution
Model	3496.603	8	252.9297	44.09247	< 0.0001	97.598
A-SL	3042.520	1	3042.52	530.3934	< 0.0001	84.924
B-Si_3N_4	311.951	1	311.7505	54.34652	< 0.0001	8.707
C-MC	39.232	1	27.2322	4.747308	0.0457	1.095
D-RM	36.620	1	33.62	5.860874	0.0286	1.022
AB	15.980	1	15.98001	2.785747	0.1158	0.446
BC	8.883	1	8.482656	1.478756	0.2428	0.248
A^2	37.723	1	37.72255	6.576059	0.0216	1.053
C^2	3.696	1	3.695539	0.644232	0.4347	0.103
Residual	86.045	21	5.736346			2.402
Cor Total	3582.649	29				100.00
R-Square: 97.62%		Adjusted R-square: 95.41%			Predicted R-square: 92.39%	

Where A is solid loading (SL), B is Si_3N_4 content, C is monomer content (MC), D is ratio of monomers (RM)

From the above results, it has been observed that SL, Si_3N_4, MC, RM, and SL^2, are significant model terms, and response of each are shown in the Figures 5.12(a), (b), (c) and (d) respectively. The regression model generated for flexural strength was given in Eqn. 5.4, in the coded form.

$$FS = 80.60 + 13A + 4.16B + 1.23C + 1.37D - AB - 0.73BC - 3.82A^2 + 1.19C^2 \quad (5.4)$$

From Figure 5.12(a) and (b), it is observed that flexural strength increases with solid loading and Si_3N_4 content. Micro-cracks occur in green bodies when the solid loading is low. This may be due to the increase of drying and sintering shrinkages as the space between the particles in the slurry is huge. At low solids loading and Si_3N_4 content the density of the composite decreases during sintering. Therefore, the flexural strength of porous SiO_2–Si_3N_4 sintered ceramic composite is low at lower solids loading and higher the solid loading increases the flexural strength. During sintering, the monomers are burnt out leaving pores. Few pores in the composite will be replaced by the cristobalite which is formed during the sintering. Hence, there is a little significant effect of monomers content and their ratio on the flexural strength of SiO_2–Si_3N_4 ceramic composites as shown in Figure 5.12(c) and (d).

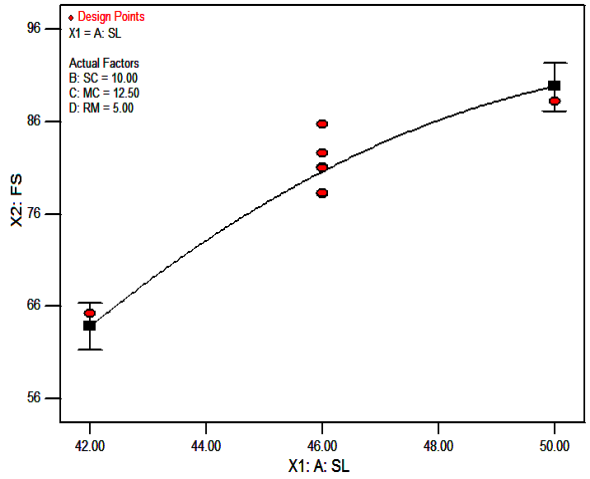

Figure 5.12(a). Effect of SL on FS.

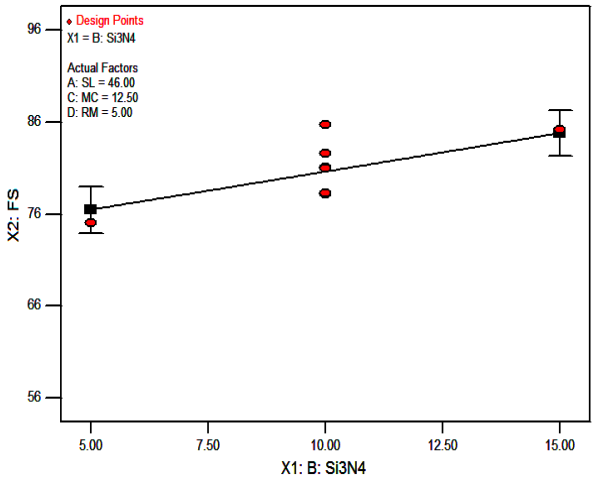

Figure 5.12(b). Effect of Si_3N_4 on FS.

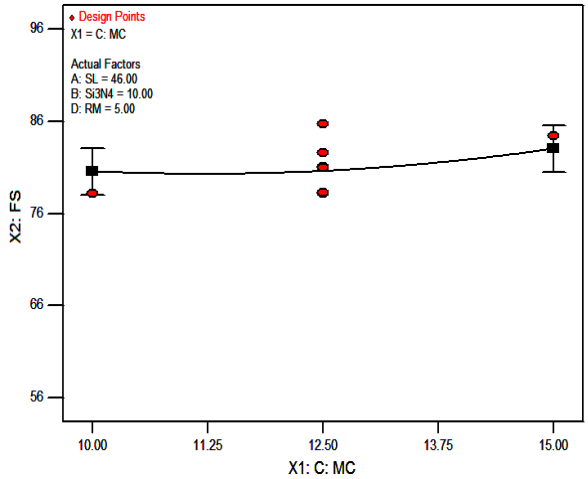

Figure 5.12 (c). Effect of MC on FS.

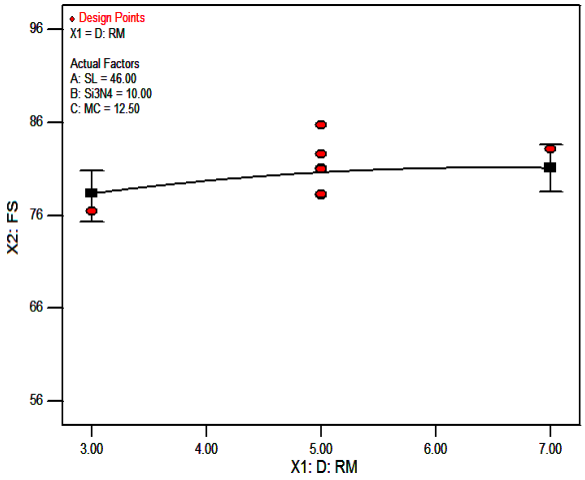

Figure 5.12 (d). Effect of RM on FS.

Figure 5.12. Effect of process parameters on flexural strength

5.3.1.1. Optimization of flexural strength using desirability function

The optimum value of flexural strength is calculated using desirability function (Refer section 1.8.3) where the user can opt for goal, lower and upper limits of various variables (here A, B, C, and D) as shown in Table 5.14.

Table 5.14. The range of input parameters and flexural strength for desirability.

Name	Goal	Lower Limit	Upper Limit
A-SL (vol %)	maximize	42	50
B-Si_3N_4 content (wt %)	in range	5	15
C-MC (wt %)	in range	10	15
D-RM	in range	3	7
FS (MPa)	maximize	56.19	95.12

The aim of optimization is to evaluate the best combinational set of inputs for maximization of flexural strength. This is indicated by the desirability of RSM analysis. The maximum value of flexural strength is to be chosen for maximum desirability index for various sets of inputs. A set of 10 optimal solutions is derived and tabulated in Table 5.15 for the particular set of input range (Table 5.14). The desirability of flexural strength is shown in Figures 5.13 as ramp graph. The desirability of each parameter and flexural strength and combined parameters is shown in Figures 5.14 as a bar graph. The prediction of response to a particular response characteristic is indicated by the dot on each of the ramps. The overall desirability of the flexural strength is found to be 0.993.

Table 5.15. Optimal solutions for flexural strength.

Number	SL	Si_3N_4	MC	RM	FS	Desirability
1	50	15	15	6.37	94.618	0.993
2	50	15	15	6.39	94.615	0.993
3	50	15	15	6.67	94.585	0.993
4	50	15	15	5.81	94.579	0.993
5	50	14.87	15	6.39	94.558	0.993
6	50	15	15	5.71	94.555	0.993
7	50	14.99	15	5.55	94.506	0.992
8	50	14.89	15	5.39	94.399	0.991
9	49.97	14.8	15	6.05	94.496	0.990
10	49.95	15	15	6.33	94.573	0.989

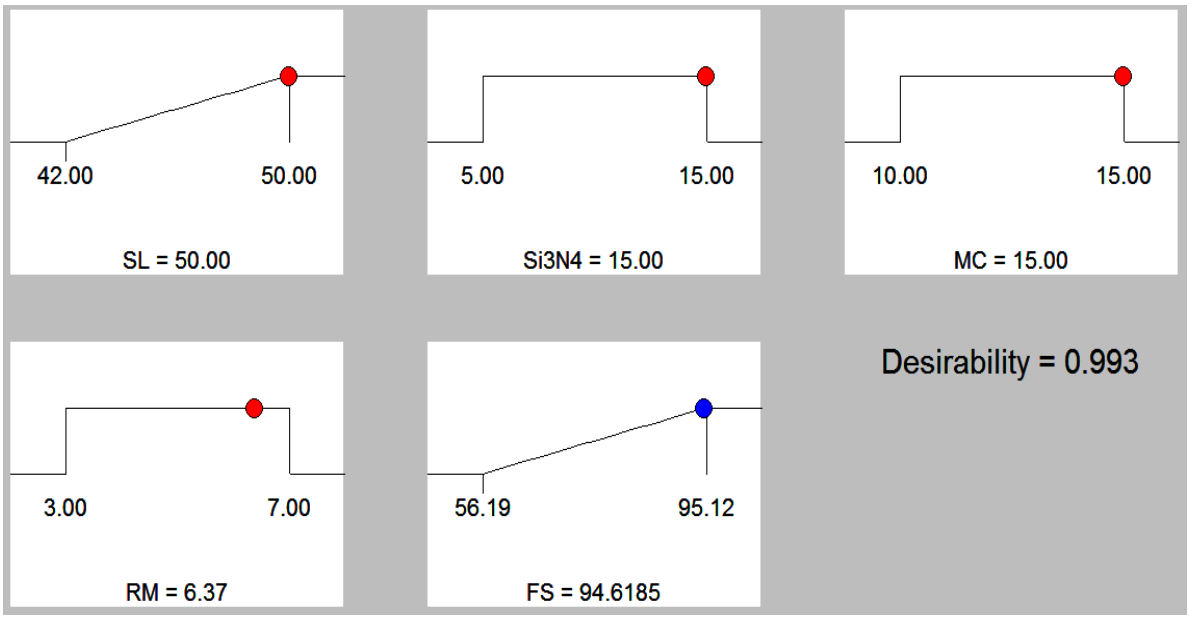

Figure 5.13. Ramp graphs of desirability function for flexural strength of SiO_2–Si_3N_4 ceramic composite.

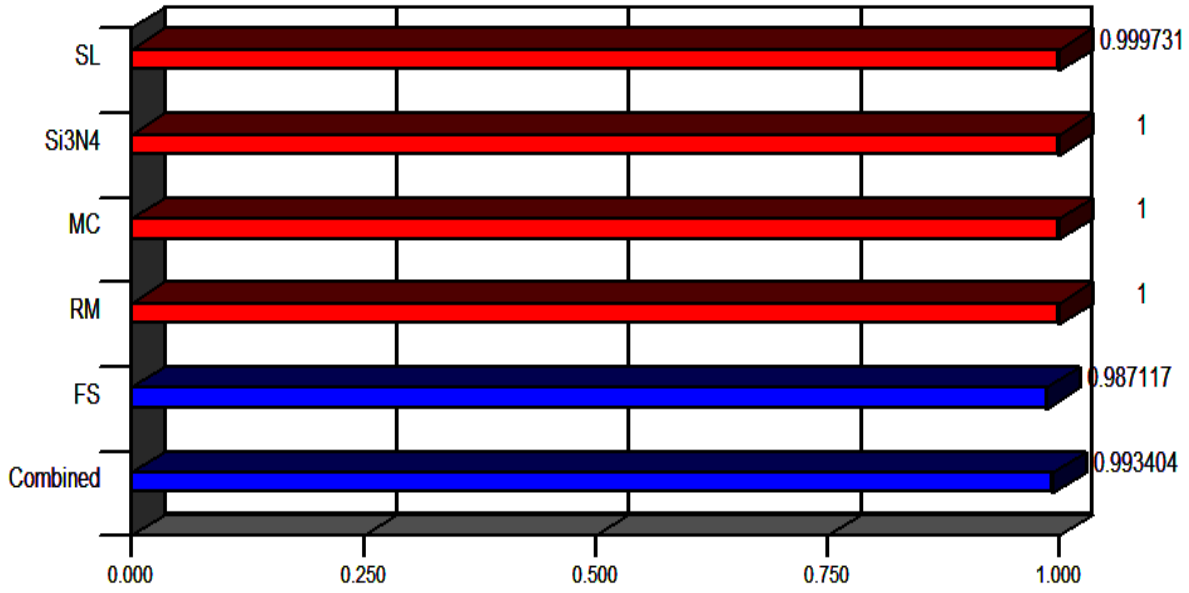

Figure 5.14. Bar graphs of desirability function.

5.3.2. Regression model for porosity

A regression model for the porosity of SiO_2–Si_3N_4 ceramic composite is fitted using the experimental results (Table 4.8). ANOVA has been applied on the experimental results for porosity and the ANOVA results are given in Table 5.16.

Table 5.16. ANOVA results for porosity.

Source	Sum of Squares	df	Mean Square	F Value	p-value Prob > F	Percentage Contribution
Model	158.6867	12	13.22389	27.62487	< 0.0001	95.122
A-SL	105.009	1	105.6089	220.6183	< 0.0001	62.946
B-Si3N4	0.00436	1	0.004356	0.009099	0.9251	0.003
C-MC	17.8802	1	17.8802	37.35197	< 0.0001	10.718
D-RM	8.55601	1	8.556006	17.8736	0.0006	5.129
AB	3.26706	1	3.267056	6.824922	0.0182	1.958
AC	0.79656	1	0.796556	1.664016	0.2143	0.477
AD	0.34516	1	0.345156	0.721036	0.4076	0.207
CD	4.54756	1	4.547556	9.499903	0.0068	2.726
A^2	1.9225	1	1.922496	4.016119	0.0613	1.152
B^2	9.07376	1	9.073755	18.95519	0.0004	5.439
C^2	0.17326	1	0.17326	0.361942	0.5554	0.104
D^2	6.74593	1	6.745934	14.09234	0.0016	4.044
Residual	8.13782	17	0.478695			4.878
Cor Total	166.8245	29				100.00

R-Square: 95.12% Adjusted R-square: 91.67% Predicted R-square: 82.75%

Where A is solid loading (SL), B is Si_3N_4 content, C is monomer content (MC), D is ratio of monomers (RM)

From the above results, it has been observed that SL, MC, RM, interaction of MC and RM, $Si_3N_4^2$, and RM^2 are significant model terms, and response of each is shown in the Figures 5.15(a), (b), (c), (d) and (e). The regression model generated for porosity was given in Eqn. 5.5, in the coded form.

$$Por. = 37.06 - 2.42A - 0.016B - C - 0.69D - 0.45AB + 0.22AC + 0.15AD - 0.53CD - 0.86A^2 - 1.87B^2 + 0.26C^2 + 1.61D^2 \quad (5.5)$$

In Figure 5.15(a), it can be seen that the porosity of sintered body decreases with the increase in solid loading. The ceramic particles are compacted, reducing the pores in the composite with an increase in solid loading. This densifies the ceramic composite. From

Figure 5.15(b), it is observed that Si_3N_4 content has a significant effect on the porosity. As the Si_3N_4 content increases there is a rise in the porosity and then declines on further addition of Si_3N_4 powder. The rise in the porosity is due to the loose packing of Si_3N_4 particles in SiO_2 ceramics. As the content of Si_3N_4 powder increases the pores in the composite are reduced that increases the density of the composite causing the lower porosity.

The porosity of sintered body increases with monomer content as shown in Figure 5.15(c). The pores of sintered body largely initiate from the left over micro-space of the organic polymers in the green body during organic binder burnout. The distribution and intensity of pores depend on the monomer content. Thus more the monomer content more is the porosity in the ceramic body. Figure 5.15(d) show the decrease in porosity with the increase of monomers ratio. Higher porosity is obtained on further increase in the monomer ratio. The increase in the ratio of monomers to cross-linker sometimes initiates micro-crack propagation that causes higher porosity. The interaction effects of monomer content and ratio of monomers can be seen in Figure 5.15(e).

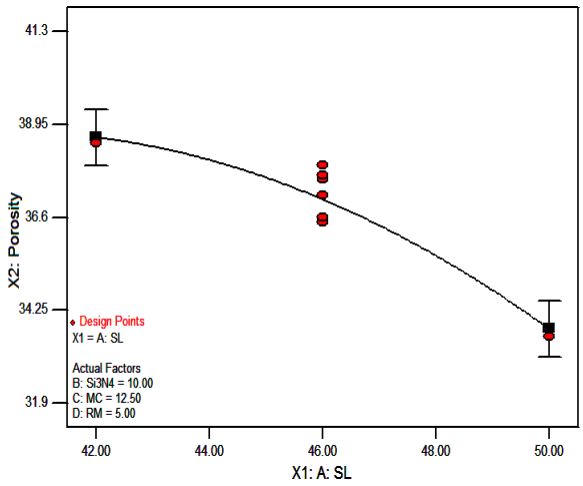

Figure 5.15. (a). Effect of SL on porosity

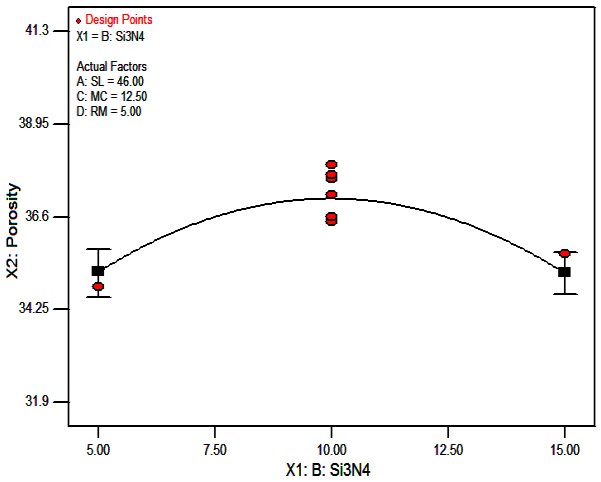

Figure 5.15.(b). Effect of Si_3N_4 on porosity.

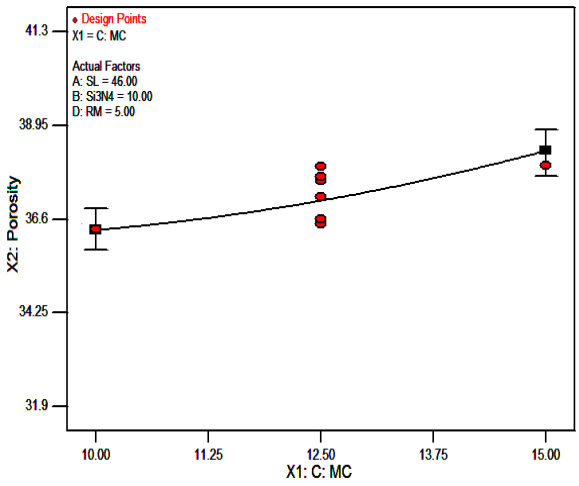

Figure 5.15.(c). Effect of MC on porosity.

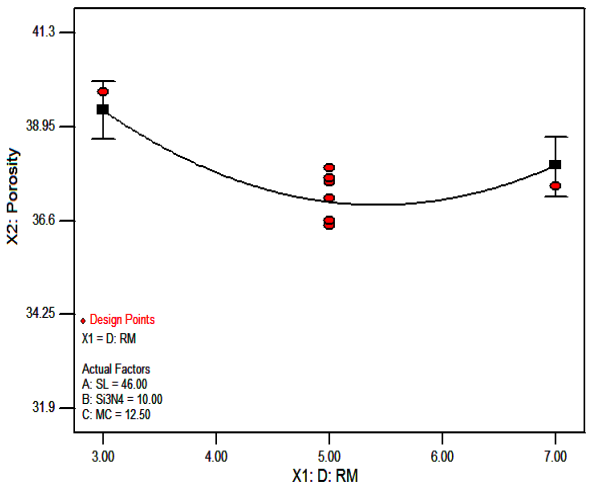

Figure 5.15.(d). Effect of RM on porosity.

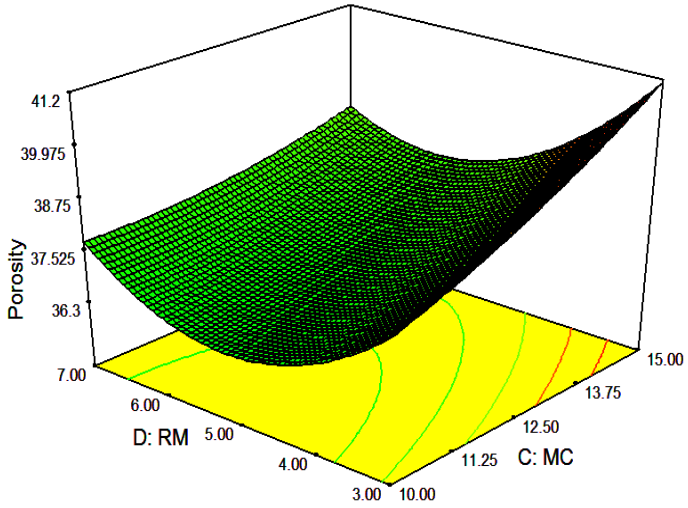

Figure 5.15.(e). Effect of MC and RM on porosity.

Figure 5.15. Effect of process parameters on porosity

5.3.2.1. Optimization of porosity using desirability function

The optimum value of flexural strength is calculated using desirability function (Refer section 1.8.3) where the user can opt for goal, lower and upper limits of various variables (here A, B, C, and D) as shown in Table 5.17.

Table 5.17. The range of input parameters and porosity for desirability.

Name	Goal	Lower Limit	Upper Limit
A-SL (vol %)	maximize	42	50
B-Si_3N_4 content (wt %)	in range	5	15
C-MC (wt %)	in range	10	15
D-RM	in range	3	7
Por. (%)	maximize	31.95	41.28

The aim of optimization is to evaluate the best combinational set of inputs for maximization of porosity. This is indicated by the desirability of RSM analysis. The maximum value of porosity is to be chosen for maximum desirability index for various sets of inputs. A set of 10 optimal solutions is derived and tabulated in Table 5.18 for the particular set of input range (Table 5.17). The desirability of porosity is shown in Figures 5.16 as ramp graph. The desirability of each parameter and porosity and combined parameters is shown in Figures 5.17 as a bar graph. The prediction of response to a particular response characteristic is indicated by the dot on each of the ramps. The overall desirability of the porosity is found to be 0.809.

Table 5.18. Optimal solutions for porosity.

Number	SL	Si_3N_4	MC	RM	Por.	Desirability
1	49.26	9.49	15	3	38.688	0.809
2	49.17	9.46	15	3	38.767	0.809
3	49.26	9.9	15	3	38.669	0.809
4	49.21	9.92	15	3	38.718	0.809
5	48.87	9.43	15	3	39.033	0.808
6	49.5	9.47	15	3.03	38.399	0.805
7	48.85	10.62	15	3	38.970	0.803
8	48.76	10.85	15	3	39.006	0.800
9	49.24	9.46	15	3.08	38.533	0.799
10	48.71	11.01	15	3	39.025	0.797

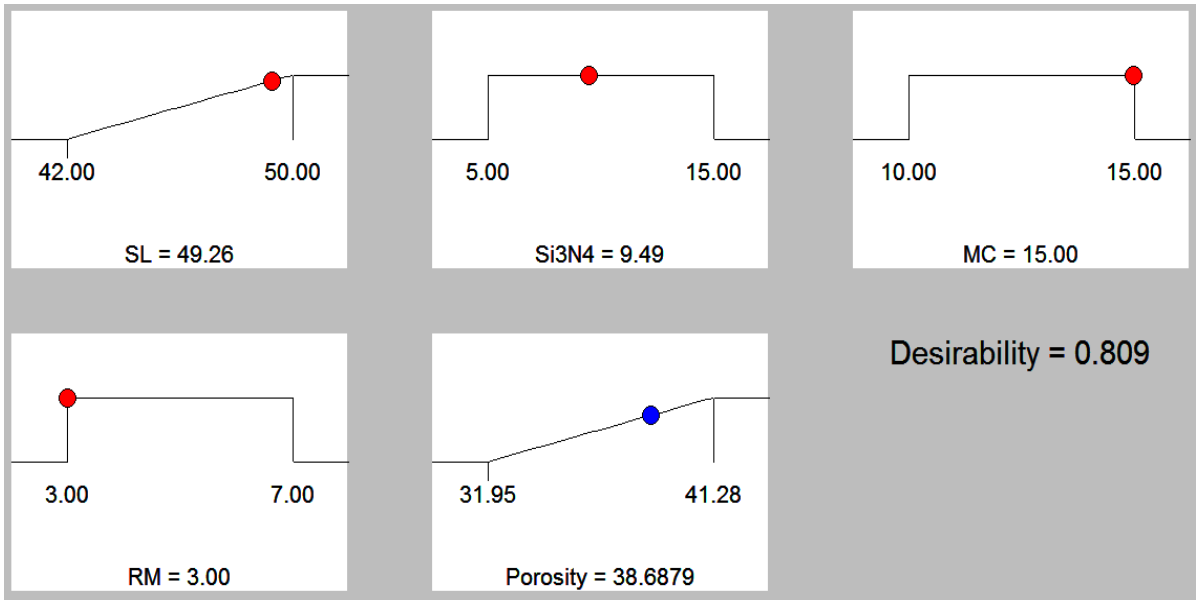

Figure 5.16. Ramp graphs of desirability function for the porosity of SiO_2–Si_3N_4 ceramic composite.

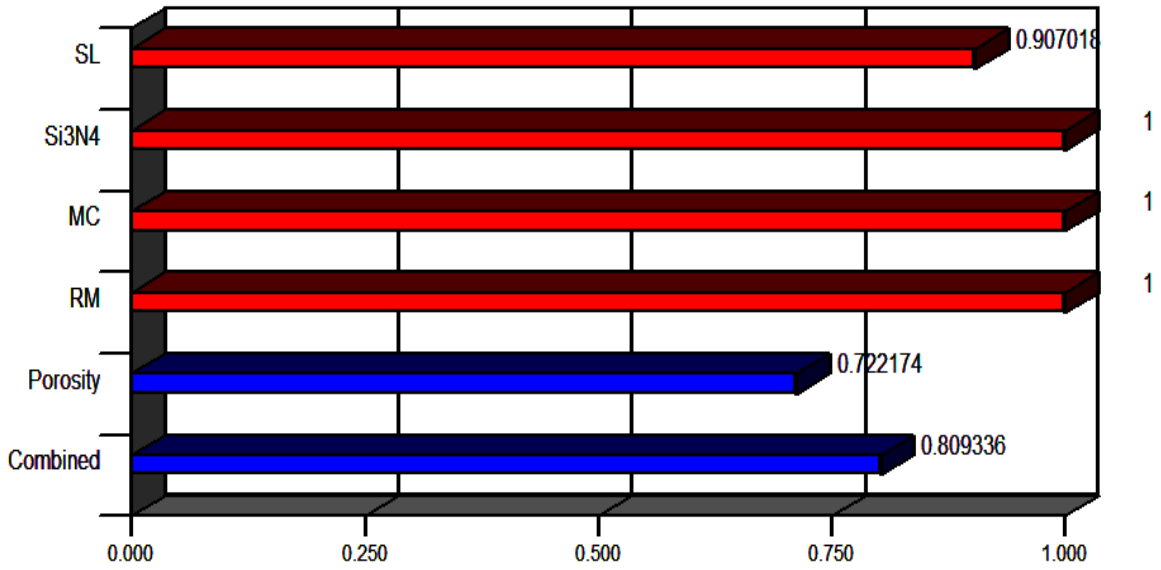

Figure 5.17. Bar graphs of desirability function for porosity.

5.3.3. Regression model for dielectric constant

A regression model for dielectric constant of SiO_2–Si_3N_4 ceramic composite is fitted using the experimental results (Table 4.8). ANOVA has been applied on the experimental results for dielectric constant and the ANOVA results are given in Table 5.19.

Table 5.19. ANOVA results for dielectric constant.

Source	Sum of Squares	df	Mean Square	F Value	p-value Prob > F	Percentage Contribution
Model	4.100	9	0.350244	33.45971	< 0.0001	95.840
A-SL	2.950	1	3.05045	291.4172	< 0.0001	68.969
B-Si3N4	0.001	1	0.000556	0.053074	0.8205	0.013
C-MC	0.339	1	0.338939	32.37969	< 0.0001	7.923
D-RM	0.097	1	0.0968	9.247549	0.0074	2.263
BD	0.074	1	0.074256	7.093888	0.0164	1.736
A^2	0.171	1	0.1708	16.31696	0.0009	3.993
B^2	0.178	1	0.177517	16.95865	0.0007	4.150
C^2	0.039	1	0.039355	3.759641	0.0693	0.920
D^2	0.251	1	0.35134	33.56438	< 0.0001	5.875
Residual	0.178	20	0.010468			4.160
Cor Total	4.278	29				100.00
R-Square: 95.93%		Adjusted R-square: 93.07%			Predicted R-square: 87.36%	

Where A is solid loading (SL), B Si_3N_4 content, C is monomer content (MC), D is ratio of monomers (RM)

From the above results, it has been observed that SL, MC, RM, SL^2, $Si_3N_4{}^2$, RM^2, interactions of Si_3N_4 and RM, and interactions of Si_3N_4, MC and RM are significant model terms, and are shown in the Figures 5.18(a), (b), (c), (d) and (e). The regression model generated for dielectric constant was given in Eqn. 5.6, in the coded form.

$$DE = 7.40 + 0.04A + 5.556\times10^{-3}B - 0.14C + 0.073D + 0.068BD + 0.26A^2 + 0.26B^2 - 0.12C^2 - 0.37D^2 \quad (5.6)$$

Figure 5.18(a) show the increase in density of SiO_2–Si_3N_4 ceramic composite with the increase in solid loading. This will lead to the reduction of pores that causes the increase of dielectric constant. From Figure 5.18(b), it can be seen that the dielectric constant initially decreases when Si_3N_4 content is in the range of 5 wt% to 10 wt%. This is due to the increase in the surface area of pores. There is a rise in the dielectric constant on further increasing the

Si_3N_4 content from 10 wt% to 15 wt%. This may be due to the increase in the density of the ceramic composite which reduces the transfer of electromagnetic waves through it.

In Figure 5.18(c), as the monomer content increases the dielectric constant decreases monotonically. The increase in monomer content decreases the density of sintered ceramic due to the formation of large pores during binder burnout. Thus an increase in the monomer content will lower the density and dielectric properties of ceramics. In Figure 5.18(d), it can be observed that the dielectric constant increases as the ratio of monomers increase from 3 to 5. This increase is due to the higher binding effect between the ceramic particles that leads to low pores. Further the dielectric constant decreases as the monomer ratio increases from 5 to 7, due to the excessive binding effect, agglomeration of ceramic particles takes place followed by the formation of micro cracks. The interaction effects of Si_3N_4 content and ratio of monomers on dielectric constant can be seen in Figure 5.18(e).

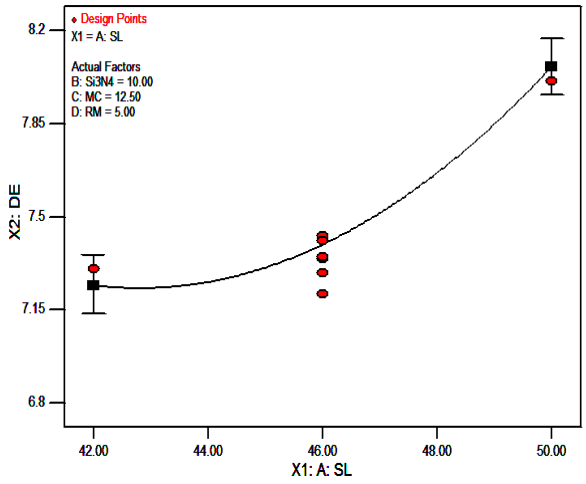

Figure 5.18(a). Effect of SL on DE.

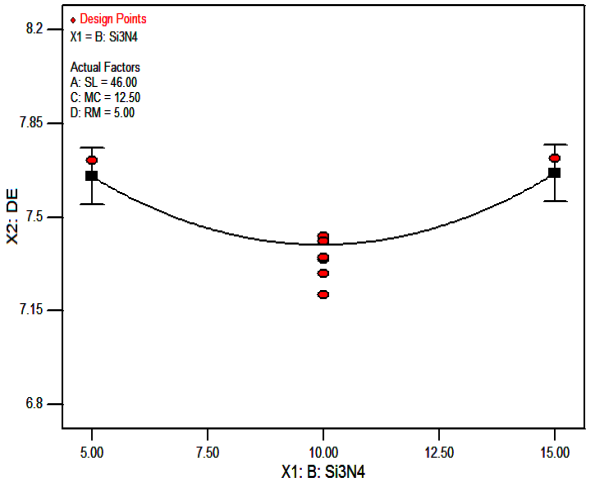

Figure 5.18(b). Effects of Si_3N_4 on DE.

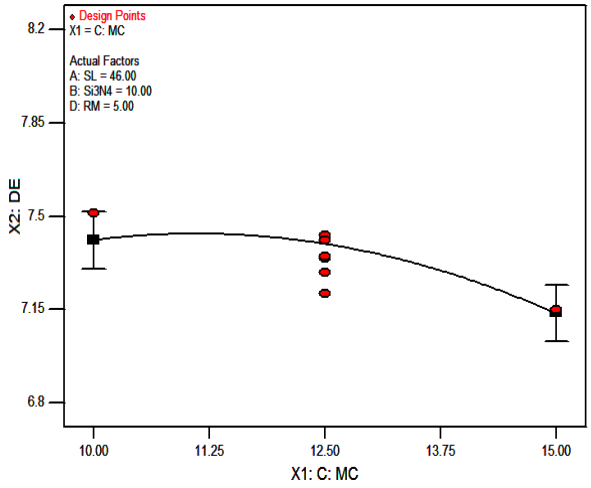

Figure 5.18(c). Effect of MC on DE.

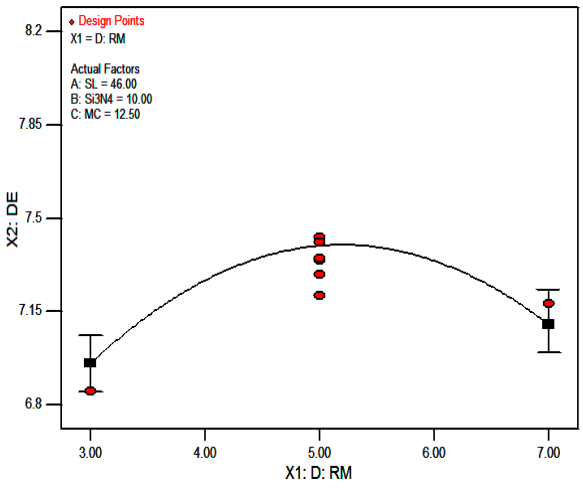

Figure 5.18(d). Effect of RM on DE.

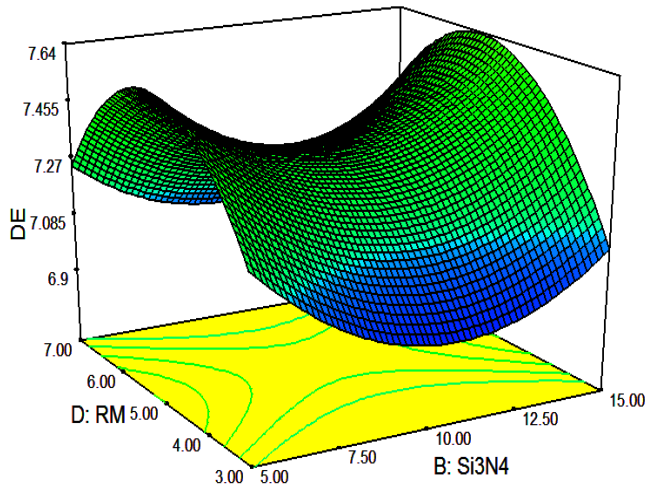

Figure 5.18(e). Effect of Si_3N_4 and RM on DE.

Figure 5.18. Effect of process parameters on dielectric constant

5.3.3.1. Optimization of dielectric constant using desirability function

The optimum value of dielectric constant is calculated using desirability function (Refer section 1.8.3) where the user can opt for goal, lower and upper limits of various variables (here A, B, C, and D) as shown in Table 5.20.

Table 5.20. Range of input parameters and dielectric constant for desirability

Name	Goal	Lower Limit	Upper Limit
A-SL (vol %)	maximize	42	50
B-Si_3N_4 content (wt %)	in range	5	15
C-MC (wt %)	in range	10	15
D-RM	in range	3	7
DE	minimize	6.8	8.14

The aim of optimization is to evaluate the best combinational set of inputs for minimization of dielectric constant. This is indicated by the desirability of RSM analysis. The maximum value of dielectric constant is to be chosen for maximum desirability index for various sets of inputs. A set of 10 optimal solutions is derived and tabulated in Table 5.21 for the particular set of input range (Table 5.20). The desirability of dielectric constant is shown in Figures 5.19 as ramp graph. The desirability of each parameter and dielectric constant and combined parameters is shown in Figures 5.20 as a bar graph. The prediction of response to a particular response characteristic is indicated by the dot on each of the ramps. The overall desirability of the dielectric constant is found to be 0.816.

Table 5.21. Optimal solutions for dielectric constant.

Number	SL	Si_3N_4	MC	RM	DE	Desirability
1	48.43	9.84	15	3	7.031	0.816
2	48.51	9.89	15	3	7.045	0.815
3	48.26	9.29	15	3	7.005	0.814
4	47.95	9.29	15	3	6.953	0.812
5	47.66	9.24	15	3	6.907	0.807
6	47.98	8.53	15	3	6.975	0.806
7	48.26	9.53	15	3.08	7.034	0.804
8	49.09	10.87	15	3	7.165	0.803
9	47.87	7.98	15	3	6.978	0.798
10	48.1	11.28	14.77	3.01	7.027	0.796

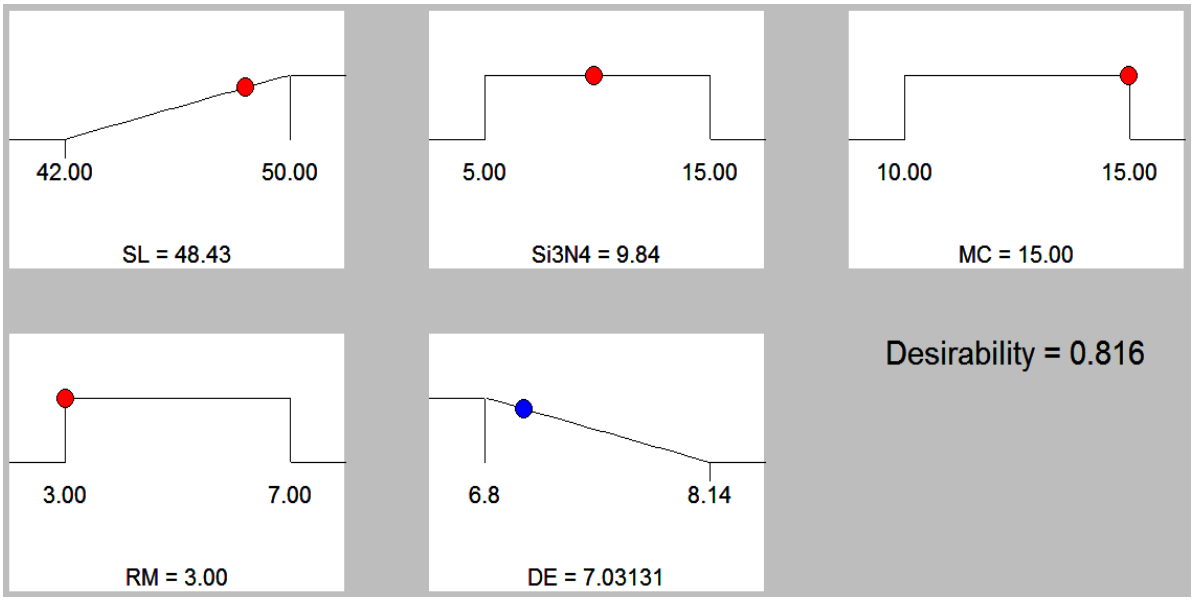

Figure 5.19. Ramp graph of desirability function for dielectric constant of SiO_2–Si_3N_4 ceramic composite.

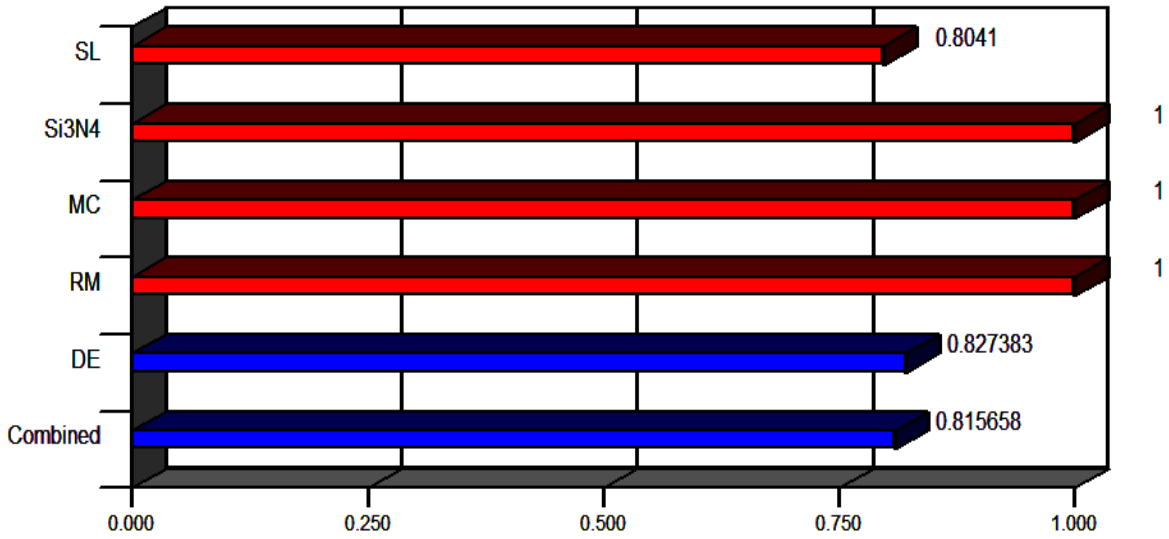

Figure 5.20. Bar graph of desirability function for dielectric constant.

5.3.4. Multi-response optimization using desirability function

Multi-response optimization using desirability function was carried out in combination with response surface methodology to surmount the difficulty of inconsistent responses of single response optimization. The range and goals of input parameters i.e. solid loading, monomer content, and ratio of monomers and the responses i.e. flexural strength, porosity and dielectric constant are given in Table 5.22.

Table 5.22. Range of input parameters and responses for desirability

Name	Goal	Lower Limit	Upper Limit
A-SL (vol %)	maximize	42	50
B-Si_3N_4 content (wt %)	in range	5	15
C-MC (wt %)	is in range	10	15
D-RM	is in range	3	7
FS (MPa)	maximize	56.19	95.12
Por. (%)	maximize	31.95	41.28
DE	minimize	6.8	8.14

The aim of optimization is to evaluate the best set of inputs for maximization of flexural strength and porosity, and minimization of dielectric constant. This is indicated by the desirability of RSM analysis. The optimum value of responses is to be chosen for maximum desirability index for various sets of inputs. A set of 10 optimal solutions is derived and tabulated in Table 5.23 for the particular set of input range (Table 5.22). The desirability of output responses i.e. flexural strength, porosity and dielectric constant is shown in Figures 5.21 as ramp graph. The desirability of each parameter and each response and combined parameters are shown in Figures 5.22 as a bar graph. The overall desirability of the responses is found to be 0.803.

Table 5.23. Set of optimal solutions for SiO_2–Si_3N_4 ceramic composite.

Number	SL	Si_3N_4	MC	RM	FS	Por.	DE	Desirability
1	47.95	10.43	15	3	86.173	39.767	6.949	0.808
2	47.95	10.33	15	3	86.107	39.777	6.948	0.808
3	47.91	10.34	14.97	3	85.998	39.780	6.947	0.806
4	47.93	11.12	15	3	86.580	39.670	6.957	0.806
5	47.92	11.26	15	3	86.644	39.649	6.958	0.806
6	47.82	11.37	15	3	86.493	39.705	6.944	0.805
7	47.86	9.29	15	3	85.233	39.866	6.938	0.803
8	47.65	10.47	15	3.06	85.627	39.862	6.927	0.800
9	47.38	9.3	14.86	3	83.894	40.101	6.887	0.791
10	47.27	12.51	15	3	85.994	39.763	6.907	0.790

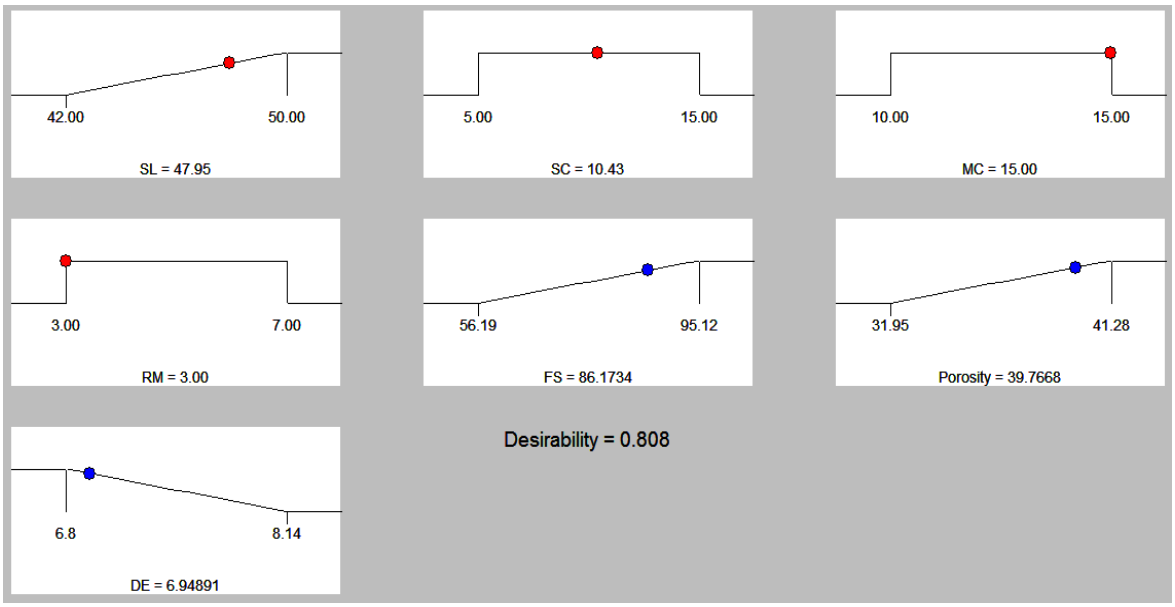

Figure 5.21. Ramp graphs of desirability function for SiO_2–Si_3N_4 ceramic composite.

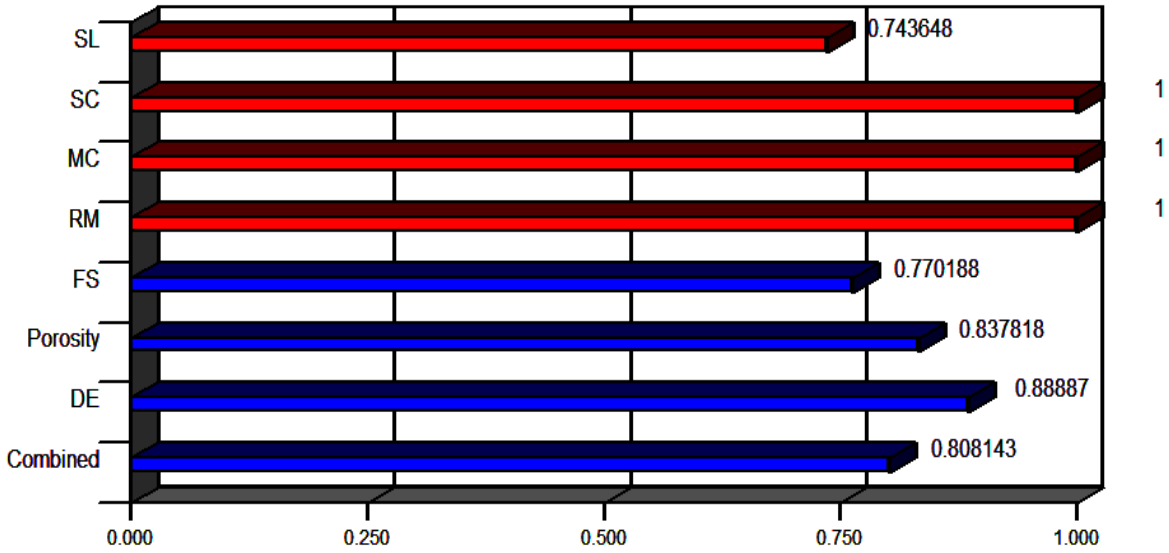

Figure 5.22. Bar graphs of desirability function for SiO_2–Si_3N_4 ceramic composite.

5.3.5. Confirmation tests

The values of responses i.e. flexural strength, porosity and dielectric constant obtained by experimental runs are compared with predicted regression models for flexural strength, porosity and dielectric constant for SiO_2–Si_3N_4 ceramic composite. The error between experimental and predicted values is predicted in Table 5.24 for all responses. It is found that a maximum error of ±3.10% in flexural strength, ±3.03% in porosity and ±3.05% in dielectric constant existing. Hence it can be declared that the predicted models are confirming with

experimental values. Hence the tests are confirmed and recommended that the models are accurate.

Table 5.24. Error between experimental and predicted values

Run order	SL (vol %)	Si_3N_4 (wt %)	MC (wt %)	RM	Flexural Strength (MPa)			Porosity (%)			Dielectric Constant (K)		
					Expt.	Pred.	Error	Expt.	Pred.	Error	Expt.	Pred.	Error
1	42	5	10	3	56.19	54.98	2.15	37.53	37.71	-0.48	7.22	7.20	0.21
2	46	10	12.5	7	83.16	81.06	2.53	37.18	37.98	-2.15	7.32	7.10	3.06
3	50	15	10	3	92.66	92.24	0.46	32.61	32.09	1.59	7.81	7.78	0.37
4	42	15	10	3	67.89	67.35	0.79	38.41	38.58	-0.45	6.95	6.96	-0.11
5	46	5	12.5	5	75.02	76.46	-1.92	34.16	35.20	-3.04	7.71	7.65	0.78
6	42	5	15	3	58.13	59.49	-2.34	40.36	40.32	0.09	6.82	6.79	0.39
7	42	15	15	7	70.69	71.37	-0.97	38.94	38.46	1.24	6.89	6.95	-0.90
8	46	10	12.5	5	82.67	80.59	2.51	37.67	37.05	1.64	7.29	7.39	-1.40
9	46	10	12.5	3	76.15	78.32	-2.85	39.82	39.36	1.16	6.85	6.95	-1.49
10	42	15	15	3	69.15	68.95	0.29	41.28	41.20	0.20	6.80	6.79	0.20
11	46	15	12.5	5	85.16	84.79	0.44	35.87	35.17	1.96	7.72	7.66	0.80
12	50	5	15	7	89.36	90.22	-0.97	35.13	34.38	2.13	7.76	7.77	-0.14
13	50	15	15	7	93.88	94.50	-0.66	33.15	33.45	-0.90	7.81	7.78	0.44
14	46	10	12.5	5	80.98	80.59	0.48	36.59	37.05	-1.27	7.35	7.39	-0.58
15	50	15	10	7	95.12	94.09	1.09	31.95	32.07	-0.39	8.14	8.17	-0.41

Run order	SL (vol %)	Si_3N_4 (wt %)	MC (wt %)	RM	Flexural Strength (MPa)			Porosity (%)			Dielectric Constant (K)		
					Expt.	Pred.	Error	Expt.	Pred.	Error	Expt.	Pred.	Error
16	46	10	13	5	82.59	80.59	2.42	36.48	37.05	-1.57	7.41	7.39	0.24
17	46	10	13	5	78.26	80.59	-2.98	37.92	37.05	2.28	7.34	7.39	-0.71
18	50	5	10	3	84.22	83.86	0.43	32.55	33.03	-1.46	8.03	8.03	0.03
19	42	15	10	7	68.12	69.35	-1.81	37.23	37.98	-2.00	7.33	7.35	-0.28
20	46	10	15	5	84.38	83.02	1.61	37.95	38.31	-0.95	7.15	7.13	0.26
21	46	10	10	5	78.13	80.56	-3.11	36.34	36.32	0.07	7.51	7.41	1.37
22	50	5	10	7	87.29	86.90	0.45	33.11	33.01	0.31	7.91	7.89	0.22
23	50	5	15	3	88.59	86.76	2.06	36.71	36.53	0.48	7.63	7.62	0.17
24	50	10	13	5	87.26	89.78	-2.89	33.58	33.77	-0.56	8.01	8.06	-0.63
25	46	10	13	5	78.19	80.59	-3.08	37.16	37.05	0.29	7.43	7.39	0.51
26	46	10	13	5	81.09	80.59	0.61	37.55	37.05	1.32	7.21	7.39	-2.53
27	50	15	15	3	92.19	92.22	-0.04	35.18	35.60	-1.19	7.64	7.61	0.40
28	42	10	13	5	65.23	63.78	2.23	38.47	38.62	-0.38	7.41	7.24	2.33
29	42	5	10	7	57.88	58.17	-0.50	38.19	37.10	2.85	6.99	7.07	-1.13
30	42	5	15	7	63.27	63.10	0.27	37.16	37.58	-1.14	6.92	6.95	-0.40

5.4. Results and analysis of SiO_2–BN ceramic composites

5.4.1. Regression model for flexural strength

A regression model for flexural strength of SiO_2–BN ceramic composite is fitted using the experimental results (Table 4.11). ANOVA has been applied on the experimental results for flexural strength and the ANOVA results are given in Table 5.25.

Table 5.25. ANOVA results for flexural strength.

Source	Sum of Squares	df	Mean Square	F Value	p-value Prob > F	Percentage Contribution
Model	3541.214	8	258.9827	44.74187	< 0.0001	97.607
A-SL	3132.890	1	3132.889	541.2381	< 0.0001	86.352
B-BN	273.156	1	273.1564	47.19051	< 0.0001	7.529
C-MC	23.165	1	23.16536	4.002048	0.0639	0.639
D-RM	56.463	1	56.46302	9.754555	0.0070	1.556
AB	21.091	1	21.09106	3.643692	0.0756	0.581
BC	9.136	1	9.135506	1.578251	0.2282	0.252
A^2	13.086	1	13.08581	2.260706	0.1535	0.361
D^2	12.227	1	12.22698	2.112333	0.1667	0.337
Residual	86.826	21	5.788375			2.393
Cor Total	3628.039	29				100.00
R-Square: 97.66%		Adjusted R-square: 95.47%			Predicted R-square: 93.02%	

Where A is solid loading (SL), B is BN content, C is monomer content (MC), D is ratio of monomers (RM)

From above results, it has been observed that SL, BN, and RM, are significant model terms, and the response of each are shown in the Figures 5.23(a), (b) and (c) respectively. The regression model generated for flexural strength is given in Eqn. 5.7, in the coded form.

$$FS = 63.16 + 13.19A + 3.90B + 1.13C + 1.77D - 1.15AB - 0.76BC - 2.25A^2 - 2.17D^2 \quad (5.7)$$

From Figure 5.23(a) and (b), it is observed that flexural strength increases with solid loading and BN content. Micro-cracks occur in green bodies when the solid loading is less.

This may be due to the increase of drying and sintering shrinkages as the space between any two particles in the slurry is huge. During sintering the density of the composite decreases at a lower solid loading and BN content. Therefore, the flexural strength of porous SiO_2–BN sintered ceramic composite is low at lower solids loading and increases with the solid loading. In Figure 5.23(c), it can be observed that the flexural strength increases as the ratio of monomers increase from 3 to 5. This increase is due to the higher binding effect between the ceramic particles that leads to higher density in the ceramic composite. Further, the flexural strength decreases as the monomer ratio increases from 5 to 7, due to the excessive binding effect, agglomeration of ceramic particles takes place followed by the formation of micro cracks.

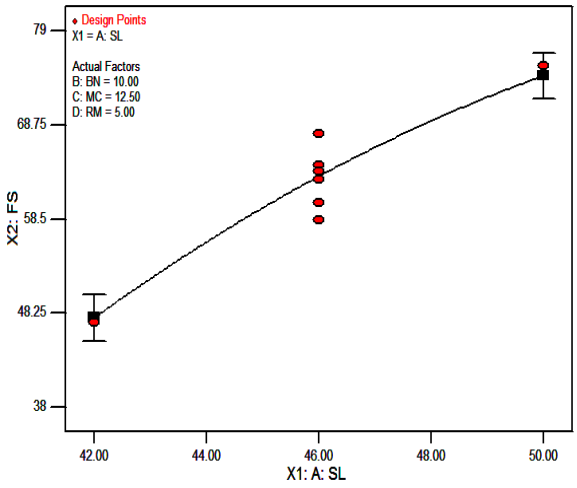

Figure 5.23(a). Effect of SL on FS.

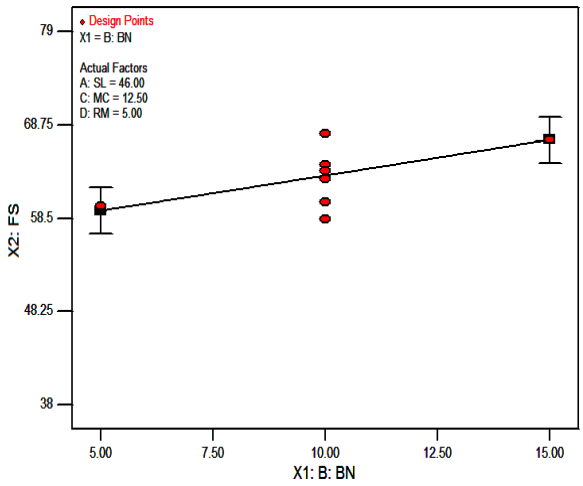

Figure 5.23(b). Effect of BN on FS.

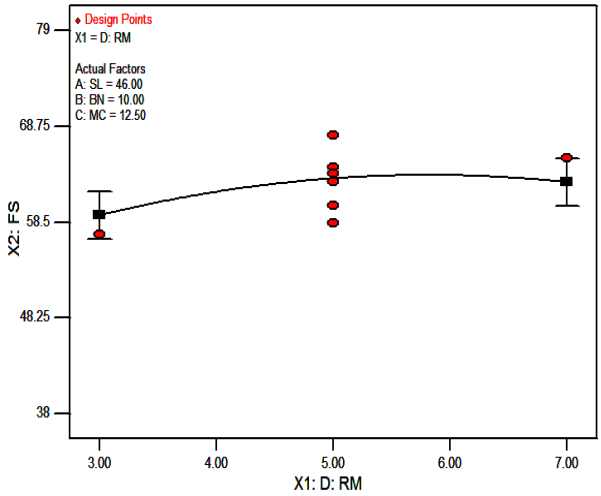

Figure 5.23(c). Effect of RM on FS.

Figure 5.23. Effect of process parameters on flexural strength

5.4.1.1. Optimization of flexural strength using desirability function

The optimum value of flexural strength is calculated using desirability function (Refer section 1.8.3) where the user can opt for goal, lower and upper limits of various variables (here A, B, C, and D) as shown in Table 5.26.

Table 5.26. The range of input parameters and flexural strength for desirability.

Name	Goal	Lower Limit	Upper Limit
A-SL (vol %)	maximize	42	50
B-BN content (wt %)	in range	5	15
C-MC (wt %)	in range	10	15
D-RM	in range	3	7
FS (MPa)	maximize	38.11	78.19

The aim of optimization is to evaluate the best combinational set of inputs for maximization of flexural strength. This is indicated by the desirability of RSM analysis. The maximum value of flexural strength is to be chosen for maximum desirability index for various sets of inputs. A set of 10 optimal solutions is derived and tabulated in Table 5.27 for the particular set of input range (Table 5.26). The desirability of flexural strength is shown in Figures 5.24 as ramp graph. The desirability of each parameter and flexural strength and combined parameters is shown in Figures 5.25 as a bar graph. The prediction of response to a particular response characteristic is indicated by the dot on each of the ramps. The overall desirability of the flexural strength is found to be 0.995.

Table 5.27. Optimal solutions for flexural strength.

Number	SL	BN	MC	RM	FS	Desirability
1	50	15	14.75	5.99	77.761	0.995
2	50	14.99	15	6.41	77.704	0.994
3	50	15	14.13	5.95	77.626	0.993
4	50	15	15	6.57	77.611	0.993
5	50	15	14.06	6.09	77.602	0.993
6	50	15	15	6.59	77.599	0.993
7	50	14.54	15	5.56	77.551	0.992
8	50	14.97	15	5.2	77.514	0.992
9	50	15	10.1	5.88	77.500	0.991
10	50	15	13.31	5.92	77.492	0.991

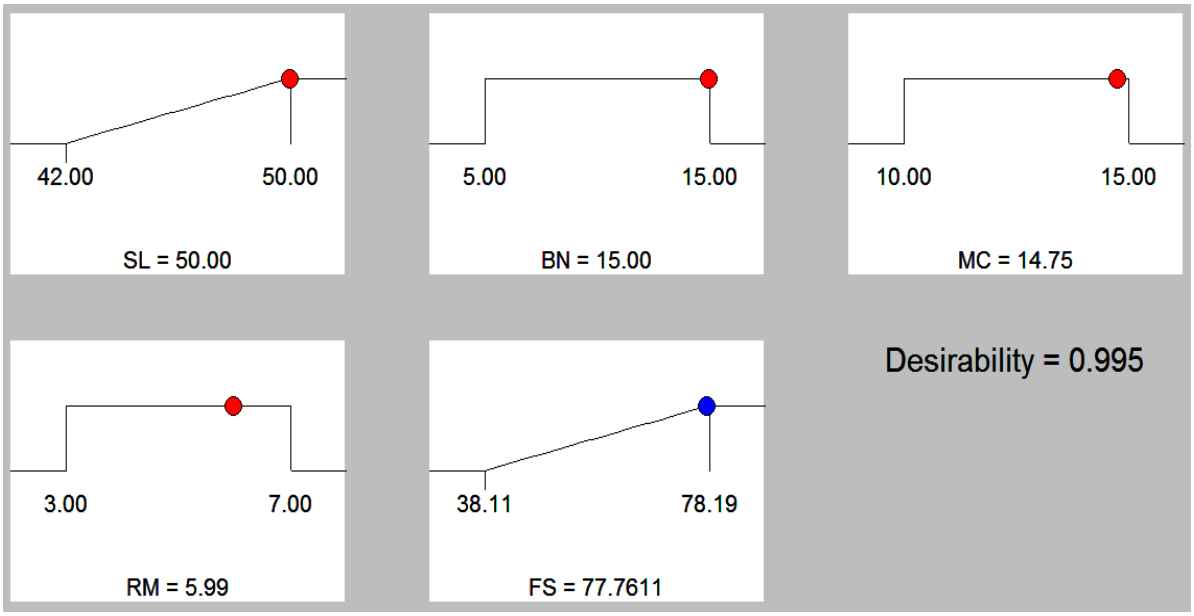

Figure 5.24. Ramp graph of desirability function for flexural strength of SiO_2–BN ceramic composite.

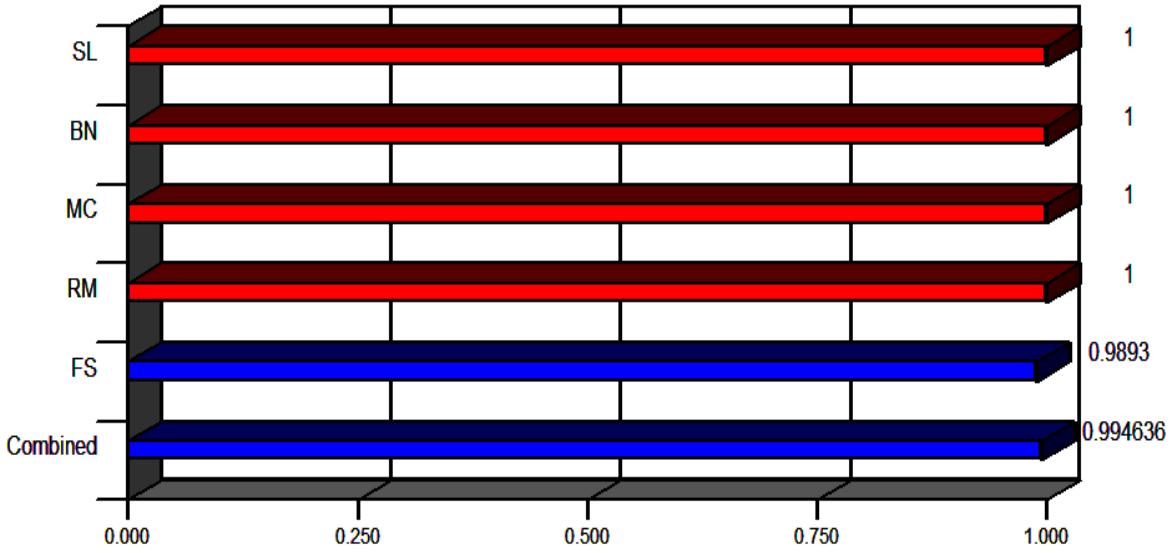

Figure 5.25. Bar graph of desirability function.

5.4.2. Regression model for porosity

A regression model for the porosity of SiO_2–BN ceramic composite is fitted using the experimental results (Table 4.11). ANOVA has been applied on the experimental results for porosity and the ANOVA results are given in Table 5.28.

Table 5.28. ANOVA results for porosity.

Source	Sum of Squares	df	Mean Square	F Value	p-value Prob > F	Percentage Contribution
Model	118.481	14	6.856034	38.8316	< 0.0001	98.387
A-SL	82.112	1	86.81227	491.6924	< 0.0001	68.186
B-BN	0.076	1	0.07605	0.430736	0.5251	0.063
C-MC	4.500	1	4.5	25.48736	0.0004	3.737
D-RM	2.226	1	2.22605	12.60803	0.0045	1.849
AB	1.369	1	1.3689	7.753255	0.0178	1.137
AC	2.205	1	2.205225	12.49008	0.0047	1.831
AD	3.186	1	3.186225	18.04633	0.0014	2.646
BC	5.198	1	5.1984	29.443	0.0002	4.317
BD	0.250	1	0.25	1.415964	0.2591	0.208
CD	0.426	1	0.525625	2.977065	0.1124	0.353
A^2	5.048	1	6.047685	34.25323	0.0001	4.192
B^2	2.580	1	2.579558	14.61025	0.0028	2.142
C^2	1.259	1	1.259384	7.132972	0.0218	1.046
D^2	8.046	1	8.045612	45.5692	< 0.0001	6.681
Residual	1.942	15	0.176558			1.613
Cor Total	120.423	29				100.00
R-Square: 98.45% Adjusted R-square: 95.91% Predicted R-square: 80.45%						

Where A is solid loading (SL), B is BN content, C is monomer content (MC), D is ratio of monomers (RM)

From the above results, it has been observed that SL, MC, RM, interaction of SL and BN, interaction of SL and MC, interaction of SL and RM, interaction of BN and MC, SL^2, BN^2, MC^2, and RM^2, are significant model terms, and the response of each are shown in the Figures 5.26(a), (b), (c), (d), (e), (f), (g) and (h). The regression model generated for porosity was given in Eqn. 5.8, in the coded form.

$$Por. = 21.02 - 2.20A + 0.19B + 0.5C - 1.06D - 0.29AB + 0.37AC - 0.45AD - 0.57BC - 0.12BD - 0.18CD - 1.53A^2 - B^2 + 0.7C^2 + 1.76D^2 \quad (5.8)$$

The porosity of sintered body decreases with the increase of solid loading as shown in Figure 5.26(a). As the solid loading increases, the ceramic particles are tightly packed. This densifies the ceramic composite reducing the pores in the composite. From Figure 5.26(b), it is observed that BN content has a significant effect on the porosity. As the BN content increases there is a rise in the porosity and then declines on further addition of BN powder. The rise in the porosity is due to the loose packing of BN particles in SiO_2 ceramics. As the content of BN powder increases the pores in the composite are reduced that increases the density of the composite causing the lower porosity.

The porosity of sintered body increases with the increase of monomer content as seen in Figure 5.26(c). The pores of sintered body largely initiate from the left over micro-space of the organic polymers in the green body during organic binder burnout. The distribution and intensity of pores depend on the monomer content. In Figure 5.26(d) the porosity decreases initially with the increase of monomers ratio and then rises on further increase in the monomer ratio. The increase in the ratio of monomers to cross-linker sometimes initiates micro-crack propagation that causes higher porosity. The interaction effects of solid loading and BN content, solid loading and monomer content, solid loading and ratio of monomers, and BN content and monomer content can be seen in Figures 5.26(e), (f), (g) and (h).

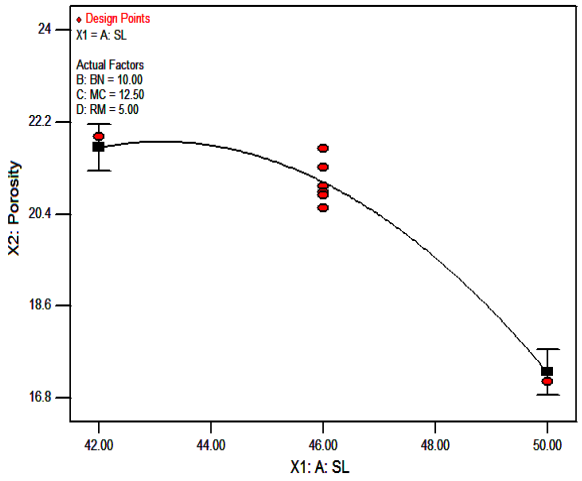

Figure 5.26(a). Effect of SL on porosity.

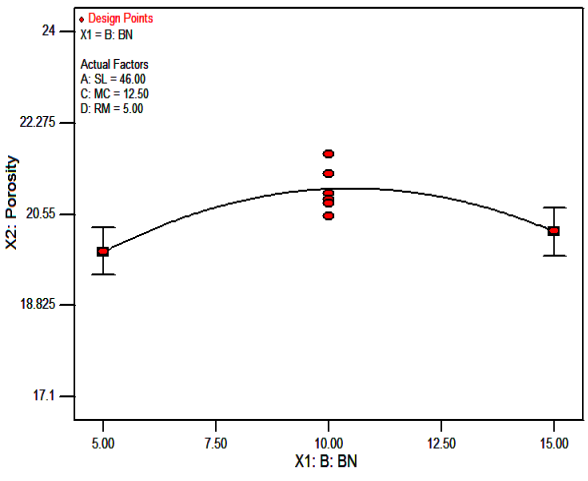

Figure 5.26(b). Effects of BN on porosity.

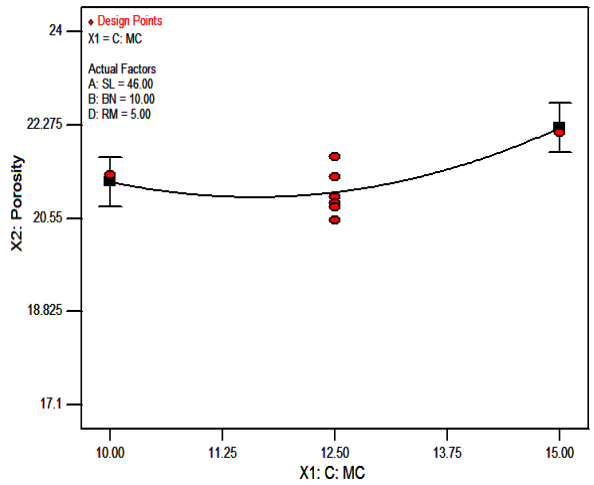

Figure 5.26(c). Effect of MC on porosity.

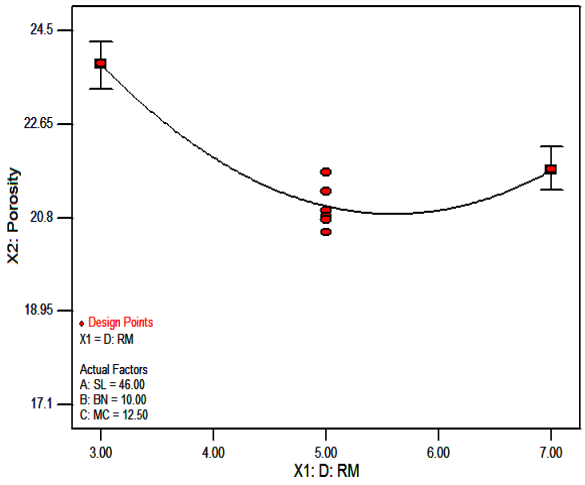

Figure 5.26(d). Effect of RM on porosity.

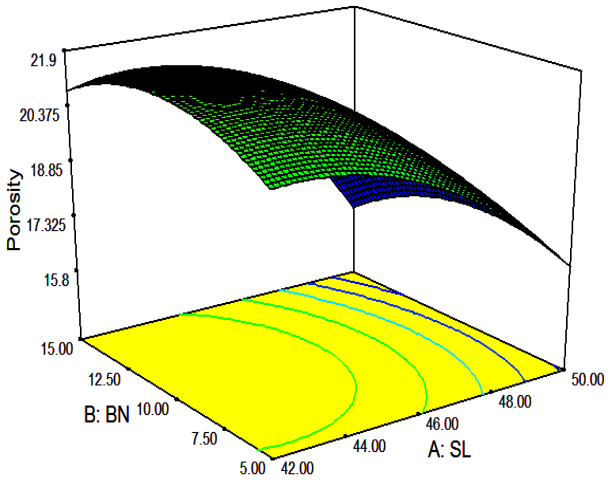

Figure 5.26(e). Effect of SL and BN on porosity.

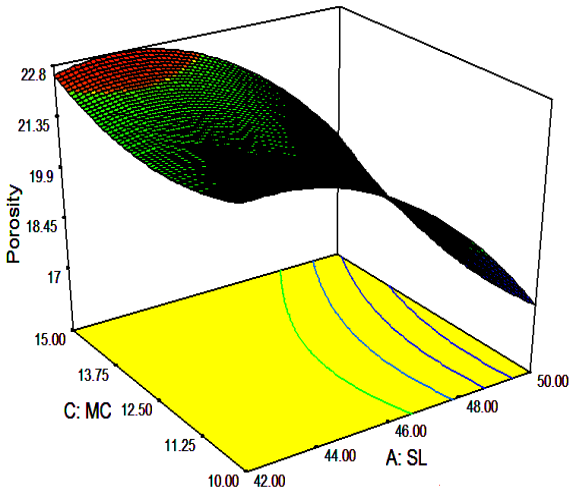

Figure 5.26(f). Effect of SL and MC on porosity.

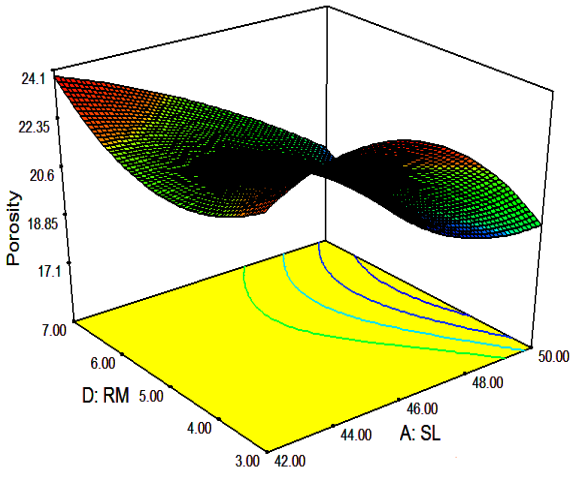

Figure 5.26(g). Effect of SL and RM on porosity.

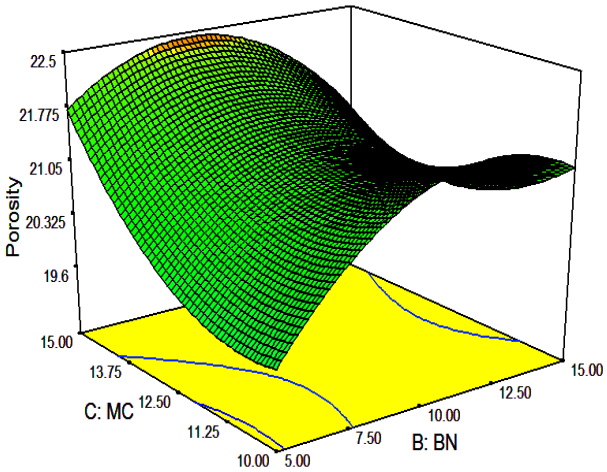

Figure 5.26(h). Effect of BN and MC on porosity.

Figure 5.26. Effect of process parameters on porosity

5.4.2.1. Optimization of porosity using desirability function

The optimum value of porosity is calculated using desirability function (Refer section 1.8.3) where the user can opt for goal, lower and upper limits of various variables (here A, B, C, and D) as shown in Table 5.29.

Table 5.29. Range of input parameters and porosity for desirability

Name	Goal	Lower Limit	Upper Limit
A-SL (vol %)	maximize	42	50
B-BN content (wt %)	in range	5	15
C-MC (wt %)	in range	10	15
D-RM	in range	3	7
Por. (%)	maximize	17.12	23.99

The aim of optimization is to evaluate the best combinational set of inputs for maximization of porosity. This is indicated by the desirability of RSM analysis. The maximum value of porosity is to be chosen for maximum desirability index for various sets of inputs. A set of 10 optimal solutions is derived and tabulated in Table 5.30 for the particular set of input range (Table 5.29). The desirability of porosity is shown in Figures 5.27 as ramp graph. The desirability of each parameter and porosity and combined parameters is shown in Figures 5.28 as a bar graph. The prediction of response to a particular response characteristic is indicated by the dot on each of the ramps. The overall desirability of the porosity is found to be 0.869.

Table 5.30. Optimal solutions for porosity.

Number	SL	BN	MC	RM	Por.	Desirability
1	48.29	8.11	15	3	23.715	0.869
2	48.3	8.15	15	3	23.712	0.869
3	48.32	7.97	15	3	23.689	0.869
4	48.27	7.78	15	3	23.732	0.869
5	48.3	8.88	15	3	23.692	0.868
6	48.33	8.27	15	3.01	23.648	0.867
7	48.07	9.57	15	3	23.869	0.863
8	48.3	10.43	15	3	23.503	0.855
9	47.35	12.17	15	3	23.988	0.818
10	48.18	12.93	15	3	22.931	0.808

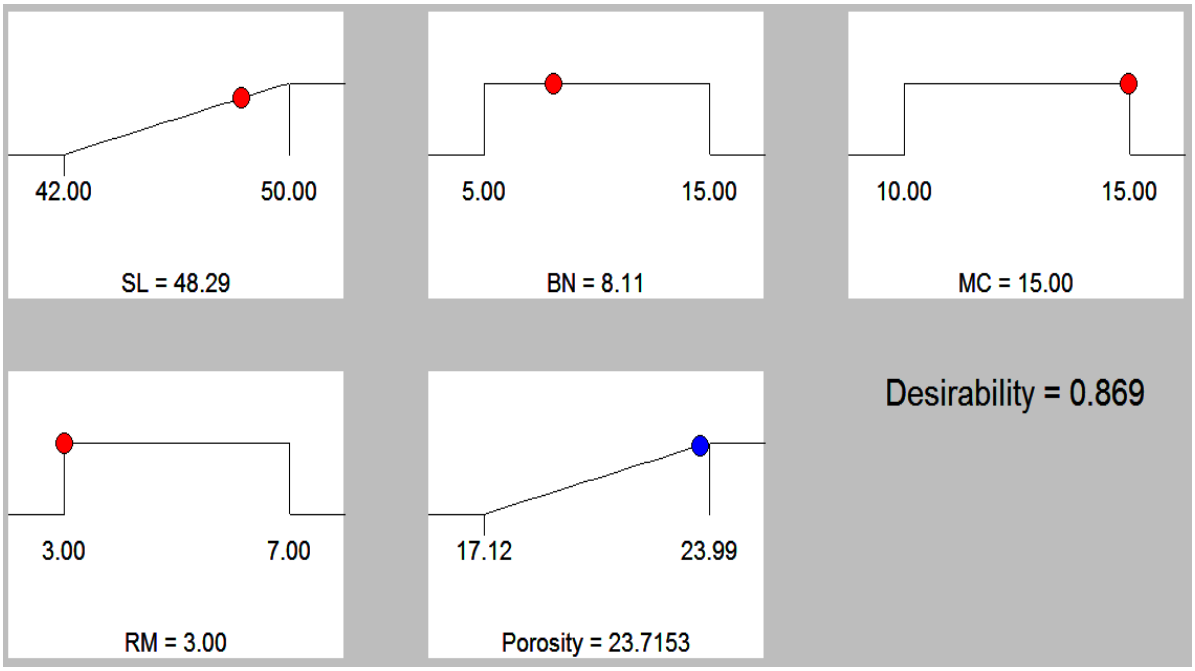

Figure 5.27. Ramp graph of desirability function for the porosity of SiO_2–BN ceramic composite.

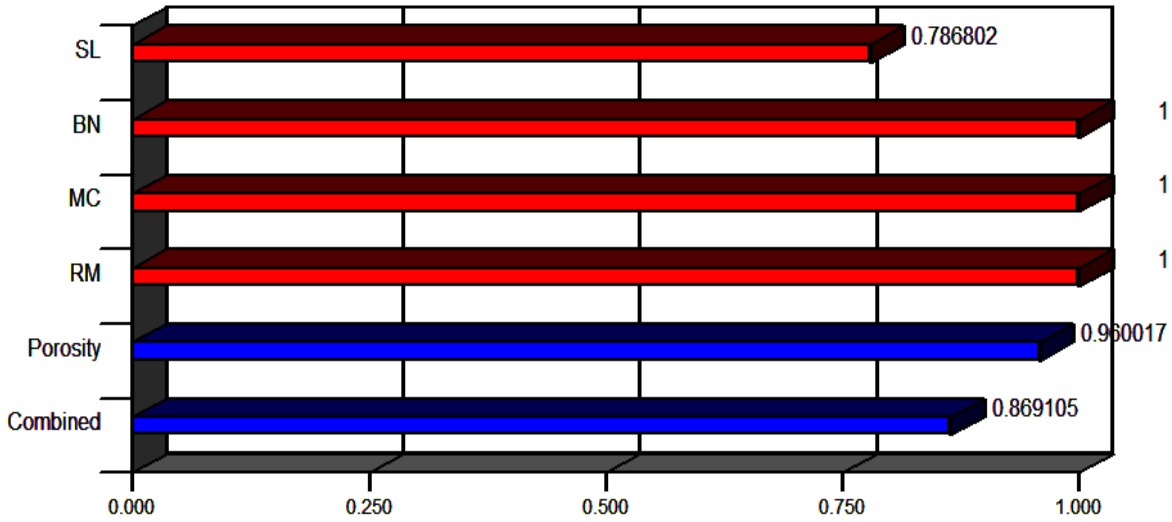

Figure 5.28. Bar graph of desirability function for porosity.

5.4.3. Regression model for dielectric constant

A regression model for dielectric constant of SiO_2–BN ceramic composite is fitted using the experimental results (Table 4.11). ANOVA has been applied on the experimental results for dielectric constant and the ANOVA results are given in Table 5.31.

Table 5.31. ANOVA results for dielectric constant

Source	Sum of Squares	df	Mean Square	F Value	p-value Prob > F	Percentage Contribution
Model	2.788	12	0.23396	23.59431	< 0.0001	94.299
A-SL	2.094	1	2.18405	220.2558	< 0.0001	70.826
B-BN	0.007	1	0.006806	0.686323	0.4189	0.230
C-MC	0.019	1	0.019339	1.950277	0.1805	0.654
D-RM	0.001	1	0.000556	0.056026	0.8157	0.019
AB	0.006	1	0.0064	0.645423	0.4328	0.216
AC	0.096	1	0.0961	9.691437	0.0063	3.250
AD	0.050	1	0.060025	6.053366	0.0249	1.692
BC	0.023	1	0.0225	2.269067	0.1503	0.761
A^2	0.146	1	0.146089	14.73275	0.0013	4.941
B^2	0.134	1	0.134044	13.518	0.0019	4.534
C^2	0.081	1	0.086335	8.706657	0.0089	2.751
D^2	0.131	1	0.158766	16.0111	0.0009	4.423
Residual	0.169	17	0.009916			5.701
Cor Total	2.957	29				100.00

R-Square: 94.34% Adjusted R-square: 90.34% Predicted R-square: 80.6%

Where A is solid loading (SL), B is BN content, C is monomer content (MC), D is ratio of monomers (RM)

From the above results, it has been observed that SL, MC, RM, SL^2, BN^2, MC^2, RM^2, interactions of SL and MC, and interactions of SL and RM are significant model terms, and the response of each are shown in the Figures 5.29(a), (b), (c), (d), (e) and (f). The regression model generated for dielectric constant was given in Eqn. 5.9, in the coded form.

$$DE = 4.62 + 0.35A - 0.019B - 0.033C + 5.556\times10^{-3}D - 0.02AB - 0.077AC + 0.061AD + 0.038BC + 0.24A^2 + 0.23B^2 - 0.18C^2 - 0.25D^2 \quad (5.9)$$

As shown in Figure 5.29(a), with the increase in solid loading, density of SiO_2 – BN ceramic composite increases that will lead to the reduction of pores that causes the increase of

dielectric constant. It can be seen in Figure 5.29(b) that the dielectric constant initially decreases from 5 wt% to 10 wt% of BN content due to the increase in the surface area of pores. On further increasing the BN content from 10 wt% to 15 wt% there is a rise in the dielectric constant due to the increase in the density of the ceramic composite that lowers the transfer of electromagnetic waves through it. In Figure 5.29(c), as the monomer content increases the dielectric constant increases and reaches a maximum point and then decreases. The increase in monomer content decreases the density of sintered ceramic composite due to the formation of large pores during binder burnout. Thus an increase in the monomer content will lower the density and dielectric properties of ceramics. Few of the pores may be replaced by the BN ceramic particles causing an increase in the dielectric constant at monomer content of 12.5 wt%.

In Figure 5.29(d), it can be observed that the dielectric constant increases as the ratio of monomers increase from 3 to 5. This increase is due to the higher binding effect between the ceramic particles that leads to low pores. Further the dielectric constant decreases as the monomer ratio increases from 5 to 7, due to the excessive binding effect, agglomeration of ceramic particles takes place followed by the formation of micro cracks. The interaction effects of solid loading and monomer content and solid loading and ratio of monomers on dielectric constant can be seen in Figures 5.29(e) and (f).

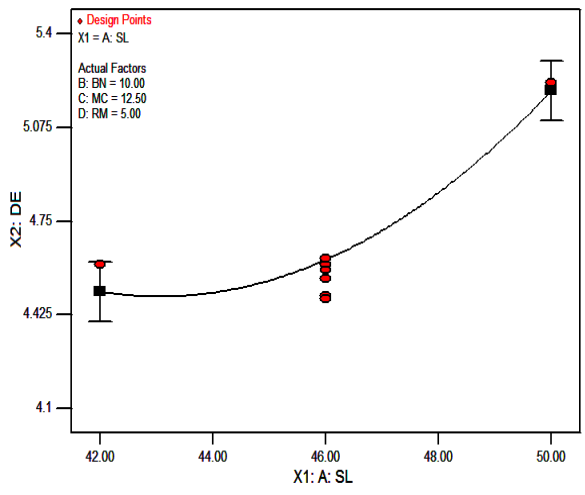

Figure 5.29(a). Effect of SL on DE.

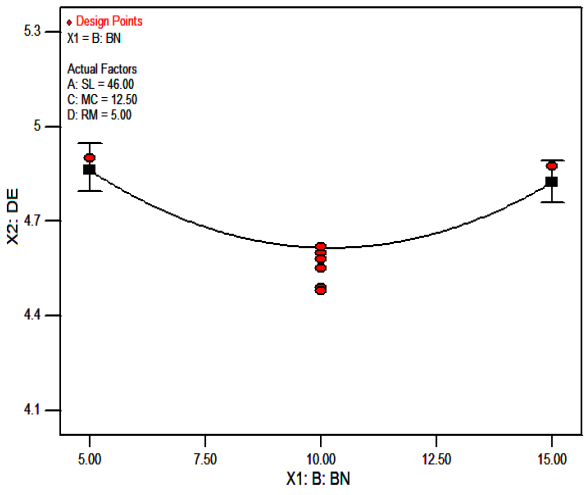

Figure 5.29(b). Effects of BN on DE.

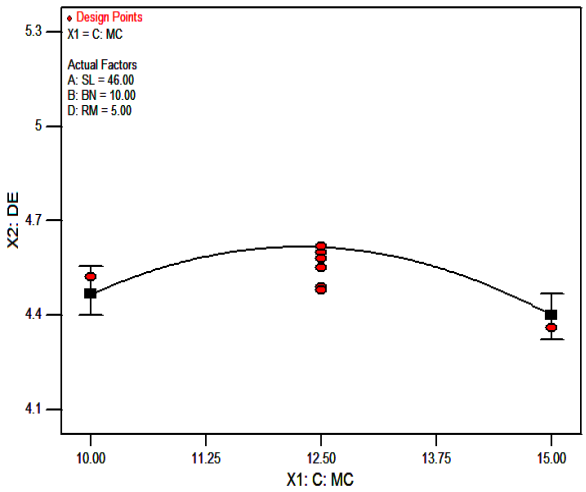

Figure 5.29(c). Effect of MC on DE.

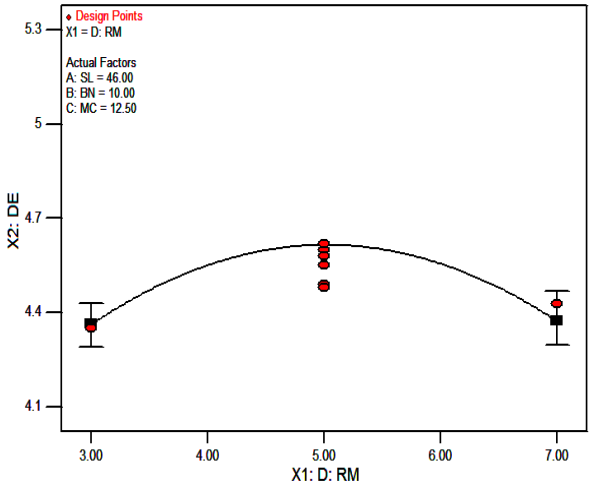

Figure 5.29(d). Effect of RM on DE.

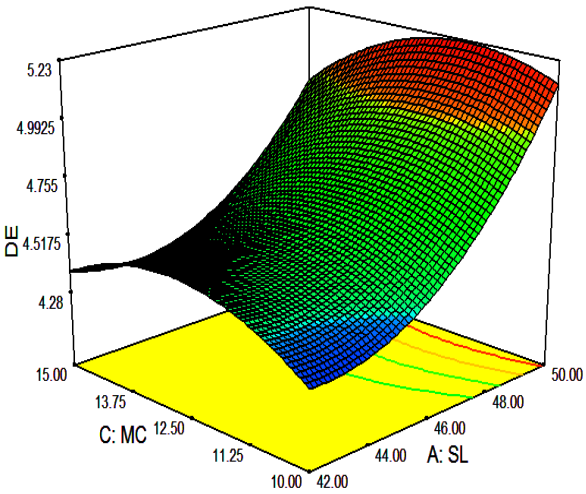

Figure 5.29(e). Effect of SL and MC on DE.

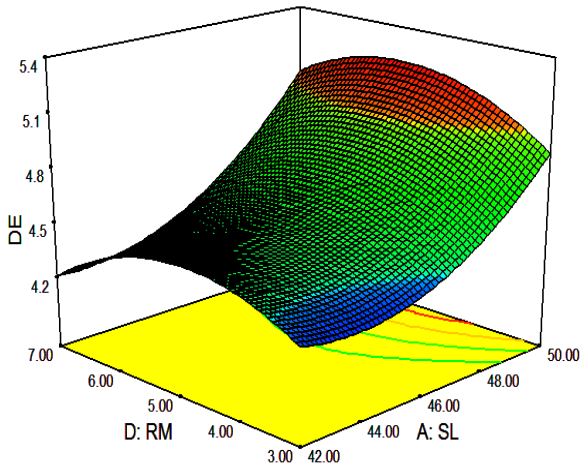

Figure 5.29(f). Effect of SL and RM on DE.

Figure 5.29. Effect of process parameters on dielectric constant.

5.4.3.1. Optimization of dielectric constant using desirability function

The optimum value of dielectric constant is calculated using desirability function (Refer section 1.8.3) where the user can opt for goal, lower and upper limits of various variables (here A, B, C, and D) as shown in Table 5.32.

Table 5.32. The range of input parameters and dielectric constant for desirability.

Name	Goal	Lower Limit	Upper Limit
A-SL (vol %)	maximize	42	50
B-BN content (wt %)	in range	5	15
C-MC (wt %)	in range	10	15
D-RM	in range	3	7
DE	minimize	4.12	5.23

The aim of optimization is to evaluate the best combinational set of inputs for minimization of dielectric constant. This is indicated by the desirability of RSM analysis. The maximum value of dielectric constant is to be chosen for maximum desirability index for various sets of inputs. A set of 10 optimal solutions is derived and tabulated in Table 5.33 for the particular set of input range (Table 5.32). The desirability of dielectric constant is shown in Figures 5.30 as ramp graph. The desirability of each parameter and dielectric constant and combined parameters is shown in Figures 5.31 as a bar graph. The prediction of response to a particular response characteristic is indicated by the dot on each of the ramps. The overall desirability of the dielectric constant is found to be 0.793.

Table 5.33. Optimal solutions for dielectric constant.

Number	SL	BN	MC	RM	DE	Desirability
1	48.46	10	15	3	4.366	0.793
2	48.6	10.14	15	3	4.385	0.793
3	48.28	9.37	15	3	4.343	0.792
4	48.85	10.09	15	3	4.418	0.792
5	48.39	10.35	15	3	4.360	0.791
6	47.89	8.5	15	3	4.312	0.781
7	49.13	7.74	15	3	4.488	0.772
8	47.99	9.68	15	7	4.382	0.757
9	48.02	9.79	15	7	4.386	0.757
10	47.98	9.88	15	7	4.380	0.757

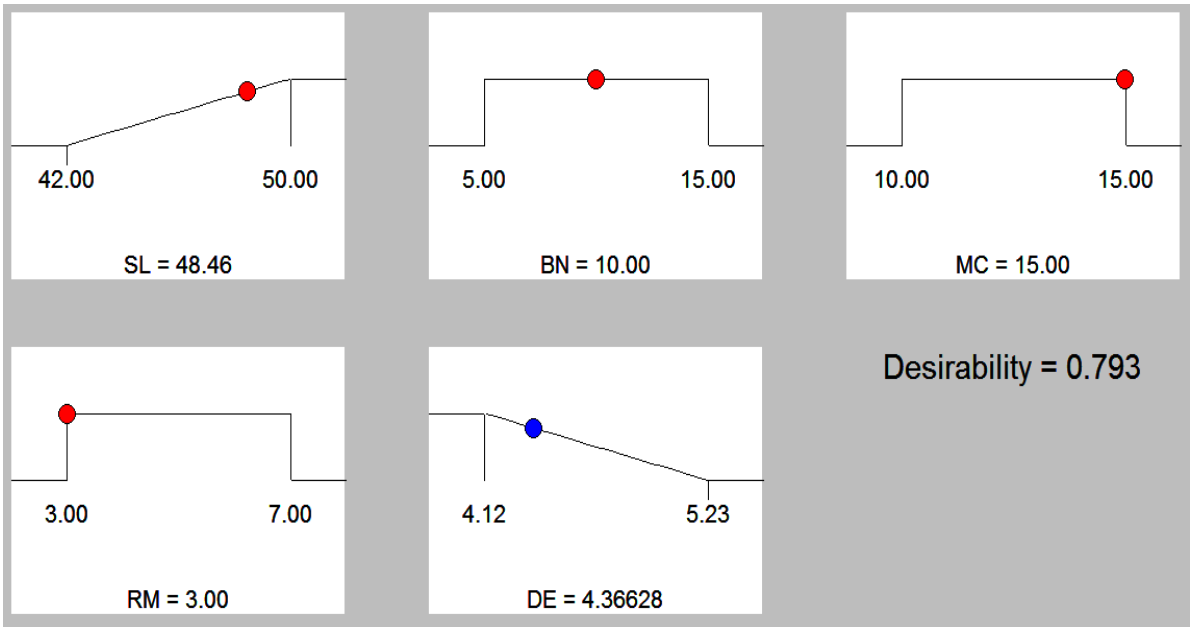

Figure 5.30. Ramp graph of desirability function for dielectric constant of SiO2 – BN ceramic composite.

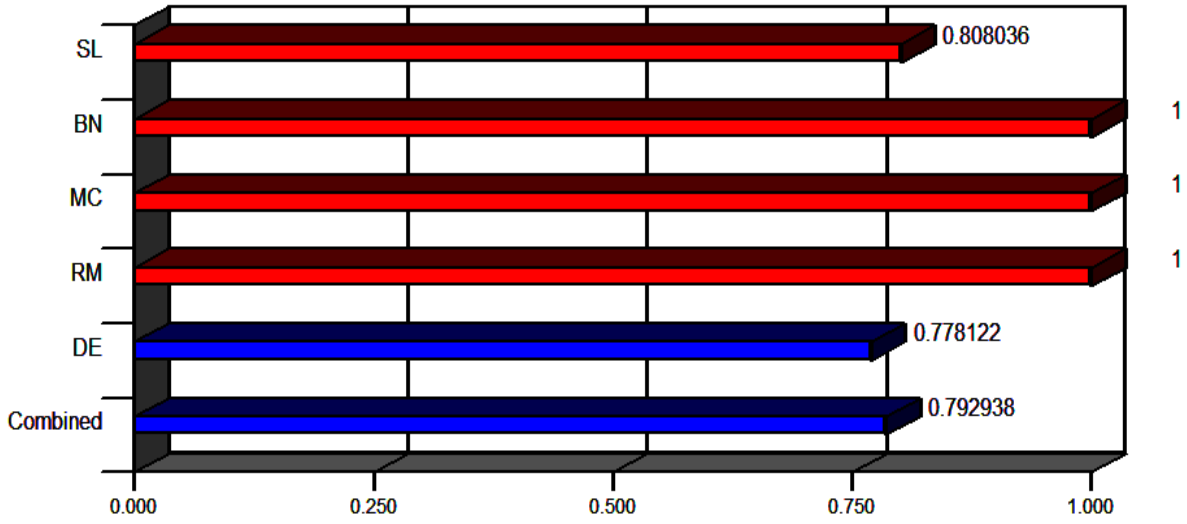

Figure 5.31. Bar graph of desirability function for dielectric constant.

5.4.4. Multi-response optimization using desirability function

Multi-response optimization using desirability function was carried out in combination with response surface methodology to surmount the difficulty of inconsistent responses of single response optimization. The range and goals of input parameters i.e. solid loading, monomer content, and ratio of monomers and the responses i.e. flexural strength, porosity and dielectric constant are given in Table 5.34.

Table 5.34. The range of input parameters and responses for desirability.

Name	Goal	Lower Limit	Upper Limit
A-SL (vol %)	maximize	42	50
B-BN content (wt %)	in range	5	15
C-MC (wt %)	is in range	10	15
D-RM	is in range	3	7
FS (MPa)	maximize	38.11	78.19
Por. (%)	maximize	17.12	23.99
DE	minimize	4.12	5.23

The aim of optimization is to evaluate the best combinational set of inputs for maximization of flexural strength and porosity, and minimization of dielectric constant. This is indicated by the desirability of RSM analysis. The optimum value of responses is to be chosen for maximum desirability index for various sets of inputs. A set of 10 optimal solutions is derived and tabulated in Table 5.35 for the particular set of input range (Table 5.34). The desirability of output responses i.e. flexural strength, porosity and dielectric constant is shown in Figures 5.32 as ramp graph. The desirability of each parameter and each response and combined parameters are shown in Figures 5.33 as a bar graph. The overall desirability of the responses is found to be 0.812.

Table 5.35. Set of optimal solutions for SiO_2–BN ceramic composite.

Number	SL	BN	MC	RM	FS	Por.	DE	Desirability
1	47.97	9.68	15	3	66.301	23.958	4.307	0.812
2	47.95	9.75	15	3	66.301	23.961	4.305	0.812
3	47.96	9.49	15	3	66.184	23.988	4.306	0.812
4	48.06	9.89	15	3	66.643	23.841	4.317	0.812
5	48.17	9.41	15	3	66.714	23.782	4.330	0.811
6	47.92	9.9	15	3.01	66.313	23.956	4.304	0.811
7	47.95	8.8	15	3.02	65.901	23.989	4.318	0.807
8	47.72	11.62	15	3	66.598	23.822	4.314	0.800
9	47.01	10.55	15	3	64.085	24.626	4.220	0.779
10	48.23	13.52	15	3	68.799	22.630	4.472	0.756

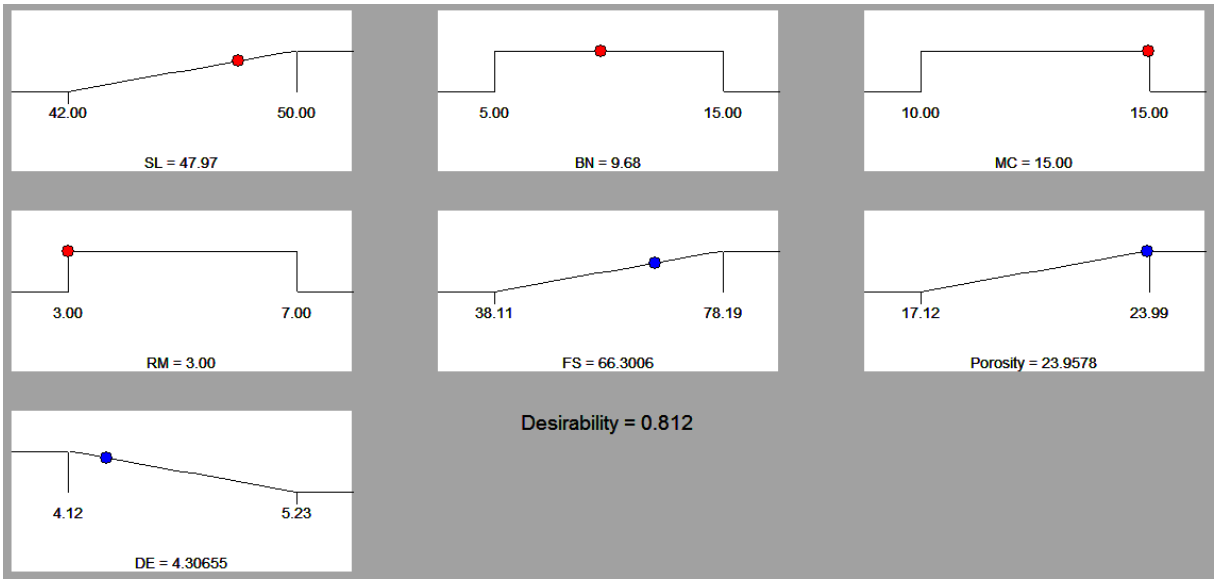

Figure 5.32. Ramp graphs of desirability function for SiO_2–BN ceramic composite.

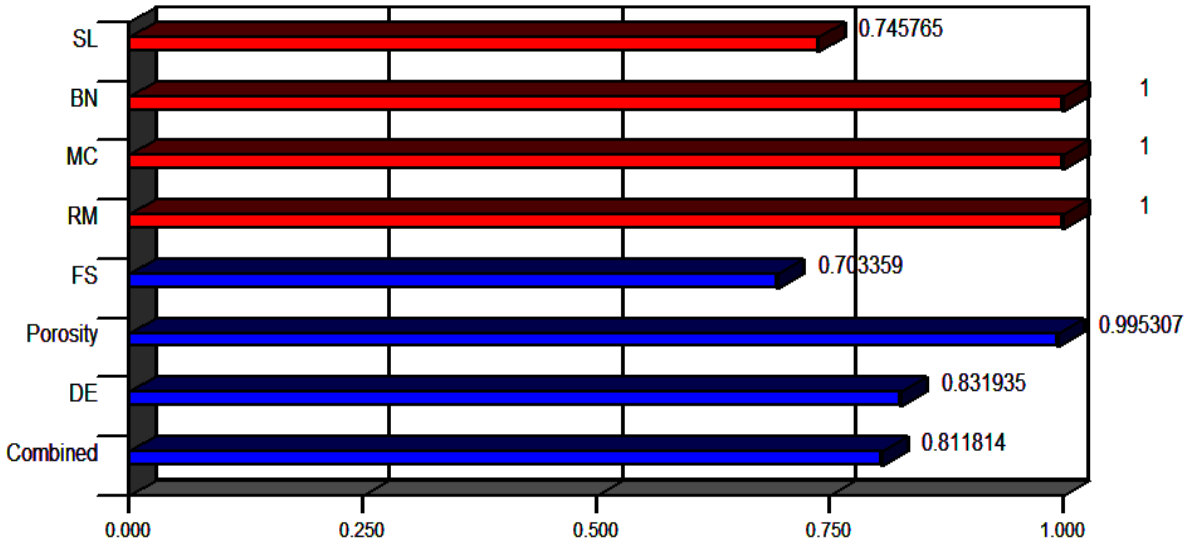

Figure 5.33. Bar graphs of desirability function for SiO_2–BN ceramic composite.

5.4.8. Confirmation tests

The values of responses i.e. flexural strength, porosity and dielectric constant obtained by experimental runs are compared with predicted regression models for flexural strength, porosity and dielectric constant for SiO_2–BN ceramic composite. The error between experimental and predicted values is predicted in Table 5.36 for all responses. It is found that a maximum error of ±3.45% in flexural strength, ±3.06% in porosity and ±3.13% in dielectric constant existing. Hence it can be declared that the predicted models are confirming with

experimental values. Hence the tests are confirmed and recommended that the models are accurate.

Table 5.36. Error between experimental and predicted values

Run order	SL (vol %)	BN (wt %)	MC (wt %)	RM	Flexural Strength (MPa)			Porosity (%)			Dielectric Constant (K)		
					Expt.	Pred.	Error	Expt.	Pred.	Error	Expt.	Pred.	Error
1	46	10	15	5	66.28	64.55	2.60	22.13	22.22	-0.42	4.34	4.40	-1.39
2	46	10	12.5	3	57.43	59.22	-3.11	23.86	23.84	0.08	4.35	4.36	-0.28
3	50	15	10	3	71.65	72.57	-1.28	19.08	18.93	0.76	4.98	5.01	-0.50
4	46	10	10	5	61.13	62.29	-1.89	21.35	21.22	0.60	4.61	4.47	3.13
5	46	10	12.5	5	62.77	63.16	-0.62	21.31	21.02	1.34	4.58	4.62	-0.77
6	46	10	12.5	7	64.98	62.76	3.42	21.75	21.73	0.08	4.51	4.37	3.03
7	50	5	10	3	66.29	65.92	0.57	17.46	17.36	0.57	5.12	5.08	0.80
8	46	5	12.5	5	59.84	59.30	0.90	19.85	19.83	0.09	4.9	4.86	0.77
9	50	5	10	7	69.18	69.64	-0.67	17.83	18.23	-2.26	5.1	5.21	-2.21
10	42	15	10	7	51.19	52.17	-1.92	23.89	24.11	-0.94	4.12	4.12	-0.11
11	50	10	12.5	5	75.18	74.11	1.43	17.12	17.30	-1.06	5.23	5.20	0.55
12	42	15	15	7	52.51	53.13	-1.18	23.71	23.54	0.72	4.21	4.29	-1.88
13	50	5	15	3	70.58	69.49	1.54	21.22	21.27	-0.26	4.82	4.78	0.76
14	50	15	15	7	76.45	77.22	-1.01	17.8	17.95	-0.83	5	4.99	0.14
15	46	10	12.5	5	64.37	63.16	1.88	20.83	21.02	-0.93	4.62	4.62	0.10

Run order	SL (vol %)	BN (wt %)	MC (wt %)	RM	Flexural Strength (MPa)			Porosity (%)			Dielectric Constant (K)		
					Expt.	Pred.	Error	Expt.	Pred.	Error	Expt.	Pred.	Error
16	42	15	10	3	49.89	48.48	2.83	23.12	23.30	-0.77	4.14	4.24	-2.32
17	46	10	12.5	5	61.08	63.16	-3.41	20.51	21.02	-2.51	4.55	4.62	-1.44
18	42	10	12.5	5	47.22	47.72	-1.06	21.91	21.69	0.99	4.6	4.50	2.07
19	42	5	10	7	39.88	40.22	-0.85	23.58	23.21	1.57	4.25	4.28	-0.67
20	46	10	12.5	5	65.42	63.16	3.45	21.69	21.02	3.07	4.49	4.62	-2.79
21	46	10	12.5	5	61.12	63.16	-3.34	20.94	21.02	-0.40	4.6	4.62	-0.34
22	50	15	10	7	78.19	77.00	1.52	17.23	17.04	1.12	5.16	5.14	0.41
23	42	5	15	7	45.22	44.20	2.26	23.15	23.57	-1.83	4.32	4.29	0.63
24	50	5	15	7	71.22	72.88	-2.33	20.53	20.08	2.18	4.95	4.92	0.67
25	42	15	15	3	50.34	49.77	1.13	22.23	22.11	0.55	4.52	4.40	2.65
26	46	15	12.5	5	67.13	67.10	0.05	20.24	20.22	0.09	4.91	4.82	1.76
27	42	5	15	3	40.35	41.55	-2.98	23.99	23.91	0.32	4.35	4.40	-1.25
28	46	10	12.5	5	63.67	63.16	0.80	20.76	21.02	-1.28	4.48	4.62	-3.02
29	50	15	15	3	73.21	73.12	0.12	19.13	19.23	-0.52	4.83	4.86	-0.61
30	42	5	10	3	38.11	37.23	2.30	21.35	21.48	-0.62	4.41	4.39	0.46

5.5. Results and analysis of SiO_2–Si_3N_4–BN ceramic composites

5.5.1. Regression model for flexural strength

A regression model for flexural strength of SiO_2–Si_3N_4–BN ceramic composite is fitted using the experimental results (Table 4.14). ANOVA has been applied on the experimental results for flexural strength and the ANOVA results are given in Table 5.37.

Table 5.37. ANOVA results for flexural strength

Source	Sum of Squares	df	Mean Square	F Value	p-value Prob > F	Percentage Contribution
Model	15520.037	13	857.3869	134.8584	< 0.0001	98.826
A-SL	7210.695	1	7210.695	1134.171	< 0.0001	45.915
B- Si_3N_4	1960.497	1	1960.497	308.3668	< 0.0001	12.484
C-BN	5485.130	1	5485.13	862.7564	< 0.0001	34.927
D-MC	35.353	1	35.3532	5.560707	0.0253	0.225
E-RM	67.539	1	67.53901	10.62322	0.0029	0.430
AB	27.528	1	27.5282	4.329912	0.0464	0.175
AC	45.220	1	45.22005	7.112664	0.0124	0.288
BC	409.839	1	409.8385	64.46352	< 0.0001	2.610
BD	26.938	1	26.9378	4.237048	0.0486	0.172
CE	4.914	1	4.914112	0.772941	0.3865	0.031
A^2	1.966	1	1.965824	0.309205	0.5824	0.013
C^2	207.823	1	207.8231	32.68851	< 0.0001	1.323
D^2	36.595	1	36.5949	5.756013	0.0231	0.233
Residual	184.373	36	6.357681			1.174
Cor Total	15704.409	49				100.000
R-Square: 98.93% Adjusted R-square: 98.20% Predicted R-square: 97.08%						

Where A is solid loading (SL), B is Si_3N_4 content, C is BN content, D is monomer content (MC), E is ratio of monomers (RM)

From the above results, it has been observed that SL, Si_3N_4, BN, interaction of Si_3N_4 and BN and BN^2 are significant model terms, and the response of each are shown in the Figures 5.34(a), (b), (c) and (d). The regression model generated for flexural strength is given in Eqn. 5.10, in the coded form.

$$FS = 103.78 + 14.56A + 7.59B + 12.70C + 1.02D + 1.41E - 0.93AB + 1.19AC + 3.58BC - 0.92BD - 0.39CE - 0.89A^2 - 9.17C^2 - 3.85D^2 \quad (5.10)$$

From Figure 5.34(a), (b) and (c), it is observed that flexural strength increases with solid loading, Si_3N_4 content, and BN content. Micro-cracks occur in green bodies when the solid loading is too low, due to the increase of drying and sintering shrinkages as the space between the particles in the slurry is huge. The density of the composites decreases at too low solids loading, during sintering. Therefore, the flexural strength of porous SiO_2–Si_3N_4–BN sintered ceramic composite is low at lower solids loading, and high flexural strength at high solids loading. However, the probability of occurrence of micro-cracks increases in the green body due to the inconsistency of the slurry at too high contents Si_3N_4 and BN ceramics.

The influence of Si_3N_4 is as expected, flexural strength increases monotonously with the addition of Si_3N_4 as shown in Figure 5.34(b). The interlocking microstructure formed by rod-like Si_3N_4 grains was in favor of enhancing the mechanical properties of ceramic at both room and elevated temperatures. In this composite ceramic Si_3N_4 with the large bonding effect of SiO_2 also blunted the sharp angles of the pores, which was more significant, making it difficult for the crack to propagate. Thus Si_3N_4 when added with SiO_2 forming composite increase the flexural strength of the ceramic composite.

The influence of BN content on flexural strength of SiO_2–Si_3N_4–BN ceramic composites is giving interesting results. The flexural strength was expected to decrease with the increase of BN content due to very high sintering temperature BN. But as shown in Figure 5.34(c), there is an increase in flexural strength with increase in BN content and then it is tending to decrease. This initial increase might be due to the presence of SiO_2 particles that act as a sintering aid between Si_3N_4 and BN particles, which makes a dense structure. This can also decrease the porosity. When the BN content increases beyond a limit, flexural strength is tending to decrease. This might be due to the agglomeration of BN and thus SiO_2 cannot form bonds with all BN particles. The graphs in Figure 5.34(a), (b) and (c), shows an

almost same pattern of increase in the flexural strength. The excessive formation cristobalite can be avoided during sintering by the addition of Si_3N_4 and BN ceramics. The interaction effects of Si_3N_4 and BN ceramics on flexural strength can be seen in Figure 5.34(d).

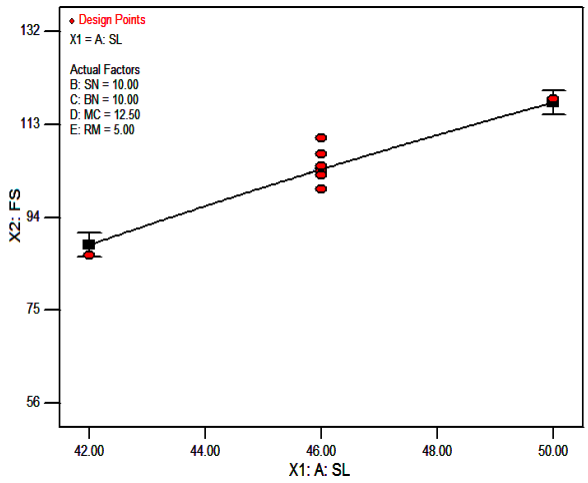

Figure 5.34(a). Effect of SL on FS.

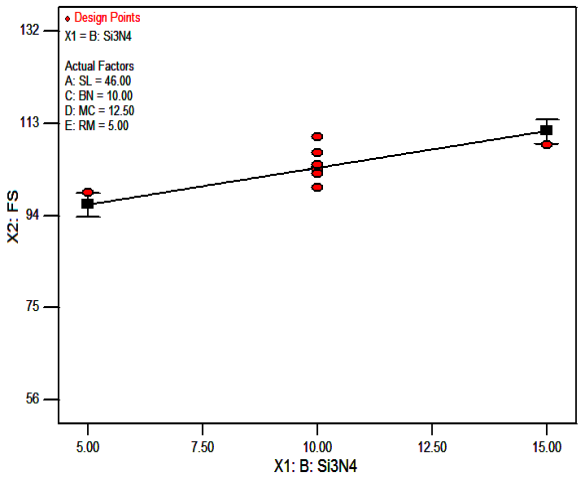

Figure 5.34(b). Effects of Si_3N_4 on FS.

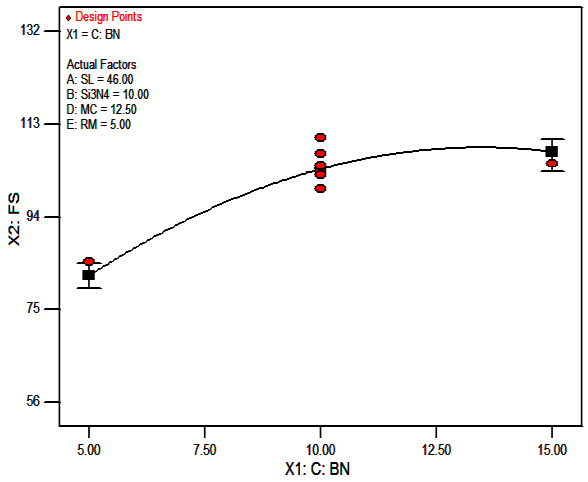

Figure 5.34(c). Effects of BN on FS.

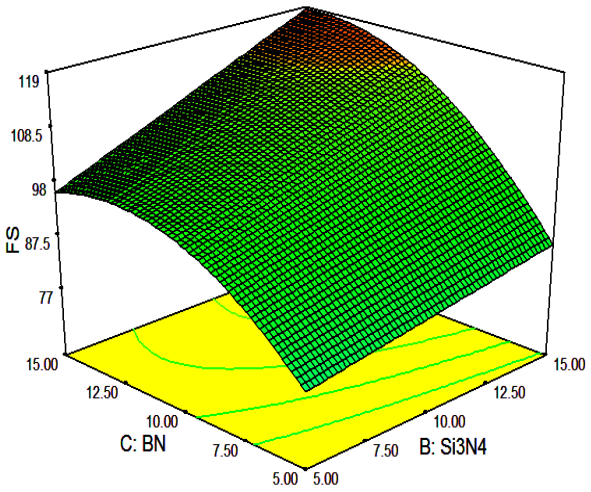

Figure 5.34(d). Effects of Si_3N_4 and BN on FS.

Figure 5.34. Effect of process parameters on flexural strength.

5.5.1.1. Optimization of flexural strength using desirability function

The optimum value of flexural strength is calculated using desirability function (Refer section 1.8.3) where the user can opt for goal, lower and upper limits of various variables (here A, B, C, D, and E) as shown in Table 5.38.

Table 5.38. The range of input parameters and flexural strength for desirability.

Name	Goal	Lower Limit	Upper Limit
A-SL (vol %)	maximize	42	50
B-Si_3N_4 content (wt %)	in range	5	15
C-BN content (wt %)	in range	5	15
D-MC (wt %)	in range	10	15
E-RM	in range	3	7
FS (MPa)	maximize	56.53	131.26

The aim of optimization is to evaluate the best combinational set of inputs for maximization of flexural strength. This is indicated by the desirability of RSM analysis. The maximum value of flexural strength is to be chosen for maximum desirability index for various sets of inputs. A set of 10 optimal solutions are derived and tabulated in Table 5.39 for the particular set of input range (Table 5.38). The desirability of flexural strength is shown in Figures 5.35 as ramp graph. The desirability of each parameter and flexural strength and combined parameters is shown in Figures 5.36 as a bar graph. The prediction of response to a particular response characteristic is indicated by the dot on each of the ramps. The overall desirability of the flexural strength is found to be 1.

Table 5.39. Optimal solutions for flexural strength

Number	SL	Si_3N_4	BN	MC	RM	FS	Desirability
1	50	14.71	13.53	11.15	6.95	131.277	1
2	50	14.88	14.53	11.53	4.52	131.270	1
3	50	14.97	14.18	12	3.29	131.292	1
4	50	14.58	13.69	11.57	6.79	131.667	1
5	50	14.61	14.81	12.08	5.86	131.938	1
6	50	13.98	13.81	12.99	6.99	131.389	0.999
7	50	14.65	14.62	12.02	4.46	131.269	0.999
8	50	14.69	13.38	12.31	6.2	131.860	0.999
9	50	14.98	14.79	11.66	3.83	131.356	0.999
10	50	14.85	13.51	13.71	6.79	132.000	0.999

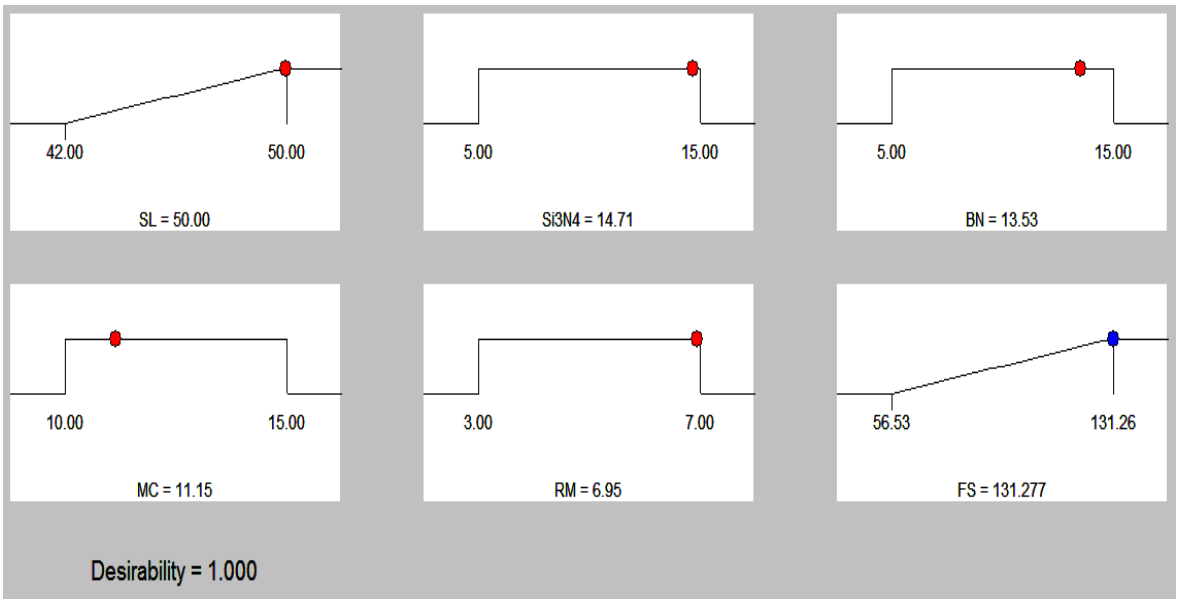

Figure 5.35. Ramp graphs of desirability function for flexural strength of SiO_2–Si_3N_4–BN ceramic composite.

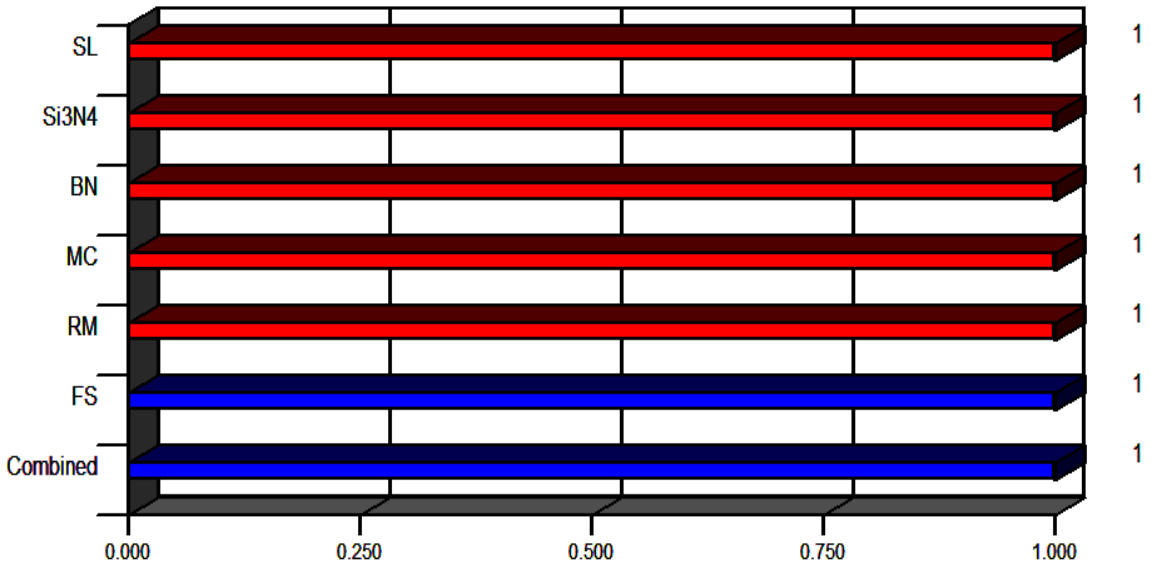

Figure 5.36. Bar graph of desirability function.

5.5.2. Regression model for porosity

A regression model for the porosity of SiO_2– Si_3N_4–BN ceramic composite is fitted using the experimental results (Table 4.14). ANOVA has been applied on the experimental results for porosity and the ANOVA results are given in Table 5.40.

Table 5.40. ANOVA results for porosity.

Source	Sum of Squares	df	Mean Square	F Value	p-value Prob > F	Percentage Contribution
Model	494.958	20	26.48388	26.91404	< 0.0001	94.549
A-SL	261.877	1	261.8768	266.1302	< 0.0001	50.025
B-Si3N4	46.730	1	46.72999	47.48899	< 0.0001	8.927
C-BN	85.131	1	85.13059	86.51331	< 0.0001	16.262
D-MC	0.655	1	0.655247	0.66589	0.4211	0.125
E-RM	2.582	1	2.582262	2.624204	0.1161	0.493
AB	8.415	1	8.415253	8.551936	0.0066	1.608
AC	25.543	1	25.54338	25.95826	< 0.0001	4.879
AD	4.256	1	4.255903	4.325029	0.0465	0.813
AE	0.538	1	0.538203	0.546945	0.4655	0.103
BC	20.560	1	20.56008	20.89402	< 0.0001	3.927
BD	0.682	1	0.681528	0.692598	0.4121	0.130
BE	4.012	1	4.011528	4.076685	0.0528	0.766
CD	11.246	1	11.24565	11.42831	0.0021	2.148
CE	1.744	1	1.743778	1.772101	0.1935	0.333
DE	4.388	1	4.388203	4.459478	0.0434	0.838
A^2	0.128	1	0.12839	0.130475	0.7206	0.025
B^2	2.584	1	2.5842	2.626173	0.1159	0.494
C^2	12.657	1	12.65707	12.86265	0.0012	2.418
D^2	0.474	1	0.474142	0.481843	0.4931	0.091
E^2	0.756	1	0.755924	0.768202	0.3880	0.144
Residual	28.537	29	0.984017			5.451
Cor Total	523.495	49				100.00
R-Square: 94.89%		Adjusted R-square: 91.36%		Predicted R-square: 85.29%		

Where A is solid loading (SL), B is Si_3N_4 content, C is BN content, D is monomer content (MC), E is ratio of monomers (RM)

From the above results, it has been observed that SL, Si_3N_4, BN, interaction of SL and Si_3N_4, interaction of SL and BN, interaction of Si_3N_4 and BN, interaction of BN and MC and BN^2 are significant model terms, and the response of each are shown in the Figures 5.37(a), (b), (c), (d), (e), (f) and (g). The regression model generated for porosity is given in Eqn. 5.11, in the coded form.

$$Por. = 32.90 - 2.78A - 1.17B - 1.58C + 0.14D - 0.28E - 0.51AB - 0.89AC + 0.36AD - 0.13AE - 0.80BC - 0.15BD - 0.35BE - 0.59CD - 0.23CE - 0.37DE - 0.23A^2 + 1.02B^2 + 2.26C^2 - 0.44D^2 - 0.55E^2 \quad (5.11)$$

From Figure 5.37(a) it can be seen that the porosity of sintered body decreases with the increase of solid loading. As the solid loading increases the ceramic particles are tightly compacted by reducing the pores in the composite thus densifying the ceramic composite.

The porosity of sintered body decreases with the increase of Si_3N_4 content as shown in Figure 5.37(b). The interlocking microstructure formed by rod-like Si_3N_4 grains was in favor of enhancing the mechanical properties of the ceramic composite. SiO_2 is having excellent bonding with Si_3N_4, which makes a dense structure, and thus porosity of sintered body decreases. The decrease of porosity is more rapid initially with an increase of Si_3N_4 content and the less rapid. This might be due to the agglomeration of ceramic powder when it exceeds the limit.

BN having very high sintering temperature fails to sinter in this ceramic preparation, and the porosity of this ceramic composite might increase with an increase in BN content. But as shown in Figure 5.37(c), the increase of BN content causes a decrease in porosity to a certain limit and then increases. The initial decrease in porosity might be because, the SiO_2 particles act as a sintering aid between Si_3N_4 and BN particles and makes excellent bond among the ceramic particles, which makes a dense structure. Porosity is a combining result from green density and sintering shrinkage; increasing green density or shrinkage decreases the porosity. After a certain limit, the porosity is found to increase, which may be due the agglomeration of BN powder and SiO_2 is unable to make the bond.

From Figure 5.37(b) and (c), it is observed that Si_3N_4 and BN content has significant effects on the porosity. As the Si_3N_4 and BN content increases there is a reduction in the porosity due to tight packing of Si_3N_4 and BN particles in SiO_2–Si_3N_4–BN ceramic composite. As the content of Si_3N_4 and BN powder increases, the pores in the composite are reduced that increases the density of the composite causing the lower porosity. The interaction effects of SL and Si_3N_4, the interaction of SL and BN, the interaction of Si_3N_4 and BN, the interaction of BN and MC can be seen in Figure 5.37(d), (e), (f) and (g).

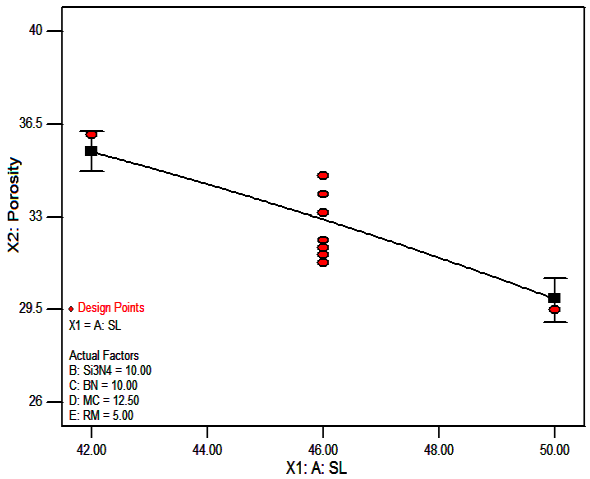

Figure 5.37(a). Effect of SL on porosity.

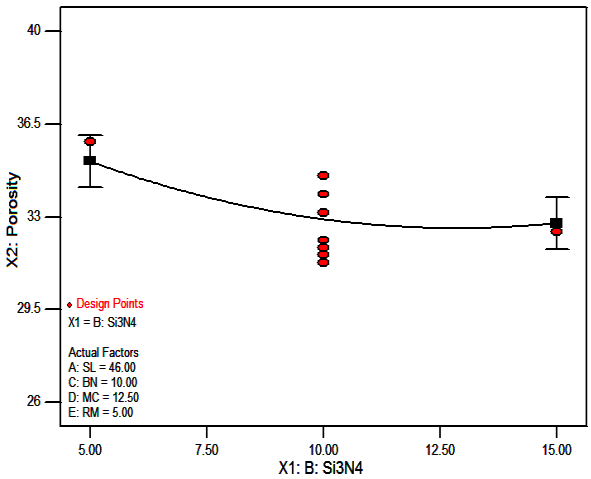

Figure 5.37(b). Effects of Si_3N_4 on porosity.

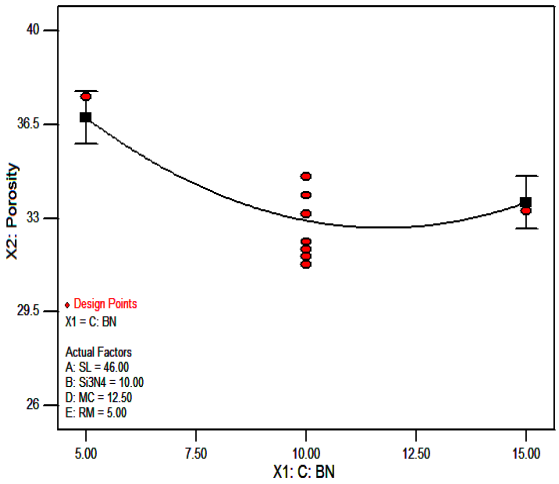

Figure 5.37(c). Effect of BN on porosity.

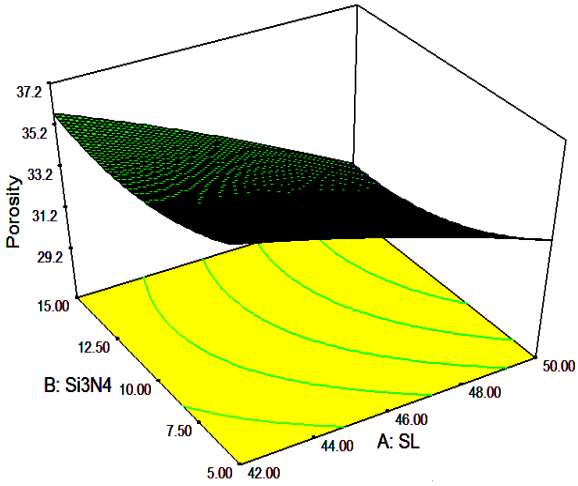

Figure 5.37(d). Effects of SL and Si_3N_4 on porosity.

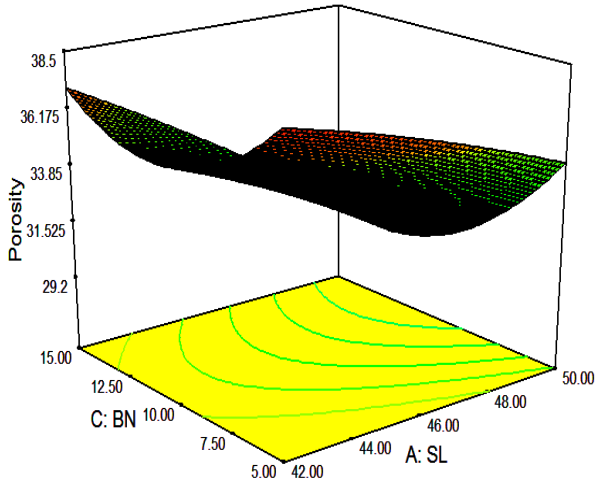

Figure 5.37(e). Effects of SL and BN on porosity.

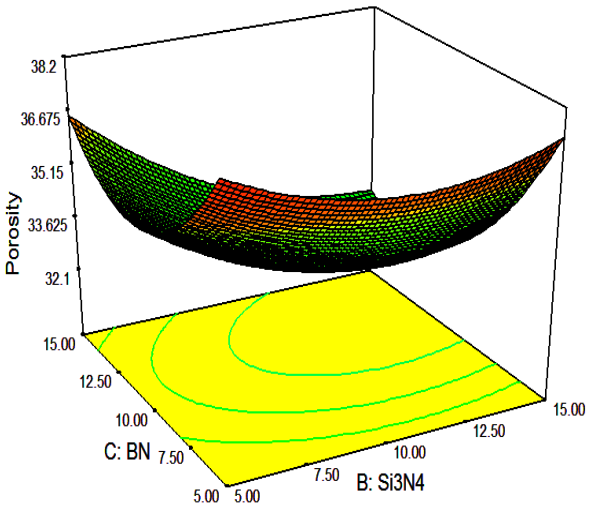

Figure 5.37(f). Effects of Si_3N_4 and BN on porosity.

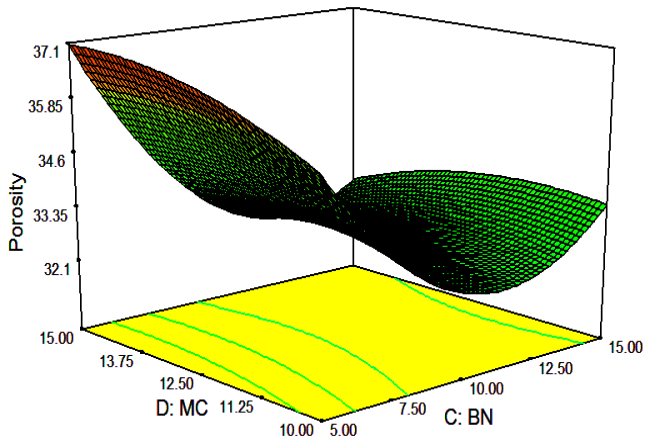

Figure 5.37(g). Effect of BN and MC on porosity.

Figure 5.37. Effect of process parameters on porosity

5.5.2.1. Optimization of porosity using desirability function

The optimum value of porosity is calculated using desirability function (Refer section 1.8.3) where the user can opt for goal, lower and upper limits of various variables (here A, B, C, D, and E) as shown in Table 5.41.

Table 5.41. The range of input parameters and porosity for desirability.

Name	Goal	Lower Limit	Upper Limit
A-SL (vol %)	maximize	42	50
B-Si_3N_4 content (wt %)	in range	5	15
C-BN content (wt %)	in range	5	15
D-MC (wt %)	in range	10	15
E-RM	in range	3	7
Por. (%)	maximize	26.15	39.38

The aim of optimization is to evaluate the best combinational set of inputs for maximization of porosity. This is indicated by the desirability of RSM analysis. The maximum value of porosity is to be chosen for maximum desirability index for various sets of inputs. A set of 10 optimal solutions is derived and tabulated in Table 5.42 for the particular set of input range (Table 5.41). The desirability of porosity is shown in Figures 5.38 as ramp graph. The desirability of each parameter and porosity and combined parameters is shown in Figures 5.39 as a bar graph. The prediction of response to a particular response characteristic

is indicated by the dot on each of the ramps. The overall desirability of the porosity is found to be 0.917.

Table 5.42. Optimal solutions for porosity

Number	SL	Si_3N_4	BN	MC	RM	Por.	Desirability
1	49.94	5	5	14.84	4.89	37.351	0.917
2	50	5	5	14.77	5.39	37.260	0.916
3	49.9	5	5	14.41	5.09	37.269	0.911
4	50	5.28	5	14.67	4.64	37.127	0.911
5	50	5.21	5.01	15	5.62	37.080	0.909
6	49.99	5	5.08	15	6.09	36.973	0.904
7	49.67	5	5	15	4.04	37.425	0.904
8	50	5	5	13.86	6.23	36.869	0.900
9	50	5	5	13.4	5.88	36.846	0.899
10	49.89	5	5	13.21	4.05	36.745	0.889

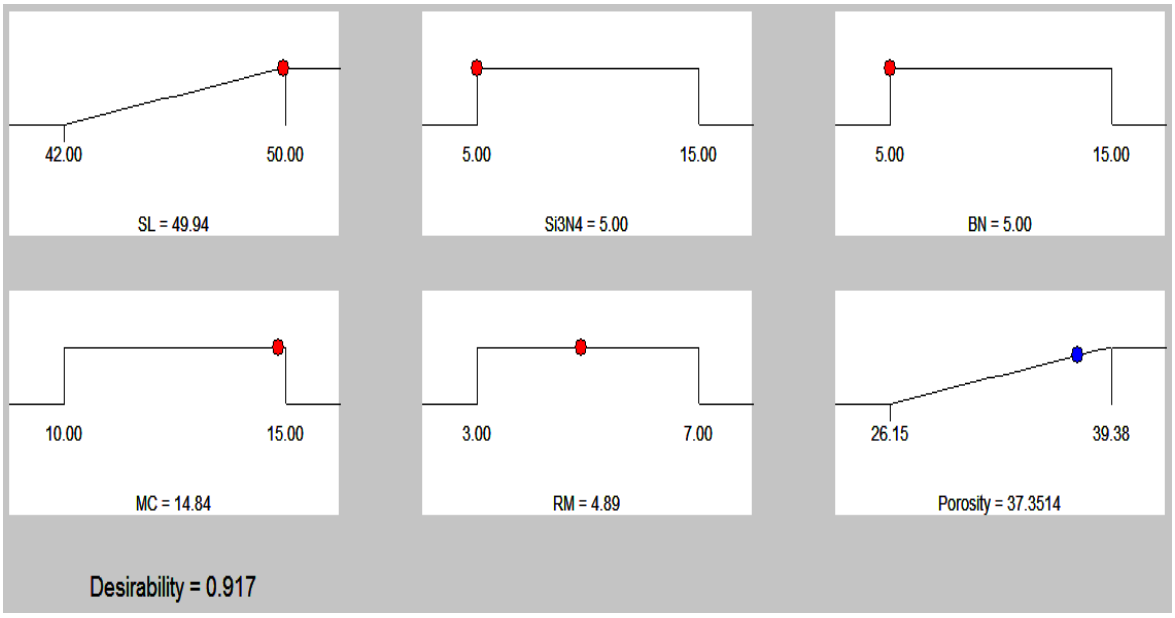

Figure 5.38. Ramp graphs of desirability function for the porosity of SiO_2–Si_3N_4–BN ceramic composite.

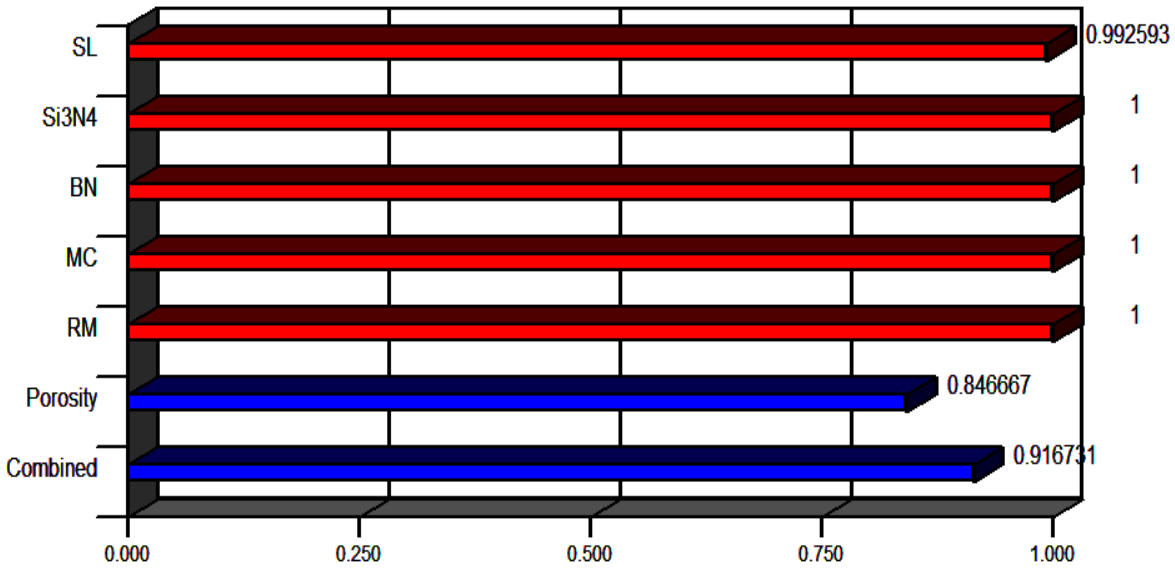

Figure 5.39. Bar graph of desirability function for porosity.

5.5.3. Regression model for dielectric constant

A regression model for dielectric constant of SiO_2–Si_3N_4–BN ceramic composite is fitted using the experimental results (Table 4.14). ANOVA has been applied on the experimental results for dielectric constant and the ANOVA results are given in Table 5.43.

Table 5.43. ANOVA results for dielectric constant.

Source	Sum of Squares	df	Mean Square	F Value	p-value Prob > F	Percentage Contribution
Model	21.681	20	1.00178	40.77248	< 0.0001	97.352
A-SL	0.898	1	0.8978	36.54051	< 0.0001	4.031
B-Si3N4	18.206	1	18.20631	740.9977	< 0.0001	81.752
C-BN	0.064	1	0.064424	2.622041	0.1185	0.289
D-MC	0.180	1	0.18	7.32601	0.0123	0.808
E-RM	0.074	1	0.074356	3.026289	0.0947	0.334
AB	0.035	1	0.035113	1.429081	0.2436	0.158
AC	0.092	1	0.09245	3.76272	0.0642	0.415
AD	0.541	1	0.5408	22.01059	< 0.0001	2.428
AE	0.242	1	0.241513	9.829572	0.0045	1.084

BC	0.332	1	0.332113	13.517	0.0012	1.491
BD	0.030	1	0.030012	1.22151	0.2800	0.135
BE	0.004	1	0.00405	0.164835	0.6883	0.018
CD	0.120	1	0.12005	4.886042	0.0369	0.539
CE	0.028	1	0.027613	1.12383	0.2996	0.124
DE	0.090	1	0.090313	3.675724	0.0672	0.406
A^2	0.595	1	0.594791	24.20804	< 0.0001	2.671
B^2	0.049	1	0.048747	1.983991	0.1718	0.219
C^2	0.042	1	0.04155	1.691107	0.2058	0.187
D^2	0.020	1	0.020207	0.822434	0.3735	0.091
E^2	0.038	1	0.038407	1.563149	0.2233	0.172
Residual	0.590	29	0.02457			2.648
Cor Total	22.270	49				100

R-Square: 95.93% Adjusted R-square: 93.07% Predicted R-square: 87.36%

Where A is solid loading (SL), B is Si_3N_4 content, C is BN content, D is monomer content (MC), E is the ratio of monomers (RM).

From the above results, it has been observed that SL, Si_3N_4, interaction of SL and MC, interaction of Si_3N_4 and BN, SL^2, are significant model terms, and the response of each are shown in the Figures 5.40(a), (b) and (c). The mathematical model generated for dielectric constant was given in Eqn. 5.12, in the coded form.

$$DE = 5.82 + 0.67A + 0.73B - 0.044C + 0.30D - 0.047E - 0.033AB - 0.054AC - 0.13AD + 0.087AE + 0.10BC + 0.031BD + 0.011BE + 0.061CD - 0.029CE + 0.053DE - 0.49A^2 - 0.14B^2 + 0.13C^2 - 0.09D^2 + 0.12E^2 \quad (5.12)$$

The dielectric properties are closely related to material density. The greater the density of ceramics, the greater is the dielectric constant. As shown in Figure 5.40(a), with the increase of solid loading, the increase in density of SiO_2–Si_3N_4–BN ceramic composite will lead to the increase of dielectric constant. The density starts decreasing when the solid loading increases beyond a point due to increase in surface area of pores, and agglomeration of ceramic particles followed by formation of micro cracks. In Figure 5.40(b), as the Si_3N_4 content increases the dielectric constant increases monotonically. The increase in Si_3N_4

content increases the density of sintered ceramic composite that lowers the transfer of electromagnetic waves through it. The interaction effects of SL and MC, the interaction of Si_3N_4 and BN can be seen in Figure 5.40(c) and (d). The addition of BN ceramics could be able to achieve the optimized dielectric constant of the ceramic composites.

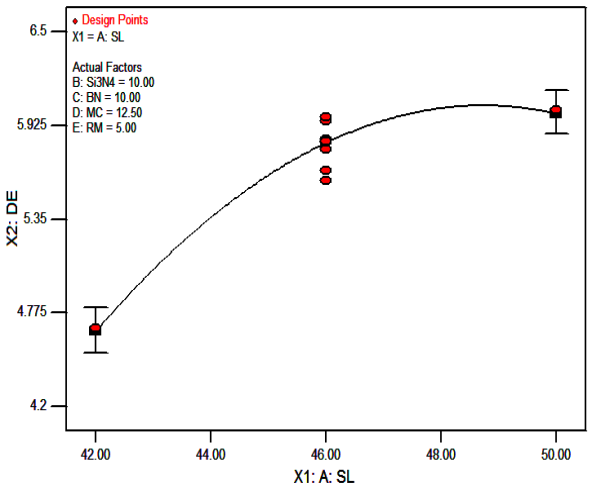

Figure 5.40(a). Effect of SL on DE.

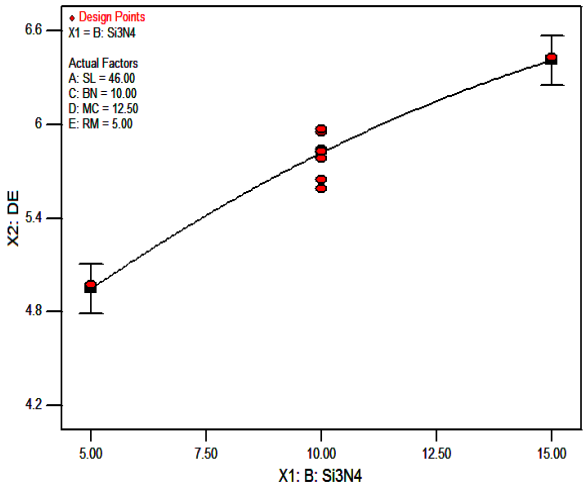

Figure 5.40(b). Effects of Si_3N_4 on DE.

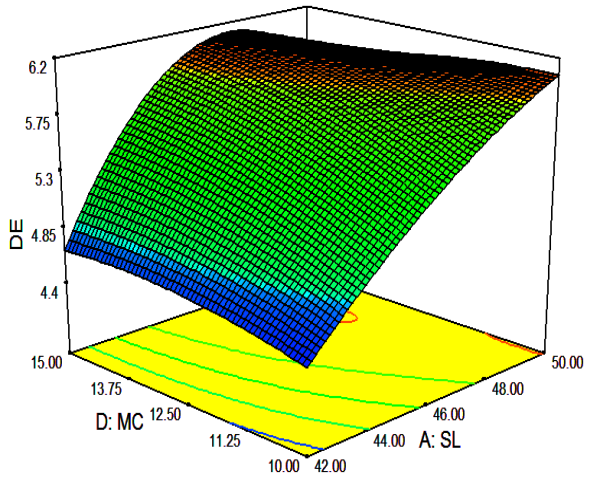

Figure 5.40(c). Effects of SL and MC on DE.

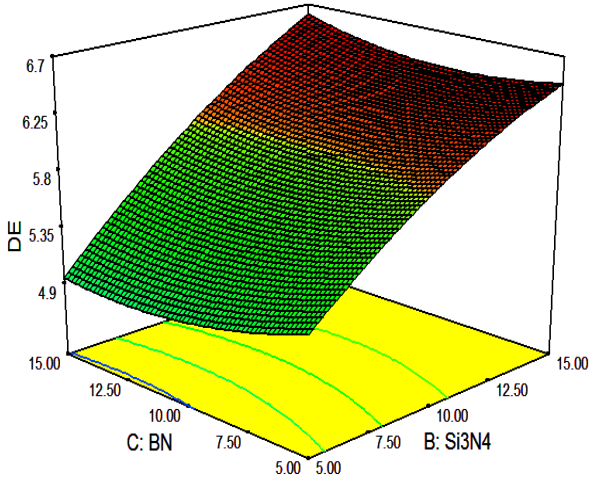

Figure 5.40(d). Effects of Si_3N_4 and BN on DE.

Figure 5.40. Effect of process parameters on dielectric constant

5.5.3.1. Optimization of dielectric constant using desirability function

The optimum value of dielectric constant is calculated using desirability function of (Refer section 1.8.3) where the user can opt for goal, lower and upper limits of various variables (here A, B, C, D and E) as shown in Table 5.44.

Table 5.44. The range of input parameters and dielectric constant for desirability.

Name	Goal	Lower Limit	Upper Limit
A-SL (vol %)	maximize	42	50
B-Si_3N_4 content (wt %)	in range	5	15
C-BN content (wt %)	in range	5	15
D-MC (wt %)	in range	10	15
E-RM	in range	3	7
DE	minimize	4.26	6.47

The aim of optimization is to evaluate the best combinational set of inputs for minimization of dielectric constant. This is indicated by the desirability of RSM analysis. The maximum value of dielectric constant is to be chosen for maximum desirability index for various sets of inputs. A set of 10 optimal solutions is derived and tabulated in Table 5.45 for the particular set of input range (Table 5.44). The desirability of dielectric constant is shown in Figures 5.41 as ramp graph. The desirability of each parameter and dielectric constant and combined parameters is shown in Figures 5.42 as a bar graph. The prediction of response to a particular response characteristic is indicated by the dot on each of the ramps. The overall desirability of the dielectric constant is found to be 0.988.

Table 5.45. Optimal solutions for dielectric constant.

Number	SL	Si_3N_4	BN	MC	RM	DE	Desirability
1	50	5	14.95	15	5.42	4.312	0.988
2	50	5	13.74	15	4.69	4.316	0.987
3	50	5	14.16	15	5.98	4.341	0.981
4	50	5	13.18	15	5.89	4.351	0.979
5	50	5.01	11.54	15	4.87	4.367	0.975
6	50	5.03	11.89	14.99	4.22	4.378	0.973
7	50	5	12	15	3.25	4.430	0.961
8	50	5	15	10.19	6.58	4.471	0.951
9	50	5	10.42	15	3.35	4.473	0.951
10	50	5.02	15	10.11	6.65	4.478	0.949

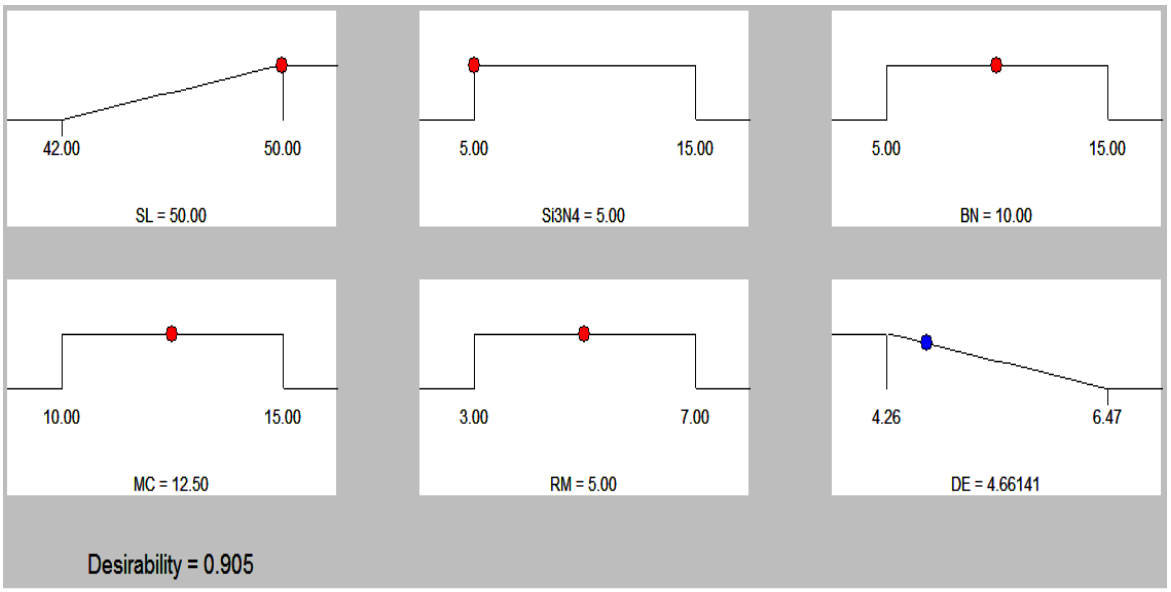

Figure 5.41. Ramp graph of desirability function for dielectric constant of SiO_2–Si_3N_4–BN ceramic composite.

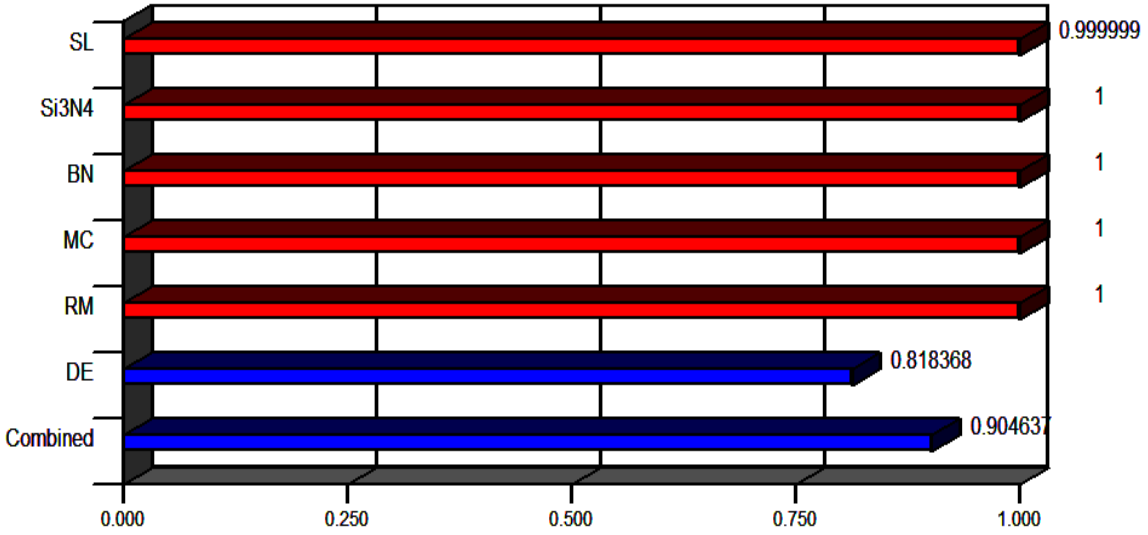

Figure 5.42. Bar graph of desirability function for dielectric constant.

5.5.4. Multi-response optimization using desirability function

Multi-response optimization using desirability function was carried out in combination with response surface methodology to surmount the difficulty of inconsistent responses of single response optimization. The range and goals of input parameters i.e. solid loading, monomer content, and ratio of monomers and the responses i.e. flexural strength, porosity and dielectric constant are given in Table 5.46.

Table 5.46. The range of input parameters and responses for desirability.

Name	Goal	Lower Limit	Upper Limit
A-SL (vol %)	maximize	42	50
B-Si_3N_4 content (wt %)	in range	5	15
C-BN content (wt %)	in range	5	15
D-MC (wt %)	is in range	10	15
E-RM	is in range	3	7
FS (MPa)	maximize	56.53	131.26
Porosity (%)	maximize	26.15	39.38
DE	minimize	4.26	6.47

The aim of optimization is to evaluate the best combinational set of inputs for maximization of flexural strength and porosity, and minimization of dielectric constant. This is indicated by the desirability of RSM analysis. The optimum value of responses is to be chosen for maximum desirability index for various sets of inputs. A set of 10 optimal solutions is derived and tabulated in Table 5.47 for the particular set of input range (Table 5.46). The desirability of output responses i.e. flexural strength, porosity and dielectric constant is shown in Figures 5.43 as ramp graph. The desirability of each parameter and each response and combined parameters are shown in Figures 5.44 as a bar graph. The overall desirability of the responses is found to be 0.776.

Table 5.47. Set of optimal solutions for SiO_2–Si_3N_4–BN ceramic composite.

Sl. No.	SL	Si_3N_4	BN	MC	RM	FS	Por.	DE	Desirability
1	49.99	5	15	13.87	4.56	111.671	33.183	4.422	0.776
2	50	5	15	14.28	4.41	111.179	33.125	4.390	0.776
3	50	5	15	14.24	4.17	111.138	33.153	4.407	0.775
4	50	5	15	12.66	4.77	111.936	33.224	4.480	0.773
5	49.98	5	15	14.9	3.63	109.712	33.040	4.387	0.768
6	49.99	5	15	12.07	4.99	111.409	33.181	4.494	0.768
7	50	5	13.88	15	3.87	110.902	32.585	4.349	0.763
8	50	5	13.29	14.77	3.86	111.691	32.488	4.384	0.760
9	50	5	13.15	15	3.94	111.258	32.434	4.352	0.760
10	50	5	14.93	15	3	109.440	32.882	4.433	0.759

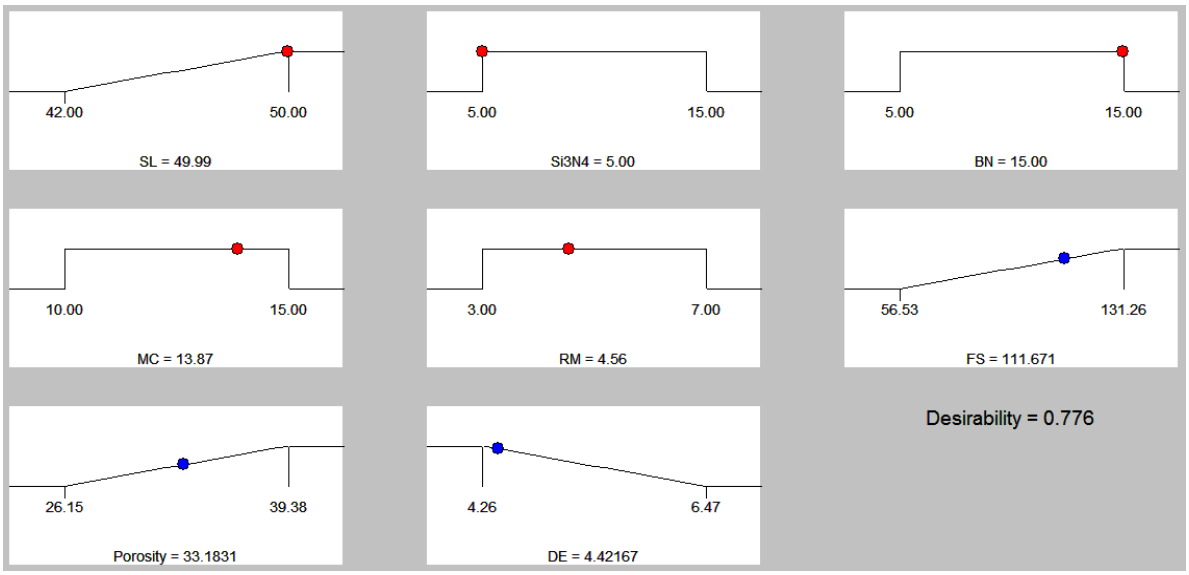

Figure 5.43. Ramp graphs of desirability function for SiO_2–Si_3N_4–BN ceramic composite.

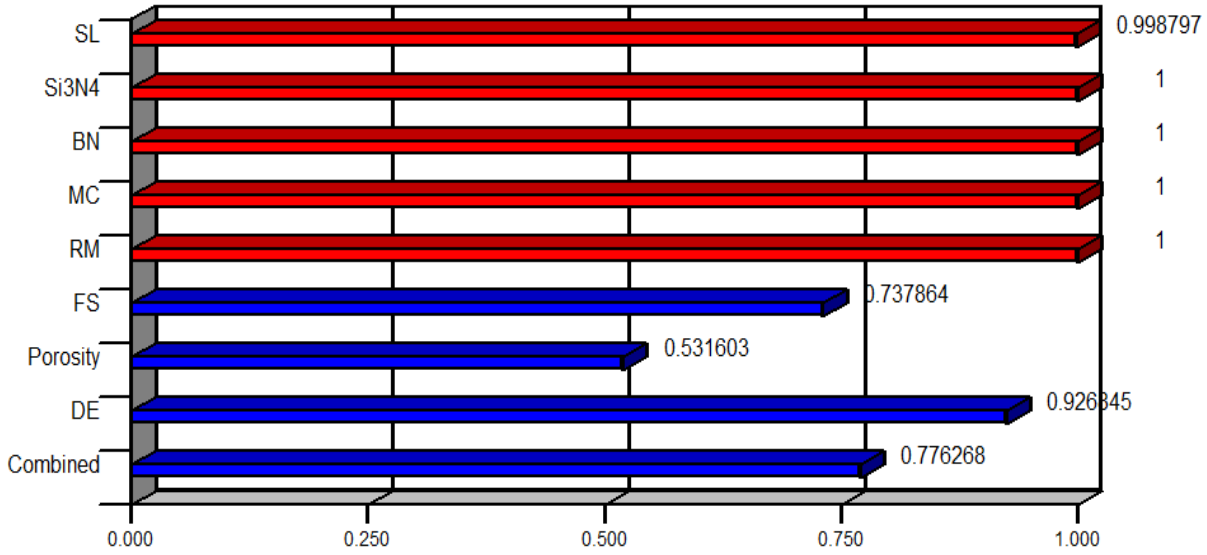

Figure 5.44. Bar graphs of desirability function for SiO_2–Si_3N_4–BN ceramic composite.

5.5.5. Confirmation tests

The values of responses i.e. flexural strength, porosity and dielectric constant obtained by experimental runs are compared with predicted regression models for flexural strength, porosity and dielectric constant for SiO_2–Si_3N_4–BN ceramic composite. The error between experimental and predicted values is predicted in Table 5.48 for all responses. It is found that a maximum error of ±3.44% in flexural strength, ±3.29% in porosity and ±3.24% in dielectric constant existing. Hence it can be declared that the predicted models are confirming with experimental values. Hence the tests are confirmed and recommended that the models are accurate.

Table 5.48. Error between experimental and predicted values

Run order	SL (vol %)	Si_3N_4 (wt %)	BN (wt %)	MC (wt %)	RM	Flexural Strength (MPa)			Porosity (%)			Dielectric Constant (K)		
						Expt.	Pred.	Error	Expt.	Pred.	Error	Expt.	Pred.	Error
1	46	15	10	12.5	5	108.72	111.36	-2.43	32.45	32.75	-0.93	6.43	6.44	-0.16
2	46	10	10	12.5	5	103.97	103.78	0.18	33.14	32.90	0.72	5.45	5.63	-3.24
3	50	15	5	10	7	96.59	95.50	1.12	33.41	32.68	2.19	6.47	6.46	0.11
4	46	10	10	12.5	5	102.52	103.78	-1.23	31.58	32.50	-2.92	5.83	5.83	0.06
5	50	15	5	15	3	93.11	91.88	1.32	35.86	35.63	0.64	5.65	5.71	-0.97
6	42	5	15	10	7	73.15	73.75	-0.82	38.91	39.53	-1.60	4.29	4.18	2.57
7	42	5	15	10	3	71.94	71.91	0.04	39.26	38.84	1.06	4.45	4.53	-1.73
8	46	10	10	12.5	5	104.53	103.78	0.72	31.82	32.90	-3.40	6.08	5.93	2.52
9	50	15	5	15	7	95.23	95.68	-0.47	32.24	33.25	-3.13	5.98	6.08	-1.68
10	42	15	5	10	3	65.48	67.14	-2.54	37.63	38.25	-1.65	5.97	6.06	-1.49
11	42	5	5	15	7	64.29	62.77	2.37	38.94	38.88	0.17	4.26	4.34	-1.85
12	50	15	15	10	7	131.26	129.38	1.43	26.15	26.84	-2.66	6.45	6.52	-1.06
13	46	10	10	12.5	5	103.76	103.78	-0.02	31.25	32.12	-2.79	5.78	5.83	-0.80
14	46	10	10	12.5	5	106.87	103.78	2.89	34.56	33.42	3.29	5.82	5.83	-0.11
15	50	5	5	15	7	91.23	91.23	0.00	37.21	36.61	1.62	5.03	4.99	0.78
16	42	5	5	15	3	56.54	58.19	-2.90	38.48	38.73	-0.66	4.45	4.36	2.11

Run order	SL (vol %)	Si_3N_4 (wt %)	BN (wt %)	MC (wt %)	RM	Flexural Strength (MPa)			Porosity (%)			Dielectric Constant (K)		
						Expt.	Pred.	Error	Expt.	Pred.	Error	Expt.	Pred.	Error
17	46	10	15	12.5	5	103.26	106.81	-3.44	33.25	33.58	-1.00	5.85	5.91	-1.06
18	42	5	5	10	3	56.53	55.54	1.75	36.36	36.97	-1.67	4.45	4.55	-2.19
19	50	5	5	10	3	83.59	84.29	-0.83	33.68	33.76	-0.23	5.39	5.39	0.00
20	50	15	15	15	7	129.64	130.11	-0.36	27.64	26.93	2.56	6.39	6.38	0.14
21	50	5	15	10	3	107.23	105.41	1.69	32.54	32.06	1.47	4.81	4.70	2.35
22	46	10	10	12.5	3	101.24	102.56	-1.30	32.75	32.63	0.38	5.95	6.00	-0.81
23	46	10	5	12.5	5	84.75	81.91	3.35	37.52	36.75	2.06	6.09	6.00	1.47
24	42	15	15	15	3	99.25	98.07	1.19	36.37	35.73	1.75	6.18	6.36	-2.89
25	42	10	10	12.5	5	86.28	88.32	-2.37	36.31	35.45	2.37	4.68	4.67	0.31
26	50	10	10	12.5	5	118.28	117.45	0.70	29.48	29.90	-1.42	6.02	6.01	0.22
27	50	15	15	15	3	127.47	127.88	-0.32	28.37	28.36	0.04	6.15	6.12	0.44
28	50	5	5	15	3	87.19	87.65	-0.53	37.54	36.98	1.48	4.86	4.88	-0.33
29	42	5	15	15	3	75.42	75.82	-0.53	38.12	38.24	-0.31	4.68	4.58	2.11
30	42	15	5	15	3	69.54	67.32	3.19	39.38	39.43	-0.13	6.22	6.18	0.60
31	42	15	5	15	7	68.29	70.53	-3.28	38.57	38.16	1.07	5.93	6.00	-1.11
32	42	15	15	10	3	98.71	97.83	0.89	37.13	36.92	0.56	6.12	5.99	2.13
33	42	5	15	15	7	78.37	78.13	0.30	37.82	37.45	0.98	4.34	4.45	-2.44

Run order	SL (vol %)	Si_3N_4 (wt %)	BN (wt %)	MC (wt %)	RM	Flexural Strength (MPa)			Porosity (%)			Dielectric Constant (K)		
						Expt.	Pred.	Error	Expt.	Pred.	Error	Expt.	Pred.	Error
34	50	15	15	10	3	126.78	127.62	-0.66	27.39	28.09	-2.55	6.39	6.47	-1.30
35	46	10	10	12.5	5	99.68	102.78	-3.11	32.11	32.90	-2.47	6.06	5.89	2.86
36	46	10	10	12.5	5	103.52	103.78	-0.25	33.14	32.90	0.72	5.68	5.83	-2.58
37	42	15	5	10	7	71.51	70.78	1.03	38.75	38.46	0.76	5.64	5.66	-0.34
38	46	10	10	12.5	5	105.42	103.78	1.56	33.85	32.90	2.80	5.84	5.83	0.23
39	50	5	15	10	7	105.15	106.94	-1.70	32.86	32.23	1.90	4.41	4.48	-1.63
40	46	10	10	15	5	98.37	100.95	-2.62	32.12	32.60	-1.51	6.05	6.03	0.27
41	50	15	5	10	3	91.36	92.18	-0.90	33.47	32.99	1.43	6.29	6.30	-0.16
42	42	5	5	10	7	58.94	58.94	-0.01	38.64	38.59	0.13	4.38	4.32	1.43
43	42	15	15	15	7	102.35	100.61	1.70	32.38	33.43	-3.23	6.16	6.05	1.73
44	50	5	15	15	3	109.48	109.34	0.13	32.19	32.92	-2.26	4.35	4.43	-1.79
45	46	10	10	12.5	7	105.48	105.38	0.10	32.39	32.07	0.97	5.98	5.90	1.27
46	46	10	10	10	5	100.28	98.91	1.36	33.25	32.33	2.78	5.45	5.44	0.21
47	50	5	5	10	7	85.37	87.38	-2.36	33.87	34.86	-2.93	5.25	5.29	-0.81
48	42	15	15	10	7	99.58	99.89	-0.32	36.29	36.20	0.26	5.32	5.47	-2.87
49	46	5	10	12.5	5	98.76	96.17	2.62	35.84	35.10	2.07	4.97	4.94	0.53
50	50	5	15	15	7	112.35	111.35	0.89	31.08	31.61	-1.69	4.49	4.43	1.44

5.6. Comparison of all responses of SiO_2, SiO_2–Si_3N_4, SiO_2–BN and SiO_2–Si_3N_4–BN ceramic composites

The results presented in Table 5.11, Table 5.23, Table 5.35 and Table 5.47 are multi-objective optimized values of flexural strength, porosity and dielectric constant i.e. responses with maximum desirability as per RSM analysis. The maximum values of flexural strength for each composite i.e. SiO_2 (S1), SiO_2–Si_3N_4 (S2), SiO_2–BN (S3) and SiO_2–Si_3N_4–BN (S4) have been shown in Figure 5.45. Thus the hybrid ceramic composite of SiO_2 (i.e. SiO_2–Si_3N_4–BN) has the maximum flexural strength of 111.67 MPa. Hence it is further concluded that if maximum flexural strength is a choice the hybrid composite SiO_2–Si_3N_4–BN is best. Next best would be S2. The flexural strength is minimum for SiO_2 ceramics. Hence SiO_2 composites such as S2 and S3 or SiO_2 hybrid composite such as S4 are preferable.

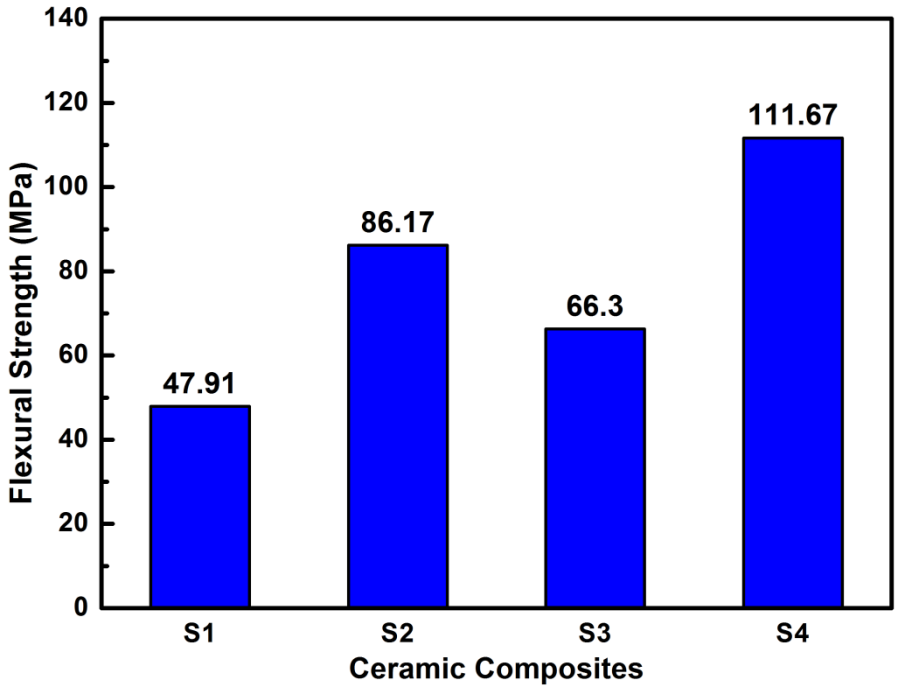

Figure 5.45. Comparison of flexural strength obtained for various ceramic composites.

Similarly, the maximum values of porosity and dielectric constant are presented in Figure 5.45 and Figure 5.46 respectively. The maximum porosity is obtained for S2 ceramic whereas porosity of S3 is minimum among the S1, S2, S3 and S4 composites. Porosity enhances wave transparent behavior of a ceramic which is one of the most desirable properties of radomes. Hence based on porosity, S2 compositely is preferable among all of

the S1, S2, S3 and S4 composites. The dielectric constant of a radome must be minimum. Hence with respect to dielectric constant, S1 is preferable among all ceramic composites but the flexural strength is low for S1.

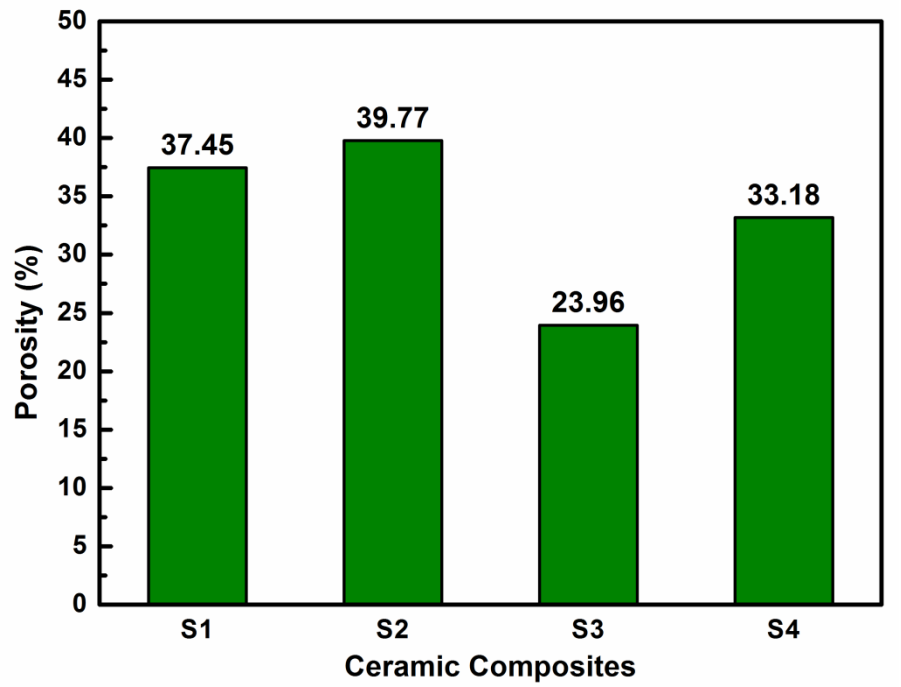

Figure 5.46. Comparison of porosity obtained for various ceramic composites.

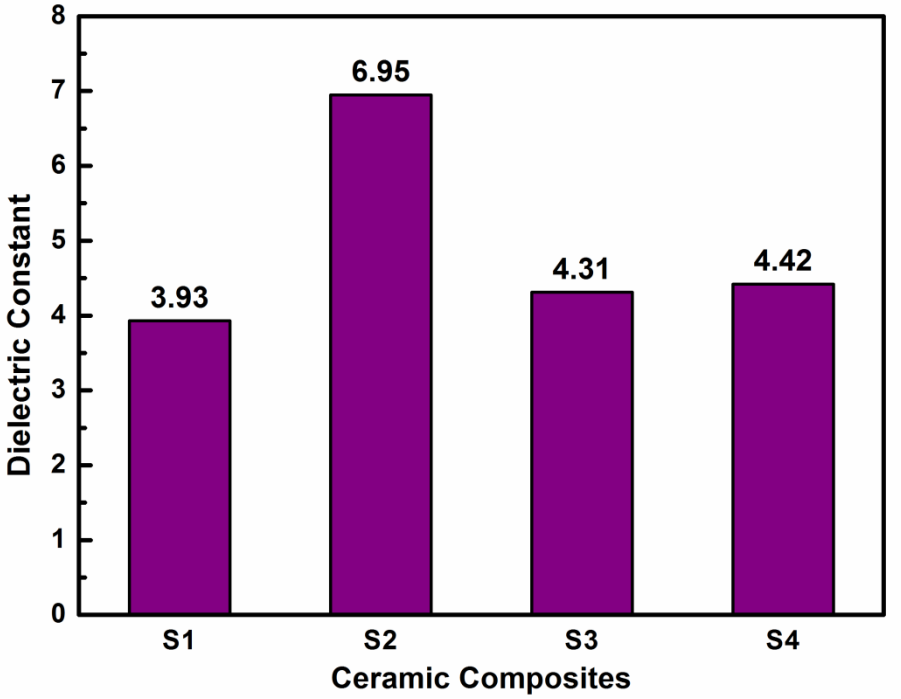

Figure 5.47. Comparison of dielectric constant obtained for various ceramic composites.

Upon comparison of the maximum values of flexural strength, porosity and dielectric constant for S1, S2, S3, and S4, one has to take trade-off decision for selecting appropriate and best radome materials among S1, S2, S3 and S4. The following Table 5.49 is made considering higher value as very good, lower value poor and medium value as good in case of flexural strength and porosity, whereas lower value as very good, higher value as poor and medium value as good in case of dielectric constant for radomes.

Table 5.49. Comparison of S1, S2, S3 and S4 ceramic composites.

Ceramics	Flexural strength	Porosity	Dielectric constant
S1	Poor	Good	Very Good
S2	Good	Very Good	Poor
S3	Poor	Poor	Good
S4	Very Good	Good	Good

From the above Table 5.49, it can be deduced that S1 is having the lower flexural strength and good porosity and dielectric constant, hence such material may be considered for lower range missile radomes. Among the above four materials, S3 has no good properties and hence it may not be a good radome material however by the addition of Si_3N_4 in S3 the properties enhances. S2 may be suitable as a medium range missile radome material.

Summary

RSM analysis of each response i.e. flexural strength (FS), porosity (Por), and dielectric constant (DE) is done for the SiO_2, SiO_2–Si_3N_4, SiO_2–BN and SiO_2–Si_3N_4–BN ceramic composites prepared by gelcasting method and regression models were developed. ANOVA has been applied on the experimental results for each response to investigate the significance of process parameters and their contributions. The parameters that influence these responses are solid loading (SL), monomer content (MC), ratio of monomers (RM), Si_3N_4 content, and BN content respectively. Optimum process parameters were evaluated for maximum flexural strength, maximum porosity and minimum dielectric constant using RSM coupled with desirability function to optimize multiple responses. A comparison is made for the optimal multiobjective optimized values of flexural strength, porosity and dielectric constant i.e. responses with maximum desirability as per RSM analysis of all the ceramic composites.

CHAPTER 6

CONCLUSIONS AND SCOPE FOR FUTURE WORK

6.1. Conclusions

The following conclusions were drawn from the present work

- Fused Silica (SiO_2) based ceramic composites such as SiO_2–Si_3N_4, SiO_2–BN and SiO_2–Si_3N_4–BN have been successfully produced using gelcasting method.

- The rheological behavior of the SiO_2 suspensions including SiO_2–Si_3N_4, SiO_2–BN and SiO_2–Si_3N_4–BN by varying dispersant content, pH value and solid loading has been thoroughly studied and useful ranges of solid loading (SL), monomer content (MC), ratio of monomers (RM), Si_3N_4 and BN contents were decided based on trial experiments and they are as follows.

  1. Solid loading: 68 to 72 vol% for SiO_2 ceramics and 42 to 50 vol% for SiO_2–Si_3N_4, SiO_2–BN and SiO_2–Si_3N_4–BN ceramic composites
  2. Monomer content: 10 to 15 wt%
  3. Ratio of monomers: 3 to 7
  4. Si_3N_4 content: 5 to 15 wt%
  5. BN content: 5 to 15 wt%

- Darvan 821A is recommended as a dispersant and a dosage of 0.5 wt% showed better results over other dispersants in the suspension of ceramic particles as 0.5 wt% Darvan 821A gives the maximum zeta potential value for all SiO_2 suspensions.

- Tests for flexural strength, porosity and dielectric constant were conducted for all the samples of SiO_2, SiO_2–Si_3N_4, SiO_2–BN and SiO_2–Si_3N_4–BN and found that the values of flexural strength, porosity, and dielectric constant are within range of values published in the literature. SiO_2 has low flexural strength whereas SiO_2–Si_3N_4–BN ceramic composite has maximum flexural strength. Comparatively the dielectric constant of SiO_2–Si_3N_4–BN ceramic composite is higher than SiO_2 ceramics.

- The regression models for the analysis of responses such as flexural strength, porosity, and dielectric constant are developed and the effects of the process parameters on these responses are studied.

- The optimum process parameters for maximum flexural strength, maximum porosity, and minimum dielectric constant were evaluated using RSM coupled with desirability function to optimize multiple responses.

- The values of responses i.e. flexural strength, porosity and dielectric constant obtained by experimental runs are compared with predicted regression models for flexural strength, porosity and dielectric constant for SiO_2, SiO_2–Si_3N_4, SiO_2–BN and SiO_2–Si_3N_4–BN ceramic composites.

- The error between experimental and predicted values are evaluated and the maximum error is found to be as follows

Ceramics	Flexural strength	Porosity	Dielectric constant
SiO_2	±2.04%	±2.74%	±0.99%
SiO_2–Si_3N_4	±3.10%	±3.03%	±3.05%
SiO_2–BN	±3.45%	±3.06%	±3.13%
SiO_2–Si_3N_4–BN	±3.44%	±3.29%	±3.24%

Hence it can be declared that the predicted models are confirming with experimental values. Hence the tests are confirmed and recommended that the models are accurate. Thus the RSM models developed for flexural strength, porosity, and dielectric constant can be used to evaluate SiO_2 based ceramic composites.

- It has been found that SiO_2 ceramics is having a lower flexural strength and good porosity and dielectric constant, hence such material may be considered for lower range missile radomes.

- The percentage of improvement or decrement in flexural strength, porosity and dielectric constant for SiO_2–Si_3N_4, SiO_2–BN and SiO_2–Si_3N_4–BN ceramic composites compared with SiO_2 ceramics are evaluated and given below.

SiO_2 base	SiO_2–Si_3N_4	SiO_2–BN	SiO_2–Si_3N_4–BN
Flexural strength	+79.85%	+38.38%	+133.08%
Porosity	+6.19%	-36.02%	-11.40%
Dielectric constant	-76.84%	-9.66%	-12.47%
+ % Increase		- % Decrease	

From the above, it is concluded that a newly developed SiO_2–Si_3N_4–BN ceramic composite is best with respect to strength. Hence this material may be recommended for radomes of medium/lower range missiles.

- Among SiO_2, SiO_2–Si_3N_4, SiO_2–BN and SiO_2–Si_3N_4–BN ceramic composites, SiO_2–BN has no good properties and hence it may not be a good radome material however by the addition of Si_3N_4 in SiO_2–BN the properties enhances. SiO_2–Si_3N_4 ceramic composite may be suitable as a medium range missile radome material.

6.2. Scope for future work

- Fabrication of SiO_2 based ceramic composites such as SiO_2, SiO_2–Si_3N_4, SiO_2–BN and SiO_2–Si_3N_4–BN using gelcasting has been thoroughly investigated in the present work and still there is a scope for further investigation such as considering Si_3N_4 and BN as basic ceramics.
- In this work, only four types of dispersants were used for dispersion of SiO_2 suspensions. Other dispersants such as acrylic acid-2-acrylamido-2-methypropane sulfonic acid copolymer (AA-AMPS) etc., may be used.
- Low-toxic monomers such as 2-hydroxyethyl methacrylate (HEMA) and *N*,*N'*-dimethylacrylamide (DMAA) etc can be used in further studies.
- Further, some studies can be carried out on SiO_2 based ceramic composites by adding other allied ceramics such as Zirconium oxide, Aluminium oxide etc. to enhance the properties of SiO_2 ceramics required for a radome such as flexural strength, porosity and dielectric constant.
- In the present work only rheological and mechanical properties were evaluated. Electrical and electronic properties may be evaluated in the further work.

APPENDIX

1. Colloidal Processing

A colloidal system consists of two phases, a finely distributed particulate phase, and a dispersion medium phase. In colloidal ceramic processing, the dispersed particulate phase is often a solid while the dispersion medium is usually a liquid. Such systems are advantageous since the packing uniformity of the casted green body is much better when compared with traditional powder consolidation methods. This helps in producing a superior, more homogenous microstructure during sintering. The use of a high solids loaded suspension reduces the shrinkage during the drying and sintering procedures while enhancing sinterability. For producing dense ceramics, it is of importance to make the colloidal suspension with the highest solids loading possible with a low enough viscosity so that the slurry can be easily handled, deaired, and poured.

In colloidal ceramic processing, the stable dispersion of ceramic particles is critical for achieving high packing uniformity. When particles are adequately adjacent together, attractive Van der Waals forces can motivate particles to coagulate and settle out of the suspension (Lu, 2012). Such agglomerates can lead to defects in the ceramic part and therefore are not desirable. In order to keep these particles apart, it is necessary to create a repulsive barrier between the particles.

2. Electric Double Layer (EDL) stabilization

One important method to prevail attractive Van der Waals forces is to establish a repulsive barrier via the electric double layer. When oxide particles interact with a polar medium like water, the surfaces develop a charge. There are four sources of this charge:

- Surface group ionization,
- Specific ion adsorption,
- Ion exchange
- A solution of specific ions out of the surface.

The resulting charged surface will attract counter ions from the medium. These counter ions will adsorb onto the particle surface creating a monolayer, which is known as the Stern layer (Stern, 1924). The monolayer is usually not enough to compensate for the surface

charge. Therefore, additional diffuse ions are bound to the surface at a distance away from the particle. This is the diffuse layer. Both the diffuse layer and Stern layer form the electric double layer (Gouy, 1910 and Chapman, 1913) as shown in Figure 1.

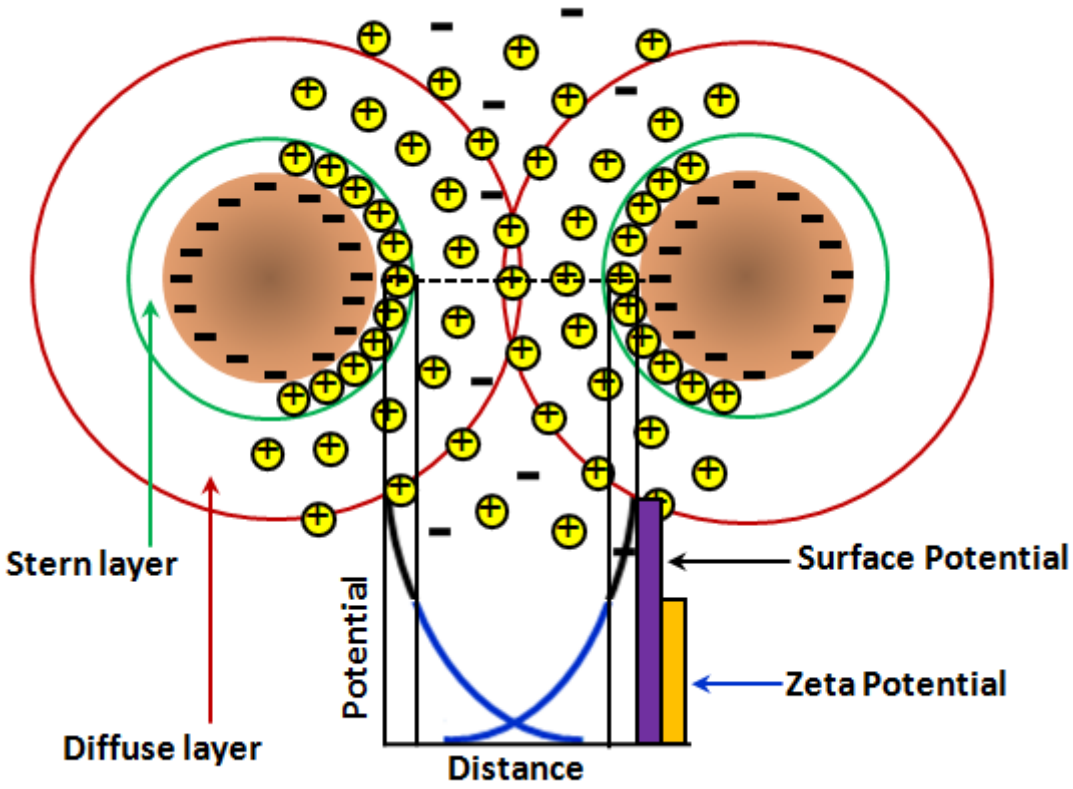

Figure 1. Schematic representation of electrical double layer

To determine the electric double layer force of a particle, it is necessary to measure its surface potential. However, it is not directly possible to measure the potential at the surface of the particle because of hydrodynamic nature of the system which gives rise to a fine monolayer of liquid attached to the particles (Hunter, 1981). Therefore, the zeta potential is measured as shown in Figure 1. The zeta potential is a measure of the potential at the hydrodynamic shear plane of the particle (Yang et al., 2003). This is measured by setting the particle in motion by a sound wave or an electric field (Hunter, 2001). The particles will undergo movement and which will cause a shear plane to develop. This shear plane is in between the stern and diffuse layer. The zeta potential is therefore not a direct measurement of stern potential but a close one and is a measure of the stability of the colloidal system.

3. Colloidal Stability

There are several methods to prevail the attractive Van der Waals forces in colloidal dispersions. These methods involve modifying the surface of the particles by electric charges (electrostatic stabilization), by polymers (steric stabilization) or a blend of both (electrosteric stabilization) (Yang et al., 2003).

3.1. Electrostatic stabilization (DLVO theory)

As mentioned earlier, the charged surfaces of particles will create a double layer which will stabilize the system. When two particles come together, their double layers interact creating repulsion as shown in Figure 1.7. The interaction of the particle double layers changes the entropy due to a local excess of charges. This creates an osmotic pressure which forces liquid to flow between the particles to lower the charge buildup due to the interaction of the double layers (Horn, 1995). This will lead to the separation of the particles.

The DLVO theory suggests that the total energy (stability) of the colloidal system is the combination of the attractive Van der Waals forces and the repulsive electric double layer forces (Verwey et al., 1948). Typically the sum of the attractive and repulsive forces results in one maximum and two minima as shown in Figure 2.

The height of the maximum, which is the net energy barrier, helps to resist particles from coming into contact. Merely a small amount of particles with the effective kinetic energy can prevail this energy barrier, and therefore, the system will be colloidally stable. The two minima in Figure 1.8 are because of the Van der Waals attraction forces. At the primary minima, strong coagulation occurs which is can be irreversible. However, in the secondary minimum, the coagulation is weaker. This occurs since the particles are divorced by quite large distances after coagulation. These weak coagulates can be reversed and be broken up into a dispersed suspension. By altering the ionic strength of the medium the repulsive electric double layer is able to be changed.

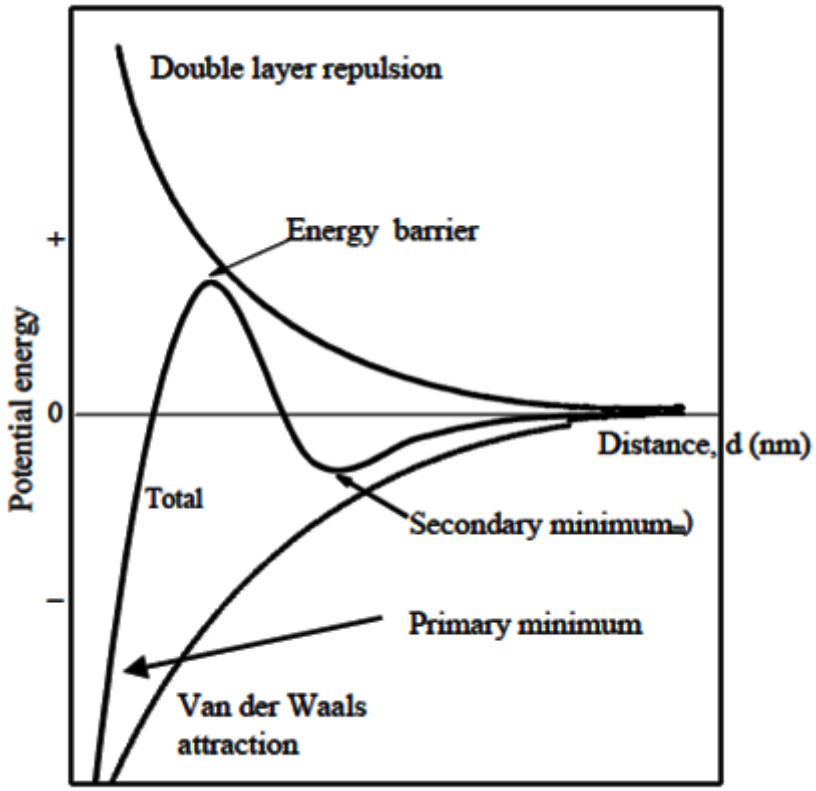

Figure 2. DLVO theory

By altering the ionic strength of the solution, the range of repulsive electric double layer can be changed and the strength of repulsion can also be varied using this mechanism. For instance, with numerous oxide surfaces in water, the charge is determined by proton association/dissociation with surface hydroxyl groups (Ma et al., 2003 and Ma et al. 2005).

$$-M-H_2O^+ \xleftarrow{H^+} -M-OH \xrightarrow{OH^-} -M-O^- + H_2O$$

Charged oxide surfaces can be produced in water when the M-OH surface sites react with either H_3O+ or OH- ions. By governing the pH, the net surface charge can be either positive (acidic conditions), neutral, or negative (basic conditions). The pH that produces a neutral surface is called iso-electric point (IEP). At IEP, the thickness of the double layer is zero, the van der Waals attraction dominates the inter-particle reaction, and thus, flocculation occurs.

3.2. Steric and electrosteric stabilization

An alternative way of dispersing particle is by steric and electrosteric means. There are situations where a small electric double-layer barrier exists, which is too low to stabilize. For these cases, steric (Lange, 1989) and electrosteric stabilization (Biggs and Healy, 1994) have been developed. Since this study did not involve these stabilization methods, a brief description is provided.

Steric stabilization involves organic macromolecules which adsorb to the surface of the particles. For a good steric dispersant, the macromolecules should accumulate onto the surface and be able to be soluble in the dispersing medium (Sigmund et al., 2005). This dispersant modifies the particle surface. If such particles approach one another, the adsorbed polymer layers will interact and penetrate into another. This results in a decrease of the freedom of the polymer movement and therefore changes the entropy of the system (Yaghobizadeh et al., 2014). An increase in the osmotic pressure will result causing liquid to flow in, which will separate and disperse the particles. It is important that enough polymer is added to the system for complete surface coverage. If this does not happen, the polymer chain may adsorb on different particles creating a network which flocculates the system.

Electrosteric forces involve molecules such as polyelectrolytes which provide both steric and electric double layer repulsion. Polyelectrolytes have ionizable side groups, which can then create a charge along the chain (electric double layer interaction) while the chain itself creates steric effects. Electrostatic stabilization is advantageous since it uses long range electric double layer potential but does not decrease at small distances due to the steric effect.

REFERENCES

1. Ahmed, S.M. (2015), "Design and Analysis of Horizontal Axis Windmill Turbine Blade", *International Journal of Innovative Research & Development*, 4, 275-302.
2. Albano, M. P. and Garrido, L. B. (2003), "Influence of yttria-alumina surface coating on the colloidal processing of silicon nitride slips," *Ceram. Int.*, 29, 829–836.
3. Baader, F.H., Graule, T.J. and Gauckler, L.J. (1996), "Direct coagulation casting - A new green shape technique. Part II: Application to alumina", *Ind. Ceram.*, 16, 36-40.
4. Balamurugana, K., Mishrab, M.K., Sathiyab, P. and Sait, A.N. (2014), "Weldability Studies and Parameter Optimization of AISI 904L Super Austenitic Stainless Steel Using Friction Welding", *Materials Research*, 17, 908-919.
5. Balzer, B., Hruschka, M.K.M. and Gauckler, L.J. (1999), "Coagulation kinetics and mechanical behavior of wet alumina green bodies produced via DCC", *J. Colloid Interface Sci.*, 216, 379-386.
6. Bell, N.S., Wang, L.W., Sigmund, W.M. and Aldinger, F. (1999), "Temperature induced forming: Application of bridging flocculation to near-net shape production of ceramic parts", *Z. Metallkd.*, 90, 388-392.
7. Bengisu, M. and Yilmaz, E. (2002), "Gelcasting of alumina and zirconia using chitosan gels", *Ceram. Int.*, 28, 431–438.
8. Bergstrom, L. and Sjostrom, E. (1999), "Temperature induced gelation of concentrated ceramic suspensions: Rheological properties", *J. Eur. Ceram. Soc.*, 19**,** 2117-2123.
9. Biggs, S. and Healy, T.W. (1994), "Electrosteric Stabilization of Colloidal Zirconia with Low-Molecular-Weight Polyacrylic-Acid-an Atomic-Force Microscopy Study", *Journal of the Chemical Society-Faraday Transactions*, 90, 3415-3421.
10. Box, G. E. P., and Draper, N. R. (1987), "Empirical Model Building and Response Surfaces", John Wiley & Sons, New York, NY.
11. Cai, K., Huang, Y. and Yang, J.L. (2003), "Gelcasting of alumina with low-toxicity HEMA system", *Journal of Inorganic Materials*, 18, 343-347.
12. Chandradass, J., Kim, K.H., Bae, D., Prasad, K., Balachandar, G., Divya, S. A. and Balasubramanian, M. (2009), "Starch consolidation of alumina: fabrication and mechanical properties", *J. Eur. Ceram. Soc.*, 29, 2219–2224.
13. Chapman, D. (1913), "A contribution to the theory of electrocapillarity", *Phil. Mag.*, 25, 475-481.

14. Chelule, K.L., Coole, T.J. and Cheshire, D.G. (2003), "An investigation into the machinability of hydroxyapatite for bone restoration implants", *Journal of Materials Processing Technology*, 135, 242–246.
15. Chen, F., Shen ,Q. and Zhang, L. (2010), "Electromagnetic optimal design and preparation of broadband ceramic radome material with graded porous structure," *Prog. Electromagn. Res.*, 105, 445-461.
16. Chen, F., Shen, Q. and Zhang L. (2010), "Electromagnetic optimal design and preparation of broadband ceramic radome material with graded porous structure," *Prog. Electromagn. Res.*, 105, 445-461.
17. Chen, Y.L., Xie, Z.P., Yang, J.L. and Huang, Y. (1999), "Alumina casting based on gelation of gelatine", *J. Eur. Ceram. Soc.*, 19, 271-275.
18. Chin, S. S. (1961), "Missile Configuration Design", Chapter:3, McGraw-Hill Book Company, Inc.
19. Crowell, G. A. (1996), "The descriptive geometry of nose cones", [Online]. Available at: http://projetosulfos.if.sc.usp.br/artigos/NoseCone_EQN2.PDF.
20. Derjaguin, B.V. and Landau, L. (1941), "Theory of stability of highly charged lyophobic sols and adhesion of highly charged particles in solutions of electrolytes", *Acta Physicochim. URSS*, 1941, 14, 633-662.
21. Dobraszczyk, B.J. and Morgenstern, M.P. (2003), "Rheology and the breadmaking process", *Journal of Cereal Science*, 38, 229–245.
22. Dong, W., Wang, C. A., Yu, L. and Ouyang, S. X. (2012), "Effect of Sintering Additive Content on Mechanical and Dielectric Properties of Porous Si_3N_4/BN Composite Ceramics", *J. of the Chinese Ceramic Society*, 40, 851-855.
23. Dong, W., Wang, C. A., Yu, L. and Ouyang, S. X. (2012), "Preparation and Properties of Porous Si_3N_4-SiO_2-BN Composite Ceramics", *Key Engineering Materials*, 512-515, 828-831.
24. Du, M., Bi, J.Q., Wang, W.L., Sun, X.L. and Long, N.N. (2011), "Microstructure and properties of SiO2 matrix reinforced by BN nanotubes and nanoparticles", *Journal of Alloys and Compounds*, 509, 9996– 10002.
25. Eichler, J. and Lesniak, C. (2008), "Boron nitride (BN) and BN composites for high-temperature applications", *J. Eur. Ceram. Soc.*, 28, 1105–1109.
26. Ekstrom, T. and Soderlund, E. (1990), "Pressureless sintering of Y2O3-CeO2-doped sialons," *J. Mater. Sci.*, 25, 4815–4821.

27. Ewais, E.M.M. and Ahmed, Y.M.Z. (2002), "Consolidation of silicon carbide in aqueous medium based on gelation of agarose", *British Ceramic Transactions*, 101, 255-258.

28. Feng, Y., Gong, H., Zhang, Y., Wang, X., Che, S., Zhao, Y. and Guo, X. (2016), "Effect of BN content on the mechanical and dielectric properties of porous BNp/Si_3N_4 ceramics", *Ceram. Int.*, 42, 661–665.

29. Fukasawa, T., Deng, Z.Y., Ando, M., Ohji, T. and Goto, Y. (2001), "Pore structure of porous ceramics synthesized from water-based slurry by freeze-dry process", *J. Mater. Sci.*, 36, 2523–2527.

30. Ganesh, I. (2011), "Development of β-SiAlON based ceramics for radome applications", *Processing and Application of Ceramics*, 5 [3], 113–138.

31. Ganesh, I. and Sundararajan, G. (2010), "Hydrolysis-induced aqueous gelcasting of β-SiAlON–SiO2 ceramic composites: The effect of AlN additive," *J. Am. Ceram. Soc.*, 93, 3180–3189.

32. Ganesh, I. and Sundararajan, G. (2010), "Hydrolysis-induced aqueous gelcasting of β-SiAlON–SiO_2 ceramic composites: The effect of AlN additive," *J. Am. Ceram. Soc.*, 93, 3180–3189.

33. Ganesh, I., Thiyagarajan, N., Jana, D.C., Barik, P.and Sundararajan, G. (2008), "An aqueous gelcasting route to dense β-$Si_4Al_2O_2N_6$–0.5SiO_2 ceramics," *J. Am. Ceram. Soc.*, 91, 1566–1571.

34. Ganesh, I., Thiyagarajan, N., Jana, D.C., Mahajan, Y.R. and Sundararajan, G. (2008a), "Aqueous gelcasting process for β-$Si_4Al_2O_2N_6$ ceramics," *J. Am. Ceram. Soc.*, 91, 3121–3124.

35. Gauckler, L.J., Graule, T. and Baader, F. (1999), "Ceramic forming using enzyme catalyzed reactions", *Mater. Chem. Phys.*, 61, 78-102.

36. Geith, A., Kulig, M., Hofmann, T. and Russel, C. (1993), "Thermal conductivity of calcium-doped aluminium nitride ceramics," *J. Mater. Sci.*, 28, 865–869.

37. Gilde, G., Patel, P., Hubbard, C., Pothier, B., Hynes, T., Croft, W. and Wells, J. (1997) "SiON low dielectric constant ceramic nanocomposite," U.S. Patent No. 5,677,252.

38. Goto, Y. and Komatsu, M. (1999), "Fracture strength and microstructure of β-SiAlON with hafnia addition," *J. Am. Ceram. Soc.*, 82, 1467–1472.

39. Gouy, G. (1910), "Constitution of the Electric Charge at the Surface of an Electrolyte*". J. Phys.* 9, 457-467.

40. Graule, T.J., Baader, F.H. and Gauckler, L.J. (1995), "Casting uniform ceramics with direct coagulation", *Chemtech*, 25, 31-37.
41. Graule, T.J., Gauckler, L.J. and Baader, F.H. (1996), "Direct coagulation casting - A new green shaping technique.Part I: Processing principles", *Ind. Ceram.*, 16, 31-35.
42. Green, T.J. and Launsby, R.G. (1995), "Using DOE to reduce costs and improve the quality of microelectronic manufacturing processes", *Int. J. Microcircuits Electron. Packag.*, 18, 290-296.
43. Greil, P. (1989), "Processing of silicon nitride ceramics," *Mater. Sci. Eng.*, 109, 27-35.
44. Gu, J., Fan, Y., Zhang, Y. H. and Wu, D. K. (2009), "Novel 3-D half-mode SICC resonator for microwave and millimeter-wave applications," *J. of Electromagnetic Waves and Applications*, 23, 1429–1439.
45. Ha, J. S. (2000), "Effect of Atmosphere Type on Gelcasting Behavior of Al2O3 and Evaluation of Green Strength", *Ceram. Int.*, 26, 251–254.
46. Han, J.C., Sun, Y.B. and Zhang, Y.M. (2010), "Dielectric properties in GHz range of porous Si_3N_4–BN–SiO_2 ceramics with considerable flexural strength prepared by low temperature sintering in air", *Materials Science and Technology*, 26, 996-1000.
47. Haris, J. N. and Welsh, E. A. (1973), Fused Silica Design Manual, AD-766494.
48. Heieh, M. Y., "Silicon nitride having low dielectric loss", U.S. Patent 4,642,299, 1987.
49. Hirosaki, N. and Okada, A. (1989), "Change in oxygen content of Y_2O_3-Nd_2O_3-doped silicon nitride during firing," *J. Am. Ceram. Soc.*, 72, 2359–2360.
50. Horn, R.G. (1995), "Particles Interactions in Suspensions", Chapter:3, Ceramic Processing, edited by Terpstra, R.A., Pex, P.P.A.C. and Vries, A.H., Chapman & Hall 1995, 58-100.
51. Hsieh, M. Y., Mizuhara, H. and Smith, P. W. (1984), "Pressureless sintered silicon nitride as a promising candidate for radome materials," 17th Symposium on Electromagnetic Windows, Atlanta, July 25‑27.
52. Hsu, S.M. and Shen, M. (2004), "Wear prediction of ceramics", Wear, 256, 867–878.
53. Huang, Y. and Yang, J. (2010), "Gelation Forming Process for Low Toxicity System", Chapter:3, *Novel Colloidal Forming of Ceramics*, Springer, p.116.
54. Huha, M.A. and Lewis, J.A. (2000), "Polymer effects on the chemorheological and drying behavior of alumina-poly(vinyl alcohol) gelcasting suspensions", *J. Am. Ceram. Soc*, 83, 1957-1963.

55. Hunn, D.L. Richardson, K.K. and Freitag, D.W. (1995), "Barium aluminosilicate reinforced in- situ with silicon nitride," *J. Am. Ceram. Soc.*, 378, 2662–68.

56. Hunter, R.J. (1981), "Zeta potential in colloid science: principles and applications", London; New York: Academic Press. xi, 386 p.

57. Hunter, R.J. (2001), "Measuring zeta potential in concentrated industrial slurries", *Colloids and Surfaces A: Physicochemical and Engineering Aspects*, 195, 205-214.

58. Janney, M. A., Nunn, S. D., Walls, C. A., Omatete, O. O., Ogle, R. B., Kirby, G. H. and McMillan, A. D. (1998a), "Gelcasting: The handbook of ceramic engineering", ed, M.N. Rahaman. Marcel Dekker Inc, New York, 1-15.

59. Janney, M.A., Omatete, O.O., Walls, C.A., Nunn, S.D., Ogle, R.J. and Westmoreland, G. (1998), "Development of low-toxicity gelcasting systems", *J. Am. Ceram. Soc*, 81, 581-591.

60. Jia, D., Zhou, L., Yang, Z., Duan, X. and Zhou, Y. (2011), "Effect of Preforming Process and Starting Fused SiO2 Particle Size on Microstructure and Mechanical Properties of Pressurelessly Sintered BNp/SiO2 Ceramic Composites", *J. Am. Ceram. Soc.*, 94, 3552–3560.

61. Jia, D.C., Zhou, Y. and Lei, T.C. (2003), "Ambient and elevated temperature mechanical properties of hot-pressed fused silica matrix composite', *J. Eur. Ceram. Soc.*, 23, 801–808.

62. Jiang, Y.G., Zhang, C.R., Cao F., Wang, S.Q., Hu, H.F. and Qi, G.J. (2007b), "Fabrication of High Performance 2.5D SiO_{2f}/Si_3N_4-BN Composites for High-temperature Application", *Advanced Engineering Materials*, 9, 114-116.

63. Jiang, Y.G., Zhang, C.R., Cao, F., Wang, S.Q., Hu, H.F. and Qi, G.J. (2007a), "Moisture behavior and effects on the mechanical properties and the microstructures of SiO_{2f}-Si_3N_4–BN amorphous composites", *J. of Non-Crystalline Solids*, 353, 2301–2305.

64. Jones, R.W. (2000), "Near net shape ceramics by freeze casting", *Industrial Ceramics*, 20, 117-120.

65. Jong, B.W., Slavens, G.J. and Traut, D.E. (1992) "Synthesis of silicon and silicon nitride powders by vapour-phase reactions", *Journal of Materials Science*, 27(22), 6086–6090.

66. Joray, R., Yu, B., Lange, F. and PollingerJ. (2002), "Optimization of an aqueous, commercial silicon nitride slurry for colloidal Isopressing", *J. Eur. Ceram. Soc.*, 22, 1061–1066.

67. Kawai, C., Matsuura, T. and Yamakawa, A. (1999), "Separation–permeation performance of porous Si3N4 ceramics composed of columnar β- Si_3N_4 grains as membrane filters for microfiltration*," J. Mater. Sci.*, 34, 893–896.

68. Kim, D.W. (2008), "Application of Design of Experiment Method for Thrust Force Minimization in Step-feed Micro Drilling", *Sensors*, 8, 211-221.

69. Kirby, K. W., Jankiewicz, A. T., Lowell, R. F. and Hallse, R. L. (2000), "Near net shape fabrication of ceramic radomes," U.S. Patent No 6,083,452.

70. Kissa, E. (1999), "Dispersions: Characterization, Testing, and Measurement", *Surfactant Science Series*, 84, CRC Press

71. Koch, D., Andresen, L., Schmedders, T. and Grathwohl, G. (2003), "Evolution of porosity by freeze casting and sintering of sol-gel derived ceramics", *Journal of Sol-Gel Science and Technology*, 26, 149-152.

72. Koetje, E. L., Simpson, F. H. and Schorsch, J. F. (1987), "Broadband high temperature radome apparatus", U.S. Patent 4,677,443.

73. Kokabi, M., Babaluo, A.A. and Barati, A. (2006), "Gelation process in low-toxic gelcast- ing systems", *J. Eur. Ceram. Soc.*,26, 3083–3090.

74. Kong, D., Yang, H., Wei, S., Li, D. and Wang, J. (2007), "Gel-casting without de-airing process using silica sol as a binder", *Ceram. Int.*, 33, 133–139.

75. Kong, L.B., Huang, Y.Z., Que, W.X., Zhang, T.S., Li, S., Zhang, J., Dong, Z.L., Tang, D.Y. (2015), "Powder Characterization and Compaction", Chapter:4, Transparent Ceramics, Part of the series Topics in Mining, Metallurgy and Materials Engineering, 191-290.

76. Kosmac, T. (1999), "The potential of the Hydrolysis Assisted Solidification (HAS) process for wet forming of engineering ceramics", *Materials Science Forum*, 161-163, 357-362.

77. Kosmac, T., Novak, S. and Krnel, K. (2001), "Hydrolysis assisted solidification process and its use in ceramic wet forming", *Z. Metallkd*, 92, 150-157.

78. Kosmac, T., Novak, S. and Sajko, M. (1997), "Hydrolysis-assisted solidification (HAS): A new setting concept for ceramic net-shaping", *J. Eur. Ceram. Soc.*, 17, 427-432.

79. Kozakoff, D.J., "Analysis of Radome-Enclosed Antennas", Artech House, Boston, 1997, 55-76.

80. Krnel, K. and Kosmac, T. (2003), "Use of hydrolysis-assisted solidification (HAS) in the formation of Si_3N_4 ceramics", *Materials Science Forum*, 413, 75-80.

81. Lange, F.F. (1989), "Powder processing science and technology for increased reliability*", J. Am. Ceram. Soc.*, 72, 3-15.

82. Laurie, J., Bagnall, C.M., Harris, B., Jones, R.W., Cooke, R.G., Russellfloyd, R.S., Wang, T.H. and Hammett, F.W. (1992), "Colloidal suspensions for the preparation of ceramics by a Freeze Casting Route", *J. of Non-Crystalline Solids*, 147, 320-325.

83. Li, D., Zhang, C., Li, B., Cao, F., Wang, S., Yang, B.and Liu, K. (2012), "Effects of oxidation treatment on properties of SiO_{2f}/SiO_2-BN composites," *J. Cent. South Univ.*, 19, 30–35.

84. Li, F., Chen, H.Y., Wu, R.Z. and Sun, B.D. (2004), "Effect of polyethylene glycol on the surface exfoliation of SiC green bodies prepared by gelcasting", *Mater. Sci. Eng. A*, 368, 255–259.

85. Li, J., Wu, T., Yu, Z., Zhang, L., Chen, G. and Guo, D. (2012), "Micro machining of pre-sintered ceramic green body", *Journal of Materials Processing Technology*, 212, 571– 579.

86. Li, X., Yin, X., Zhang, L., Cheng, L. and Qi, Y. (2009), "Mechanical and dielectric properties of porous Si_3N_4–SiO_2 composite ceramics", *Mater. Sci. Eng. A*, 500, 63–69.

87. Li, Y. and Guo, Z. (2008), "Gelcasting of WC–8wt%Co tungsten cemented carbide", *International Journal of Refractory Metals & Hard Materials*, 26, 472–477.

88. Li, Y., Guo, Z.M., Hao, J.J. and Ren, S. (2008), "Gelcasting of metal powders in nontoxic cellulose ethers system", *Journal of Materials Processing Technology*, 208, 457–462.

89. Li, C., Han, Q., Guan, Y. and Zhang, Y. (2014), "Thermal gelation of chitosan in an aqueous alkali–urea solution", *Soft Matter*, 10, 8245-8253.

90. Lin, S., Ye, F., Ma, J., Ding, J., Yang, C. and Dong, S. (2016), "Fabrication of multilayer electronic magnetic window material by Si_2N_2O decomposition", *Materials and Design*, 97, 51–55.

91. Liu, K., Zhang, C., Li, B., Wang, S. and Cao, F. (2013), "Effect of Pyrolysis Temperature on Properties of Porous Si_3N_4-BN Composites Fabricated Via PIP Route", *J. of Mater. Engg. and Performance*, 22, 3684–3688.

92. Liu, K., Zhang, C., Li, B., Wang, S. and Cao, F. (2014), "Synthesis of Porous Silicon Nitride-Boron Nitride Composites by Gel-Casting and PIP", *Journal of Materials Engineering and Performance*, 23, 2829–2833.

93. Liu, K., Zhang, C., Li, B., Wang, S. and Cao, F. (2015), "Microstructure, Mechanical and Dielectric Properties of Si_3N_4-BN Composites with Different Porosities", *Materials Science Forum*, 816, 40-47.

94. Long, N.N., Bi, J.Q., Wang, W.L., Du, M. and Bai, Y.J. (2012), "Mechanical properties and microstructure of porous BN–SiO_2–Si_3N_4 composite ceramics", *Ceram. Int.*, 38, 2381–2387.

95. Lu, K. (2012), "Nanoparticle-Based Material Shaping, in Nanoparticulate Materials: Synthesis, Characterization, and Processing", John Wiley & Sons, Inc., Hoboken, NJ, USA. doi: 10.1002/9781118408995.ch5.

96. Lu, Z., Geng, H., Zhang, M. and Hou, X. (2008), "Preparation of aluminum borate whisker reinforced aluminum phosphate wave-transparent materials," *Chin. Sci. Bull.*, 53, 3073–3076.

97. Lyons, J. S. and Starr, T. L. (1994), ''Strength and Toughness of Slip-Cast Fused-Silica Composites,'' *J. Am. Ceram. Soc.*, 77, 1673–1675.

98. Ma, J.T., Xie, Z.P., Miao, H.Z., Huang, Y. and Cheng, Y.B. (2002a), "Gelcasting of ceramic suspension in acrylamide/polyethylene glycol systems", *Ceram. Int.*, 28, 859–864.

99. Ma, J.T., Xie, Z.P., Miao, H.Z., Huang, Y. and Cheng, Y.B. (2002b), "Inhibitive role and mechanism of water-soluble polymer PVP on the surface-exfoliation problem of ceramic green bodies prepared by gelcasting", *J. Inorg. Mater.*, 3, 480–488.

100. Ma, J.T., Xie, Z.P., Miao, H.Z., Huang, Y., Cheng, Y.B. and Yang, W.Y. (2003), "Gelcasting of alumina ceramics in the mixed acrylamide and polyacrylamide systems", *J. Eur. Ceram. Soc.*, 23, 2273-2279.

101. Ma, J.T., Xie, Z.P., Miao, H.Z., Zhou, L.J., Huang, Y. and Cheng, Y.B. (2003), "Elimination of surface spallation of alumina green bodies prepared by acrylamide-based gelcasting via poly(vinylpyrrolidone)", *J. Am. Ceram. Soc.*, 86, 266-272.

102. Ma, J.T., Yi, Z.Z., Xie, Z.P., Zhou, L.J., Miao, H.Z., Zhang, B.Q. and Lin, X.P. (2005), "Gelcasting of alumina with a mixed PVP-MAM system", *Ceram. Int.*, 31, 1015-1019.
103. Mandal, H. and Hoffmann, M.J. (1999), "Preparation of multiple-cation α-SiAlON ceramics containing lanthanum", *J. Am. Ceram. Soc.*, 82, 229–232.
104. Manivannan, R., Anil Kumar, and Subrahmanyam, Ch. (2013), "Aqueous Gelcasting of Fused Silica Using Colloidal Silica Binder", J. Am. Ceram. Soc., 96, 2432-2436.
105. Mao, X, Wang, S. and Shimai S. (2006), "Preparation of Porous Silica Ceramics with Low Dielectric Constant", *Chinese Journal of Aeronautics*, 19, S239-S243.
106. Mao, X, Wang, S. and Shimai S., Dong, M. and Jin, L. (2009), "Rheological characterization of a gelcasting system based on epoxy resin", *Ceram. Int.*, 35, 415–420.
107. Millan, A.J., Baudin, C., Moreo, R. and Nieto, M.I. (2002), "Influence of gelling additives in the green properties of Al_2O_3 bodies obtained by aqueous gel casting", *Key Engineering Materials*, 206-213, 413-416.
108. Millan, A.J., Moreno, R. and Nieto, M.I. (2002), "Thermogelling polysaccharides for aqueous gelcasting - part I: a comparative study of gelling additives", *J. Eur. Ceram. Soc.*, 22, 2209-2215.
109. Millan, A.J., Nieto, M.I., Baudin, C. and Moreno, R. (2002), "Thermogelling polysaccharides for aqueous gelcasting - part II: influence of gelling additives on rheological properties and gelcasting of alumina", *J. Eur. Ceram. Soc.*, 22, 2217-2222.
110. Millan, A.J., Nieto, M.I., Moreno, R. and Baudin, C. (2002), "Thermogelling polysaccharides for aqueous gelcasting - part III: mechanical and microstructural characterization of green alumina bodies", *J. Eur. Ceram. Soc.*, 22, 2223-2230.
111. Mizutani, M. (1986), "Process for preparation sintered silicon nitride body having surface compression stress," U.S. Patent No 4,622,186.
112. Mohajeri, S., Dolati, A. and Rezagholibeiki, S. (2011), "Electrodeposition of Ni/WC nano composite in sulfate solution", *Materials Chemistry and Physics*, 129, 746–750.
113. Montgomery, D.G. (2012), "Design and Analysis of Experiments", 8th edition, John Wiley & Sons, New York, USA.
114. Moreno, R. (1992), "The role of slip additives in tape casting technology: part I–Solvents and dispersants", *Am. Ceram. Soc. Bull.*, 71, 1521–1531.

115. Moreno, R. (1992a), "The role of slip additives in tape casting technology: part II–Sovents and plasticizers", *Am. Ceram. Soc. Bull.*, 71, 1647–1657.

116. Morissette, S.L., Lewis, J.A., Cesarano, J., Dimos, D.B. and Baer, T.Y. (2000), "Solid freeform fabrication of aqueous alumina-poly(vinyl alcohol) gelcasting suspensions", *J. Am. Ceram. Soc.*, 83, 2409-2416.

117. Mortensen, A. and Suresh, S. (1995), "Functionally graded metals and metal-ceramic composites: Part 1 Processing," *Int. Mater. Rev.*, 40, 239–265.

118. Narendra Kumar, A. and Siva RamaKrishna, Ch. (2015), "Experimental Investigation and Analysis of Mechanical Properties of Chopped Strand Mat-E Glass Fiber Polyester Resin & Silica Powder Composite", *Journal of Machinery Manufacturing and Automation*, 4, 1-9.

119. Neil, J. T., Bowen, L. J. and Michaud, B. E. (1990), "Fused silica radome," U.S. Patent 4,949,095.

120. Nie, X., Yuan, N., Li, L., Yeo, T. and Gan, Y. (2005), "Fast analysis of electromagnetic transmission through arbitrarily shaped airborne radomes using precorrected-FFT method," *Prog. Electromagn. Res.*, 54, 37–59.

121. Nojoomi, A., Faghihi-Sani, M.A. and Khoshkalam, M. (2014), "Shear-rate dependence modeling of gelcast slurries: Effects of dispersant content and solid loading", *Ceram. Int.*, 40, 123–128.

122. Novak, S. and Kosmac, T. (1998), "Interactions in aqueous Al_2O_3-AlN suspensions during the HAS process", *Mater. Sci. Eng. A-Structural Materials Properties Microstructure and Processing*, 256, 237-242.

123. Novak, S., Kosmac, T., Krnel, K. and Drazic, G. (2002), "Principles of the hydrolysis assisted solidification (HAS) process for forming ceramic bodies from aqueous suspension", *J. Eur. Ceram. Soc.*, 22, 289-295.

124. Olhero, S.M., Tari, G., Coimbra, M.A. and Ferreira, J.M.F. (2000), "Synergy of polysaccharide mixtures in gelcasting of alumina", *J. Eur. Ceram. Soc.*, 20, 423-429.

125. Omatete, O.O., Janney, M.A. and Nunn, S.D. (1997), "Gelcasting: From laboratory development toward industrial production", *J. Eur. Ceram. Soc.*, 17, 407-413.

126. Omatete, O.O., Janney, M.A. and Strehlow, R.A. (1991), "Gelcasting - a new ceramic forming process", *American Ceramic Society Bulletin*, 70, 1641-1649.

127. Park, D., Lee, S. and Kim, H. (1998), "Extra-large Grains in the silicon nitride ceramics doped with yttria and hafnia," *J. Am. Ceram. Soc.*, 80, 1876–1880.

128. Prabhakaran, K., Ananthakumar, S. and Pavithran, C. (2002), "Preparation of extrudable alumina paste by coagulation of electrosterically stabilized aqueous slurries", *J. Eur. Ceram. Soc.*, 22, 153–158.

129. Prabhakaran, K., Sooraj, R., Melkeri, A., Gokhale, N.M. and Sharma, S.C. (2009), "A new direct coagulation casting process for alumina slurries prepared using poly(acrylate) dispersant", *Ceram. Int.*, 35, 979–985.

130. Pujari, V.K., Tracey, D.M., Foley, M.R., Paille, N.I., Pelletier, P.J., Sales, L.C., Willkens, C.A. and Yeckley R.L. (1995), "Reliable ceramics for advanced heat engines", *American Ceramic Society Bulletin*,. 74, 86-90.

131. Rahaman, M. N. (2003), "Ceramic processing and sintering", Second Edition, Chapter:10, Marcel Dekker, New York.

132. Ranjith Kumar, J.V., Roopa, H.N. and Ramachandra Rao, R. (2007), "Colloidal Processing And Gel Casting Of Alumina", International Conference on Advanced Materials and Composites (ICAMC-2007), Oct 24-26, 2007, Trivandrum 679 – 683.

133. Rao, R.V. (2011), "Advanced Modeling and Optimization of Manufacturing Processes", International Research and Development, Springer-Verlag, London.

134. Reed, J.S. (1995), Principles of ceramics processing. 2nd ed., New York: Wiley & Sons. xxii, 658 p.

135. Renuka, A. and Borkar, V.G. (2005), "Computer-aided analysis for tangent ogive airborne radome using physical optics method," Proceedings of Asia-Pacific Microwave Conference, 2005.

136. Rice, R. W. and Donough, W. J. (1975), "Hot-pressed Si3N4 with Zr-based additions," *J. Am. Ceram. Soc.*, 58, 264.

137. Richerson, D.W. (1992), "Modern Ceramic Engineering: Properties", Processing, and Use in Design. 2nd ed. Engineered materials; New York, Dekker. xv, 860 p.

138. Rivers, R.D. (1978), "Method of injection molding powder metal parts", Patent No. 4113480. United States.

139. Robert Traut, G. (1982), "Method of manufacturing a radome," U.S. Patent No 4,364,884.

140. Santacruz, I., Baudin, C., Moreno, R. and Nieto, M.I. (2004), "Improved green strength of ceramics through aqueous gelcasting", *Advanced Engineering Materials*, 6, 672-676.

141. Santacruz, I., Nieto, M.I. and Moreno, R. (2002), "Rheological characterization of synergistic mixtures of carrageenan and locust bean gum for aqueous gelcasting of alumina", *J. Am. Ceram. Soc.*, 85, 2432-2436.

142. Shanti, N. O., Hovis, D. B., Seitz, M. E., Montgomery, J. K., Baskin, D. M.and Faber, K. T. (2009), "Ceramic laminates by gelcasting," *Int. J. Appl. Ceram. Technol.*, 6, 593–606.

143. Shin, H., Berta, Y. and Speyer, R.F. (1995), "Effect of matrix liquid phase on interphase formation in SiC fibre-reinforced Si_2N_2O-Al_2O_3-CaO composites," *J. Mater. Sci.*, 30, 5621–5631.

144. Si, W.J., Graule, T.J., Baader, F.H. and Gauckler, L.J. (1999), "Direct coagulation casting of silicon carbide components", *J. Am. Ceram Soc.*, 82, 1129-1136.

145. Sigmund, W., Pyrgiotakis, G. and Daga, Amit. (2005), "Theory and Applications of Colloidal Processing", Chapter:11, Chemical Processing of Ceramics, edited by Sridhar, K. and Lee, B., CRC Press 2005, 2 ed., 269-302.

146. Sigmund, W.M., Bell, N.S. and Bergstrom L. (2000), "Novel powder-processing methods for advanced ceramics", *J. Am. Ceram. Soc.*, 83, 1557-1574.

147. Sofie, S.W. and Dogan, F. (2001), "Freeze casting of aqueous alumina slurries with glycerol", *J. Am. Ceram. Soc.*, 84, 1459-1464.

148. Statham, M.J., Hammett, E., Harris, B., Cooke, R.G., Jordan, R.M., and Roche, A. (1998), "Net-shape manufacture of low-cost ceramic shapes by freeze-gelation", *Journal of Sol-Gel Science and Technology*, 13, 171-175.

149. Stern, O. Z. (1924), "The theory of the electrolytic double layer" *Elektrochem*, 30, 508-516.

150. Tari, G. (2003), "Gelcasting ceramics: A review", *American Ceramic Society Bulletin*, 82, 43-46.

151. Telford, J.K. (2007), "A Brief Introduction to Design of Experiments" Johns Hopkins APL Technical Digest, 27, 224-232.

152. Terwilliger, G. R. (1974), "Properties of sintered Si_3N_4," *J. Am. Ceram. Soc.*, 57, 48-49.

153. Trompette, J.L. and Meireles, M. (2003), "Ion-specific effect on the gelation kinetics of concentrated colloidal silica suspensions", *J Colloid Interface Sci*, 263, 522–527.

154. Tsuge, A., Kudo, H. and Komeya, K. (1974), "Reaction of Si3N4 and Y_2O_3 in hot-pressing," *J. Am. Ceram. Soc.*, 57, 269–270.

155. Tsuge, A., Nishida, K. and Komatsu, M. (1975), "Effect of crystallizing the grain-boundary glass phase on the high-temperature strength of hot-pressed Si3N4 containing Y_2O_3," *J. Am. Ceram. Soc.*, 58, 323–326.

156. Vandeperre, L.J., De Wilde, A.M. and Luyten, J. (2003), "Gelatin gelcasting of ceramic components", *Journal of Materials Processing Technology*, 135, 312-316.

157. Verwey, E.J.W., Overbeek, J.T.G. and Nes, K.V. (1948), "Theory of the stability of lyophobic colloids; the interaction of sol particles having an electric double layer", New York: Elsevier Pub. Co. xi, 1-205.

158. Wan, W., Huang, C., Yang, J., Zeng, J., and Qiu,T. (2014a), "Effect of Sintering Temperature on the Properties of Fused Silica Ceramics Prepared by Gelcasting", *Journal of Electronic Materials*, 43, 2566-2572.

159. Wan, W., Yang, Zeng, J., Yao, L. and Qiu T. (2014), "Effect of solid loading on gelcasting of silica ceramics using DMAA", *Ceram. Int.*, 40, 1735–1740.

160. Wan, W., Yang, J., Qiu,T. and Huang, C. (2014b), "Study on Gelcasting of Fused Silica Glass Using Glutinous Rice Flour as Binder", *International Journal of Applied Glass Science*, 5, 401–409.

161. Wan, W., Yang, J., Zeng, J. and Qiu, T. (2013), Gelcasting of fused silica glass using a low-toxicity monomer DMAA, *Journal of Non-Crystalline Solids*, 379, 229–234

162. Wang, H., Yu, J.and Zhang J. (2010), "Preparation and properties of pressureless-sintered porous Si_3N_4," *J. Mater. Sci.*, 45 3671–3676.

163. Wang, S., Jian, D., Yang, Z., Duan, X., Tian, Z. and Zhou Y. (2013), "Effect of BN content on microstructures, mechanical and dielectric properties of porous BN/Si_3N_4 composite ceramics prepared by gel casting", *Ceram. Int.*, 39, 4231–4237.

164. Wang, Y. and Liu, J. (2009), "Aluminum phosphate – mullite composites for high-temperature radome applications," *Int. J. Appl. Ceram. Technol.*, 6, 190–194.

165. Weiru, Z., Chonghai, W., Ling, L., Jian, L. and Wen, C. (2008), "Si_3N_4-BN-SiO_2 Based Microwave-Transparent Materials", *Key Engineering Materials*, 368-372, 913-916.

166. Wen, G., Wua, G.L., Lei, T.Q., Zhou, Y. and Guob, Z. X. (2000), "Co-enhanced SiO2-BN ceramics for high-temperature dielectric applications", *J. Eur. Ceram. Soc.*, 20, 1923-1928.

167. Wu, J., Guo, J. and Li, B. (2000), "Preparation and properties of SiO2 matrix composites doped with AlN particles", *J. Mater. Sci.*, 35, 4895‑4900.

168. Xu, J., Luo, F., Zhu, D., Su, X. and Zhou, W. (2008), "Effect of presintering on the dielectric and mechanical properties of porous reaction-bonded silicon nitride," *Mater. Sci. Eng.*, 488, 167–171.

169. Yaghobizadeh, O., Hamidreza B., and Ali A. (2014), "Investigation of effect of acrylate gel maker parameters on properties of WC preforms for the production of W–ZrC composite", *International Journal of Refractory Metals and Hard Materials*, 45, 130–136.

170. Yang, J., Ferreira, M. F. and Weng, W. (1998), "Dispersion properties of silicon nitride powder coated with yttrium and aluminium precursors," *J. Colloid Interface Sci.*, 206, 274–280.

171. Yang, J., Ohji, T., Kanzaki, S., Diaz, A. and Hampshire, S. (2002), "Microstructure and mechanical properties of silicon nitride ceramics with controlled porosity," *J. Am. Ceram. Soc.*, 85, 1512–1516.

172. Yang, J., Yu, J. and Huang, Y. (2011), "Recent developments in gelcasting of ceramics", *J. Eur. Ceram. Soc.*, 31, 2569–2591

173. Yang, Y. and Sigmund, W.M. (2002), "Rheological properties and gelation threshold of temperature induced forming (TIF) alumina suspensions with variation in molecular weight of polyacrylic acid", *Journal of Materials Synthesis and Processing*, 10, 249-255.

174. Yang, Y., Laarz, E., Kaushik, S., Mueller, E. and Sigmund, W. (2003), "Forming and Drying", Chapter:3, Handbook of Advanced Ceramics, edited by Somiya, S., Aldinger, F., Spriggs, R.M., Uchino, K., Koumoto, K. and Kaneno, M., Academic Press 2003, 131-185.

175. Yang, Y.P. and Sigmund, W.M. (2001), "Effects of calcium ion addition on dispersant adsorption in temperature induced forming (TIF) alumina slurry", *Journal of Materials Science Letters*, 20, 651-653.

176. Yang, Y.P. and Sigmund, W.M. (2001), "Preparation, characterization, and gelation of temperature-induced forming (TIF) alumina slurries", *Journal of Materials Synthesis and Processing*, 9, 103-109.

177. Young, A.C., Omatete, O.O., Janney, M.A. and Menchhofer, P.A. (1991), "Gelcasting of alumina", *J. Am. Ceram. Soc.*, 74, 612–618.

178. Yu, B.C. and Lange, F.F. (2001), "Colloidal Isopressing: A New Shape-Forming Method", *Advanced Engineering Materials*,13, 276–280.

179. Yuan, B., Liu, J.X, Zhang, G.J., Kan Y.M. and Wang, P.L. (2009), "Silicon nitride/boron nitride ceramic composites fabricated by reactive pressureless sintering", *Ceram. Int.*, 35, 2155–2159.

180. Zeng, H. and Liu, K. (2015), "Machinability of Engineering Materials", Chapter:22, Handbook of Manufacturing Engineering and Technology, edited by Nee, A.Y.C., Springer 2015, 899-939.

181. Zeng, Y., Yang, J., Kondo, N., Ohji, T., Kita, H. and Kanzaki, S. (2005), "Fracture energies of tape-cast silicon nitride with β-Si3N4 seed addition," *J. Am. Ceram. Soc.*, 88, 1622–1624.

182. Zhai, H., Cai, H., Yang, X. Li, J., Guo, G. and Cao, C. (2007), "Preparation and Properties of BN-SiO_2 Composite Ceramics", *Key Engineering Materials*, 336-338, 1426-1428.

183. Zhao, Y., Zhang, Y., Gong, H., Wang, X., Sun, H. (2015), "Effects of Y_2O_3–MgO nanopowders content on mechanical and dielectric properties of porous BN/Si3N4 composites", *Ceram. Int.*, 41, 3618–3623.

184. Zheng ,Y.S., Knowles, K.M., Vieira, J.M., Lopes, A.B. and Oliveira, F.J. (2001), "Microstructure, toughness and flexural strength of self-reinforced silicon nitride ceramics doped with yttrium oxide and ytterbium oxide," *J. Microsc.*, 201, 238–249.

185. Zhou, L., Huang, Y., Xie, Z., Zimmermann, A. and Aldinger, F. (2002), "Preparation of Si3N4 ceramics with high strength and high reliability via a processing strategy," *J. Eur. Ceram. Soc.*, 22, 1347–1355.

186. Zhou, L.C., Pei, Y.M., Zhang, R.B. and Fang, D.N. (2012), "A multilayer radome wall structure with passbands having odd times of selected central frequencies," *Journal of Electromagnetic Waves and Applications*, 26, 2154–2164.

187. Zhou, L.J., Huang, Y. and Xie, Z.P. (2000), "Gelcasting of concentrated aqueous silicon carbide suspension". *J. Eur. Ceram. Soc.*, 20, 85-90.

188. Zou, C., Zhang, C., Li, B., Cao, F. and Wang, S. (2012), "Improved properties and microstructure of porous silicon nitride/silicon oxide composites prepared by sol–gel route", *Materials Science & Engineering A*, 556, 648–652.